Ref.
FAA-93-8

DOT/FAA/CT-94/10
DOT-VNTSC-FAA-93-8

FAA Technical Center
Atlantic City International Airport,
N.J. 08405

Fracture and Fatigue Strength Evaluation of Multiple Site Damaged Aircraft Fuselages - Curved Panel Testing and Analysis

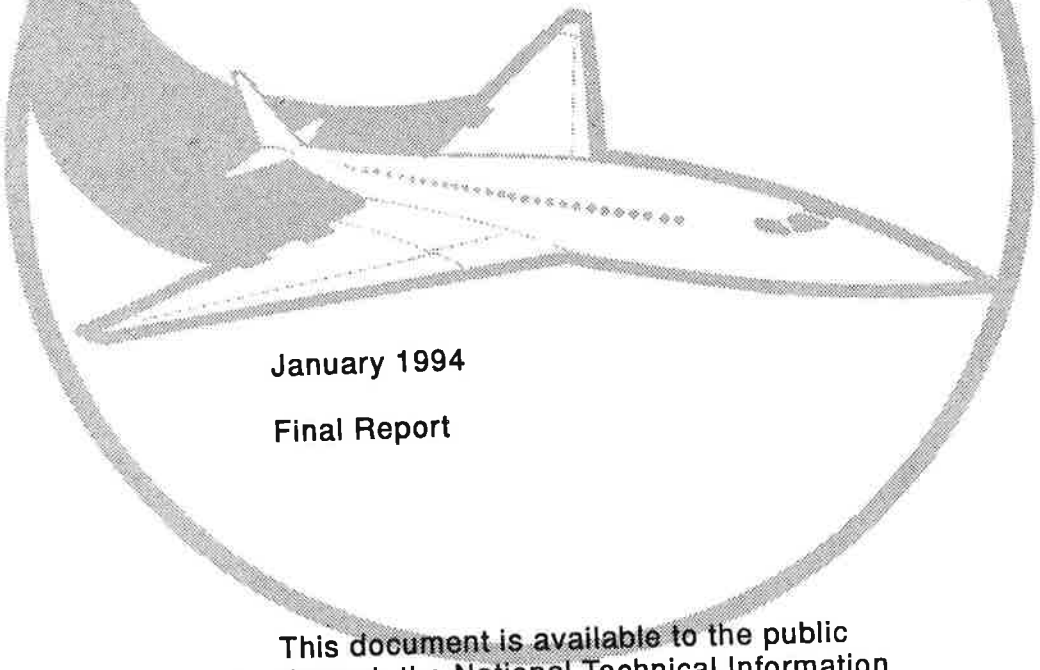

January 1994

Final Report

This document is available to the public through the National Technical Information Service, Springfield, Virginia 22161.

U.S. Department of Transportation
Federal Aviation Administration

REPORT DOCUMENTATION PAGE

Form Approved
OMB No. 0704-0188

Public reporting burden for this collection of information is estimated to average 1 hour per response, including the time for reviewing instructions, searching existing data sources, gathering and maintaining the data needed, and completing and reviewing the collection of information. Send comments regarding this burden estimate or any other aspect of this collection of information, including suggestions for reducing this burden, to Washington Headquarters Services, Directorate for information Operations and Reports, 1215 Jefferson Davis Highway, Suite 1204, Arlington, VA 22202-4302, and to the Office of Management and Budget, Paperwork Reduction Project (0704-0188), Washington, DC 20503.

1. AGENCY USE ONLY (Leave blank)	2. REPORT DATE	3. REPORT TYPE AND DATES COVERED
	January 1994	Final Report August 1989 - March 1991

4. TITLE AND SUBTITLE
Fracture and Fatigue Strength Evaluation of Multiple Site Damaged Aircraft Fuselages - Curved Panel Testing and Analysis

5. FUNDING NUMBERS
FA3H2/A3128
DTRS-57-89-D-00009
Task VA9007

6. AUTHOR(S)
G. Samavedam, D. Hoadley

7. PERFORMING ORGANIZATION NAME(S) AND ADDRESS(ES)
Foster-Miller, Inc.*
350 Second Avenue
Waltham, MA 02154-1196

8. PERFORMING ORGANIZATION REPORT NUMBER
DOT-VNTSC-FAA-93-8

9. SPONSORING/MONITORING AGENCY NAME(S) AND ADDRESS(ES)
U.S. Department of Transportation
Federal Aviation Administration Technical Center
Atlantic City, NJ 08405

10. SPONSORING/MONITORING AGENCY REPORT NUMBER
DOT/FAA/CT-94/10

11. SUPPLEMENTARY NOTES
*Under Contract to: U.S. Department of Transportation
Volpe National Transportation Systems Center
Kendall Square
Cambridge, MA 02142

12a. DISTRIBUTION/AVAILABILITY STATEMENT
This document is available to the public through the National Technical Information Service, Springfield, VA 22161

12b. DISTRIBUTION CODE

13. ABSTRACT (Maximum 200 words)

As the fleet of commercial passenger aircraft is utilized beyond their design lives, flaws have developed at the rivet holes of fuselage lap joints on some aircraft which can grow and link up into cracks of significant length. Understanding, predicting, and controlling this crack growth and the ensuing linkup requires analysis and evaluation of the structural parameters in concert with confirmation by testing representative models of the fuselage.

A dedicated test facility has been designed, built and tested for this purpose. Seven full-sized curved fuselage panels have been built and tested. This report describes the design rationale for the facility, the details of its construction and performance and the design and testing of compatible panels which simulate fuselage structural details.

Data on basic material properties of interest to the aging aircraft issue have been compiled from existing literature and from R-curve testing and rivet stiffness testing performed as part of the effort.

Analytic techniques have been developed to evaluate stress distributions and to estimate elastic stress intensity factors for flat and curved test panels. A flat test panel has been designed that demonstrates hoop stress equivalence to the curved fuselage. A 3-D FE mesh of a riveted lap joint is also presented.

14. SUBJECT TERMS
Aging Aircraft, Multiple Site Damage, Fuselage Fracture and Fatigue

15. NUMBER OF PAGES
172

16. PRICE CODE

17. SECURITY CLASSIFICATION OF REPORT	18. SECURITY CLASSIFICATION OF THIS PAGE	19. SECURITY CLASSIFICATION OF ABSTRACT	20. LIMITATION OF ABSTRACT
Unclassified	Unclassified	Unclassified	

PREFACE

In support of the Federal Aviation Administration Technical Center's Aging Aircraft Program, the John A. Volpe National Transportation Systems Center is conducting and managing research to determine if current rules for design, inspection, and maintenance are sufficient to ensure the safe operation of the aging fleet. Particular focus has been given to a phenomenon of multiple cracking that has been observed in several airplanes that have been in service for some time. This phenomenon is commonly referred to as Multiple Site Damage (MSD).

The work reported here is an experimental and analytical investigation of the fracture and fatigue strength of curved stiffened panels that are representative of a fuselage in an actual aircraft structure. Foster-Miller, Inc., under contract with the Volpe Center (Contract No. DTRS57-89-D-00009, Project No. VA9007), has designed and built a unique test facility to conduct these tests. This test facility uses dedicated fuselage panels which contain different types of intentional damage such as a midbay skin crack with and without MSD. The rationale of the test facility design, test procedures, and analytical studies of aircraft panels using finite element analysis are described in this report.

The authors wish to acknowledge the valuable assistance and advice provided by Volpe National Transportation Systems Center technical personnel involved with this project. We also thank Messrs. Douglas Thomson and John McHatton of Foster-Miller for their dedicated effort in support of the test facility preparation and panel testing activities.

METRIC/ENGLISH CONVERSION FACTORS

ENGLISH TO METRIC

LENGTH (APPROXIMATE)

1 inch (in.) = 2.5 centimeters (cm)
1 foot (ft) = 30 centimeters (cm)
1 yard (yd) = 0.9 meter (m)
1 mile (mi) = 1.6 kilometers (km)

AREA (APPROXIMATE)

1 square inch (sq in, in^2) = 6.5 square centimeters (cm^2)
1 square foot (sq ft, ft^2) = 0.09 square meter (m^2)
1 square yard (sq yd, yd^2) = 0.8 square meter (m^2)
1 square mile (sq mi, mi^2) = 2.6 square kilometers (km^2)
1 acre = 0.4 hectares (he) = 4,000 square meters (m^2)

MASS - WEIGHT (APPROXIMATE)

1 ounce (oz) = 28 grams (gr)
1 pound (lb) = .45 kilogram (kg)
1 short ton = 2,000 pounds (lb) = 0.9 tonne (t)

VOLUME (APPROXIMATE)

1 teaspoon (tsp) = 5 milliliters (ml)
1 tablespoon (tbsp) = 15 milliliters (ml)
1 fluid ounce (fl oz) = 30 milliliters (ml)
1 cup (c) = 0.24 liter (l)
1 pint (pt) = 0.47 liter (l)
1 quart (qt) = 0.96 liter (l)
1 gallon (gal) = 3.8 liters (l)
1 cubic foot (cu ft, ft^3) = 0.03 cubic meter (m^3)
1 cubic yard (cu yd, yd^3) = 0.76 cubic meter (m^3)

TEMPERATURE (EXACT)

[(x - 32) (5/9)] °F = y°C

METRIC TO ENGLISH

LENGTH (APPROXIMATE)

1 millimeter (mm) = 0.04 inch (in)
1 centimeter (cm) = 0.4 inch (in)
1 meter (m) = 3.3 feet (ft)
1 meter (m) = 1.1 yards (yd)
1 kilometer (km) = 0.6 mile (mi)

AREA (APPROXIMATE)

1 square centimeter (cm^2) = 0.16 square inch (sq in, in^2)
1 square meter (m^2) = 1.2 square yards (sq yd, yd^2)
1 square kilometer (kn^2) = 0.4 square mile (sq mi, mi^2)
1 hectare (he) = 10,000 square meters (m^2) = 2.5 acres

MASS - WEIGHT (APPROXIMATE)

1 gram (gr) = 0.036 ounce (oz)
1 kilogram (kg) = 2.2 pounds (lb)
1 tonne (t) = 1,000 kilograms (kg) = 1.1 short tons

VOLUME (APPROXIMATE)

1 milliliter (ml) = 0.03 fluid ounce (fl oz)
1 liter (l) = 2.1 pints (pt)
1 liter (l) = 1.06 quarts (qt)
1 liter (l) = 0.26 gallon (gal)
1 cubic meter (m^3) = 36 cubic feet (cu ft, ft^3)
1 cubic meter (m^3) = 1.3 cubic yards (cu yd, yd^3)

TEMPERATURE (EXACT)

[(9/5) y + 32] °C = x °F

QUICK INCH-CENTIMETER LENGTH CONVERSION

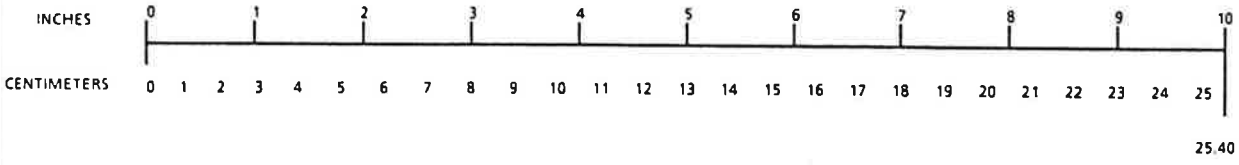

25.40

QUICK FAHRENHEIT-CELSIUS TEMPERATURE CONVERSION

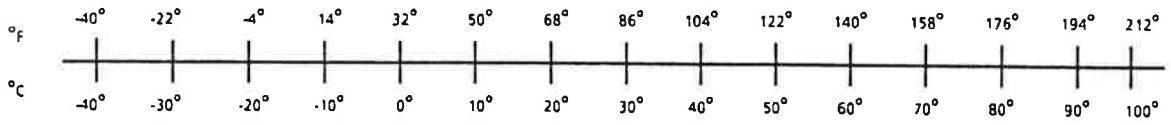

For more exact and or other conversion factors, see NBS Miscellaneous Publication 286, Units of Weights and Measures. Price $2.50. SD Catalog No. C13 10286.

TABLE OF CONTENTS

TABLE OF CONTENTS (Continued)

TABLE OF CONTENTS (Continued)

LIST OF ILLUSTRATIONS

LIST OF ILLUSTRATIONS (Continued)

LIST OF ILLUSTRATIONS (Continued)

LIST OF ILLUSTRATIONS (Continued)

LIST OF ILLUSTRATIONS (Continued)

LIST OF TABLES

1. INTRODUCTION

This document is the Final Technical Report on OMNI Technical Task Directive No. VA9007 titled, "Multiple Site Damage in Aircraft Structures." This effort is part of the Federal Aviation Administration's (FAA's) Aging Aircraft Research Program. The specific activities described in this report include the design, fabrication and shakedown testing of a test facility for the evaluation of full-scale fuselage panels under cyclic pressurization loads. Also described are the development of an analytical fracture model for a curved stiffened fuselage panel and models of riveted lap joints with multiple site damage (MSD).

1.1 Background

Damage tolerant design is an important consideration in avoiding catastrophic consequences of fatigue cracks which can cause fracture instability during the service life of aircraft structures. The U.S. Air Force prepared a comprehensive handbook on the subject in 1984 to support their MIL-A-83444 requirements. A similar document dealing with commercial aircraft requirements is apparently nonexistent. With the exception of some isolated works (Swift, (1)), the authors have not found a detailed study of damage tolerant design by a United States manufacturer published in the open literature.

Damage tolerant design of pressurized aircraft fuselage structures has been based on the predicted performance of single lead cracks in the skin. Under ideal conditions, longitudinal cracks (which are more severe than circumferential cracks due to larger hoop stress) will either be arrested at the frame or straps, or turn in the circumferential direction. The 1988 Aloha Airlines incident shows that this situation does not always occur and the crack can propagate over several frame spacings. Aging, often exemplified by bond delamination, multiple fatigue cracks at adjacent rivet holes, or cracks in straps, shear clips and frames, may also contribute to long cracks.

Even if stringent inspection schemes could be developed, evaluating the airworthiness of old aircraft with multiple cracks is a major technical problem. Multiple cracks are small, often hidden by paint and are not readily accessible for inspection. The work reported here is part of a major investigation on the effect of MSD on the damage tolerance of typical aircraft fuselage structures.

MSD may include combinations of a lead crack in the skin lap joint at a rivet line with additional small cracks in its path. The damage may be in combination with varying degrees of lap joint disbond, corrosion and doubler repair.

Damage tolerance assessment of aircraft structures includes a study of skin crack propagation or arrestability. Crack propagation under broken straps or frames and in the shear clip cutout (2) is of practical interest. It is important to ensure crack diversion, i.e., crack turning into the hoop direction from the longitudinal direction, giving rise to skin flapping for contained decompression of the fuselage. Parameters affecting this phenomenon need to be identified.

Fuselage fatigue strength at joints and splices is also of significant interest. The fatigue crack initiation phenomenon at joint rivet holes - in particular at the upper row in the outer skin of a lap joint splice - needs to be understood to facilitate joint design. Crack growth rates also must be determined, as this determines the crack inspection interval (3). The link-up of MSD leading to the failure of ligaments is an important phenomenon to be studied in this context.

To address the foregoing issues, a program has been undertaken by VNTSC on behalf of the FAA. In view of the complex structural parameters involved, testing plays a significant role. The number of variables in the fuselage design which affect its damage tolerance demand use of full-size test panels. A dedicated test facility was deemed necessary and has been designed and built by Foster-Miller under the subject contract. Major tasks are briefly described in the following paragraphs.

1.2 Program Summary

Alternate approaches were investigated for experimental evaluation of crack propagation behavior in aircraft fuselage structures. Dimensional analysis was used to evaluate the validity of scale models. The limitations of flat plate models were considered as were the practical problems of full-scale testing "in the round." The analysis and practical considerations which led to the selection of full-scale testing of curved panels are presented in Section 2 of this report.

A full-scale test fixture was designed and fabricated to allow the rapid application of realistic pressurization loads to typical fuselage panels in a controlled manner. The ratio of the hoop to axial load levels and the phasing of these loads are both important. The design and fabrication of this test facility as well as its operation are described in Section 3.

Fuselage panel configurations have been designed which faithfully represent critical construction features of the older-vintage commercial aircraft. These panels are designed to minimize the effects of boundaries and attachment. They are also designed to allow the incorporation during manufacture of specific defects like MSD, disbonding, long cracks, repairs, or simulated corrosion. Seven panels have been built to date. The design and fabrication of these panels is presented in Section 4.

Two facility shakedown tests were conducted using these panel configurations. One panel was pressure loaded to failure; the second was pressure loaded and fatigue cycled to failure. This testing is described in Section 5.

Six panel residual strength tests were conducted, four with plain skin cracks and two with lap joint damage. These tests and the results obtained are described in Section 6. A matrix describing the tests is included in Section 6.

Complete understanding of the behavior of cracks in fuselage lap joints requires data on basic material properties and the behavior of these materials when configured into lap joint shapes and assemblies. Foster-Miller conducted a search of the published literature for basic material properties. The literature search and the type of data collected are summarized in Section 7. Appropriate R-curve data were not available in the literature, nor were data on countersink rivet stiffness for sheets of the proper thickness. To provide these data a limited number of R-curve and rivet stiffness tests were performed. These tests, the resulting data and the correlation of results with existing data and theory are also discussed in Section 7.

Throughout the program, extensive analyses were performed in support of the design. Analytical techniques have also been used to predict fracture behavior of the curved stiffened panel, and behavior of the lap joints. In particular Foster-Miller has:

- Developed a finite element model using NISA 386 to elevate the Stress Intensity Factors (SIF) for a curved stiffened fuselage structure with longitudinal cracks.

- Employed numerical analysis to establish the hoop stress equivalency between the actual fuselage structure and a stiffened flat panel for fatigue testing.

- Constructed a 3-D finite element mesh of an unbonded, riveted lap joint. The rivet loads have been determined and their sensitivity to rivet stiffness has been studied.

- Investigated the MSD link-up process in a cracked lap joint in a preliminary manner using the elasto-plastic codes in NISA.

These analytical activities and the results obtained to date are presented in Section 8.

Conclusions are presented in Section 9.

2. SELECTION OF TESTING APPROACH

Many alternative approaches are possible for experimentally evaluating the behavior of cracks in aircraft fuselage panels.

Several candidate concepts were examined prior to finalizing the structural configuration of the specimen and the test fixture. These included:

- Subscale models
- Flat panels
- Full-size rounds
- Full-scale curved panels.

The relative merits and demerits of these candidate approaches are evaluated in the following paragraphs.

2.1 Subscale Models

Dimensional analysis was carried out to establish the validity and suitability of subscale models for experimental fracture mechanics studies. The important parameters governing the stability of a longitudinal crack in a fuselage skin are the geometric and stiffness parameters indicated in Figure 2-1, the skin material fracture toughness, K_c, the applied internal pressure, p, and the far field hoop stress, σ, with a companion component in the longitudinal direction. Assuming all-aluminum construction with fixed modulus and other material properties (and neglecting the influence of bonding between skin panels and stringers and shear-clips holding frames), the parameters controlling the extensional and bending stiffnesses are the cross-sectional areas of the frame, A_f, and of the stringer, A_s, the moment of inertia, I_f, of the frame, and Young's modulus, E. In addition, the rivet shear stiffness per length (assumed to be distributed along stringers and frames) is important. This can be represented by $N\tau/\ell_f$, where τ is the shear stiffness for a single rivet and N is the number of rivets.

For these 14 variables (R, ℓ_c, ℓ_f, ℓ_s, h, t, A_f, A_s, I_f, K_c, σ, p, $(N\tau/\ell_f)$, E), a set of 11 nondimensional parameters is derived using the standard procedure of dimensional analysis. Table 2-1 presents these variables.

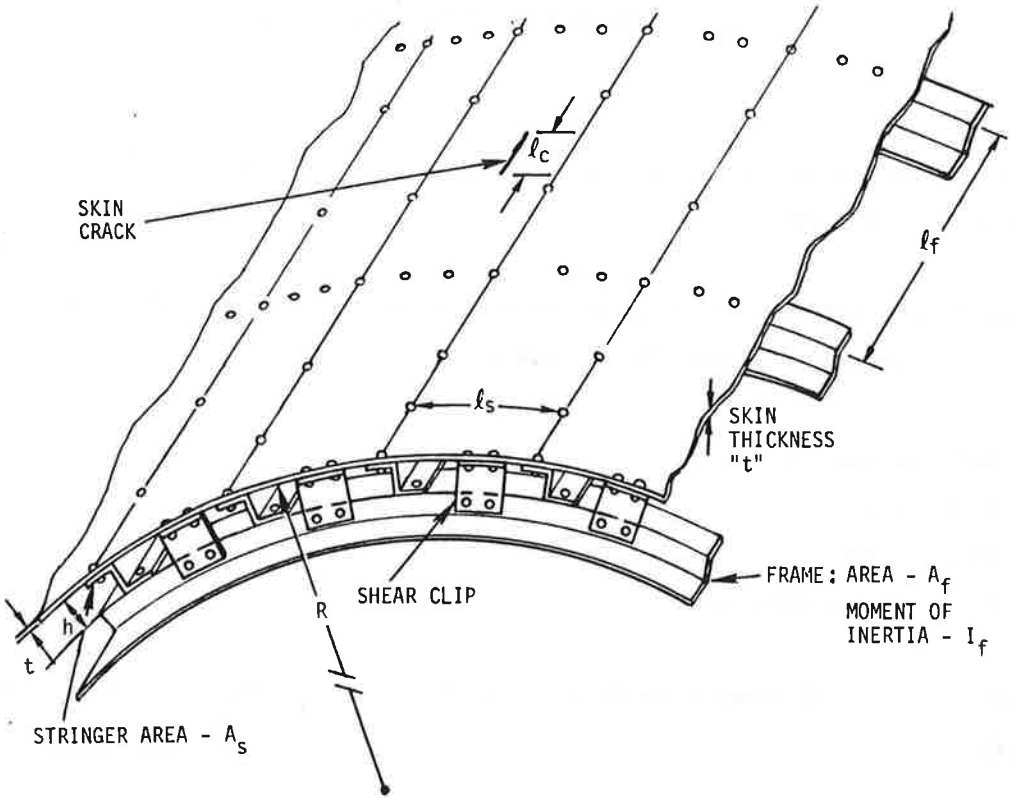

Figure 2-1. Geometric Parameters for Fuselage Panel

Table 2-1. Nondimensional Parameters

$\phi_1 = K_c^2/\sigma^2\ell_c$	$\phi_7 = R/\ell_s$
$\phi_2 = \sigma/p$	$\phi_8 = R^2/A_f$
$\phi_3 = R/t$	$\phi_9 = R^2/A_s$
$\phi_4 = R/\ell_c$	$\phi_{10} = R^4/I_f$
$\phi_5 = R/\ell_f$	$\phi_{11} = Nt/E\ell_f$
$\phi_6 = R/h$	

If we scale down the skin thickness for the model, assume K_c as a basic material property independent of skin thickness, assume that individual rivet stiffness remains constant both in the model and the prototype and the number of rivets N and their spacing is adjusted to keep ϕ_{11} constant for both the model and the prototype, then the Buckingham Pi theorem states that:

$$d_1 = F(\phi_2, \ldots \phi_{11})$$

Hence:

$$\left(\frac{K_c^2}{\sigma^2 \ell_c}\right)_{model} = \left(\frac{K_c^2}{\sigma^2 \ell_c}\right)_{prototype} \tag{2-1}$$

from which the residual strength for the prototype can be predicted, based on experimental results from the model. This implies that ϕ_2 remains the same for both model and prototype. This is a reasonable assumption since σ is a linear function of p, and a complex function of other nondimensional parameters ($\phi_3, \ldots \phi_{11}$).

In the ideal scale model referred to above, the effect of stiffeners and the curvature and bulging are all automatically accounted for in Equation (2-1). For example, in the case of an unstiffened thin shell with a longitudinal crack of size ℓ_c, the exact expression for the stress intensity factor is of the form:

$$K = \sigma\sqrt{\ell_c}\, F(\ell_c/\sqrt{Rt}) \tag{2-2}$$

The function F in the above equation remains unchanged in the case of the ideal scale model.

A significant difficulty in achieving the ideal scale model, however, is in reducing the skin thickness. Some aircraft, such as Boeing 737, have a skin thickness of 0.036 in. Thinner sheet stock is commercially available, but the construction details at the rivet line and joints may be unrealistic with reduced skin thickness. Geometrically scaling everything except the skin thickness yields the following advantages:

- The plane stress fracture toughness, K_c, will be the same both for model and prototype.

- The individual rivet shear stiffness, τ, will be the same for both structures. From Swift's work

$$\tau = \frac{1}{E}\left[\frac{C_1}{D} + \frac{C_2}{t} + \frac{C_2}{t_1}\right]$$

where D is rivet diameter, τ_1 is the thickness of the plate attached to the skin and C_1 and C_2 are constants. Since the number of rivets in the model is proportionally reduced (the rivet spacing unchanged in the model), the nondimensional parameters, ϕ_{11}, will have the same value for both model and prototype. Hence, joints and fasteners are well represented in the model.

Consider scale models where skin thickness and joint dimensions are not changed from prototype values. The thickness, t, and ϕ_3 will be eliminated from the parameters. The distribution of stress, σ, in the model will be different from that in the prototype for the same internal pressure, p. To maintain the same value of ϕ_2 in both structures, p will have to be increased by the scaling factor. There will still be some error in scaling of spatially distributed stress components in the prototype from that of the model since the skin thickness affects the stress. There will also be some error due to curvature as can be seen from Equation (2-2). It is, therefore, impossible to obtain rigorous scaling laws without scaling down the skin thickness. As stated earlier, scaling down the skin is not practical, as this itself changes the fracture toughness of the material. It does not appear expedient to rely on subscale models for the generation of practical data. The models may, however, be useful in a preliminary design of a specimen or for verification of theoretical analysis. Unfortunately, there is no computationally simple theoretical analysis to date on damage tolerance evaluation of curved fuselage structures; the technical use of scale models is, therefore, extremely limited.

2.2 Flat Panels

Stiffened flat panels have been used by Swift (1) and others to study crack propagation and fracture. Although this approach allows easy simulation of biaxial stresses, it has the following limitations:

- The absence of curvature affects the level of stress singularity at the crack tip, and hence, the stress intensity factor. This will introduce significant errors in crack growth rates and in fracture strength. Empirical equations such as the one by Swift (1) can be developed to correct for the curvature, but they are limited to particular panel configurations.

- Using a flat plate, it is difficult to simulate the bulging of the crack as it occurs in the fuselage shell under internal pressure. Bulging is a nonlinear phenomenon with significant influence on fracture.

Because of the shortcomings referred to above, the flat plate approach was not adopted in the present work.

2.3 Full-Size Rounds

Full-size round sections have been used by Boeing (4). Half rounds with semicircular end diaphragms have been tested in Sweden (5). Using air as the pressurization medium in the full round configuration raises significant safety issues. If water is used for internal pressurization, the entire structure needs to be immersed in water to compensate for pressure head. This is generally cumbersome and creates problems with instrumentation. Testing full-size round structures is very expensive and slow. The practical problems of testing of full-scale rounds and the importance of speed in obtaining large amounts of data led to rejection of this approach.

2.4 Curved Panel Under Internal Pressure

Using this method, a curved segment of stiffened aircraft panel is subjected to internal pressure, the hoop load being resisted by anchors along the straight edges. In phase with the internal pressure, the curved ends of the panel are subjected to an external longitudinal load. This load is proportioned to produce an axial stress of half of the hoop stress due to the internal pressure, as it exists in the full-scale round aircraft fuselage. A detailed description of this approach is presented in Section 3.

Curved sectors under external vacuum and longitudinal load have been tested and results reported (1). For those tests, the curved exterior section of the panel was covered by a full length and width vacuum chamber with a passive peripheral seal. Longitudinal and pressure loadings were applied independently. High power requirements and difficulties in coordinating the axial and hoop loads plagued this approach. Additionally, the pressure differentials achievable with the vacuum system are limited to atmospheric.

A ranking matrix which quantitatively compares the selected approach with the two major approaches used in the aircraft industry, viz full-size rounds and sector under vacuum, is presented in Table 2-2.

Table 2-2. Multiple Objective Ranking Matrix Scoring for Candidate Concepts

No.	Required Capability	Maximum Score	Concept I Full Cylinder Internal Pressure Load	Concept II Sector, External Vacuum and Longitudinal Loading	Concept III Sector, Internal Pressure and Longitudinal Loading
1	Boundary restraint - longitudinal	10	10	8	8
2	Boundary restraint - lateral	10	4	9	9
3	Overpressure	10	10	0	10
4	High cycling rate	10	1	5	10
5	Zero phase difference between hoop and longitudinal stresses	10	9	6	8
6	Economic panel usage and fabrication	10	8	10	10
7	Panel replacement ease	10	1	8	10
8	Low leakage	10	1	10	10
9	Safety	10	1	10	8
10	Fixture cost	10	8	9	10
	Total score	100	53	75	93

3. TEST FIXTURE DESIGN

A test fixture specially designed by and proprietary to Foster-Miller includes the following features:

- Compatibility with the selected test panel and with other test panel configurations
- Fixture to panel connections reproduce conditions of full-circle fuselage
- Panel loadings must simulate normal pressurization loads in the panel
- Capable of providing cyclic pressurization loads
- Capable of loading the panel to a pressure equivalent to one-half the panel's ultimate capacity
- Configured such that bending loads could be imposed on the panel frames should the need arise in the future.

As stated earlier, the general approach for panel testing is to anchor the two long sides and one end of the panel to the fixture. Panel loading is achieved by pulling on one curved end and pressure loading the panel on its concave side by pressurized water. The pressure load is contained by the fixture, by an inflatable seal between the fixture and the panel around the panel periphery, and by the panel itself.

An overall panel loading schematic is shown in Figure 3-1. The panel loading power source is hydraulic oil pressure. The pressure is generated by pulling a hydraulic cylinder with an Instron™ Universal Test Machine. Hydraulic pressure is routed to hydraulic cylinders which pull the panel. The pressure is also routed to a special pressure reducer. Within this unit, the hydraulic pressure line is connected to a small diameter hydraulic cylinder. This cylinder connects directly to a large diameter cylinder containing water. The pressure reduction from hydraulic oil to water is about 77:1. The low pressure side of the pressure reducer connects directly to the pressure vessel portion of the test fixture. Controlled loading of the universal test machine thus provides coordinated hoop and longitudinal loading of the test panel. Details of the test fixture, the pressure reducer, and system operation are given in the following sections.

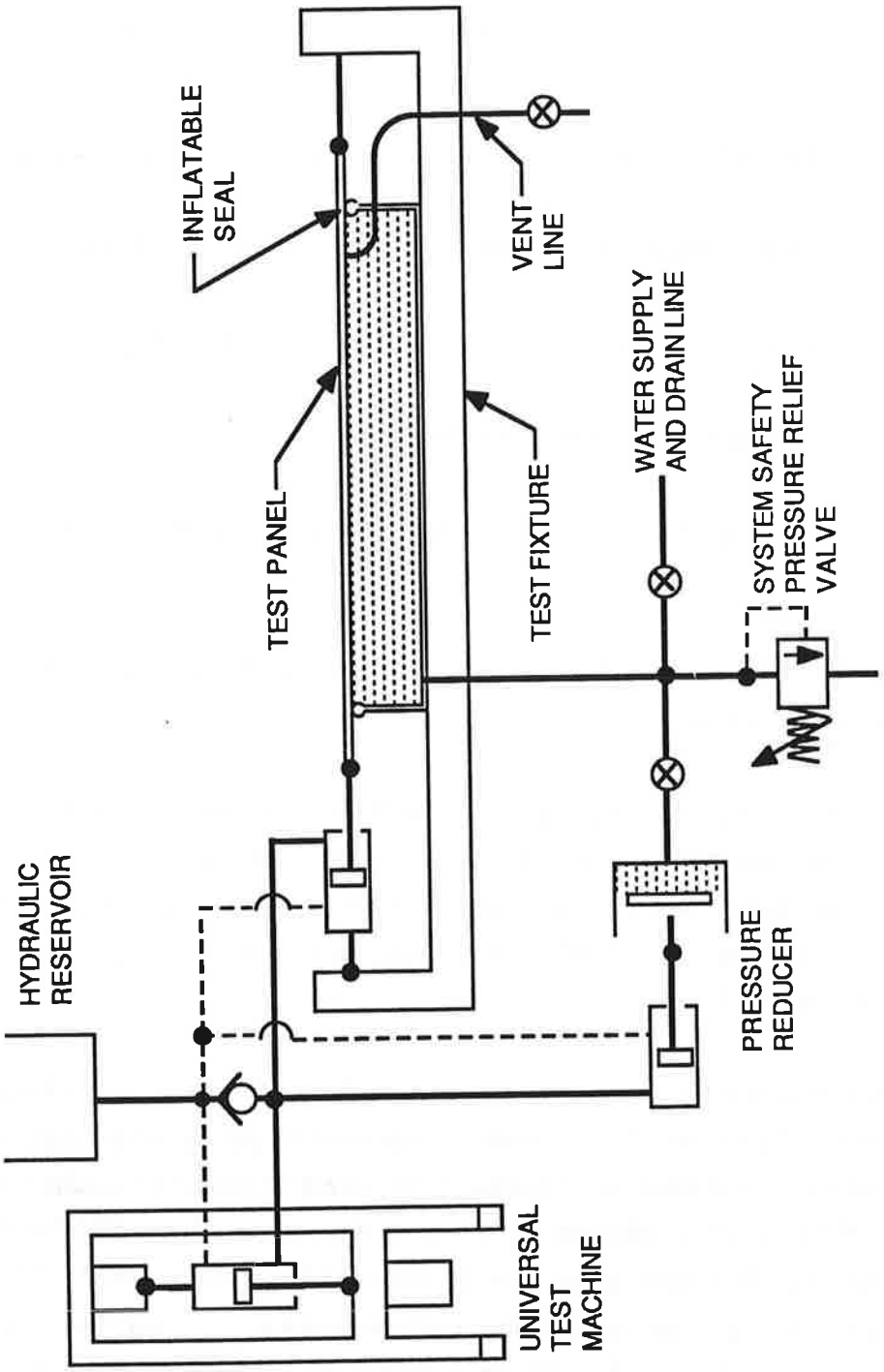

Figure 3-1. Panel Loading Schematic

3.1 Test Fixture Structure

The test fixture structure includes four major subassemblies:

- Base structure
- Inner seal frame
- Outer seal frame
- Upper structure.

The general orientation of these items is shown in Figure 3-2. The inner seal frame bolts to the base structure to form the pressure container. The outer seal frame bolts to the upper structure to form the upper frame assembly. This assembly bolts to the base structure. The assembly is removed during panel installation.

Inflatable seals are mounted to the outer and inner seal frames to sandwich the panel during pressure testing. The inner seal is the pressure seal. The outer seal balances the seal load on the panel to eliminate nonrepresentative panel loading due to the seal.

Brief descriptions of the major subassemblies follow.

3.1.1 Base Structure

The general arrangement of the base structure is shown in Figure 3-3. The assembly is of welded construction using 1/2-in. wall 10 x 10, 8 x 8 and 8 x 4 in. structural steel tubing. The frame supports a 114 x 60 in., 0.62-in. thick steel plate which forms the base of the pressure tub. Bolt holes are arranged around the periphery of this plate for the attachment of the inner seal frame. Mount points are provided at the two fixture ends for mount plates which carry the supports for the panel longitudinal loading cylinders at one end, and four anchor turnbuckles at the other. The two longitudinal side beams each carry 28 anchor points for the hoop restraint turnbuckles. Four mount points are provided for attachment of the upper frame assembly.

The base plate includes a 3-in. pressure supply/drain hole, four 10 x 20 in. access holes and two holes for instrumentation.

The base structure has been designed to minimize deflections and operate safely at pressures up to 20 psig. Base structure weight is estimated to be 11,700 lb.

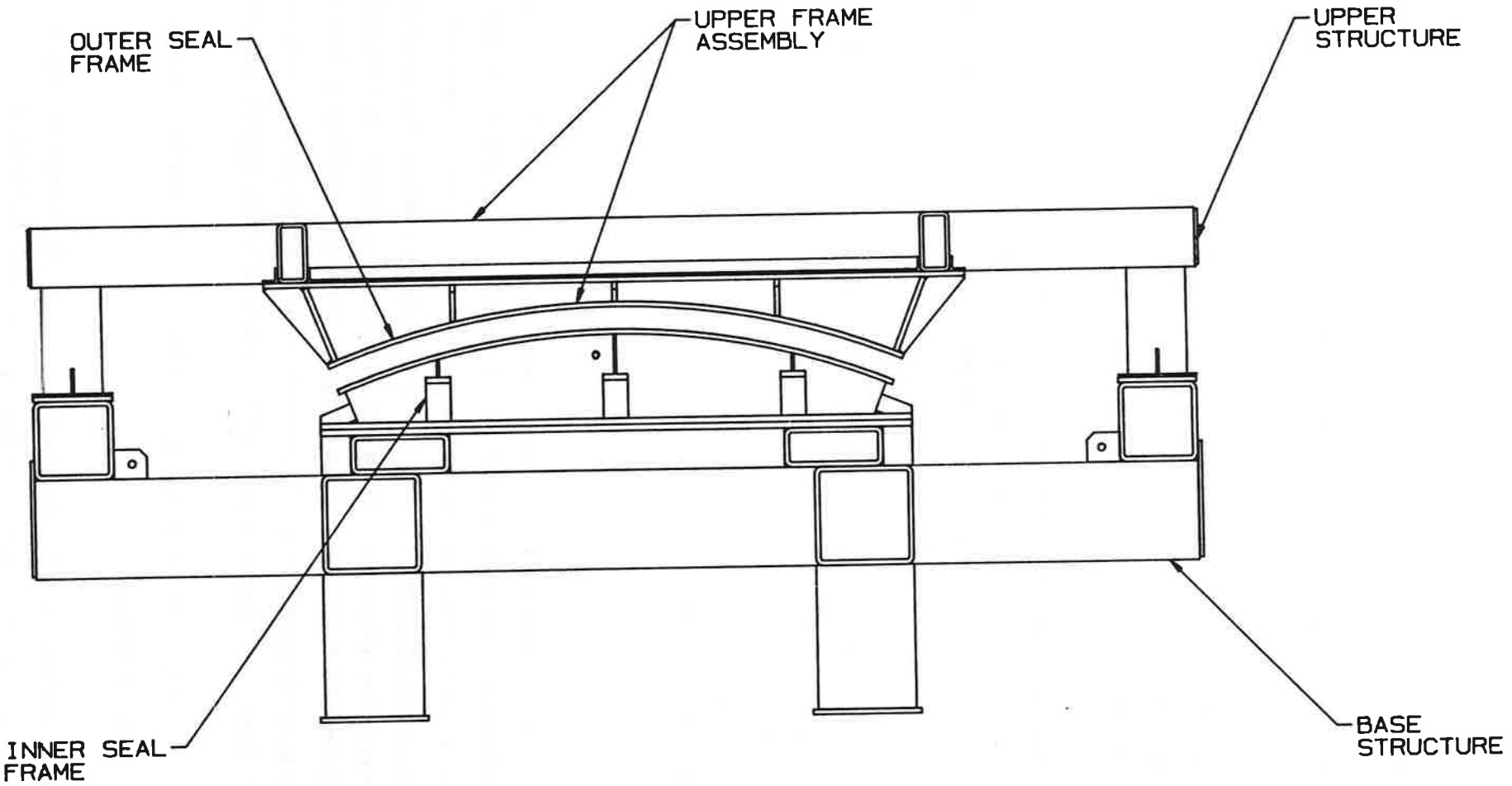

Figure 3-2. Test Fixture Major Components

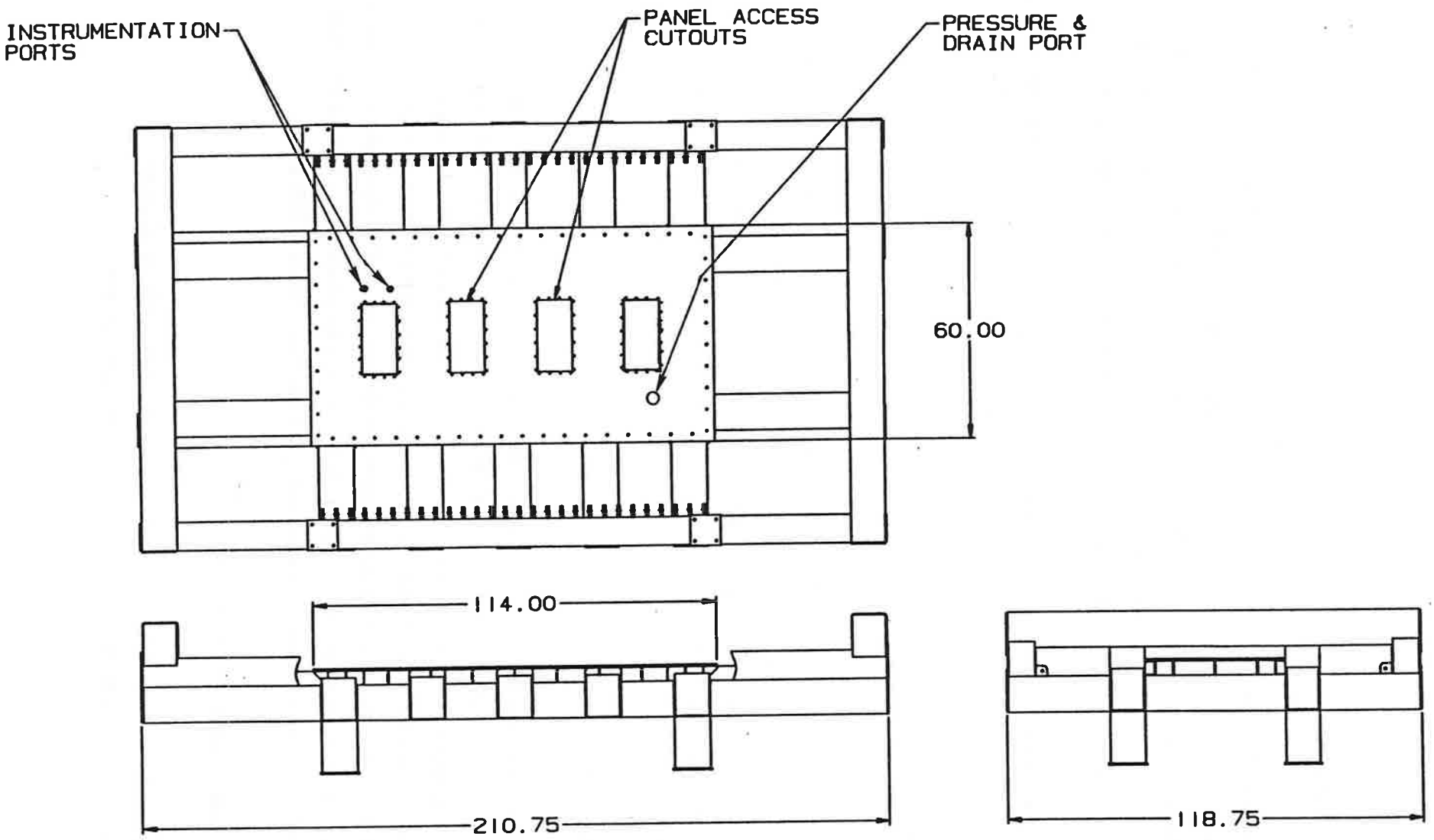

Figure 3-3. Test Fixture Base Structure

3.1.2 Inner Seal Frame

The inner seal frame is shown in Figure 3-4. The frame bolts to the base structure base plate to form the fixture pressure tub. A bead of sealant between the frame edge and the base plate provides a leak-proof water seal. The assembly is of welded steel plate construction with a 0.62-in. thick base and 0.50-in. thick webs and flanges. The upper flange provides the mount surface for the inner inflatable seal. The seal attaches to the flange with a series of angle clips.

As with the base structure, the assembly has been designed to minimize deflections and operate safely at water pressures up to 20 psig. Frame weight is estimated to be 760 lb.

3.1.3 Outer Seal Frame

The outer seal frame is shown in Figure 3-5. Its construction is similar to the inner seal frame except that the seal mount surface is concave. It is designed to bolt to the upper structure. The frame, in combination with the upper structure, has been designed for acceptable deflection of less than 0.12 in. under a maximum seal inflation pressure load of 40 psig. Deflection is limited to ensure that the outer seal travel is adequate for all test conditions. Estimated frame weight is 690 lb.

3.1.4 Upper Structure

The upper structure arrangement is shown in Figure 3-6. It is of welded construction using 6 x 3 in. steel tubing and steel angle and bolts to the upper seal frame to form the upper frame assembly. The frame includes four legs which connect to the main frame. The legs also protect the upper seal when the upper frame assembly is removed from the fixture and placed on the floor. The frame has been designed for acceptable deflection, as discussed above, under a maximum seal inflation pressure of 40 psig. It has also been designed to support two men during panel inspection operations. Estimated upper structure weight is 890 lb.

3.2 Test Fixture and Panel Assembly

The panel mounts to the test fixture through a series of mechanical connections to the panel load fingers. It is sealed by the balanced pressure seal arrangement.

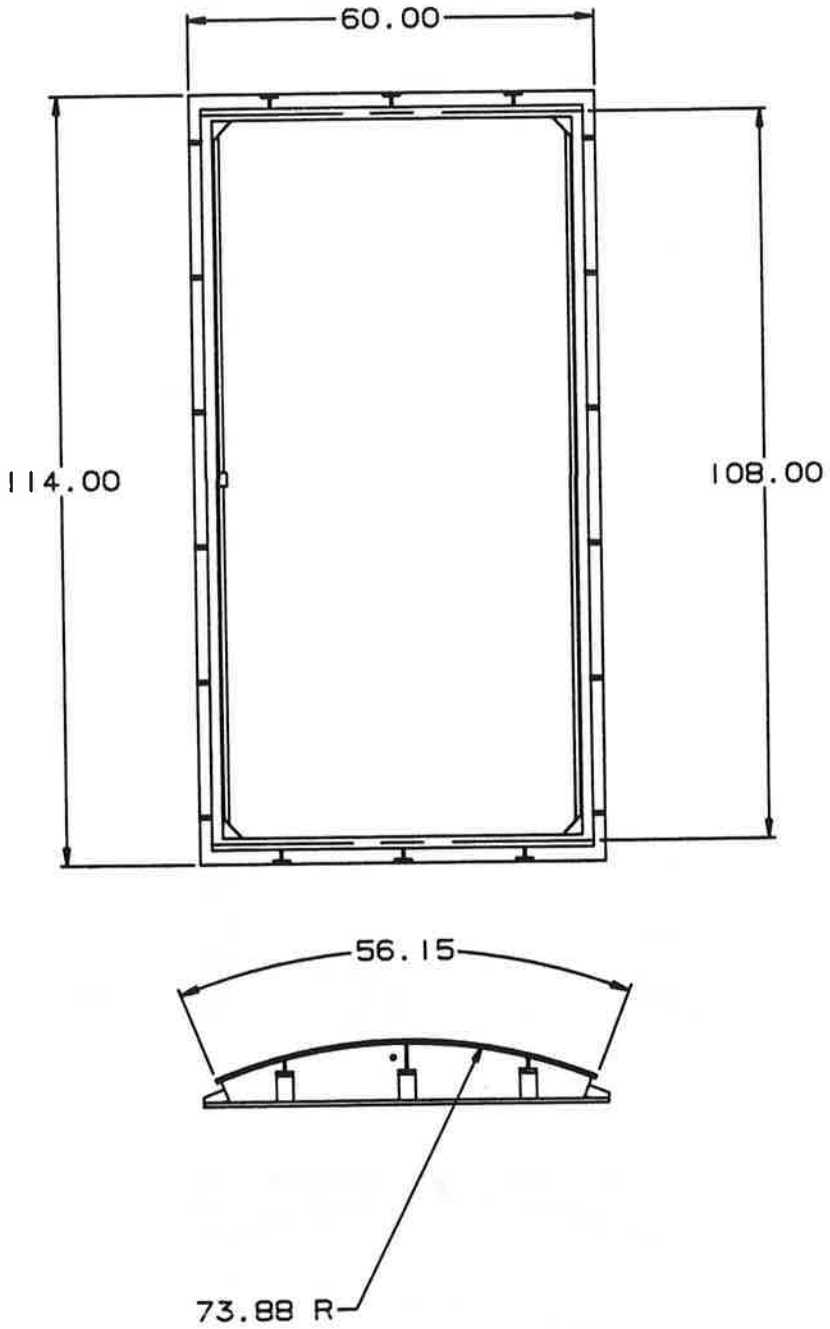

Figure 3-4. Test Fixture Inner Seal Frame

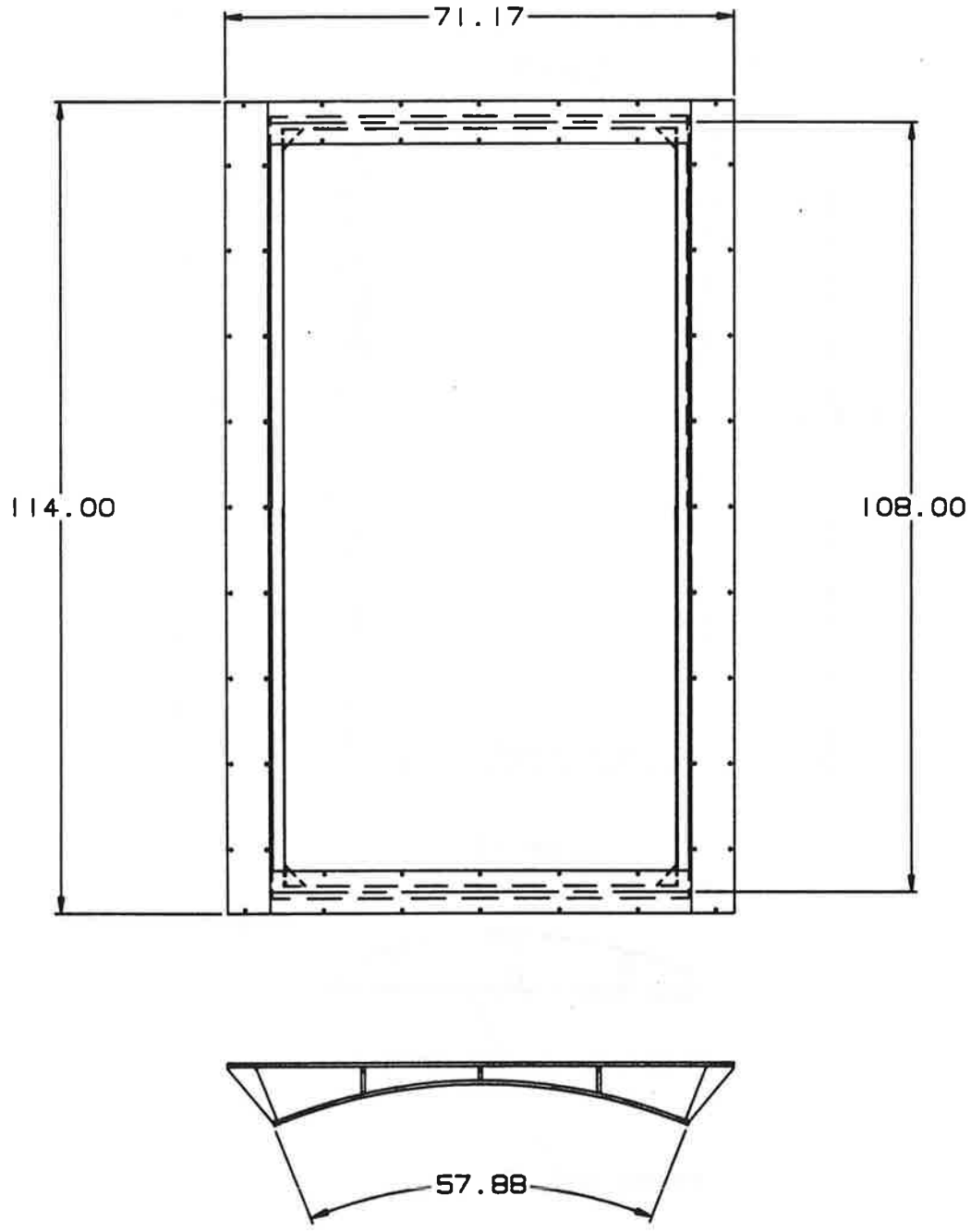

Figure 3-5. Test Fixture Outer Seal Frame

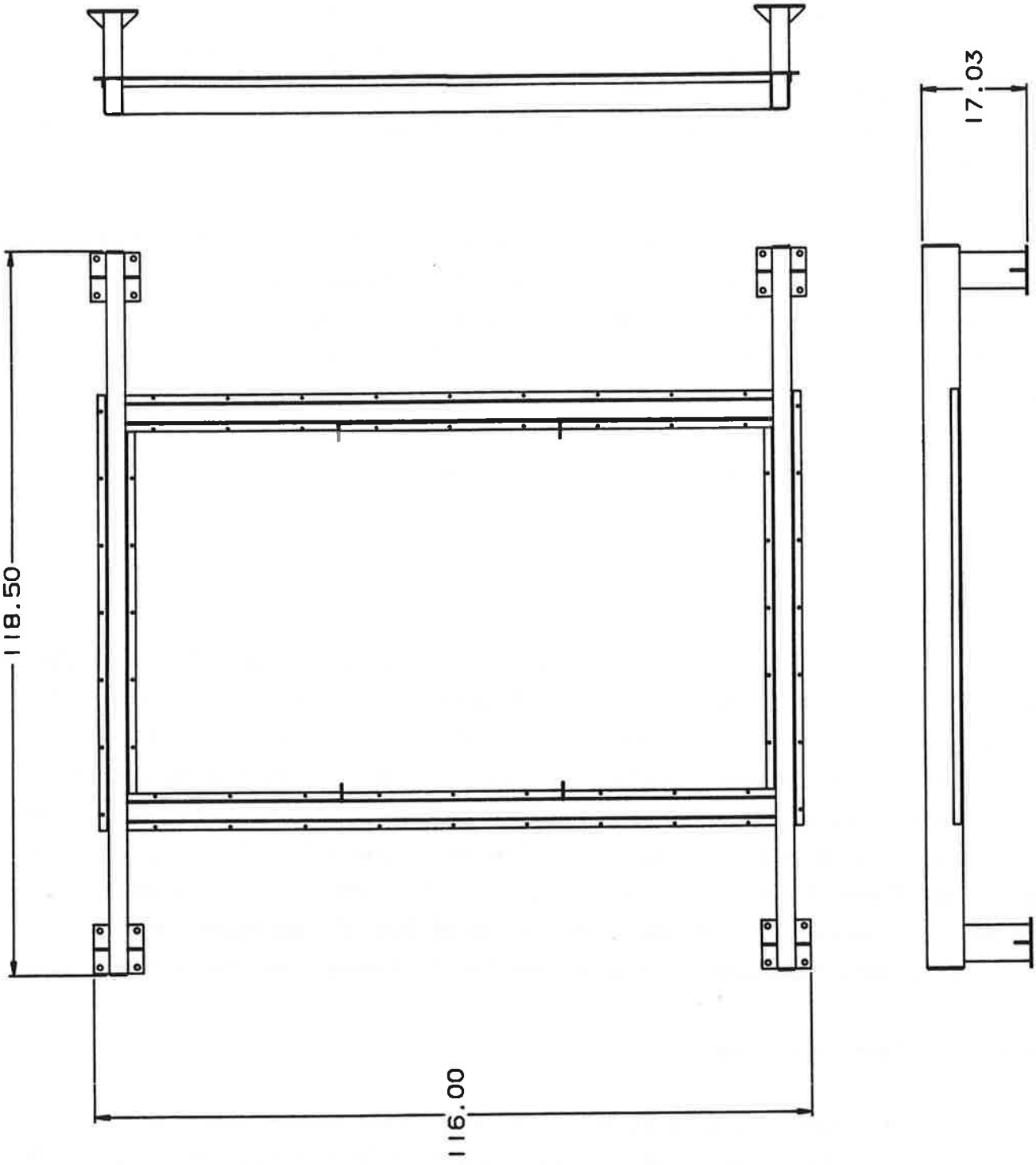

Figure 3-6. Test Fixture Upper Structure

3.2.1 Panel Skin Mechanical Connections

The two longitudinal sides of the panel are anchored to the test fixture by 28 turnbuckles along each side. The arrangement is shown in Figure 3-7. The fixture and panel geometry position the turnbuckles on the tangent lines from the test panel sector. The turnbuckles are 7/8-in. diam, each with a safe working load of 7,200 lb. Hoop load per turnbuckle at 20 psig is 6,000 lb.

The panel is restrained axially by rigid links at one end and loaded at the other end by four commonly plumbed hydraulic cylinders. A four whiffle tree arrangement is used at each end to connect the 16 panel load fingers to the four load connection points. The arrangement of a single whiffle tree is shown in Figure 3-8. A commercial Sheffer hydraulic cylinder and pivot mount are used together with a steel cylinder clevis and steel beams, links and pins. Four 1-1/4-in. turnbuckles are used at the anchor end in place of the four cylinder and clevis assemblies shown in the figure. Maximum design load in each whiffle tree at 20 psig is 10,500 lb.

3.2.2 Panel Seal

The panel is sealed around its inner periphery by a continuous inflatable rubber seal. The seal mounts to, and is supported by, the inner seal support structure. A similar seal bears on the outer panel surface. A section of the seal arrangement is shown in Figure 3-9. The selected seal is a standard section manufactured by Sealmaster Corp. of Kent, OH. The seals include molded corners and are specially manufactured to the sizes of the two seal support structures. Both seals are installed with a 0.25 in. preload deflection. This allows up to 0.50 in. of radial panel travel under load. Predicted radial panel travel at 15 psig is 0.21 in. The seals are anchored to the support frames by continuous aluminum angle-sectioned clips. The atmospheric side of the pressure seal clip includes a support flange to limit lateral seal movement under pressure.

3.2.3 Panel Frame Anchorage

Each of the six panel frames is anchored at its two ends to the fixture using a pair of links connected to an anchor bolt arrangement shown in Figure 3-9. These links are accessed through the four inspection ports in the base of the fixture pressure tub.

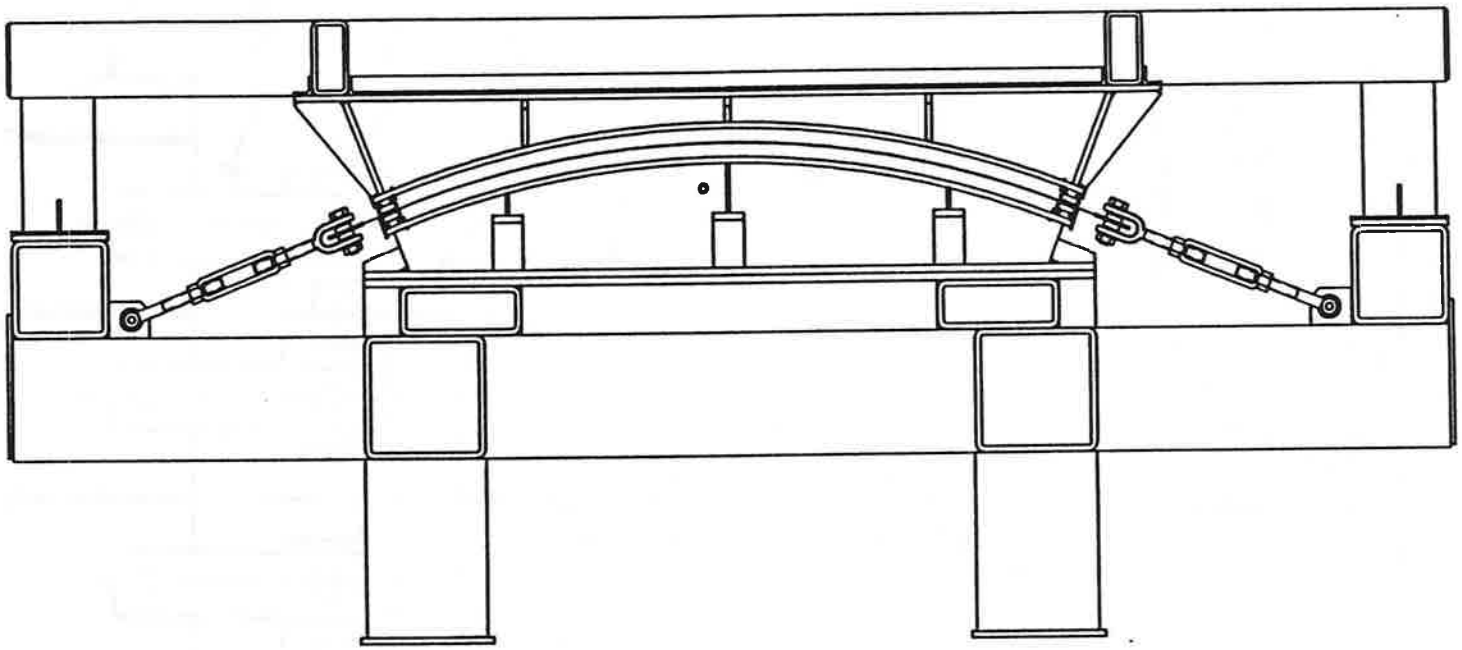

Figure 3-7. Panel Installation in Test Fixture

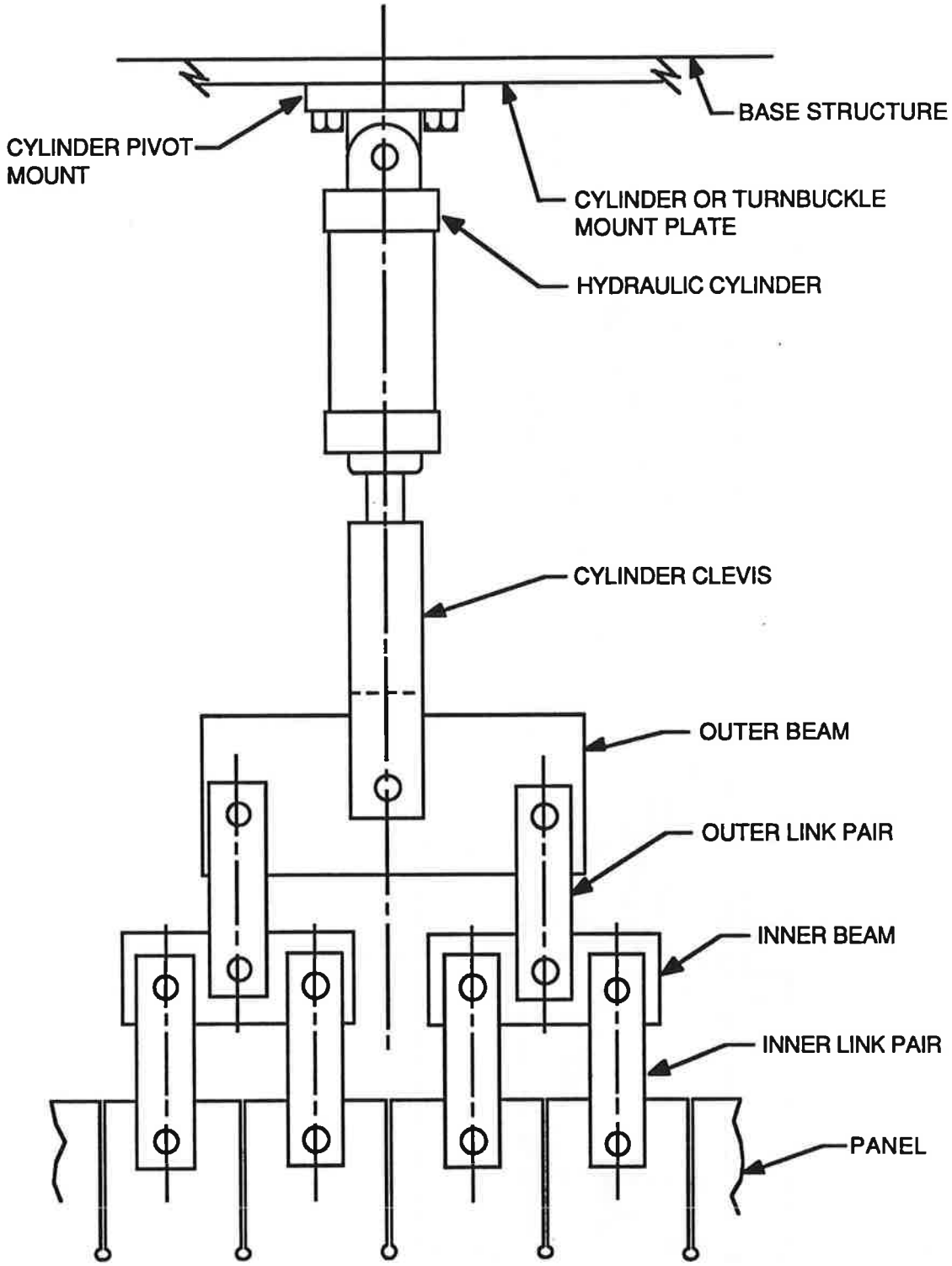

Figure 3-8. Panel Loading Whiffle Tree

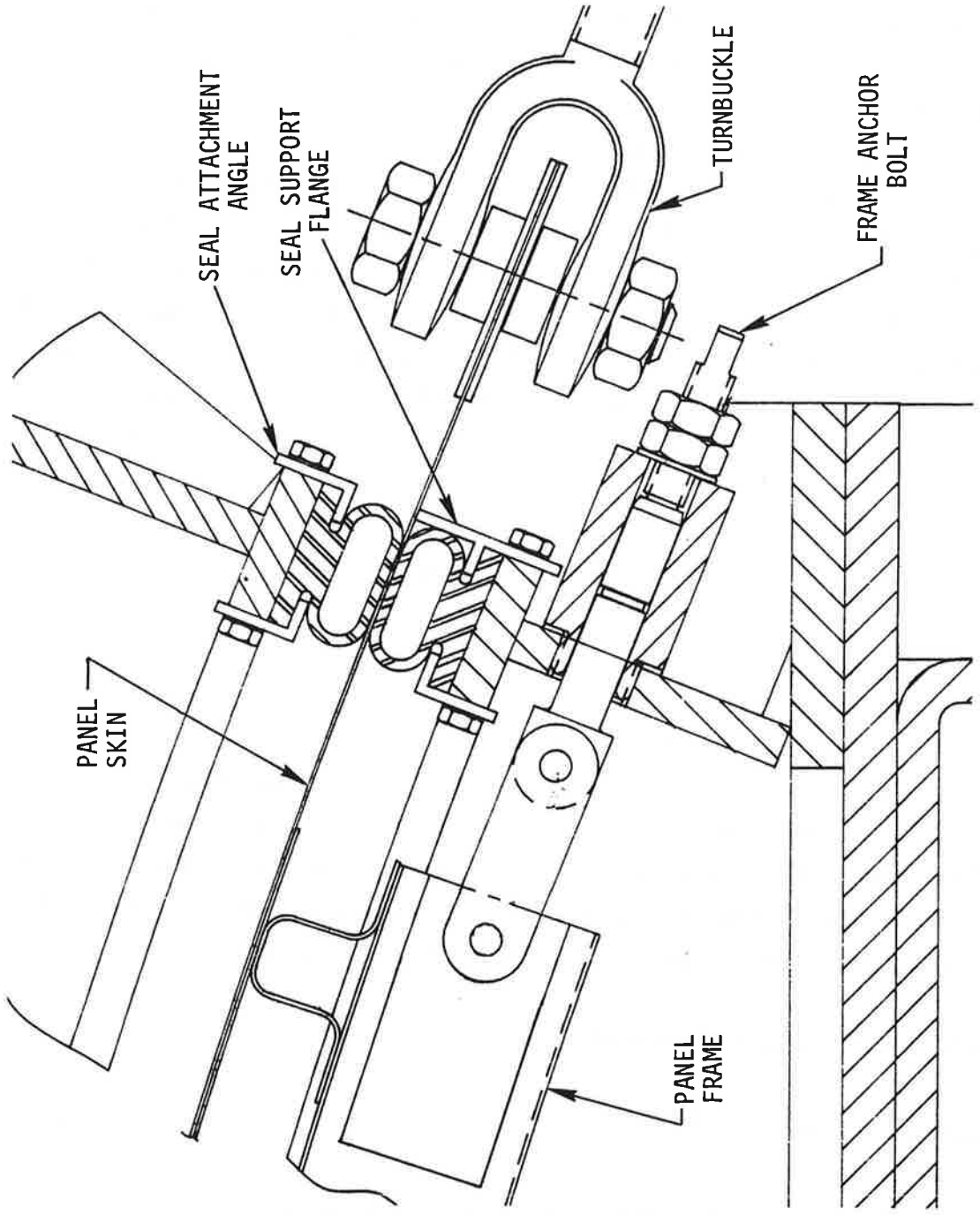

Figure 3-9. Panel Seal and Anchorage Arrangement

3.3 Pressure Reducer Assembly

The pressure reducer assembly converts the relatively high hydraulic oil pressure to the low pressure of the water system that loads the panel. The pressure reduction is achieved through differential area using a hydraulic cylinder with an effective area of 5.89 $in.^2$ driving a water piston with an effective area of 452 $in.^2$. This 77:1 reduction in combination with the selected panel geometry and the selected longitudinal panel loading cylinder size, provides the correct ratio of pressure to longitudinal loading to within 0.5 percent accuracy. The general arrangement of the pressure reducer assembly is shown in Figure 3-10. The high pressure hydraulic cylinder is a Sheffer double rod cylinder with a 5-in. stroke. It connects through an alignment coupling to a shaft that bolts directly to the piston of the low pressure cylinder. The low pressure cylinder is 24 in. in diameter and has a total stroke of 4 in. The water cylinder is of welded construction using 304 stainless steel. The seal is provided by a 24-in. diameter rolling diaphragm specially designed by Foster-Miller. The shaft is supported by a welded support structure which mounts to the main pressure reducer frame. This frame is built from 4-in. square structural steel tubing welded to form the box-shaped frame.

3.4 Testing Machine Modification

The 55-kip capacity Instron 8502 servo hydraulic testing machine requires special adapter fittings for installation of the hydraulic cylinder "coupon." The cylinder is a Sheffer 6-in. bore, 2-1/2-in. rod, 4-in. stroke unit. The mounting arrangement is shown in Figure 3-11. The cylinder body bolts to the test machine load cell through an adapter plate. The cylinder rod is attached to an alignment coupling which, in turn, threads into an adapter coupling. This coupling screws into a 2-in. diameter female thread in the test machine load cylinder.

3.5 Test Fixture Panel Testing Operation

3.5.1 Panel Installation

Panel installation into the test fixture involves the following steps:

1. Disconnect upper seal inflation air supply line and unbolt the upper frame assembly from lower frame.

2. Lift off upper frame assembly and stand it on the ground on its four legs.

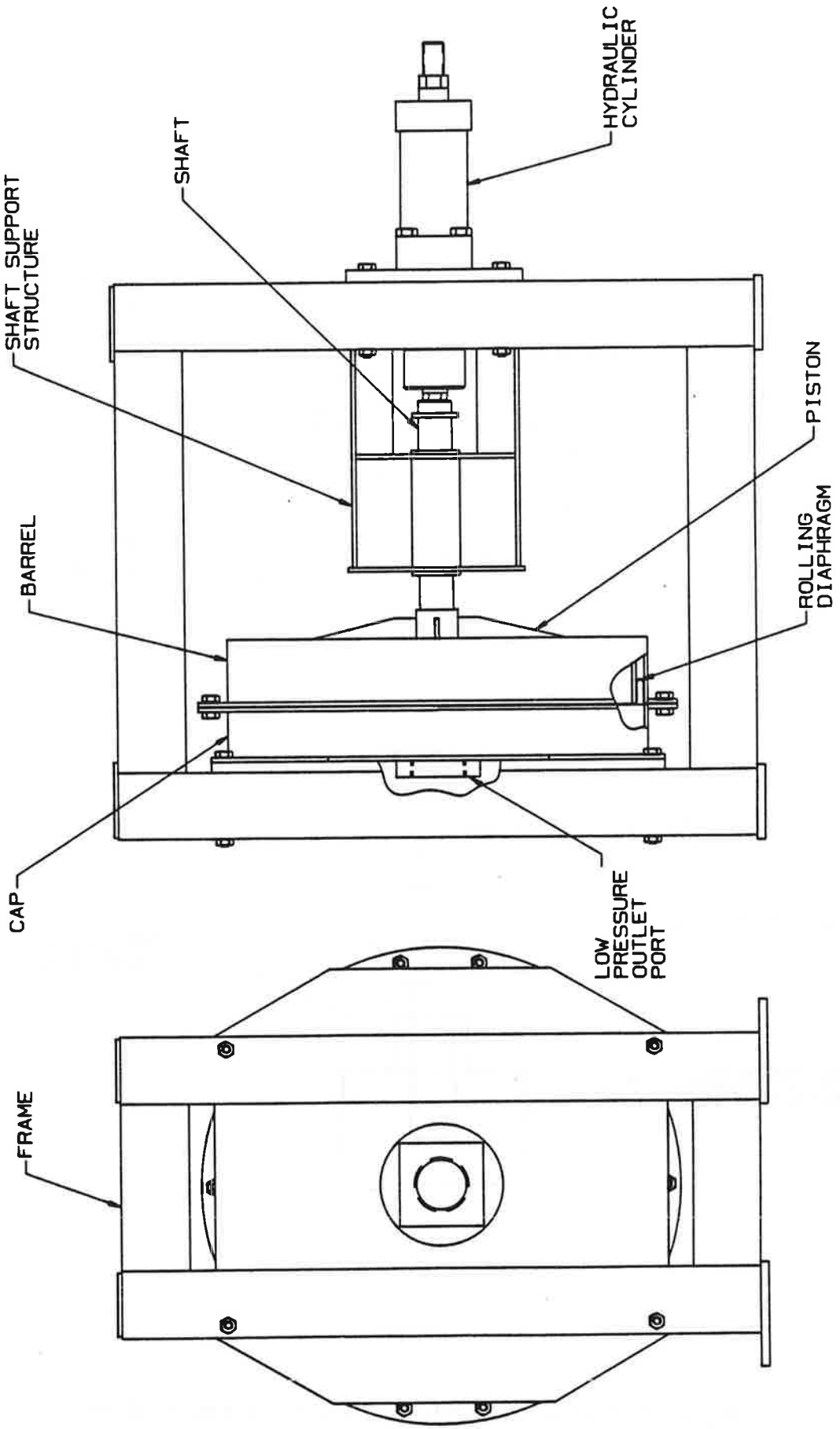

Figure 3-10. Pressure Reducer Assembly

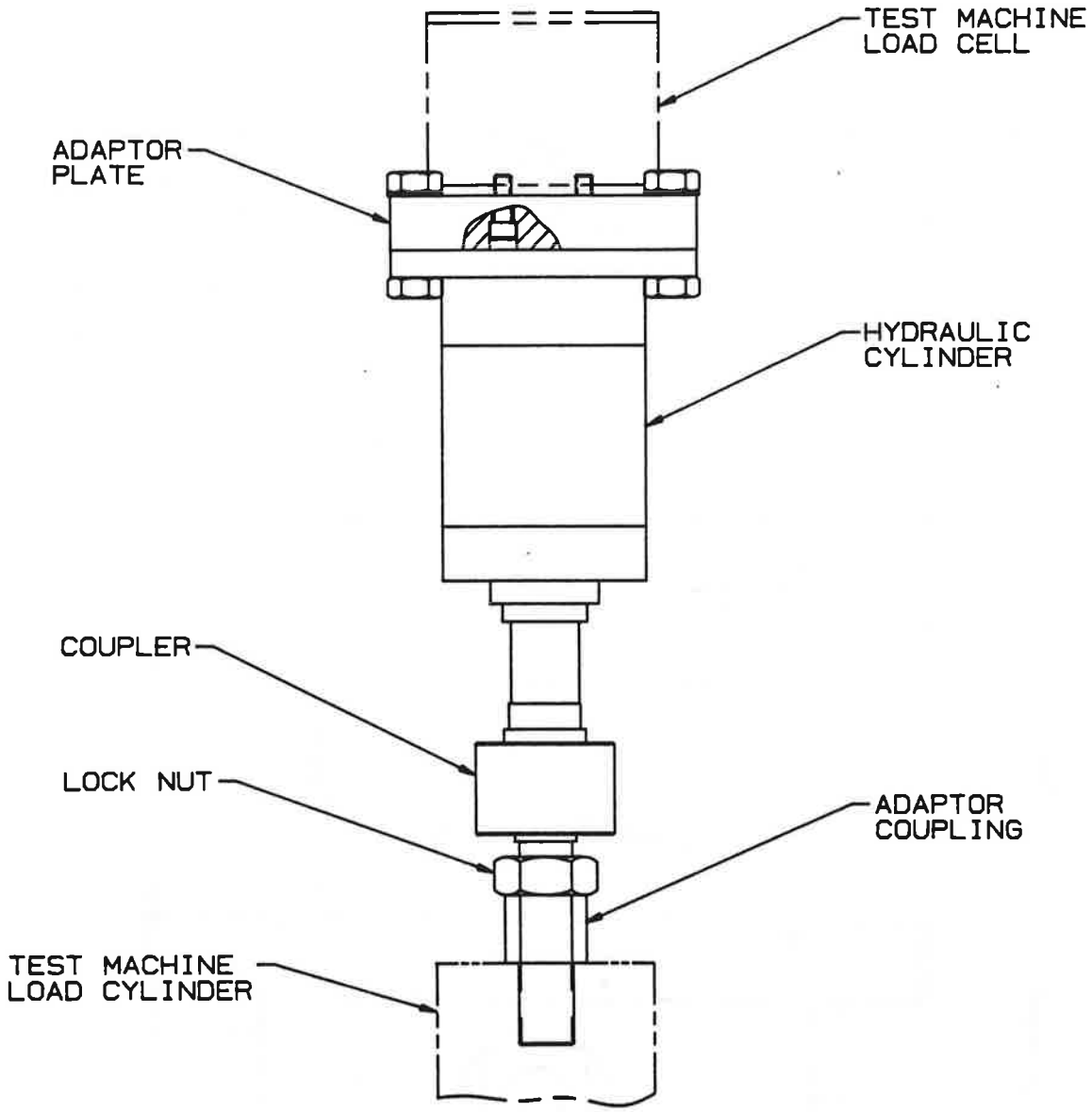

Figure 3-11. Hydraulic Cylinder Mounted in Test Machine

3. Pick up the panel, mounted in a transportation and handling fixture, and lower the assembly centrally onto test fixture lower seal.

4. Remove the panel transport and handling fixture.

5. Engage the jaws of the 56 turnbuckles with the panel side fingers by turning the buckle body. Inert the jaw pins and tighten the turnbuckle until it is hand-tight. Lock the body with the locknut.

6. Connect the whiffle tree inner link pairs to the 32 panel end fingers using pins and spring pin clips.

7. Connect the 12 panel frame anchors.

8. Close the four inspection covers.

9. Reinstall the upper frame assembly.

3.5.2 Preparation for Test

This involves the following steps:

1. Connect both of the seal inflation lines to a regulated shop air supply and inflate both seals to 25 psig.

2. Open panel vent valve and fill pressure tub with water (approximately 220 gal). Shut off the water at the supply valve when air-free water flows from both the air bleed valve on the low pressure side of the pressure reducer and from the vent line. Close both bleed valves.

3.5.3 Panel Load Testing

The overall test system setup was discussed in subsection 3.2 and shown diagrammatically in Figure 3-1. Panel loading pressures are generated by pulling the hydraulic cylinder mounted in the testing machine. Table 3-1 shows the relationship between the test machine tensile load

Table 3-1. Testing Performance Features

Feature	Panel Pressure Load (psi) 1	2	3	4	5	6	7	8	9	10	15
Test machine load (lb)	1,804	3,608	5,412	7,216	9,020	10,824	12,628	14,432	16,236	18,040	27,060
Panel hoop load per inch (lb)	75	150	225	330	375	450	525	600	675	750	1,125
Panel longitudinal load per inch (lb)	38	75	113	150	188	225	263	300	338	375	563
Fixture longitudinal load per cylinder (lb)	525	1,050	1,575	2,100	2,625	3,150	3,675	4,200	4,725	5,250	7,875
Fixture hydraulic pressure (psi)	77	154	231	308	385	463	540	617	694	771	1,156
Panel elastic radial growth (in.)	0.014	0.028	0.042	0.056	0.070	0.084	0.098	0.113	0.127	0.141	0.211
Water flow per cycle (gal)	0.37	0.73	1.10	1.47	1.84	2.20	2.57	2.94	3.30	3.67	5.51
Pressure reducer stroke (in.)	0.19	0.37	0.56	0.75	0.94	1.12	1.31	1.50	1.67	1.88	2.82
Longitudinal panel elastic stretch (in.)	0.01	0.02	0.03	0.05	0.06	0.07	0.08	0.09	0.10	0.11	0.17
Test machine stroke (in.)	0.06	0.12	0.18	0.24	0.30	0.36	0.42	0.48	0.54	0.60	0.90

and the resulting hydrostatic pressure applied to the panel and the longitudinal panel pulls. The features listed are briefly discussed below:

- Test Machine Load - The internal pressure required for cyclic testing falls between 1 and 9 psi. Estimated panel ultimate capability is about 28 psi. The test fixture has a safe operating limit of 20 psi, equivalent to a test machine load of 36,000 lb. Test machine maximum capacity is 55,000 lb. The panel and fixture assembly are protected by adjustable water and hydraulic system pressure relief valves.

- Panel Hoop Load - Panel hoop load per inch is the product of pressure and panel radius. At 15 psi, this generates a load approaching 122,000 lb on the test fixture.

- Panel Longitudinal Load - This load is half the hoop load. At 15 psi, this generates about 3,000 lb of load on the fixture ends.

- Fixture Hydraulic Pressure - The ratio of panel pressure to hydraulic pressure is 77:1. An 1,800-lb pull from the test machine generates 77 psi of hydraulic pressure. This pressure produces 1 psi of water pressure and a 2,100-lb pull on the test panel.

- Panel Radial Growth - The pressure load causes an elastic panel length change in the hoop direction. This length change causes the panel to grow radially and move upwards away from the inner pressure seal. Maximum predicted movement at 15 psi is 0.21 in. Maximum seal overall travel capability is 0.75 in.

- Water Flow - The water flow per cycle that results from the panel radial growth is about 3 gal during cyclic testing. This flow controls the testing cycle rate. A sinusoidal loading profile is used during cycle testing. The shorter the cycle time, the greater the required fluid flow rate and the greater the overpressure resulting from mechanical and fluid inertia effects. At a frequency of 0.25 Hz, the estimated overpressure is less than 0.1 psi.

- Pressure Reducer Stroke - The cyclic testing stroke of the pressure reducer is about 1.5 in. Reducer stroke capability is 4 in.

- Longitudinal Panel Elongation - During cycle testing, the panel stretches about 0.10 in.

- Test Machine Stroke - During cyclic testing, the machine strokes about 0.50 in. This equates to the oil volume required to stroke the four longitudinal panel load cylinders through 0.10 in. and the pressure reducer cylinder through 1.50 in. The testing machine has a 2.75-in. stroke capability at 0.25 Hz.

3.6 Test Fixture Flexibility

The test fixture has been designed to accommodate future needs to the extent practical. Areas of flexibility are briefly described below:

- Panel Geometry - The fixture is currently designed for a 120 x 68 in. panel with a 75-in. radius. Minor dimensional changes can be accommodated by seal compliance and by adjusting the turnbuckle tie-down lengths. Major dimensional changes for panels smaller than 120 x 68 in. and any change in panel radius between 60 and 100 in. can be accommodated by changing the sizes of the two seal support frames and the two longitudinal load support plates.

- Panel Frame Bending - A load beam attached to one or more panel frames and powered by one or more hydraulic cylinders can be mounted within the pressure tub volume. The setup can be accessed with the panel installed through the four existing access panels.

- Panel Loading - The selection of a universal test machine as the source of the panel loading provides a wide range of panel loading options, using developed and proven equipment.

3.7 Fixture Fabrication and Installation

The test fixture structure was fabricated by New England Steel Fabricators of Milford, NH. The four major component parts, namely the base structure with access doors, the inner seal frame, the outer seal frame and the upper structure, were assembled and verified by Foster-Miller inspection prior to final painting and shipment to the Foster-Miller test facility. The fixture was installed in the test area, the general arrangement of which is shown in Figure 3-12. The Instron test machine was installed first with its hydraulic power unit situated in an adjacent soundproof room. The fixture was then positioned and leveled for optimum drainage. Fixture assembly was then done through the incorporation of the following:

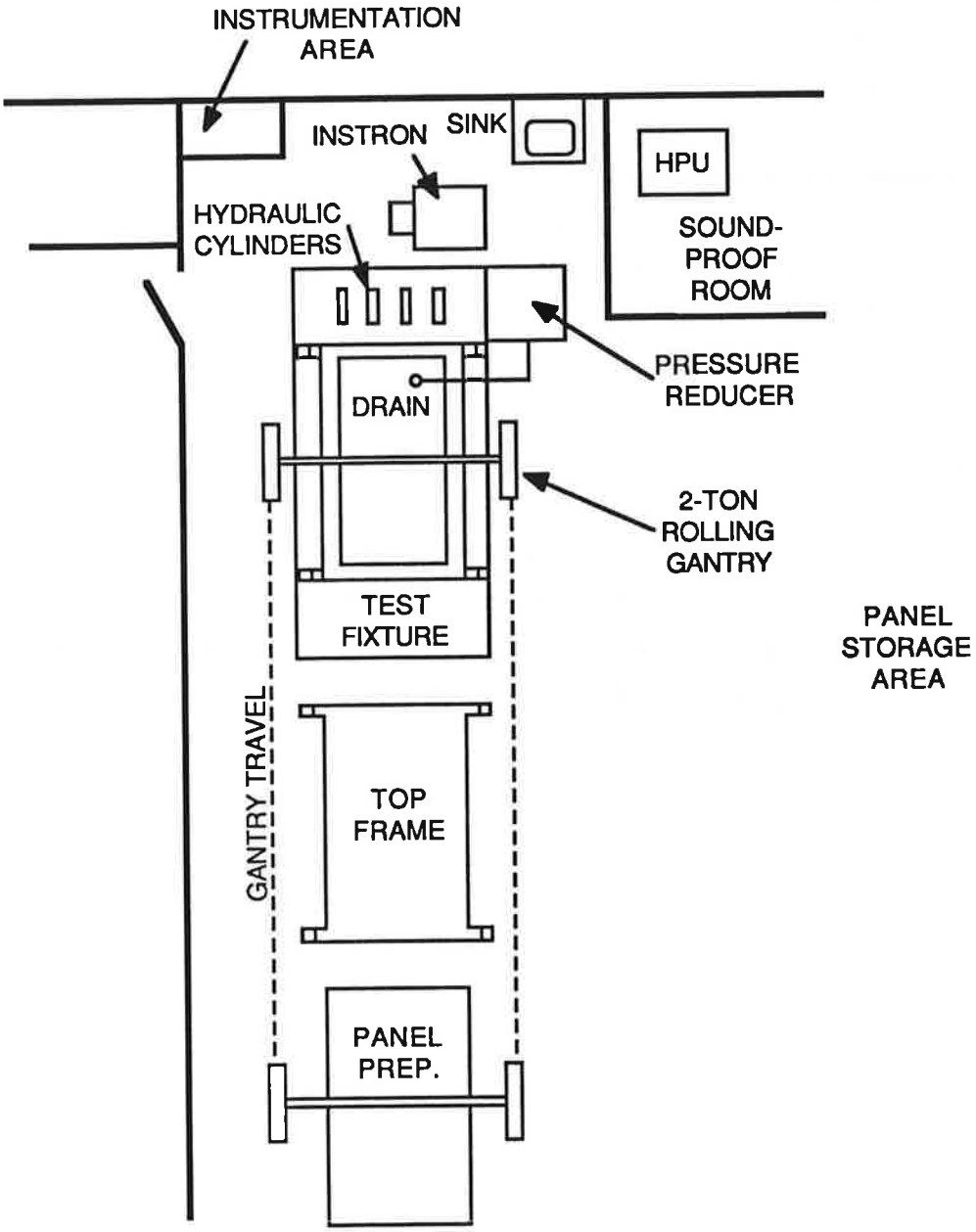

Figure 3-12. Facility Layout

- Longitudinal turnbuckles (56)
- End restraint turnbuckles (4)
- Whiffle tree assemblies (8)
- Frame anchor sets (12)
- Axial loading cylinders (4)
- Panel seal assemblies (2)
- Door gasket sets (4)
- Vent and shut-off assembly
- Pressure reducer assembly
- Instron load cylinder installation
- Hydraulic reservoir installation
- Hydraulic plumbing installation
- Three-inch diameter panel pressure plumbing
- Pressure transducer installation (2)
- Inspection platforms (2).

A travelling gantry crane was used for positioning the panel mounted in a handling fixture and for moving the fixture top frame assembly. An instrumentation area was set up adjacent to the Instron and the fixture assembly. Photographs of the entire test facility and several of the major components are presented in Figures 3-13 through 3-16.

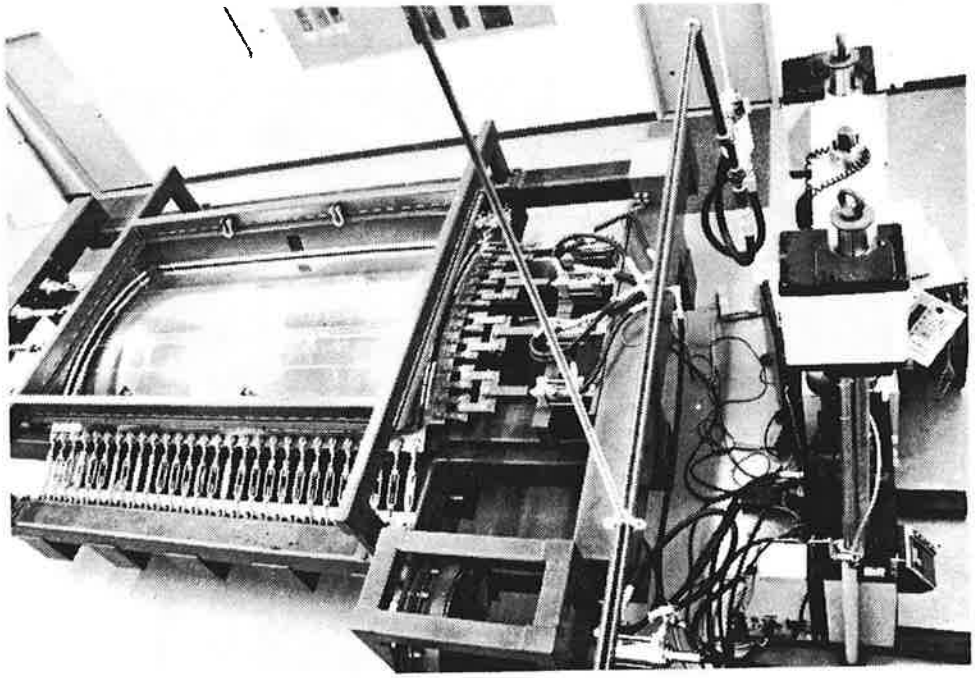

Figure 3-13. Test Facility Overview

Figure 3-14. Test Fixture Structure

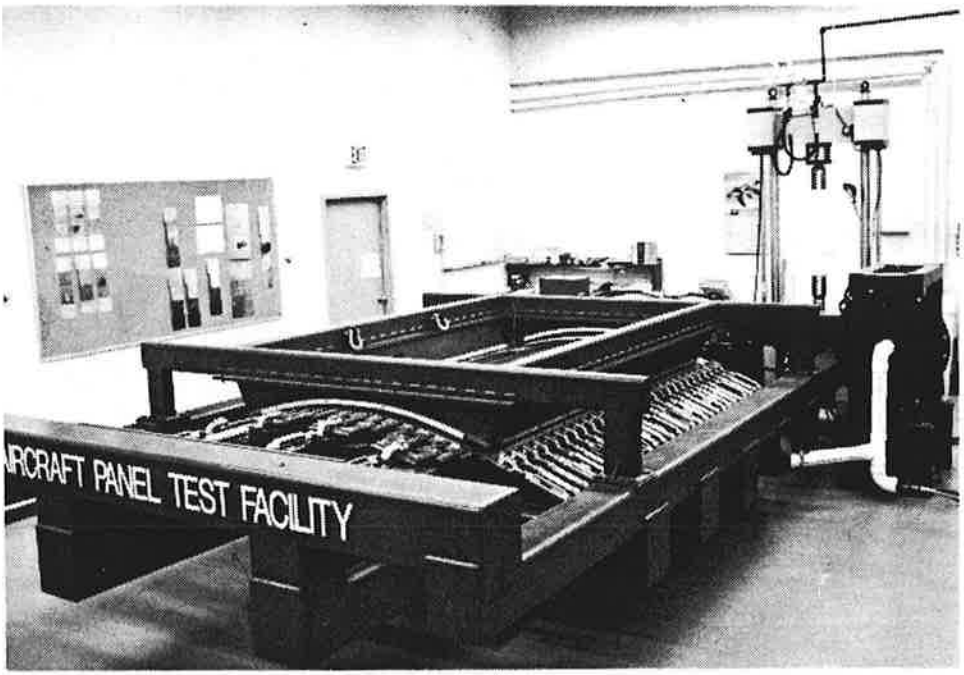

Figure 3-15. Panel Fixed End and Side Restraint

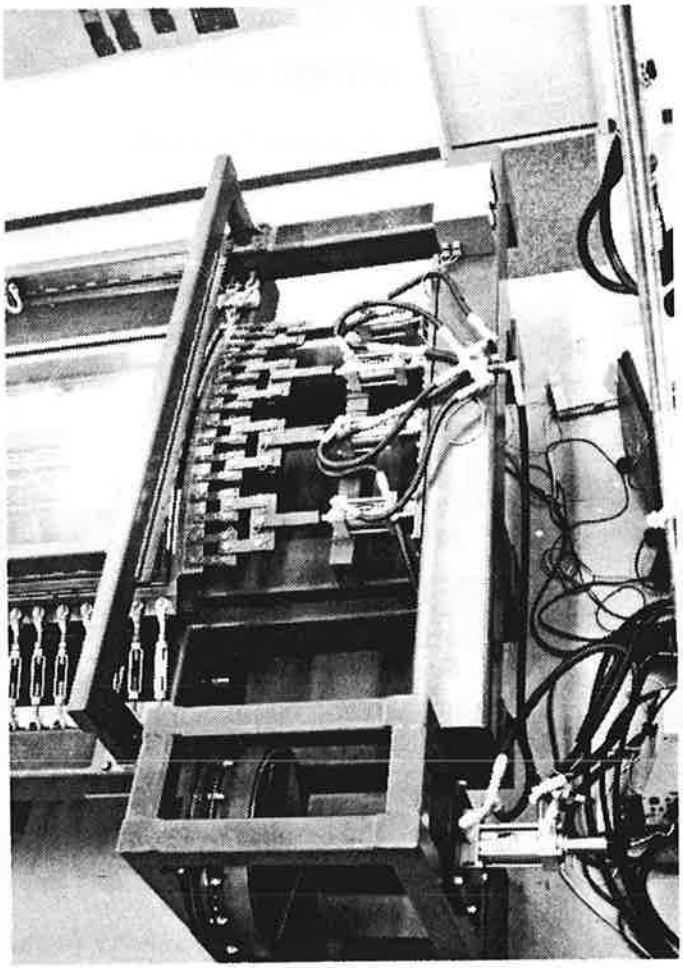

Figure 3-16. Panel End Loading Arrangement and Pressure Reducer

4. TEST PANEL DESIGN AND FABRICATION

Test panel designs were developed to include the following features:

- Represent the features of fuselage construction of older-vintage commercial aircraft used on major traffic routes
- A relatively thin-skinned shell using clad 2024-T3 aluminum alloy for the skin panels
- Stiffening in the circumferential direction by frames and in the longitudinal direction by stringers each with hat, L, Z or channel-sectioned members
- Stringers fabricated from 7075-T6 aluminum alloy sheet
- Frames fabricated from 7075-T6 aluminum alloy sheet
- Conventional rivet construction
- Skin panels joined by a single lap joint using three rows of countersunk rivets
- Configuration minimizes boundary, attachment and end effects when subjected to the biaxial loading that results from pressurization.

Two panel configurations were selected. One panel has a 20-in. tear strap spacing with an 8-in. stringer spacing, as shown in Figures 4-1 and 4-2. The second panel has a 10-in. tear strap spacing and a 9.6-in. stringer spacing, as shown in Figures 4-3 and 4-4. Major features of each panel are shown in Table 4-1. The test panels are fabricated from 0.040-in. thick clad sheet aluminum throughout. The panels include one central longitudinal splice positioned over a central stringer. The splice is joined by three longitudinal rivet rows. The center rivet row also attaches the stringer to the skin. One-inch wide tear straps are positioned in the hoop direction on 20-in. centers at each frame. Panel 2 also has tear straps between each frame. Longitudinal filler strips, also 1-in. wide, are positioned between the tear straps at the stringer locations to provide a waffle-type configuration. Faying surfaces between the skins at the lap joint and the skins and tear straps and filler strips are adhesively bonded.

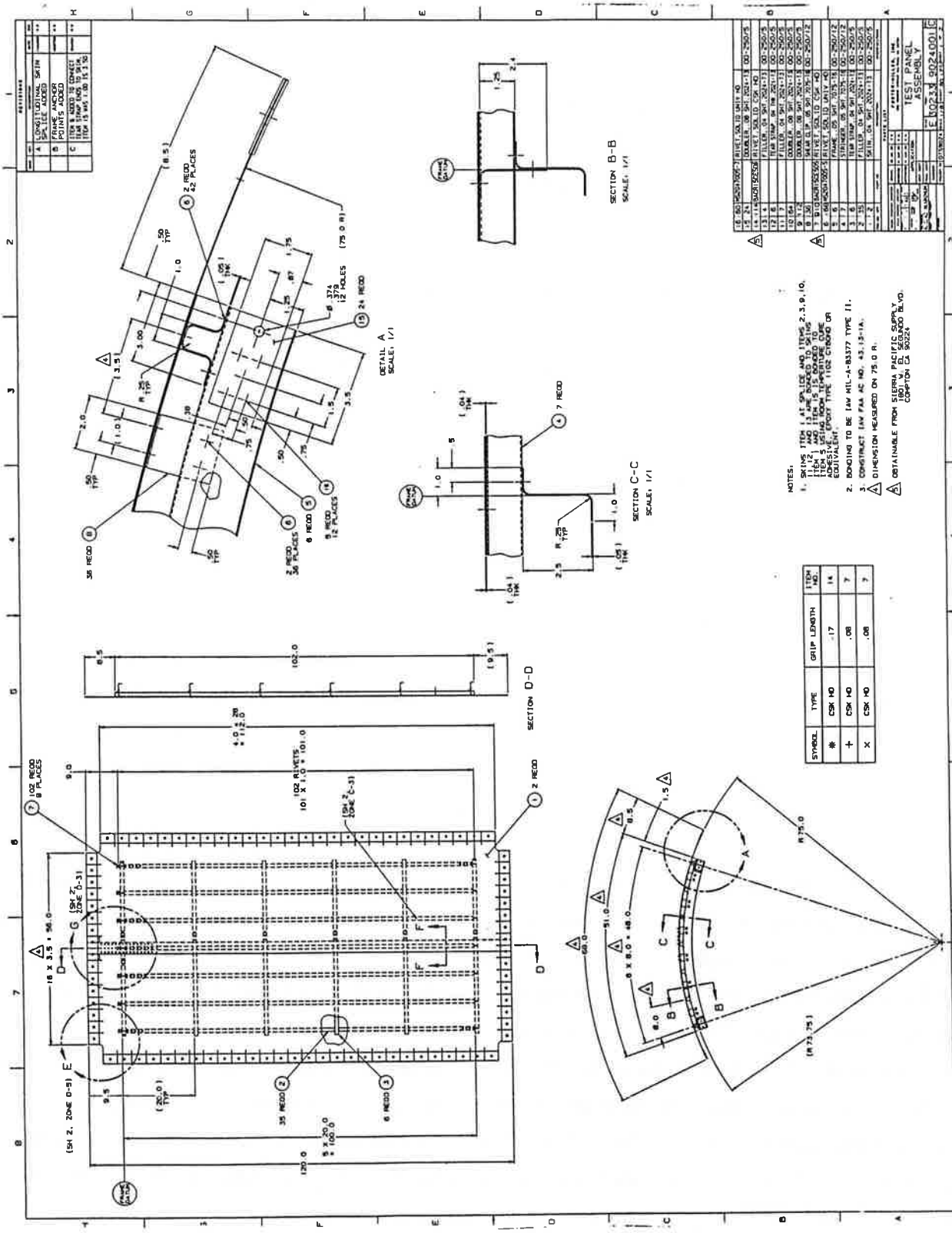

Figure 4-1. Test Panel 1

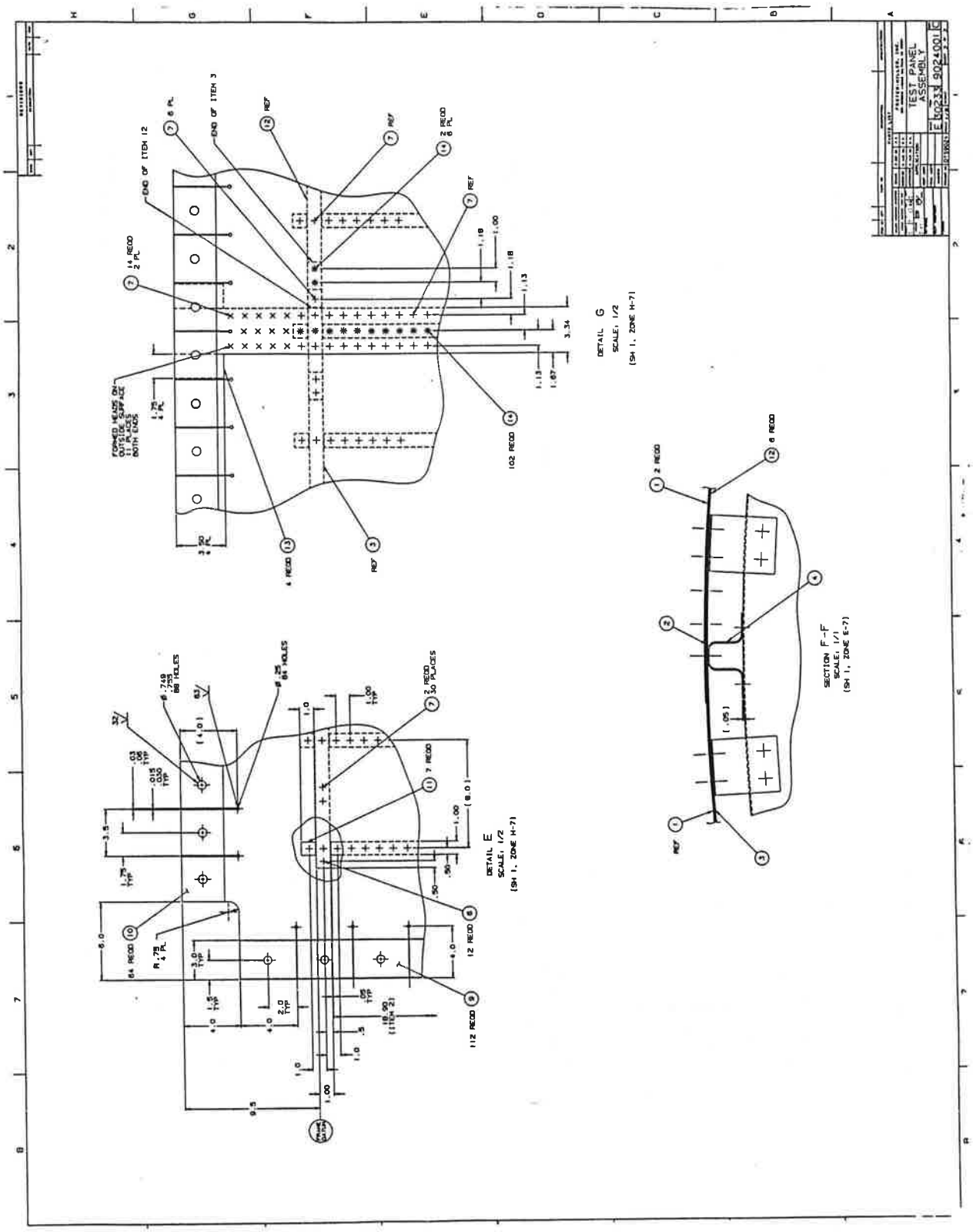

Figure 4-2. Test Panel 1 Details

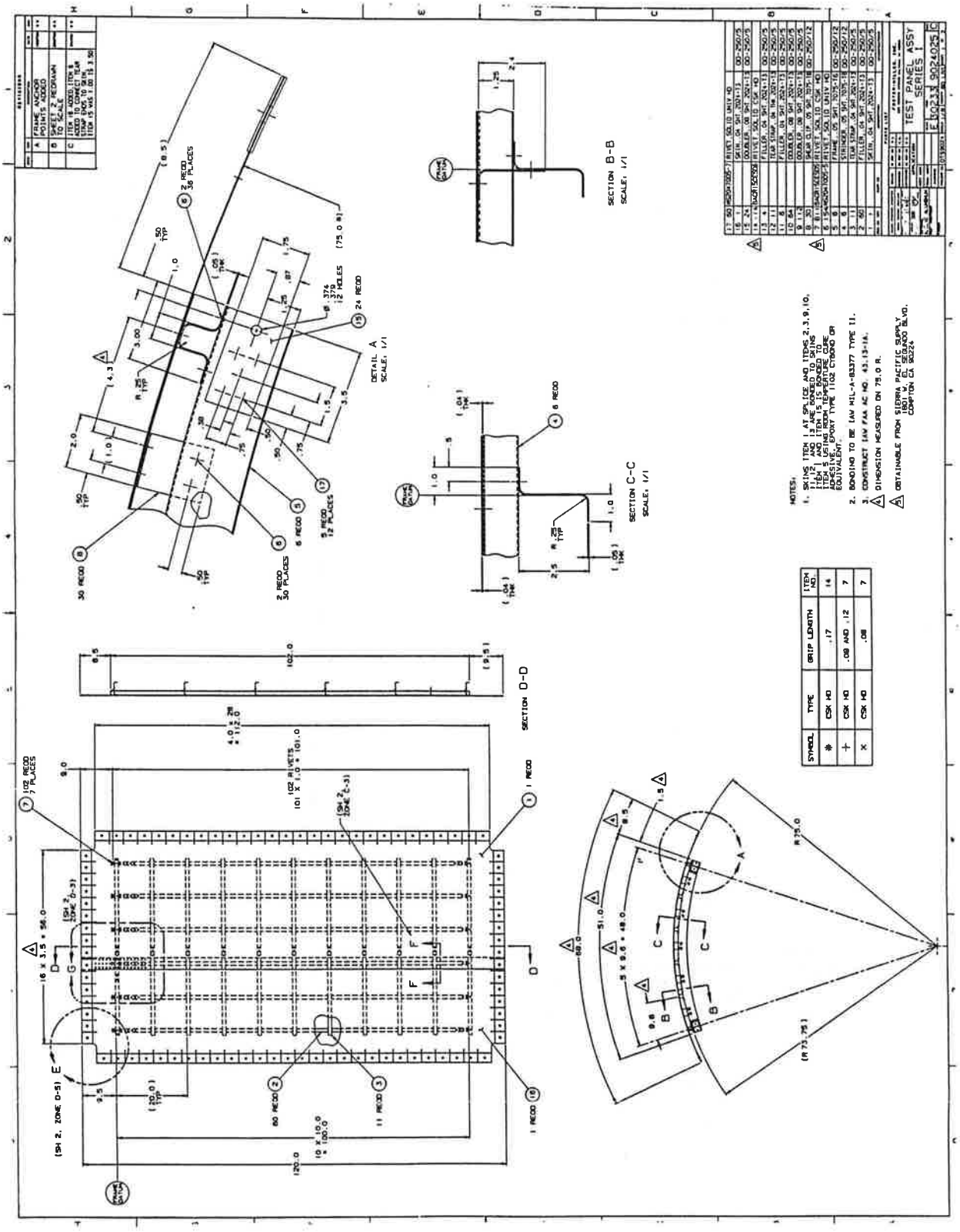

Figure 4-3. Test Panel 2

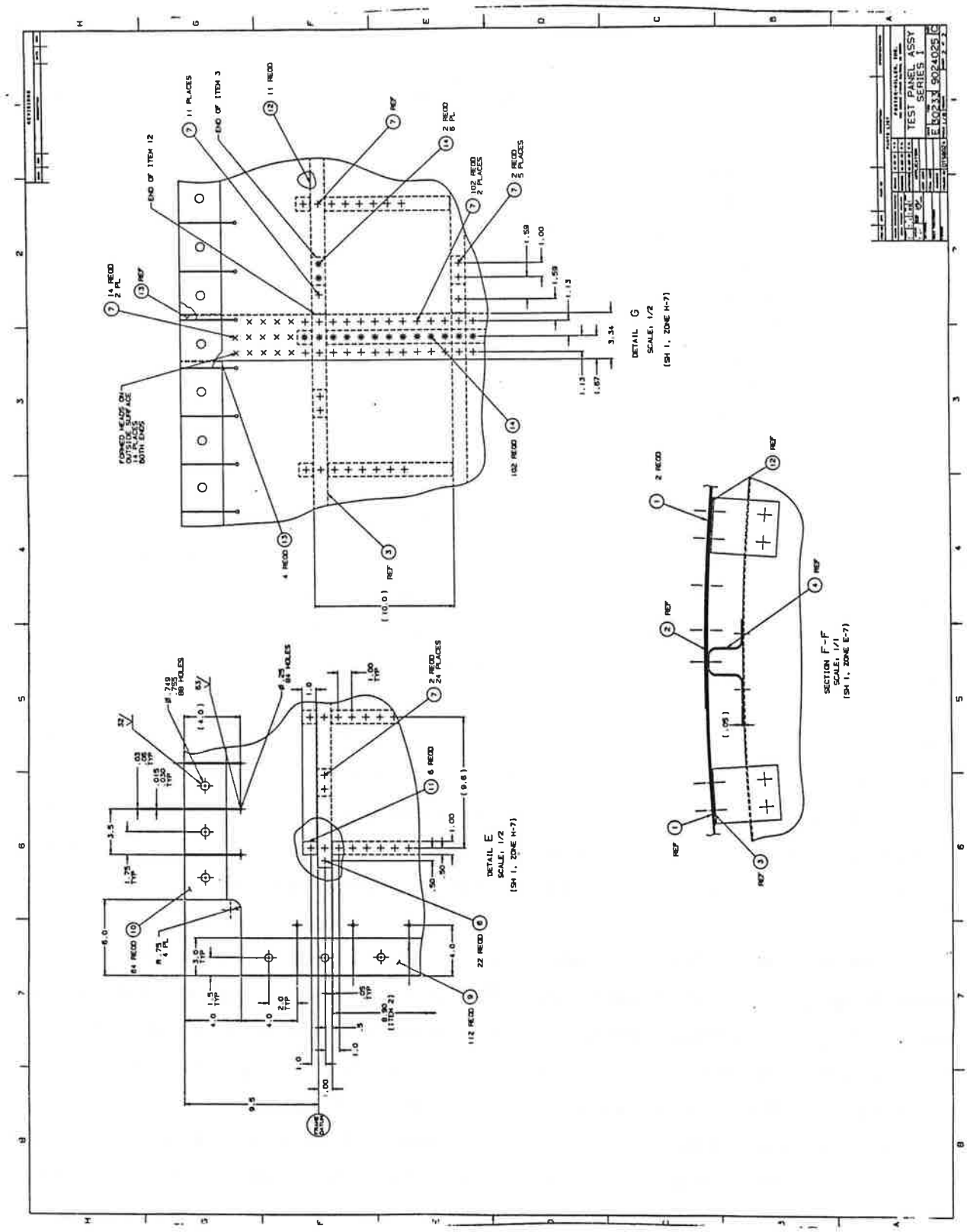

Figure 4-4. Test Panel 2 Details

Table 4-1. Panel Features

	Panel 1 Dwg 9024001	Panel 2 Dwg 9024025
Panel radius (in.)	75	75
Panel length (in.)	120	120
Panel width (developed) (in.)	68	68
Number of frames	6	6
Number of tear straps	6	12
Number of stringers	7	6
Frame spacing (in.)	20	20
Tear strap spacing (in.)	20	10
Stringer spacing (in.)	8	9.6

The stringers are of fabricated hat-section and the frames are of fabricated Z-section. Stringers are rivet-attached to the skin through the hat crown. The base of the stringer is rivet-attached to the frame flange by two universal-head rivets at each intersection. The frames are attached to the skin in each stringer bay by a fabricated angle shear-clip. All through-skin rivets are 5/32-in. diam, low profile, shear head 100-deg countersunk rivets.

The four edges of the test panel are specially prepared for connection to the test fixture. Twenty-eight fingers, each 4 in. wide, are located along each of the two longitudinal panel sides and 16 fingers, each 3.5 in. wide, are located along each of the two curved ends. Each finger is reinforced by two 0.08-in. thick aluminum reinforcing sheets, one bonded to each side of the skin. Each finger assembly includes a 3/4-in. diam centrally positioned hole.

The selected panel configurations have generic similarities to older commercial airframes currently being operated in the United States. The panels are relatively easy to fabricate and assemble. The panel periphery configuration has been selected to minimize the effects of test fixture attachment. The individual finger design provides a means of in-plane connection of the skin to the fixture. The longitudinal fingers will transmit panel hoop loads to the test rig. These fingers have been designed to provide minimal longitudinal stiffness to the panel. Similarly, the fingers on the two curved ends transmit only longitudinal loads to the rig. Their contribution to panel hoop stiffness is minimal. The panel includes a short section of unstiffened skin immediately inboard of all the load fingers. This section is clear of frames, tear straps, fillers and stringers and is provided as a clear surface for the bearing of the inflatable peripheral

seals. Rivet orientation in this region of the lap splice has been reversed to place the countersunk head on the inside surface. This provides a smooth sealing surface for the test fixture fluid pressure seal. This rivet reversal should have no influence on testing or panel performance since it is well clear of the central panel test region.

The general panel configuration is such that a wide range of configurational changes can be accommodated within the bounds of the external size and the radius. Changes that can be made to the panel with no influence on the test fixture include:

- Stringer spacing
- Tear strap spacing
- Longitudinal lap joint location
- Skin thickness
- Stringer geometry
- Frame geometry
- Tear strap geometry
- Shear clip geometry
- Shear clip location
- Rivet spacing
- Rivet size
- Rivet style
- Lap joint disbonds
- Tear strap disbonds.

A number of these build options have been included in some of the test panels built to date. A total of seven panel assemblies have been fabricated to date by East Coast Aero Tech (ECAT), Hanscom Field, MA, under the supervision of Foster-Miller. One panel was built to the 9024001 configuration of Figures 4-1 and 4-2 and six panels to the 9024025 configuration of Figures 4-3 and 4-4. Several panels were built to include damage in the form of machined-in skin cracks and disbonds at adhesive joints. Configuration details of each panel constructed to date are listed in Table 4-2.

The panels were fabricated using flat aluminum sheet stock for the skins and tear straps. Skins, tear straps, fillers and edge finger doublers were adhesively joined while flat. The skin assemblies were then formed over the pressed stringers and frames in an assembly jig where the shear clips and stringers were rivet attached to the frames.

Table 4-2. Test Panel Configurations and Built-In Damage

Panel	Configuration	Built-In Damage
1	9024001	None.
2	9024025	61-in. long full width lap joint disbond.
3	9024025	61-in. long full width lap joint disbond plus 12-in. long crack in lap joint upper rivet row.
4	9024025	None.
5	9024025	None.
6	9024025	61-in. long full width lap joint disbond plus 12-in. long crack in lap joint upper rivet row and MSD on three and eight rivets each side of crack.
7	9024025	61-in. long full width lap joint disbond plus MSD on 61 upper row rivets.

Lap joint disbond areas were created simply by elimination of the adhesive during assembly. Cracks were cut into the panel prior to bonding and riveting using 0.007-in. thick jeweler's saw blade in a table jig saw.

Photographs of typical panels and details of the built-in damage are shown in Figures 4-5 through 4-7.

Panels 3, 4, 6 and 7 were modified as a result of experience gained during fatigue testing of panel 7. The modification involved the replacement of all 30 shear clips with 36 U-shaped stringer tie brackets on the four panels. These brackets nest inside the stringers and are rivet attached to the stringer and frame webs. These modifications are shown in Figure 5-13 on page 63 as part of the discussion of testing results.

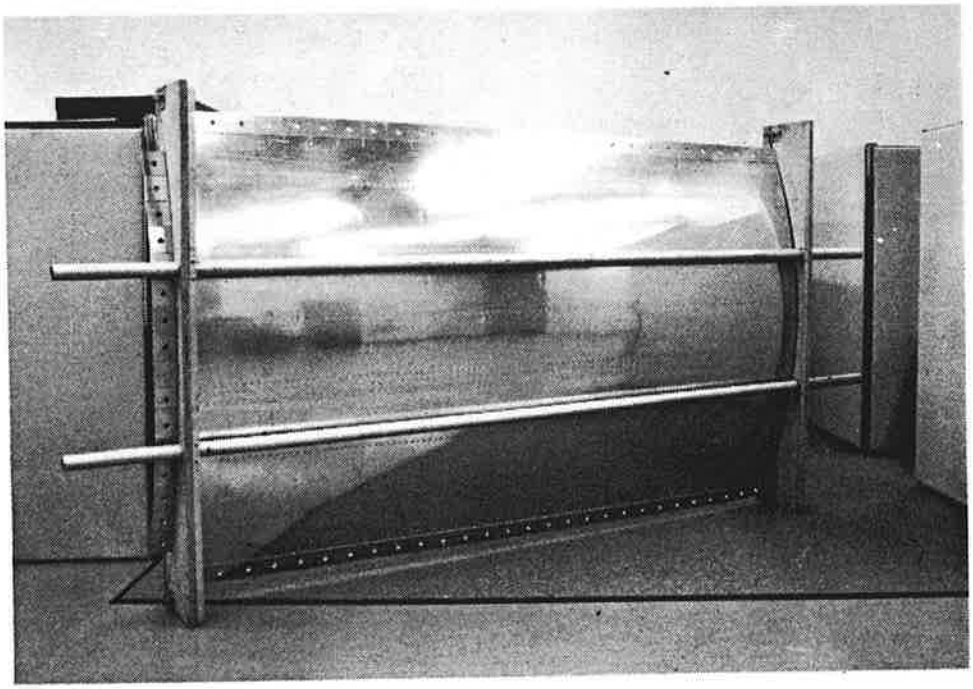

Figure 4-5. Typical Test Panel in Transport Fixture

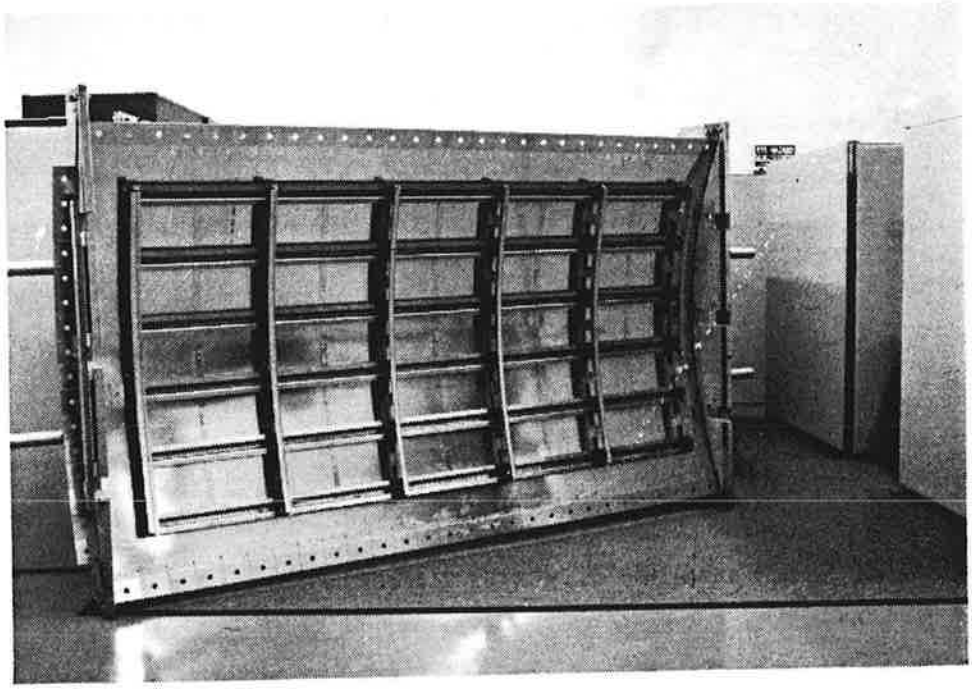

Figure 4-6. Interior of Test Panel

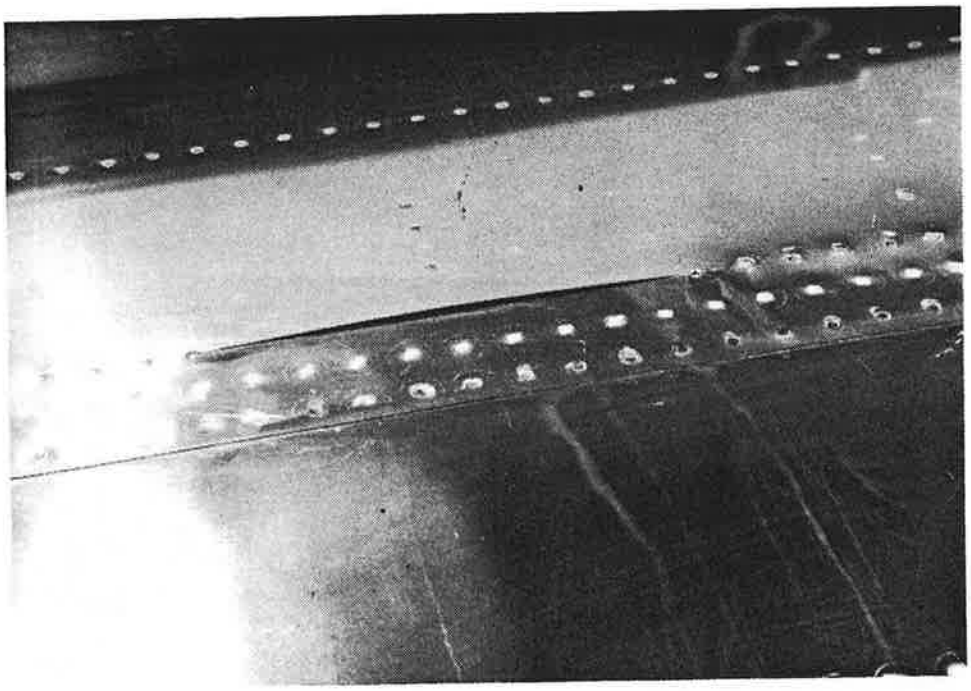

Figure 4-7. Ten-Inch "Crack" in Upper Rivet Row of Lap Joint

5. SYSTEM SHAKEDOWN TESTING

System checkout and operational shakedown tests were performed to:

- Ensure correct fit of the panel to the fixture and correct function of the fixture with the panel installed
- Check the correct operation of the instrumentation and data collection system under static and dynamic load conditions
- Establish optimum panel installation and test procedures
- Conduct panel shakedown loading tests under static, fatigue and fracture load conditions.

The shakedown tests are described in the following subsections.

5.1 System Checkout

The panel and fixture were checked for physical compatibility by installing the panel in the fixture. A series of operational tests was then conducted. Both fit and function were verified at this stage.

Fixture performance verification tests included:

- Pressure reducer operation
- Fixture and panel pressure performance
- Static input load proportioning
- Dynamic input load coordination.

These tests are briefly described in the following paragraphs.

5.1.1 Pressure Reducer Operation

The pressure medium side of the pressure reducer was filled with water and pressurized with shop air at pressures up to 20 psig. The 24-in. diam piston was positioned at several points over the 4-in. stroke range to check for correct operation of the rolling diaphragm seal. Leakproof operation was demonstrated at all stroke positions. Initial tests showed unsatisfactory operation of the diaphragm in that several creases were observed in the diaphragm wall. Liberal application of talcum powder as a dry lubricant to the outside diaphragm surface solved the problem and allowed the seal to roll as intended.

5.1.2 Fixture and Panel Performance at Pressure

A panel was installed into the test fixture. Sheet rubber was added between the panel and the lower seal at the lap joint to help accommodate the lap joint step. Both seals were inflated to 15 psig and the assembly was filled with water. Water leakage was observed coming from both lap joints at the pressure seal and from the base-mounted observation covers. The fixture was drained, a semi-rigid sealant was added to the seal at the lap joint regions and the inspection covers were tightened to a higher bolt torque. The seals were inflated to 25 psig and the assembly was filled with water. No leakage was observed at pressures up to 9 psig.

At the conclusion of the first series of pressure cycling tests, the fixture was drained and the panel was inspected from the inside. Multiple panel failures were found at the frame connections to the fixture. The 2 x 1 in. doublers had become disbonded. The region was upgraded by replacing the small bonded doublers with larger 3.5 x 2 in. doublers which were both bonded and riveted to the frame. This improvement has been incorporated in all panels.

Subsequent panel testing showed no water leakage from the fixture or panel interface and no frame anchorage damage at pressures up to 13.2 psig.

5.1.3 Static Input Load Proportioning

Tests were conducted to measure the two panel input loads to compare them to confirm correct proportionality. The primary input load is the internal pressure, which was measured with a pressure transducer. The secondary input is the axial load applied by the four hydraulic

cylinders. This load was determined by recording the hydraulic pressure and multiplying this pressure by the sum of the cylinder areas. Loads achieved at various panel pressures were plotted and compared with the required load line where:

$$\text{Required load (kips)} = \frac{pr\ell}{2000}$$

where

p = panel pressure, psi
r = panel radius, 75 in.
ℓ = panel active transverse width, 60 in.

Results derived during shakedown testing and subsequent panel testing and shown in Figure 5-1 show good correlation. Some minor variability in the data was found due predominantly, it is believed, to cylinder seal friction.

5.1.4 Dynamic Input Load Coordination

Tests were run to establish an optimum load cycle rate for the system. The minimum cycle rate is determined by the Instron machine which has a minimum capability of 0.1 Hz. Maximum cycle rate is determined by an acceptable limit for phase lag of the panel pressure to the axial load. Phase lag results from mechanical and fluid inertia effects and the fluid flow losses that occur between the pressure reducer and the fixture pressure tub. Pressure cycling tests were run at frequencies between 0.1 and 0.25 Hz and pressures between 0.5 and 8.5 psi. The driving hydraulic pressure and the panel pressure were recorded. Typical normalized plots of pressure versus time at 0.1 and 0.2 Hz are shown in Figures 5-2 and 5-3.

At 0.1-Hz (1 cycle in 10 sec) panel pressure lags hydraulic pressure by 0.5 sec. At 0.2-Hz (1 cycle in 5 sec) panel pressure lags hydraulic pressure by about 0.8 sec. At both test frequencies, load peaks occur together for a short period of time. This ensures that the panel is subjected to the maximum combined loading each time that it is cycled.

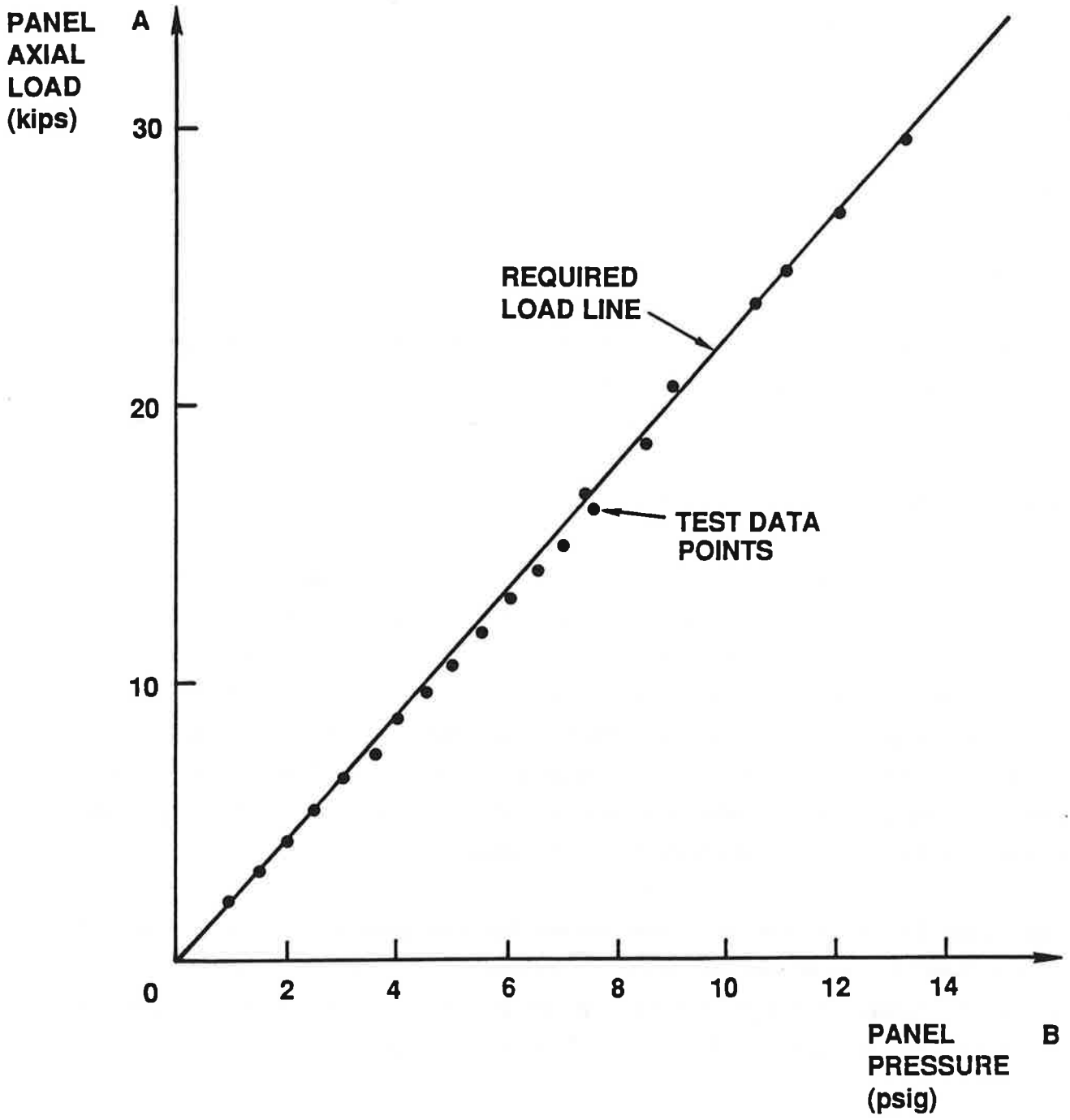

Figure 5-1. Axial Panel Load versus Pressure

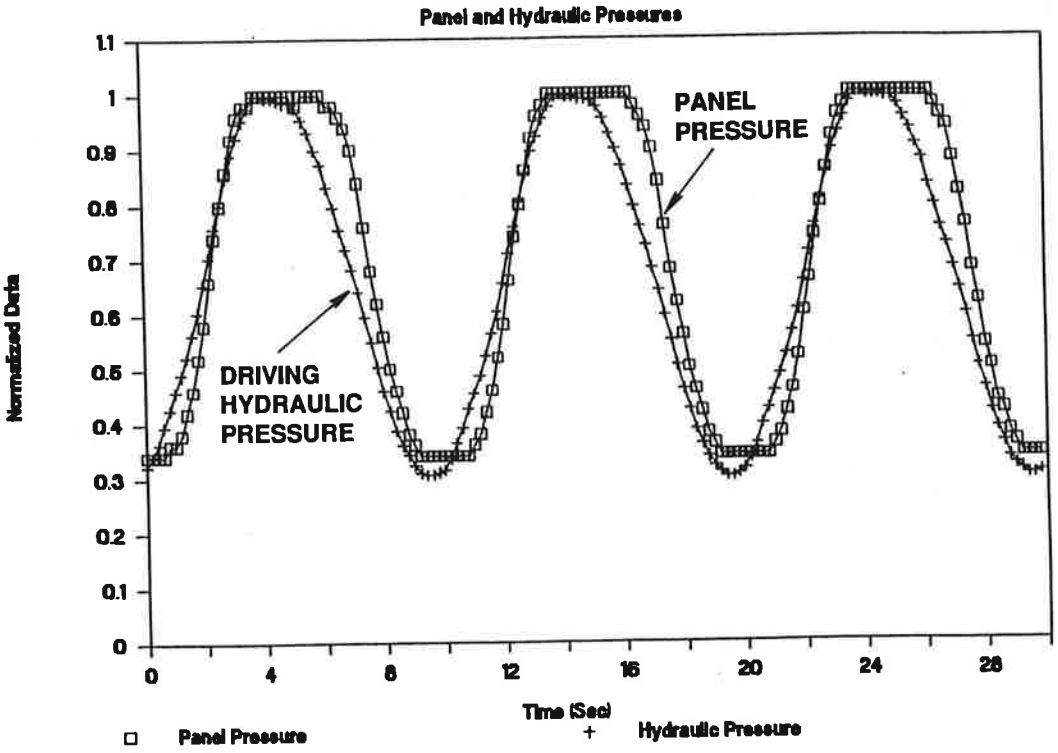

Figure 5-2. Panel and Hydraulic Pressure Profiles at 0.1 Hz Cycle Rate

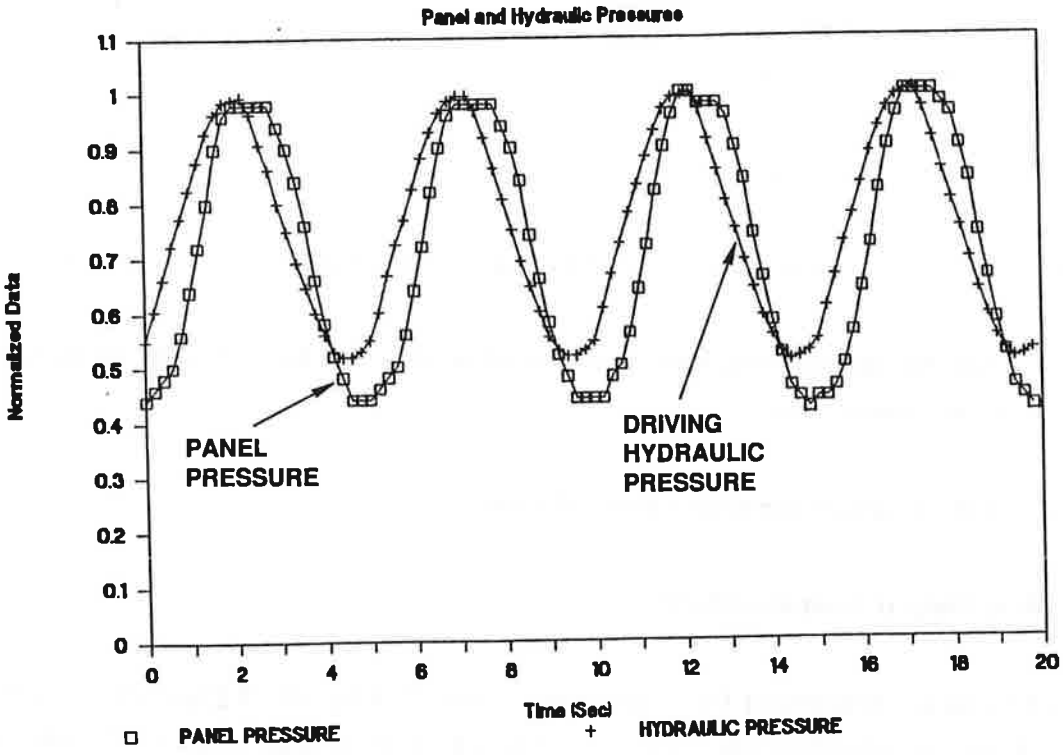

Figure 5-3. Panel and Hydraulic Pressure Profiles at 0.2 Hz Cycle Rate

5.2 Test Instrumentation

The test instrumentation can be conveniently subdivided into test input as provided by the Instron test machine, test output as provided by strain gages, extensometers and transducers and data recording equipment. The instrumentation used in these areas is described in the following paragraphs.

5.2.1 Test Input Instrumentation

Input instrumentation is provided by the Instron 8502 servo hydraulic test machine. The unit provides the following controls and displays:

- Applied load to $\pm$55 kips $\pm$ 0.5 percent
- Stroke 0 to 4 in. $\pm$ 0.02 in.
- Frequency 0.1 to 18 Hz
- Overload protection limits
- Automatic calibration
- Automatic ranging
- Square, trapezoidal and sinusoidal waveforms repeatable to 0.2 percent of reading
- Dual display showing load, position, minimum and maximum or mean amplitudes, cycle count or time
- Multiple action event detectors and limits.

5.2.2 Test Output Instrumentation

The primary test output instrumentation is provided by strain gages attached to the test panel. Gage specifications are shown in Table 5-1. The 70 gage locations for the shakedown

Table 5-1. Strain and Pressure Transducer Descriptions

Item	Manufacturer	Description
Electronic strain gage	Micromeasurements Group, Inc.	Self-compensating foil gage Single element P/N EA-13-250BF350
Panel pressure transducer	Data Instruments	Model No. AR-15 Pressure range 0 to 15 psig Accuracy ±1% Maximum overpressure 30 psig
Hydraulic oil pressure transducer	Data Instruments	Model No. AR-2000 Pressure range 0 to 2,000 psig Accuracy ±1% Maximum overpressure 4,000 psig

test panel are shown in Figure 5-4. Panel and hydraulic oil pressures are measured using transducers specified in Table 5-1. Pressure readouts are displayed on two analog/digital solid-state meters. Panel radial displacements are measured using dial gages. Crack growth is monitored using a 30X microscope.

5.2.3 Data Recording

The data acquisition system used is an ACRO 900 capable of recording 30 strain gage channels and eight analog channels. A sample rate of five samples/sec was used for both static and dynamic test data collection. The ACRO 941 strain indicator unit used has a 7 μin./in. resolution. For shakedown testing, the 70 total strain gage channels were sampled as three sets of 30, with 10 channels carried over for comparison. Two analog channels were used to record the panel and hydraulic pressures.

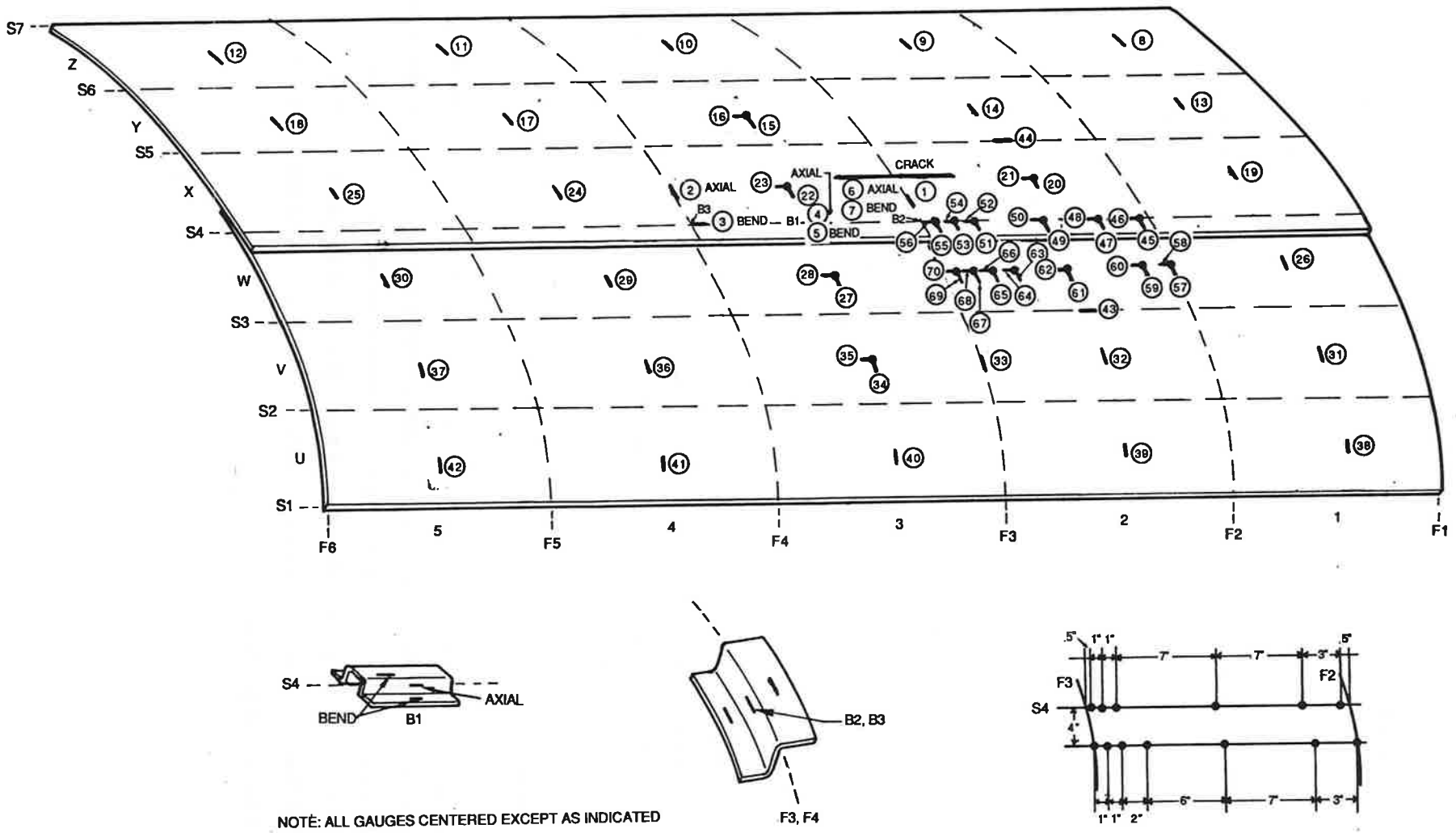

Figure 5-4. Shakedown Panel Gage Locations

5.3 Panel Shakedown Tests

Static, fatigue and fracture strength tests have been carried out to establish the panel test methodology.

5.3.1 Static Tests

Figure 5-5 shows the distributions of the top skin stress in the hoop direction, between two adjacent frames. One plot is for the mid-bay region and the other at a stringer location. Due to the stiffening action of the stringer, the stresses at the stringer are slightly reduced when compared to those at mid-bay. The slight asymmetry in the distribution is attributed to inadequate anchorage of the test panel frames to the fixture frame turnbuckle on the fixed end. This has been corrected in subsequent tests by strengthened skin doublers at the anchors as described in subsection 5.1.2.

Figures 5-6 and 5-7 show typical results for top skin stress (bending and membrane) in the circumferential and axial directions at different pressure levels. These figures show results for the case when a 16-in. crack was saw cut in the skin only across a frame and tear strap. The test data have been correlated with theoretical predictions obtained through geometrically nonlinear simulation on the computer using NISA 386 software. The nonlinearity exists in the neighborhood of the crack due to the large radial displacement.

The test data of Figure 5-6 indicates a hoop stress of 0 Ksi at 0.7 psi pressure. This is likely due to "slack" in the anchoring system in the circumferential direction which is taken up during loading. Correction of the data for this slack would produce excellent agreement between theoretical predictions and test data.

5.3.2 Fatigue Tests

Fatigue tests on the machine-cracked panel were conducted at a rate of 720 cycles/hr (0.2 Hz). Crack growth was monitored using a travelling microscope. Typical results are shown in Figure 5-8 for a crack over a frame and a crack between two adjacent frames. The stress intensity factor when the crack tip is near a frame is expected to be different from that when the crack tip is at mid-bay. Hence, the significant difference in the crack growth rates for the two cases.

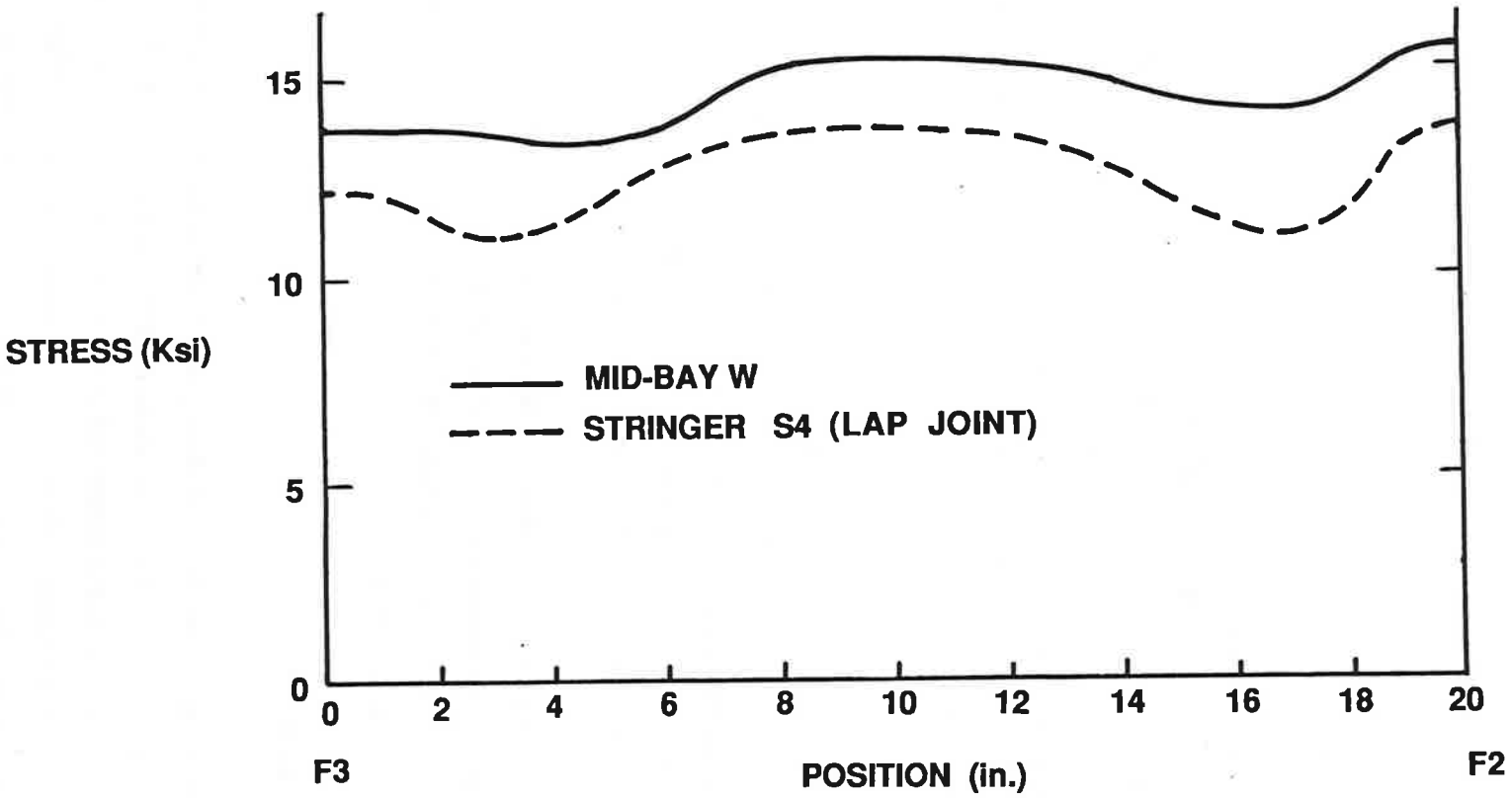

Figure 5-5. Top Skin Stress - Hoop Direction, 8.6 psi

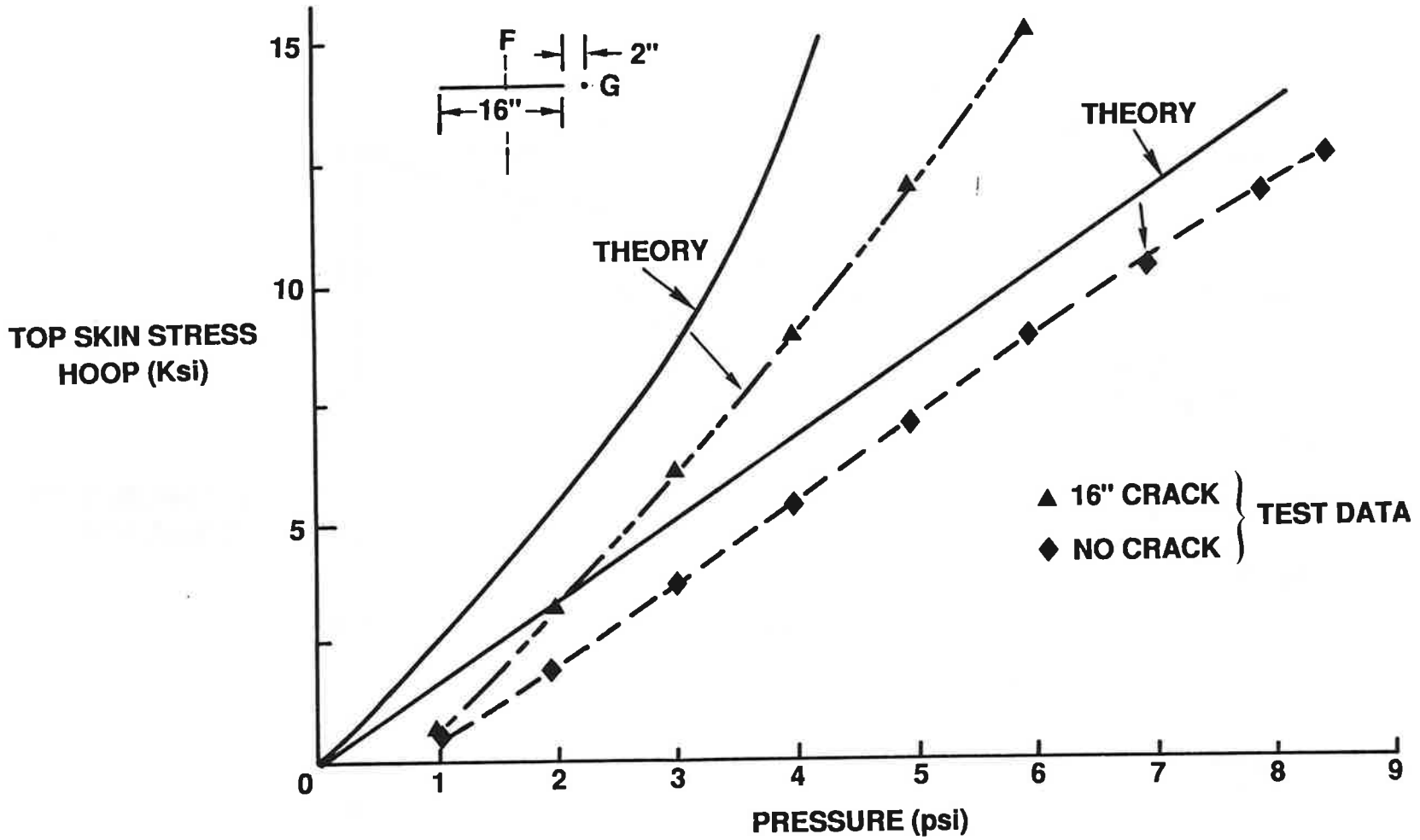

Figure 5-6. Top Skin Stress in Hoop Direction - Mid-Bay, Gages 22 and 23

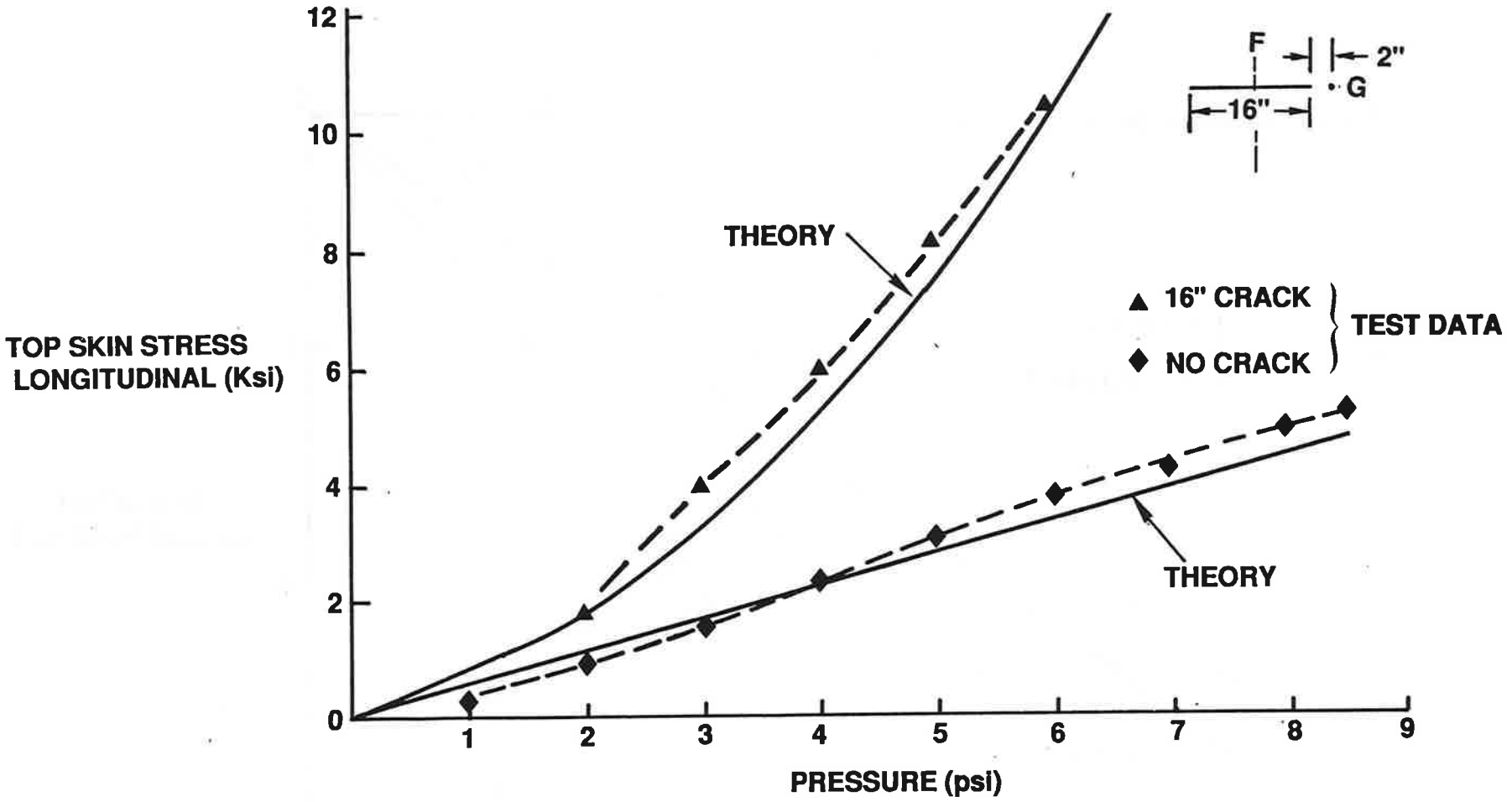

Figure 5-7. Longitudinal Top Stress - Mid-Bay, Gages 22 and 23

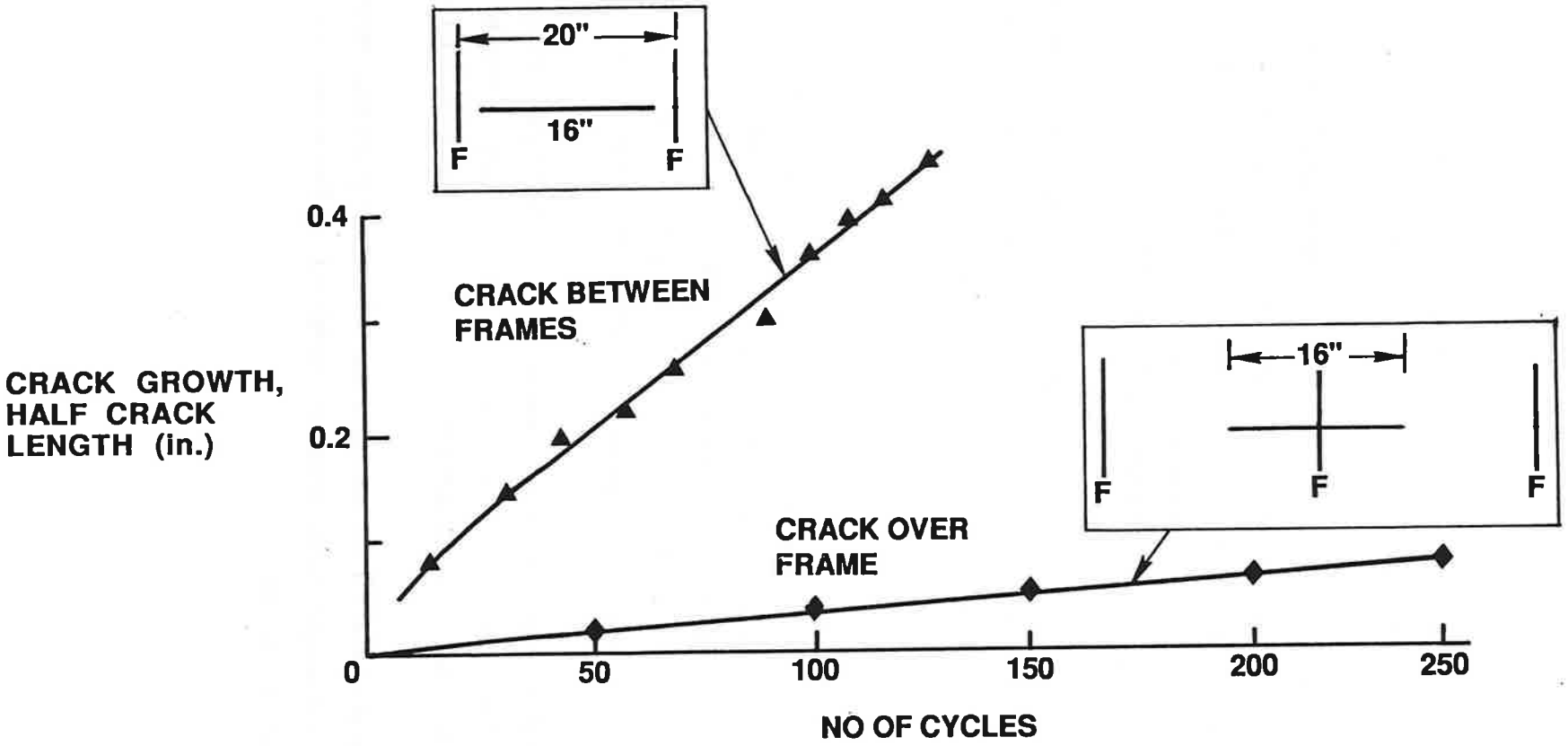

Figure 5-8. Fatigue Test Crack Growth Rate

5.3.3 Fracture Tests

Fracture tests were performed to evaluate the residual strength of cracked panels. Typical results for a 16-in. initial crack in the skin are shown in Figures 5-9 and 5-10.

The crack experienced stable growth until it reached the shear clip attachment rivet hole at the frame/strap location. At a pressure of 13.2 psig, the crack negotiated the rivet and grew suddenly by about 3.5 in. into the adjacent bay, as shown by Figure 5-11. The fracture pressure of 13.2 psig compares well with the theoretical value of 13.7 psig predicted for the panel with this type of damage using the model described in Section 8.4.

Bulging at the crack center is shown in Figure 5-12. At the time of fracture, the bulging deflection was about 1 in. The observed nonlinearity between the pressure and the bulging deflection proves the importance of large deflection theory in the analysis.

5.3.4 Lap Joint Fatigue and MSD Link-up Test

The purpose of this test was to subject the panel to high fatigue cycles and study the fatigue crack growth in the lap splice leading to the link-up of ligaments and complete panel fracture. The test would also verify the endurance of the test fixture, the structural adequacy of the panel attachments to the fixture turnbuckles and the fatigue strength of the shear clip attachment to the skin. This test was conducted with the panel configured to drawing 9024025.

After about 5,000 cycles with pressure ranging from 1.0 to 8.6 psi, a fatigue crack started forming in the head of one rivet fastener which attached a shear clip to the skin (Figure 5-13a). All shear clips were replaced by "stringer ties" which are typical in commercial aircraft.

Initial testing also revealed that the anchoring holes at the panel edge were vulnerable to fatigue cracking, and needed strengthening by additional doubler plates. The panel was modified accordingly for the test.

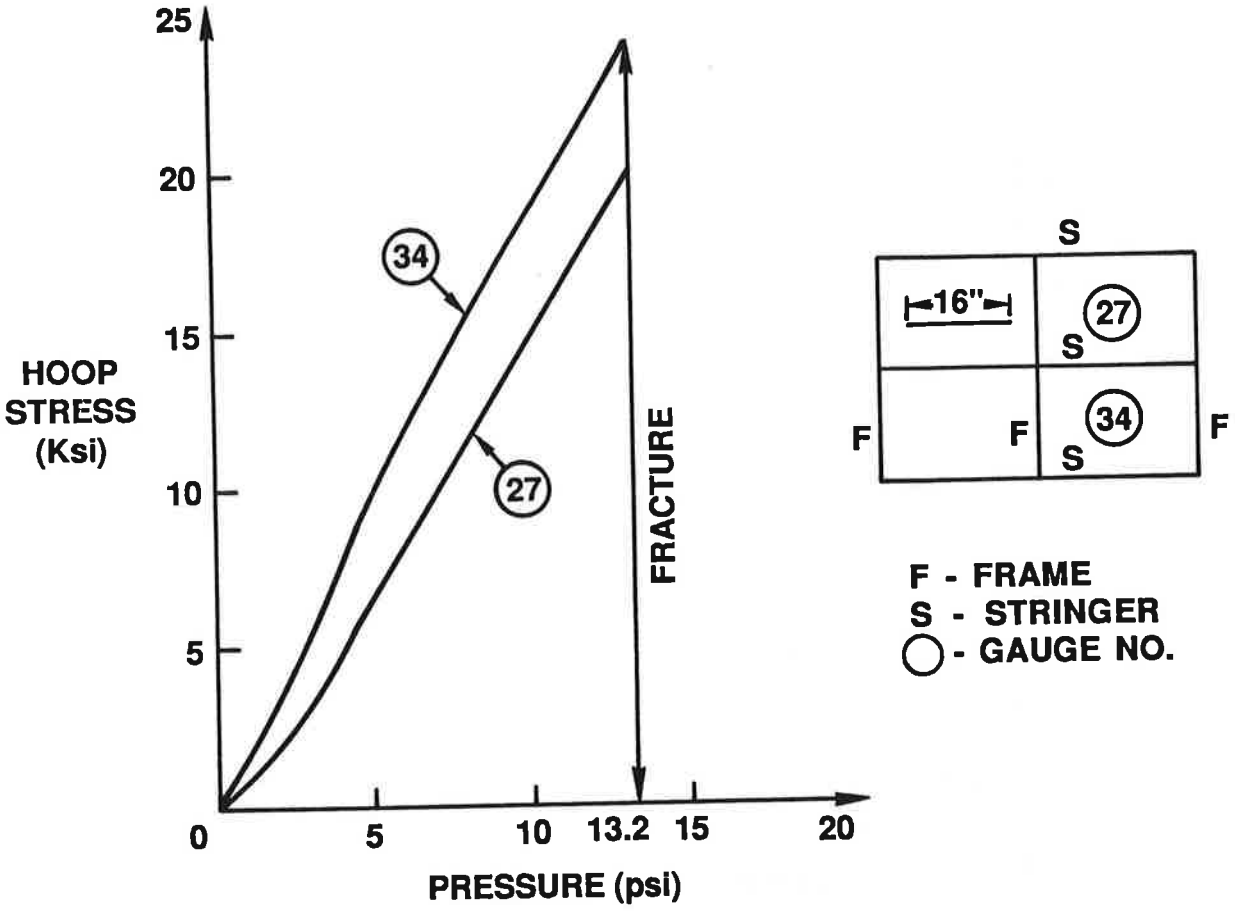

Figure 5-9. Fracture Test - Top Skin Hoop Stress

Initial Panel Damage

The lap splice was fabricated without a bond for a 61-in. length and the top skin at the upper row rivet holes was prenotched to simulate MSD. After prenotching, countersunk rivets were installed according to standard practices. The notches did not extend beyond the rivet heads and hence were not visible from outside. At the inner skin surface, a 0.5-in. bead of silicone was applied covering the skin edge to prevent water leakage through the lap joint during the test. Figure 5-14 shows schematically the initial damage and the rivet numbering system.

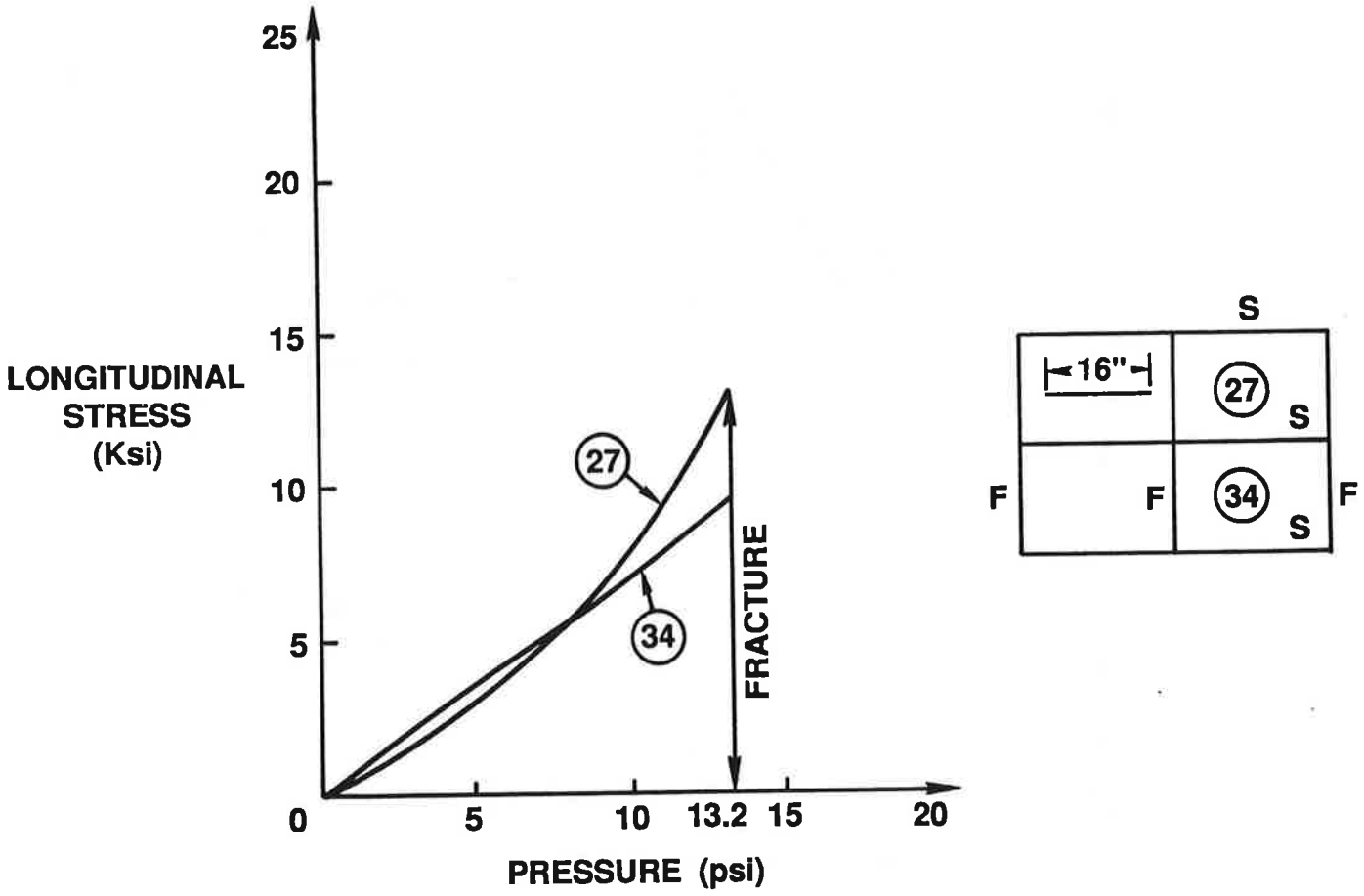

Figure 5-10. Fracture Test - Top Skin Longitudinal Stress

Test Results

Initial testing continued to 50,350 cycles with the pressure ranging from 1 to 8.6 psi. At 40,150 cycles, a crack of length 0.04 in. (from rivet head circumference to crack tip) was observed at rivet hole 6. This crack grew steadily to about 0.1 in. at 50,000 cycles. A few isolated cracks of much smaller length were also visible through an optical microscope. To accelerate the fatigue crack growth rate, the upper limit of the pressure cycle was increased by 50 percent to 13 psi. At 67,493 cycles, the crack at rivet 6 had grown to 0.37 in.

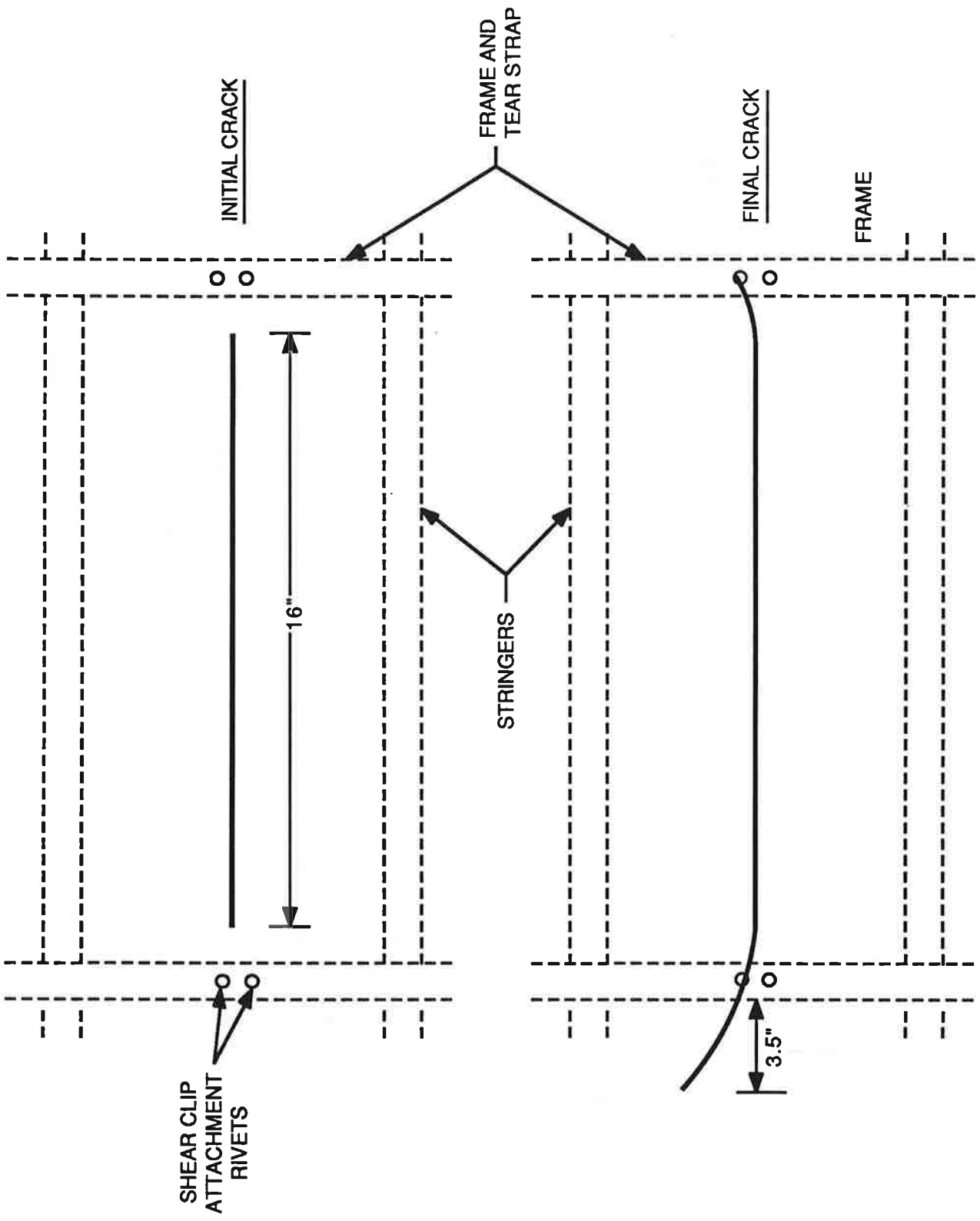

Figure 5-11. Panel Fracture

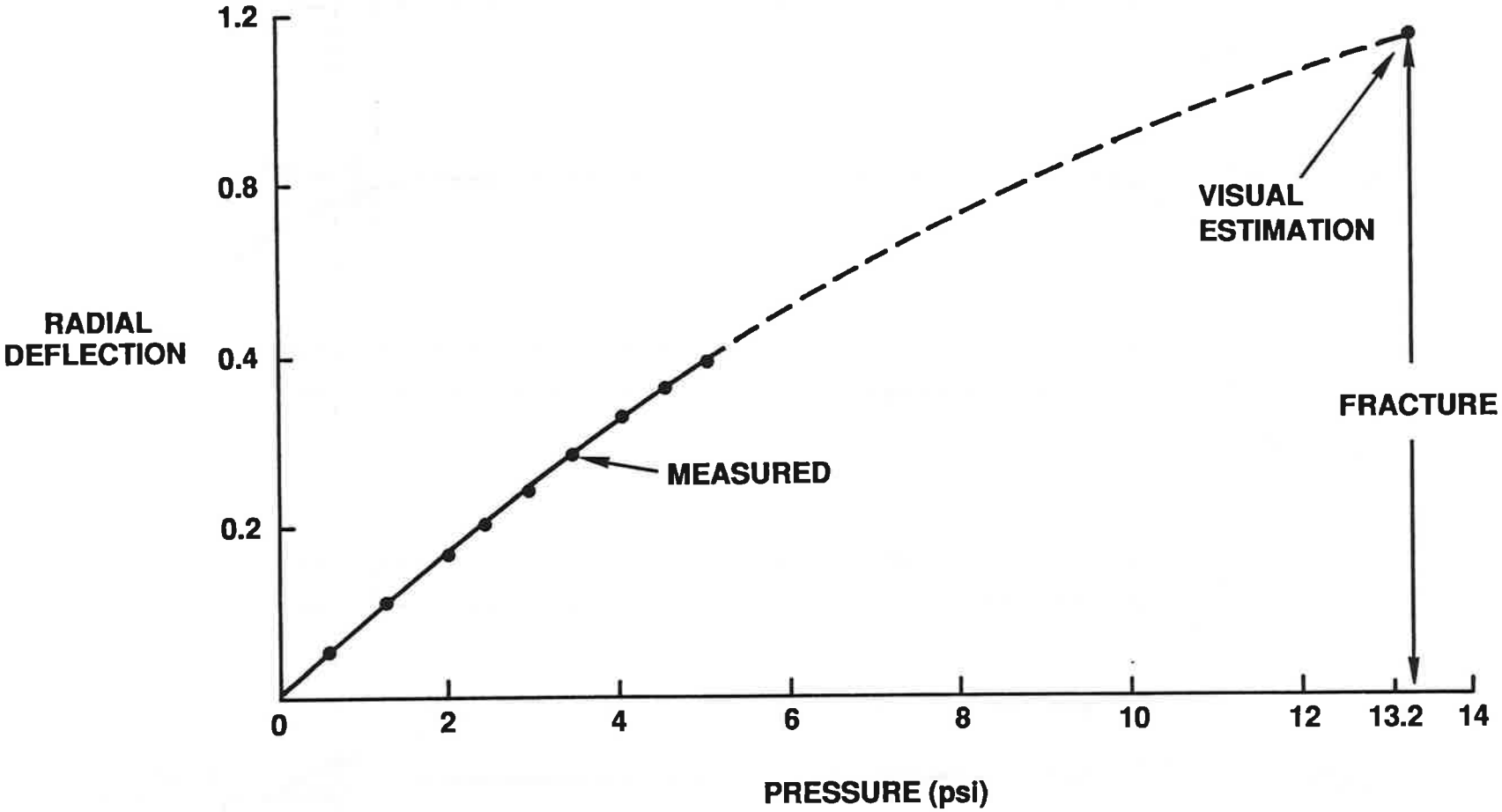

Figure 5-12. Fracture Test - Bulging at Crack Center

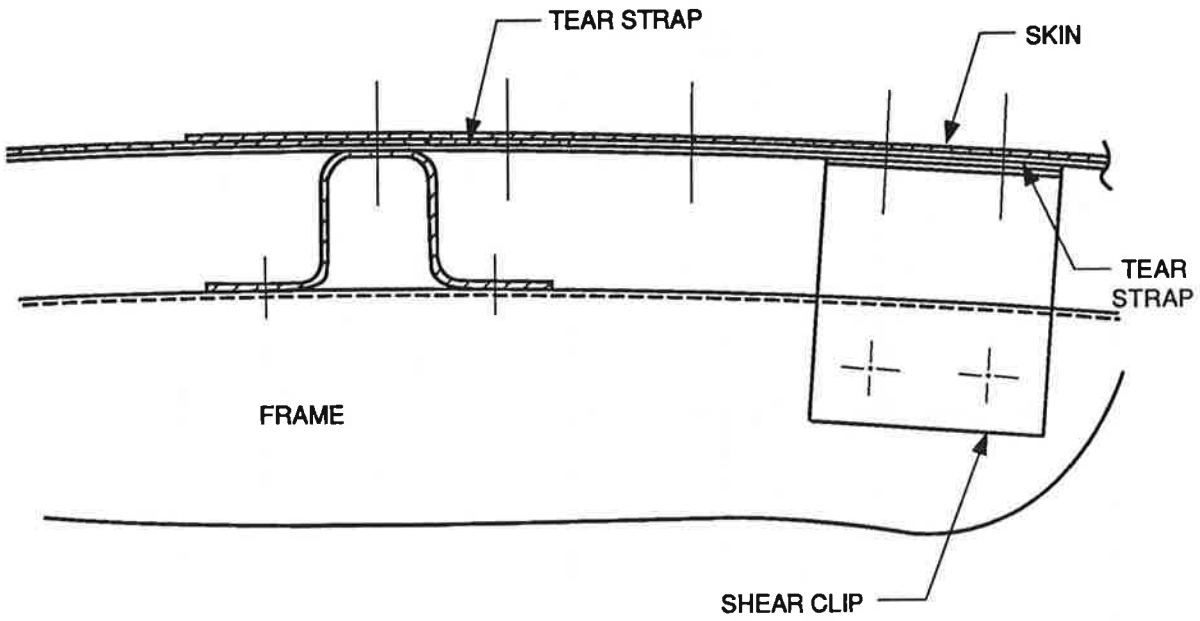

(a) SHEAR CLIP FOR USE IN RESIDUAL STRENGTH AND LOW CYCLE FATIGUE ONLY

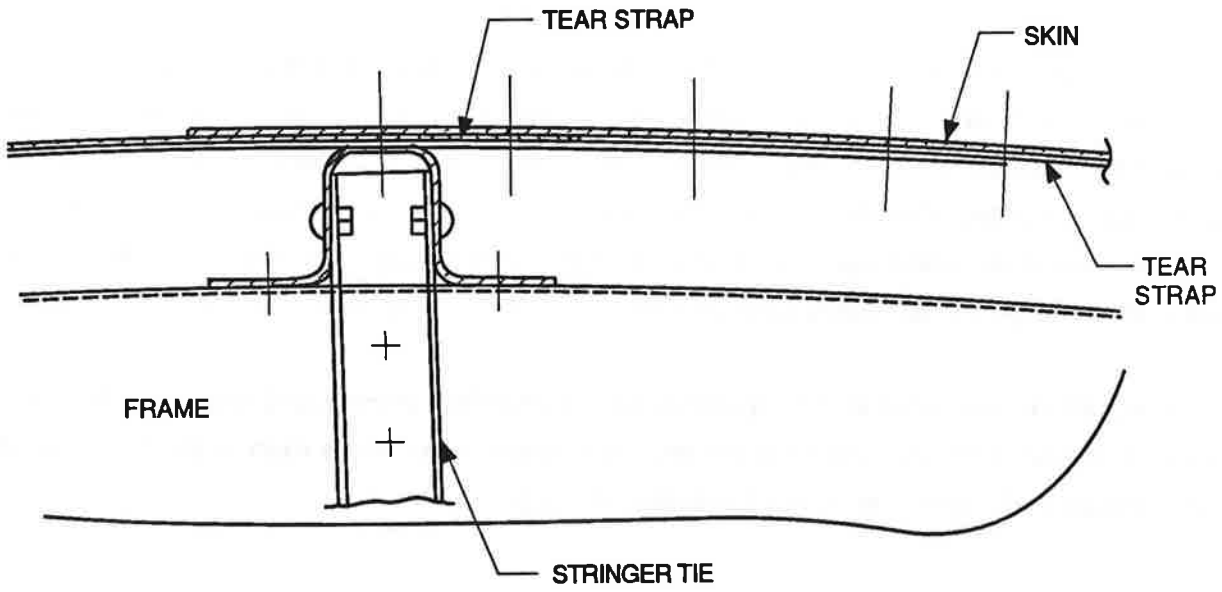

(b) STRINGER TIE FOR HIGH CYCLE FATIGUE

35-DTS 9024-3

Figure 5-13. Skin Attachment to Frame

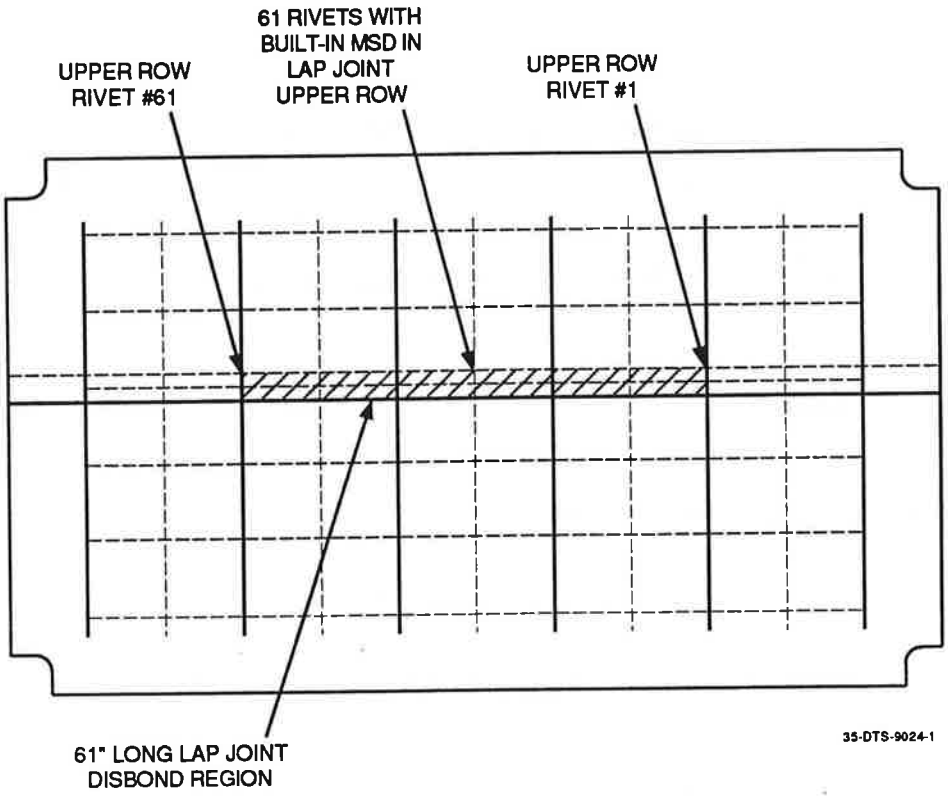

Figure 5-14. Panel Configuration and Initial Damage

Cracks grew at a total of 37 locations. Measured crack growth rates at several of these locations are indicated in Figure 5-15. From about 68,200 cycles, increasing water leakage was observed, which was attributed to cracks in the lower skin. At 68,300 cycles, a distinct noise was heard. The testing was stopped to observe the conditions of the bottom skin, which showed link-up of two ligaments at the lower lap joint rivet row. The test was continued for an additional 50 cycles, when the panel fractured in a catastrophic manner (Figures 5-16 and 5-17).

Hoop strains recorded at the lap splice are of practical interest and are presented in Figures 5-18 and 5-19. As one would expect, maximum stress levels exist at the first row of rivets. Figure 5-19 reflects an internal pressure of 8.6 psi.

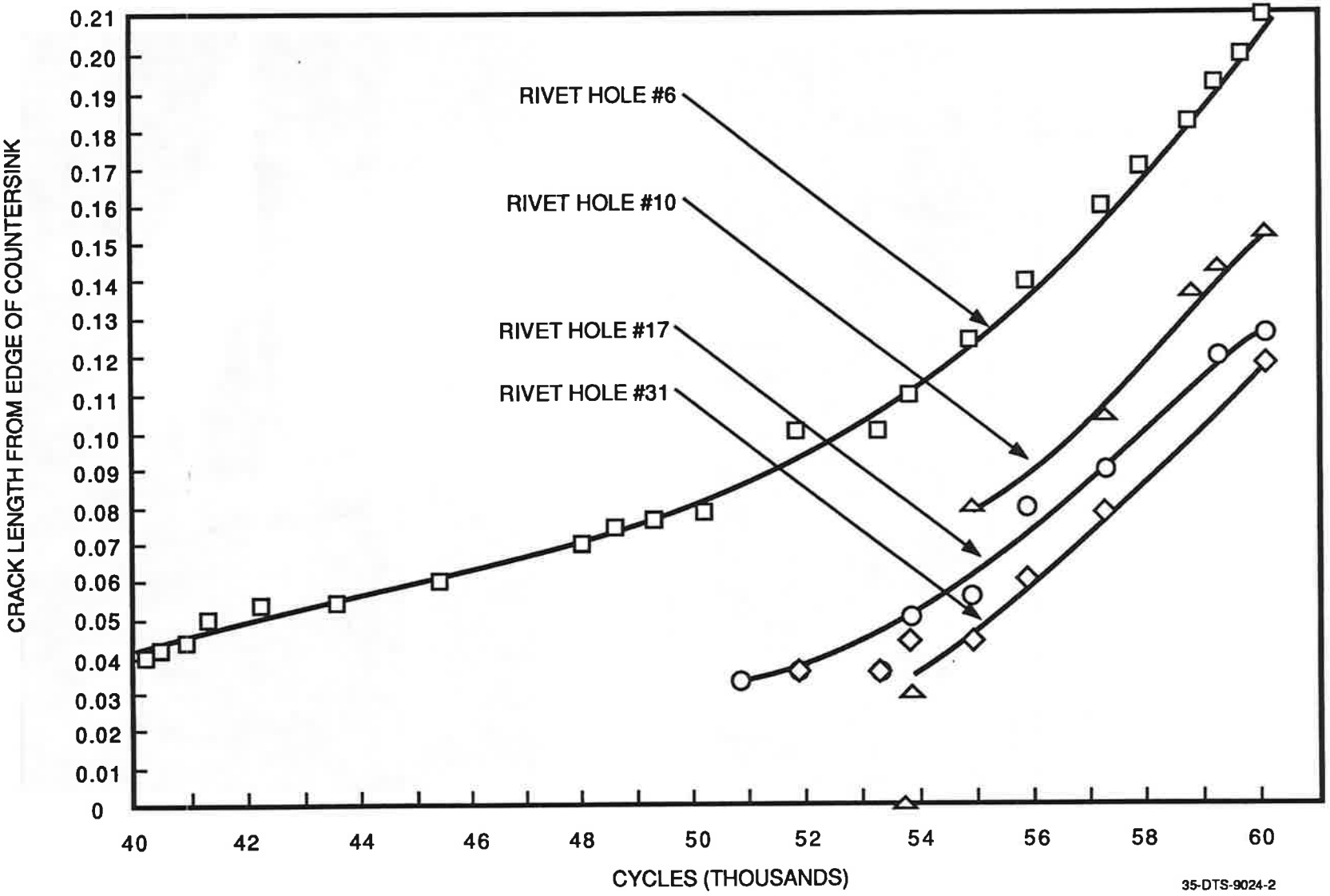

Figure 5-15. Crack Growth Data

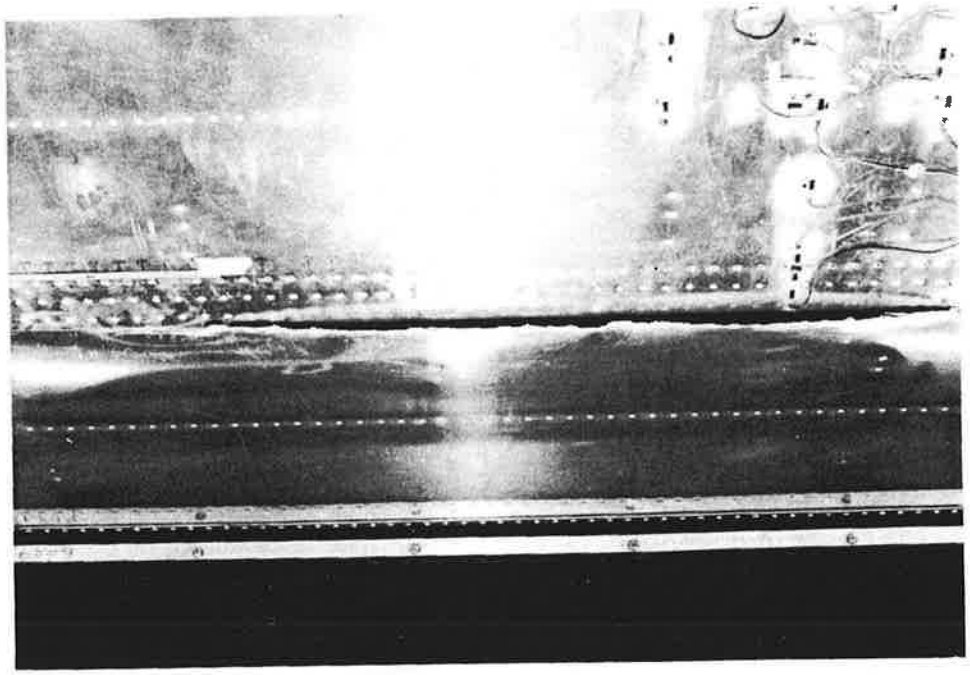

Figure 5-16. Catastrophic Panel Failure

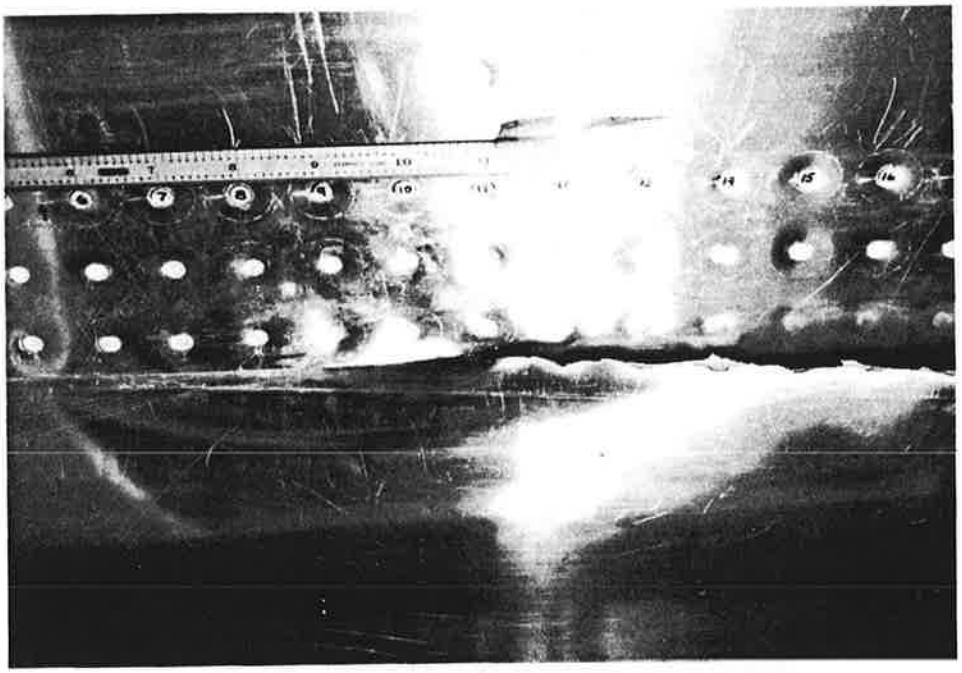

Figure 5-17. Closeup of Panel Failure

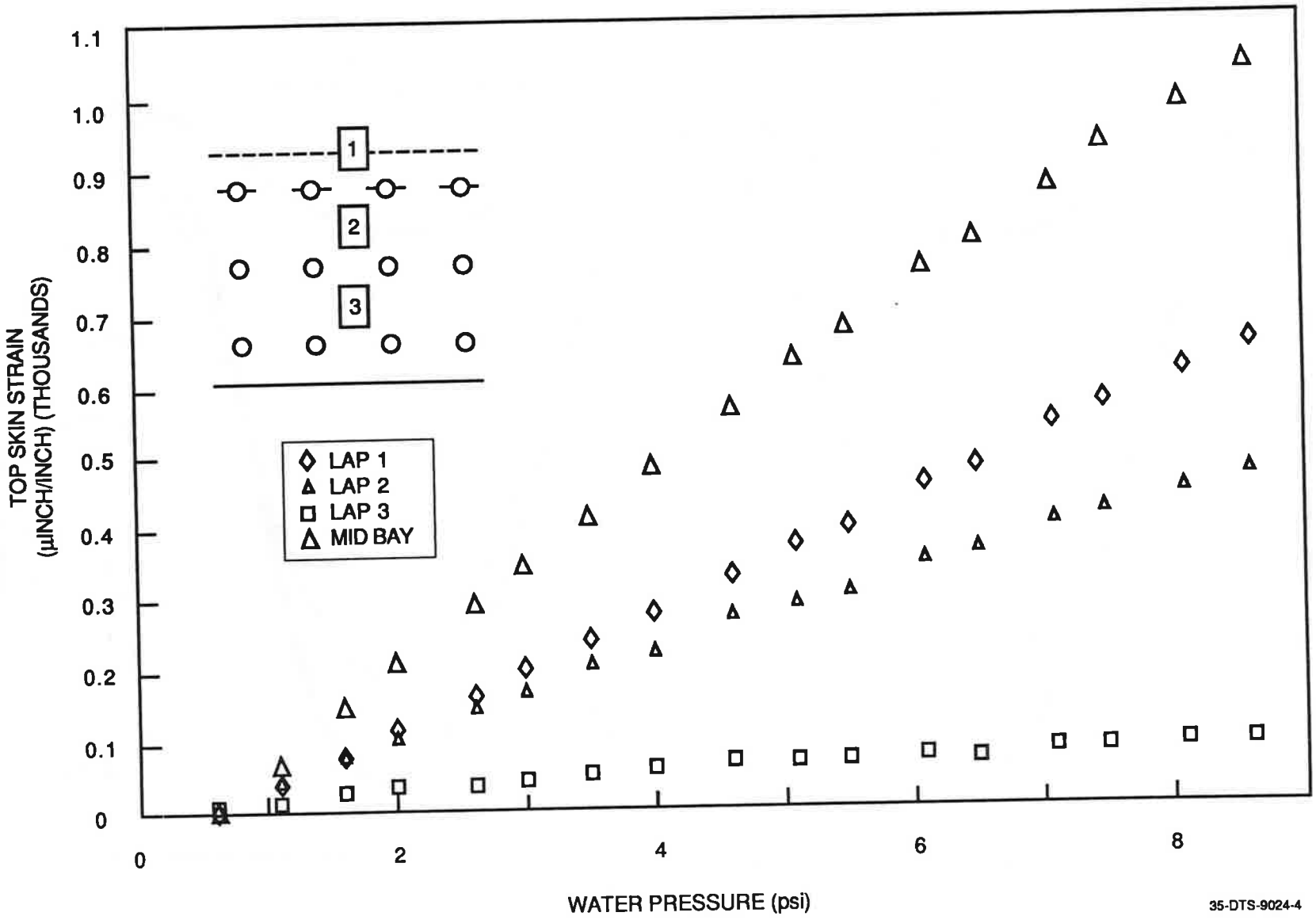

Figure 5-18. Top Skin Strain versus Internal Pressure

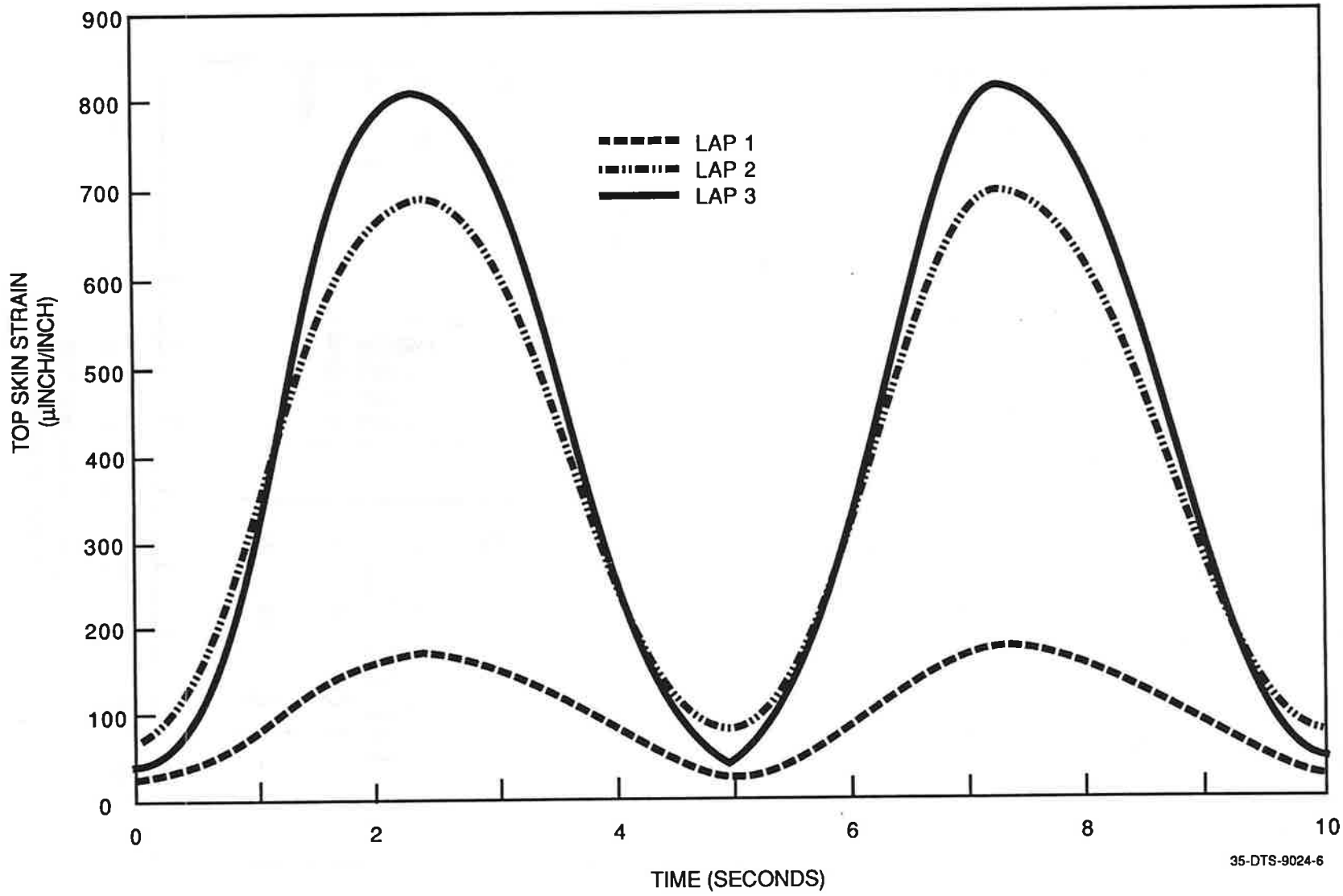

Figure 5-19. Cyclic Variation of Lap Joint Strains

Analysis

Tests to date have established conclusively that the fixture can be used for high cycle fatigue testing of aircraft fuselage panels. However, crack link-up was expected at the upper rivet row in the top skin, not in the bottom skin. Possible explanations include:

- Local bending of unbonded lap, accentuated by high internal pressure (ë50 percent over the normal operating pressure). Initial fractographic observations seem to support this explanation.

- Fretting promoted by exposure of inner skin to water.

A detailed investigation of the observed fractures is being performed by VNTSC in a separate study.

Equivalent Cycles

In presentation of the test data, it is instructive to transform the high stress cycles into equivalent stress cycles at the typical aircraft operation level of 8.6 psi. Likewise, the initial cycles at 14.1 Ksi need to be upgraded to the normal higher levels. Assuming an empirical Miner-type law, $(\sigma_1{}^{\alpha} N_1 = \sigma_2{}^{\alpha} N_2$, where, from Barsom (13), $\alpha \approx 3.3)$, Table 5-2 has been prepared. It shows that MSD cracks start appearing at about 26,000 equivalent cycles, and the final link-up and fracture at about 85,000 cycles for *this particular test panel with the initial built-in damage*.

Conclusion

The test fixture and the test panel upgraded for fatigue operation can be successfully used for full fatigue testing of aircraft fuselage panels. Using this facility, MSD generation, link-up and complete panel fracture can be studied in detail with safety.

Table 5-2. Equivalent Cycle Crack Growth at Rivet 6

Actual Applied Cycles	Water Pressure Loading	Stress Cycle (Ksi)	Equivalent Cycles at 16 Ksi	Crack Length at 6
40,150	1-8.6	14.1	26,499	0.040
40,429	1-8.6	14.1	26,683	0.042
40,905	1-8.6	14.1	26,997	0.044
41,289	1-8.6	14.1	27,251	0.050
42,245	1-8.6	14.1	27,882	0.054
43,633	1-8.6	14.1	28,798	0.054
45,455	1-8.6	14.1	30,000	0.060
48,000	1-8.6	14.1	31,680	0.070
48,613	1-8.6	14.1	32.085	0.074
49,290	1-8.6	14.1	32,531	0.076
50,178	1-8.6	14.1	33,117	0.078
50,350	1-8.6	14.1	33,231	
50,580	1-10.8	18.2	33,585	
50,802	1-13.0	22.3	34,255	
51,284	1-13.0	22.3	35,711	
51,843	1-13.0	22.3	37,399	0.100
51,994	1-13.0	22.3	37,855	
53,264	1-8.6	14.1	38,693	0.100
53,694	1-13.0	22.3	39,992	
53,800	1-13.0	22.3	40,312	0.110
54,884	1-13.0	22.3	43,585	0.124
55,890	1-13.0	22.3	46,624	0.140
57,279	1-13.0	22.3	50,818	0.160
57,929	1-13.0	22.3	52,781	0.170
58,782	1-13.0	22.3	55,357	0.182
59,254	1-13.0	22.3	56,783	0.192
59,474	1-13.0	22.3	57,447	
59,744	1-13.0	22.3	58,263	0.200
60,100	1-13.0	22.3	59,338	0.210
63,670	1-13.0	22.3	70,119	0.250
66,425	1-13.0	22.3	78,439	0.340
67,493	1-13.0	22.3	81,665	0.370
68,300	1-13.0	22.3	84,102	Linkup at two ligaments
68,350	1-13.0	22.3	85,250	Catastrophic

6. PANEL RESIDUAL STRENGTH TESTS

Six major panel tests were performed as indicated in the Test Matrix of Table 6-1. The purpose of tests Nos. 12, 13, 14 and 9 was to evaluate the residual strength of panels with mid-bay cracks. Tests Nos. 3 and 6 were to evaluate the effect of MSD in the lap splice on the panel residual strength.

Test data and correlations with analytic predictions are presented below. The residual strength is expressed in terms of the internal pressure required for panel fracture. Hoop and longitudinal stresses in the far field were measured using strain gages. The relationships between far field panel skin strains and pressure are shown in Figure 6-1.

6.1 Panels with Mid-Bay Cracks

Test Nos. 12 and 13 (16-in. Crack)

Test No. 12, with a 16-in. skin crack and no initial damage to the central tear strap at the frame, was conducted first. After initial sharpening of the crack tips by a few fatigue cycles in the range of 0 to 5 psi, the internal pressure was increased at an approximate rate of 1 psi/sec. At a pressure of 13.6 psi, the skin crack propagated rapidly to the adjacent tear straps. The tear straps successfully arrested the crack. There was a slight turning of the crack away from the stiff lap splice zone, as shown in Figure 6-2.

The damaged panel was repaired using a standard metal doubler and the test was repeated with a similar 16-in. crack in the adjacent bay on the opposite side of the lap splice, as shown in Figure 6-3. The fracture occurred at 12.4 psi. Again, the crack turned slightly away from the lap splice zone and was arrested by the tear straps. Figure 6-4 presents photographs of the panel after the fracture tests.

The results of the two tests were reasonably consistent, considering the fact that the repair no doubt had some influence on the fracture strength of the repaired panel. Video replay of the failure event in slow motion revealed that the center rivet failed first due to pullout tension. This immediately resulted in skin fracture.

Table 6-1. Initial Test Matrix for Full-Scale Test Fixture

Panel No. (Dwg. No.)	Test No./ Name	Flaw Location	Flaw and Test Description	Remarks
1 (902401)	1. Residual strength	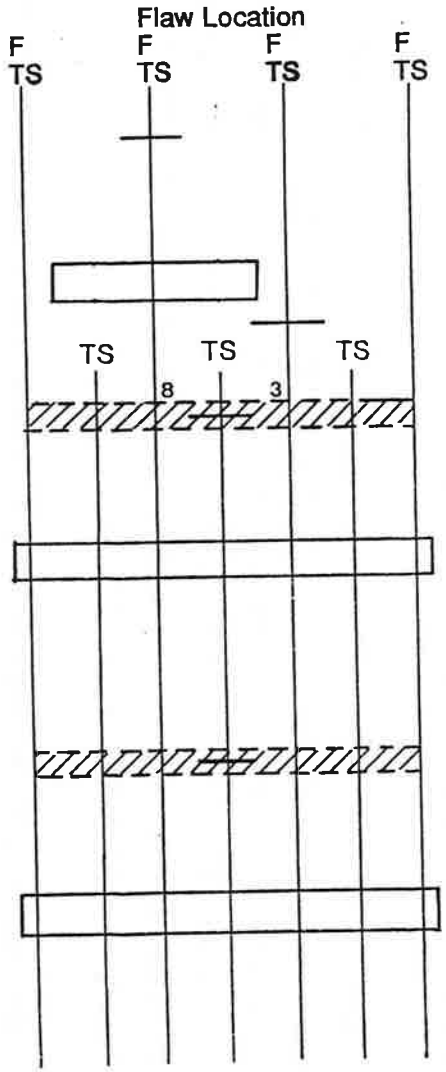	16-in. crack across a frame; circumferentially mid-bay between stringers	Completed. Failure pressure not recorded
	2. Residual strength		Metal patch after test 1, then machine second 16-in. crack and conduct test 2	Completed. Failure pressure 13.2 psi
6 (9024025)	3. Residual strength		12.4-in. lap joint crack plus MSD in top rivet row; 61-in. lap joint disbond	Completed. Failure pressure 8.5 psi
	4. Fatigue after metal patch repair		Metal patch after test 3 and conduct test 4	TBD
	5. TBD			
3 (9024025)	6. Residual strength		12.4-in. lap joint crack; top rivet row; 61-in. lap joint disbond	Completed. Failure pressure 10.5 psi
	7. Fatigue after composite repair		Composite patch after test 6 and conduct test 7	TBD
	8. TBD		TBD	TBD

Table 6-1. Initial Test Matrix for Full-Scale Test Fixture (Continued)

Panel No. (Dwg. No.)	Test No./ Name	Flaw Location	Flaw and Test Description	Remarks
4 (9024025)	9. Residual strength	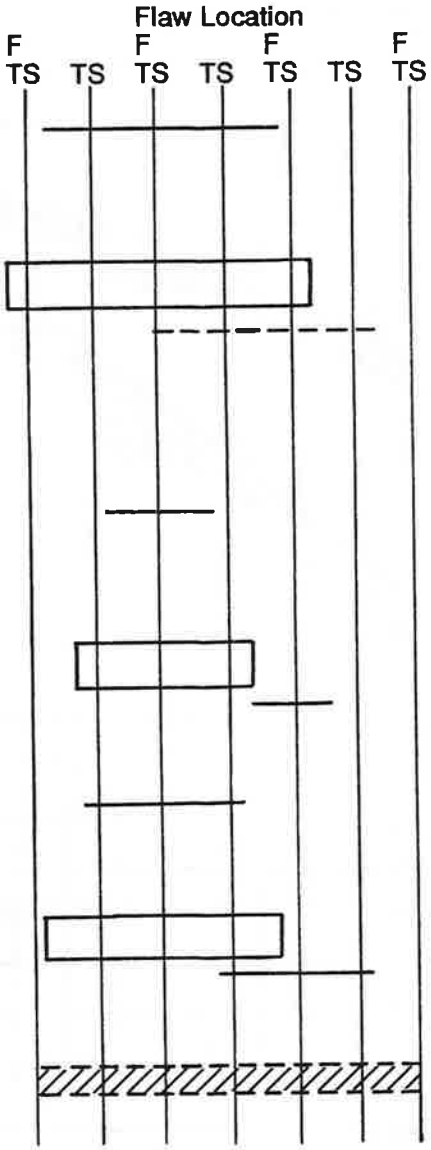	36-in. crack; circumferentially mid-bay between stringers	Completed. Failure pressure 7.4 psi
	10. Fatigue after metal patch repair		Metal patch after test 9, then machine second crack and conduct test 10; crack length TBD	TBD
	11. TDD			TBD
2 (9024025)	12. Residual strength		16-in. crack; circumferentially mid-bay between stringers; 61-in. lap joint disbond	Completed. Failure pressure 12.4 psi
	13. Residual strength		Metal patch after test 12; then machine second 16-in. crack and conduct test 13	Completed. Failure pressure 13.6
5 (9024025)	14. Residual strength		24-in. crack; circumferentially mid-bay between stringers	Completed. Failure pressure 9.6 psi
	15. Residual strength		Metal patch after test 12; then machine second 16-in. crack and conduct test 15	TBD
7 (9024025)	16. Fatigue life		MSD on 61 upper lap joint rivets; 61-in. lap joint disbond	Completed. Failed at 68,352 cycles

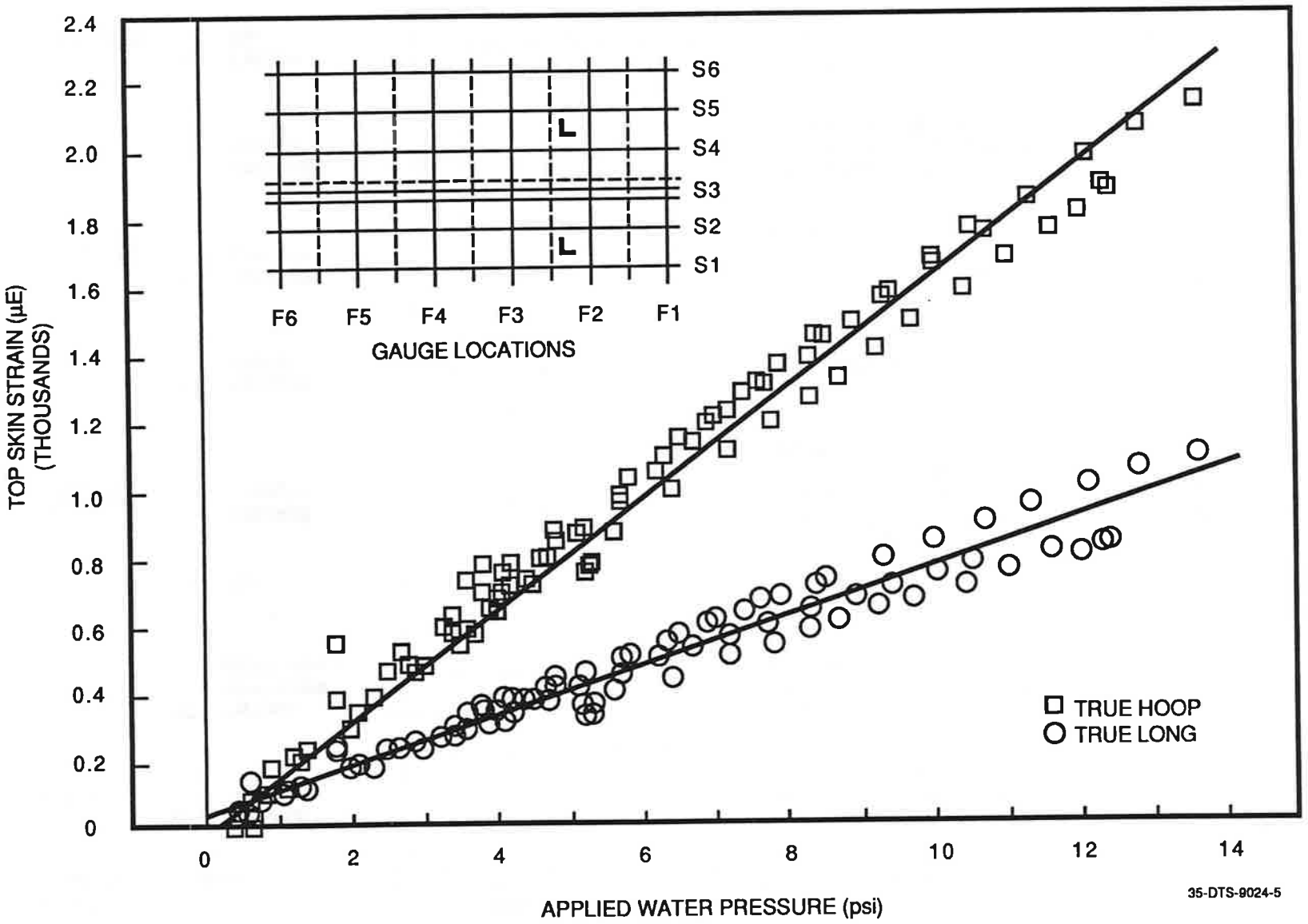

Figure 6-1. True Hoop and Longitudinal Top Skin Strains

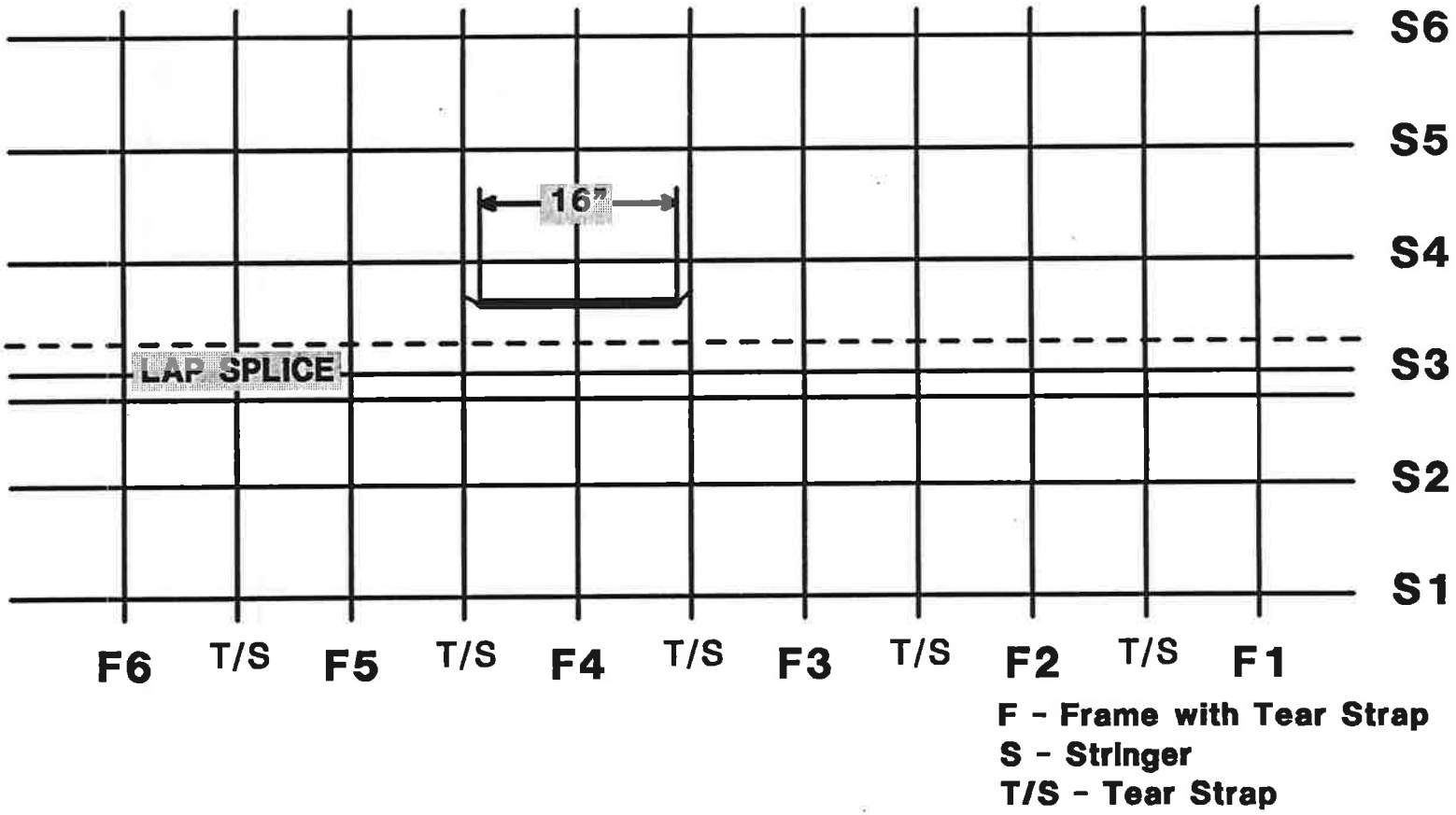

Figure 6-2. Initial Location of 16-in. Crack

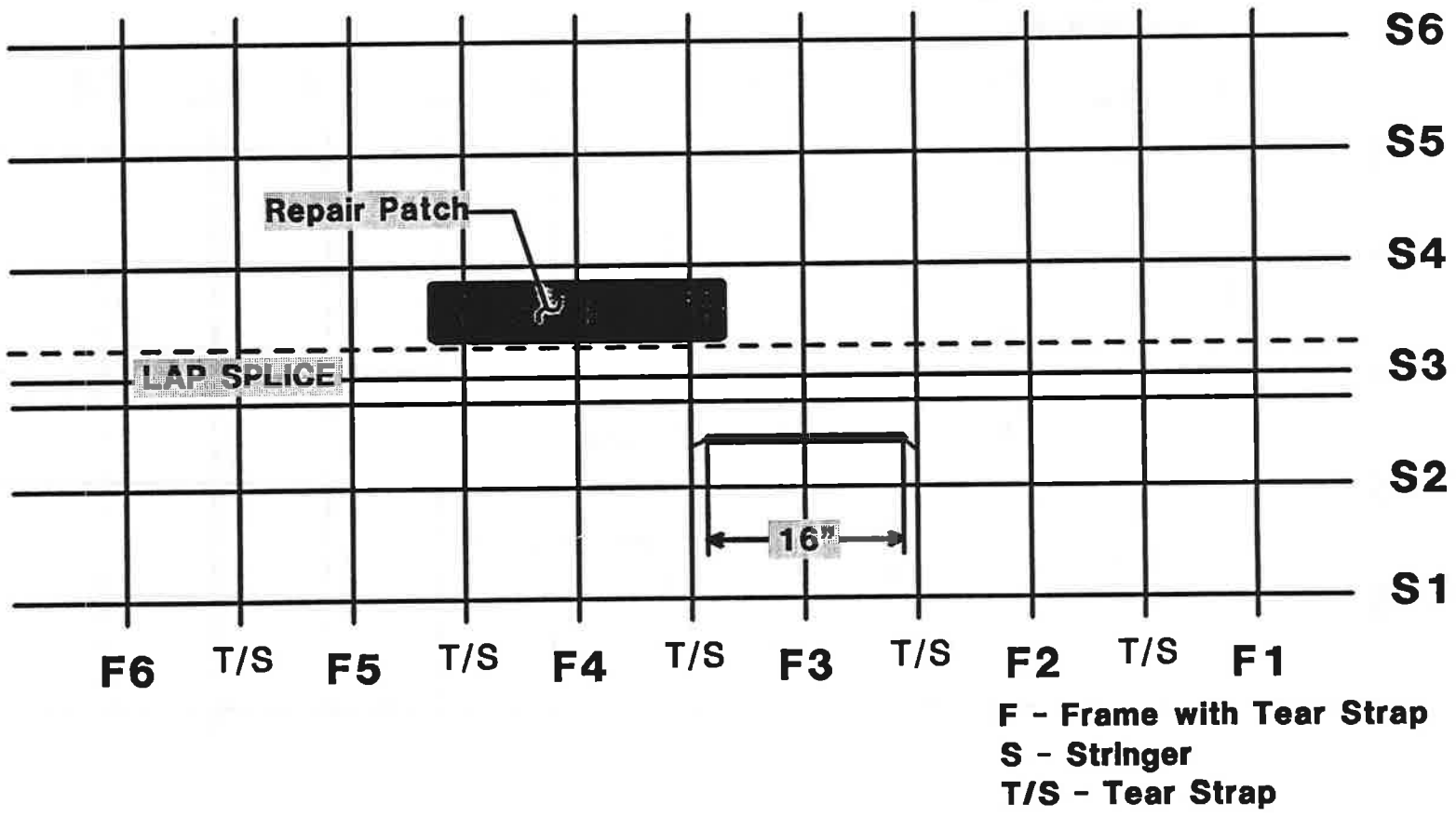

Figure 6-3. Initial and Final Locations of 16-in. Crack in Repaired Panel (Test No. 13)

a) ORIGINAL PANEL

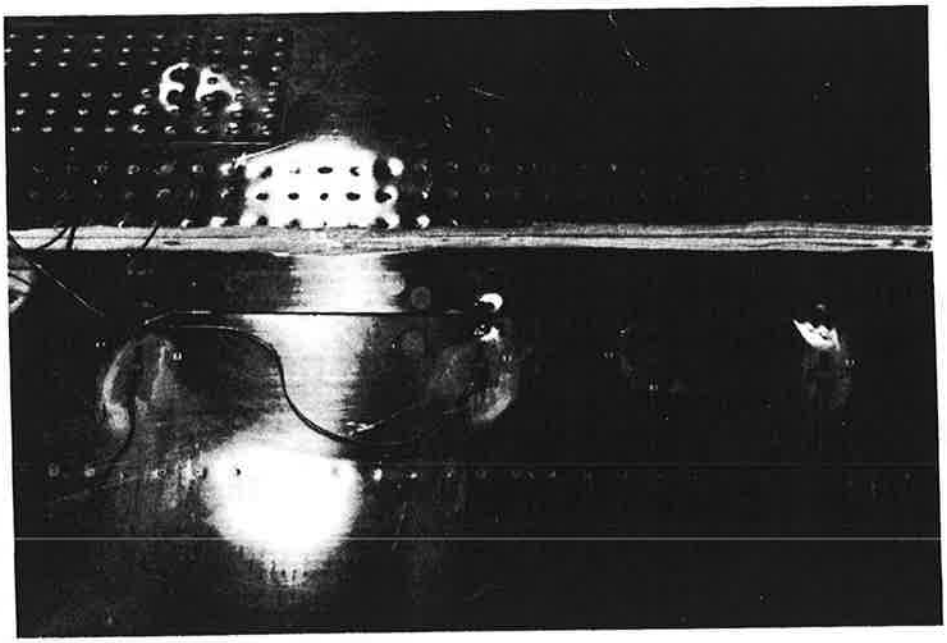

b) REPAIRED PANEL

Figure 6-4. Sixteen-Inch Crack Fracture

Analytic modeling using NISA-386 software has been carried out to determine the stress intensity factors (SIF) and stress levels in the tear straps. Details of modeling and evaluation of SIF using singular elements are presented in Section 8. The results for the case of a 16-in. skin crack in this fuselage structure with tear straps is shown in Figure 6-5. The computer model predicts the crack tip SIF reaching the critical limit [which is approximately taken to be at 150 Ksi √in. for 0.04 in. thick AL 2024-T3 (1)] at about 12 psi which is close to the average value of 13.0 psi for the two tests. No tear strap failure is predicted or observed in the test.

Test No. 14 (24-in. Crack)

A 24-in. long skin crack was cut symmetrically over a frame, as shown in Figure 6-6. Again, care was taken to ensure no initial damage to the tear straps. The pressure level was increased at the rate of 1 psi/sec. Pressure at panel failure was found to be 9.6 psi. The crack extended and turned at the nearest frames, F3 and F5, as shown in Figure 6-6 and 6-7. "Flapping" of the damaged skin portion did occur. The underside view of the damage with broken straps is seen in Figure 6-8.

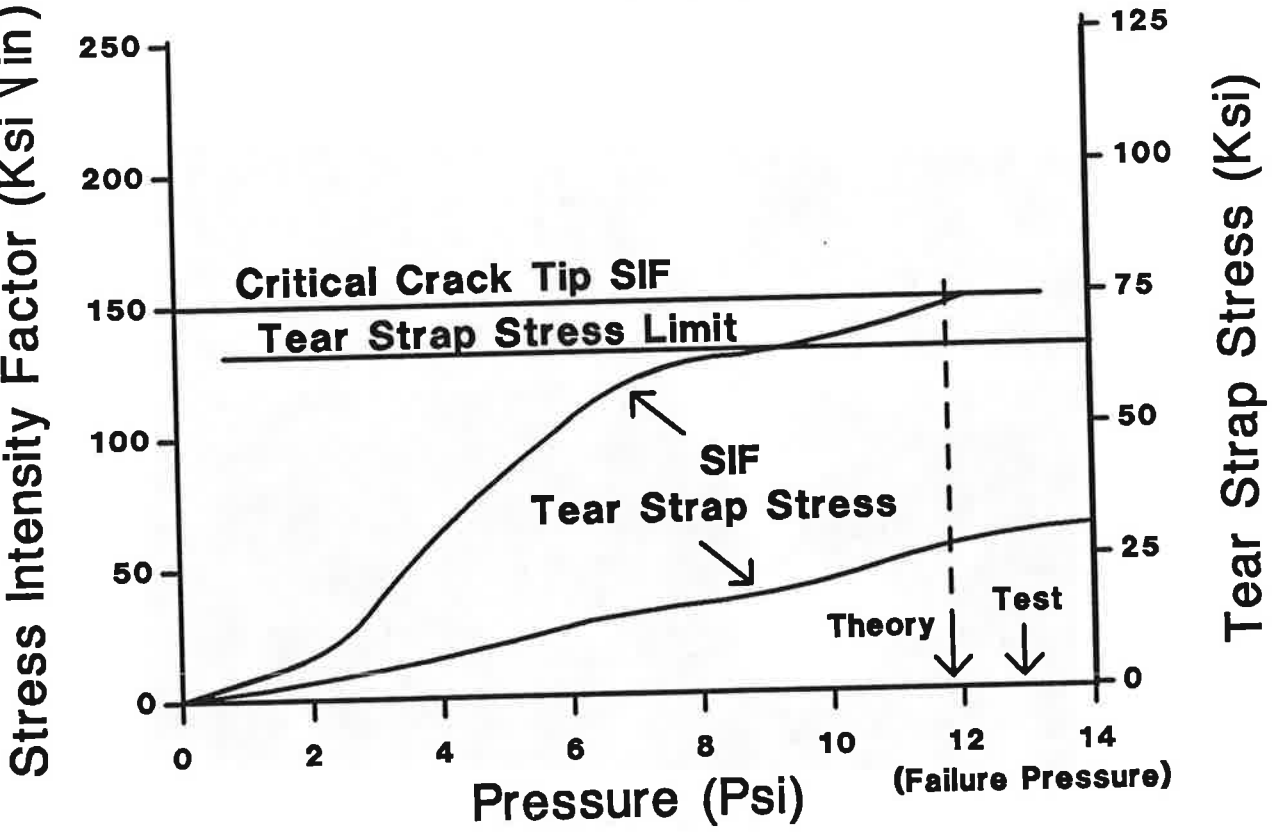

Figure 6-5. Analytic Predictions for 16-in. Crack

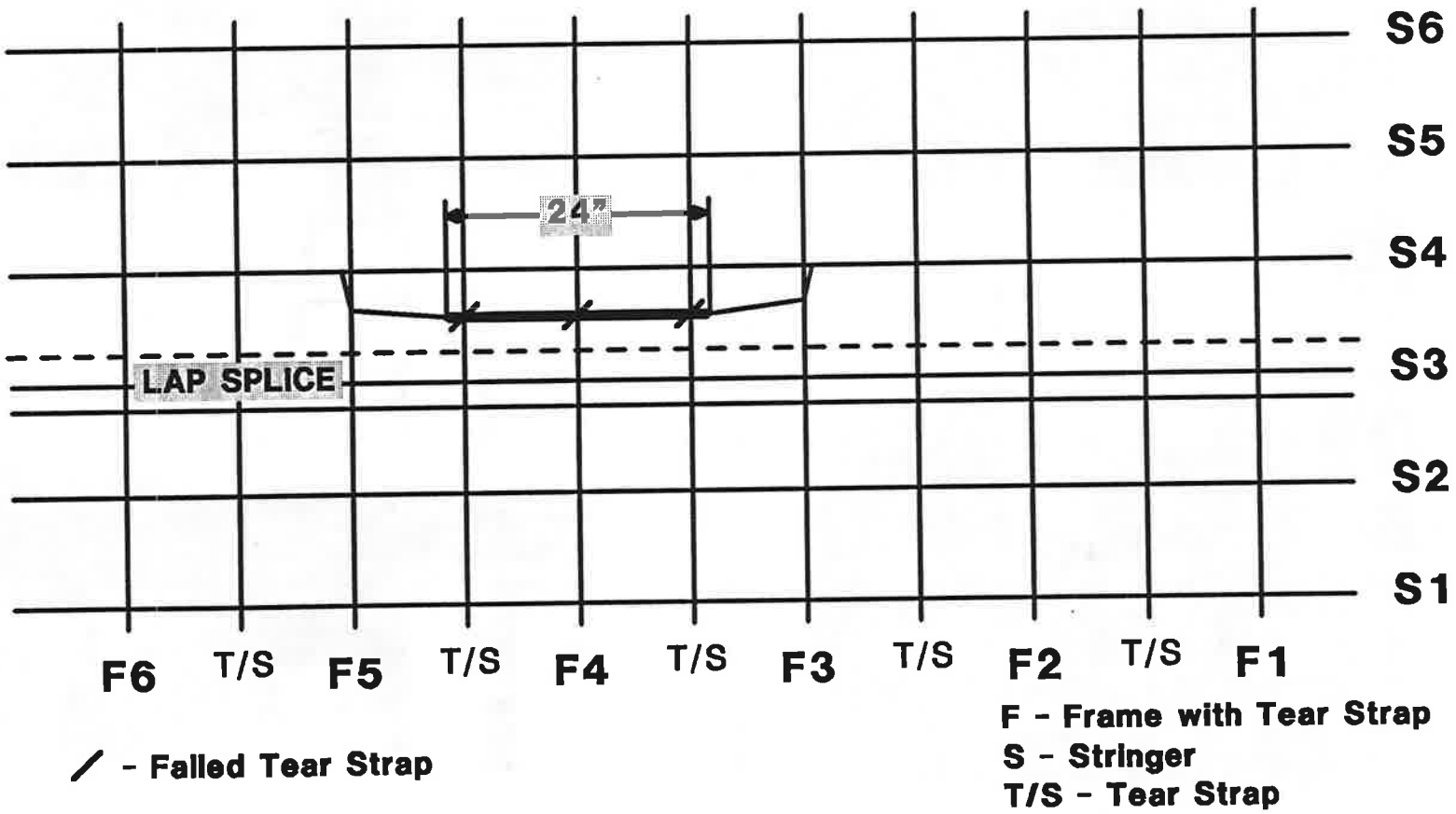

Figure 6-6. Panel with 24-in. Initial Skin Crack

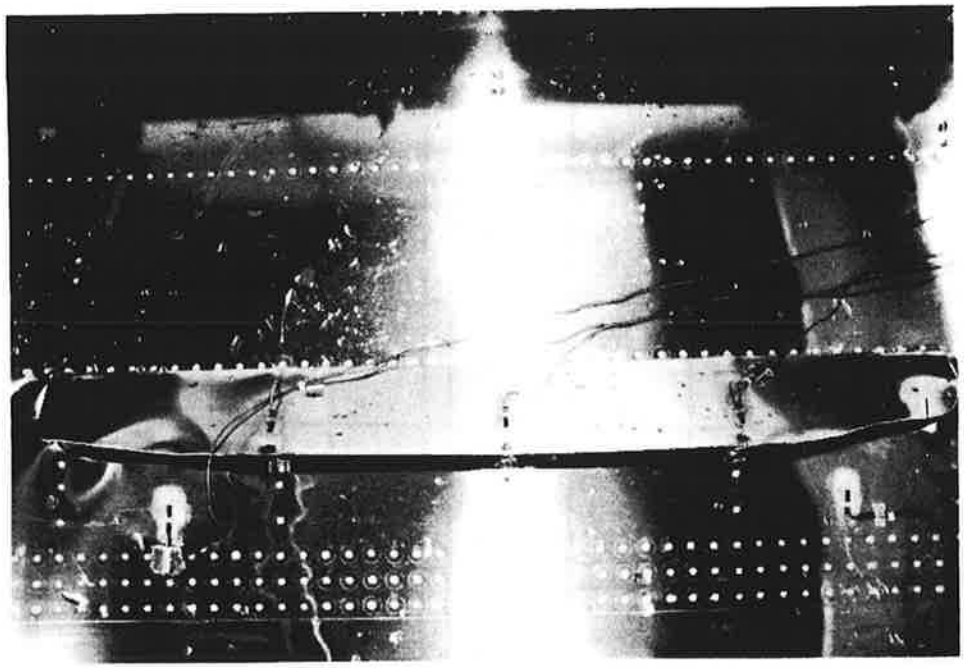

Figure 6-7. Flapping of Damaged Skin with Initial 24-in. Skin Crack

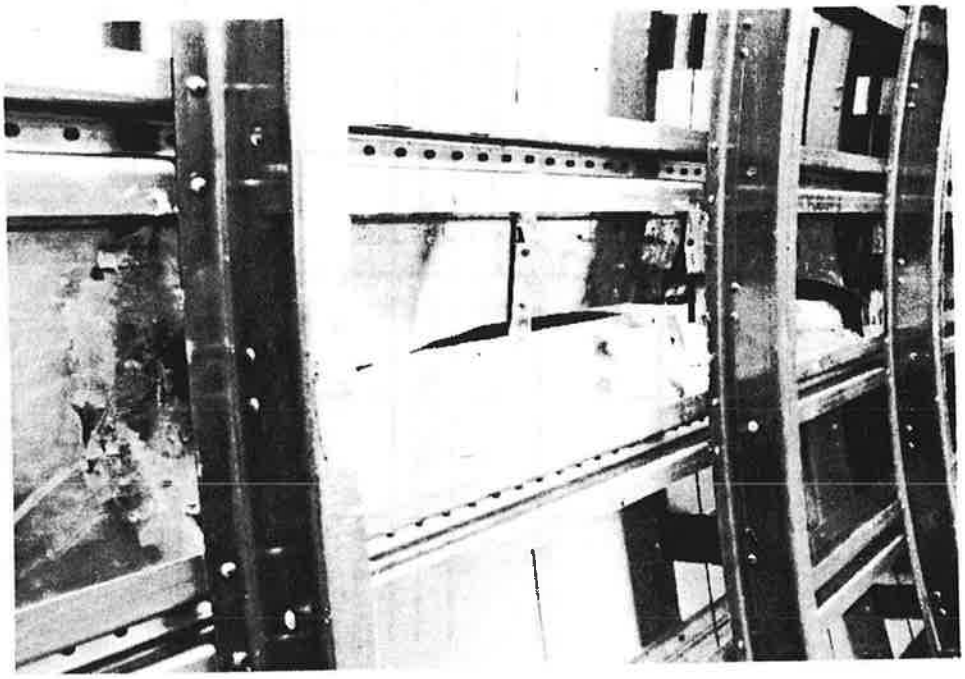

Figure 6-8. Underside View of Damaged Panel with 24-in. Initial Crack

Pressure variation and crack growth with time are shown in Figure 6-9. The panel failure event was recorded using a video camera. Review of the video in slow motion has allowed us to identify the various failure mechanisms. These are presented schematically in Figure 6-10. Again, the center rivet failed first. Mid-bay tear straps then failed in tensile fracture, increasing the stress intensity levels at the crack tips and thus causing fast skin fracture. As the crack grew to the nearest frames, F3 and F5, the center tear strap at F4 failed. The crack turned at the frames, as one would expect in the ideal situation, causing decompression. No damage to frames occurred.

Analytic results from the computer modeling are presented in Figure 6-11. With increased pressure, the stress in the mid-bay tear strap (between frames) rises at a faster rate than the crack SIF and reaches the critical limit of 65 Ksi at about 9.5 psi. As stated earlier, the tear straps failed at this pressure level (9.6 psi). With broken tear straps, the model predicts an SIF well above the critical level and hence the skin crack propagation. Computer simulation has not been carried out beyond this failure mode.

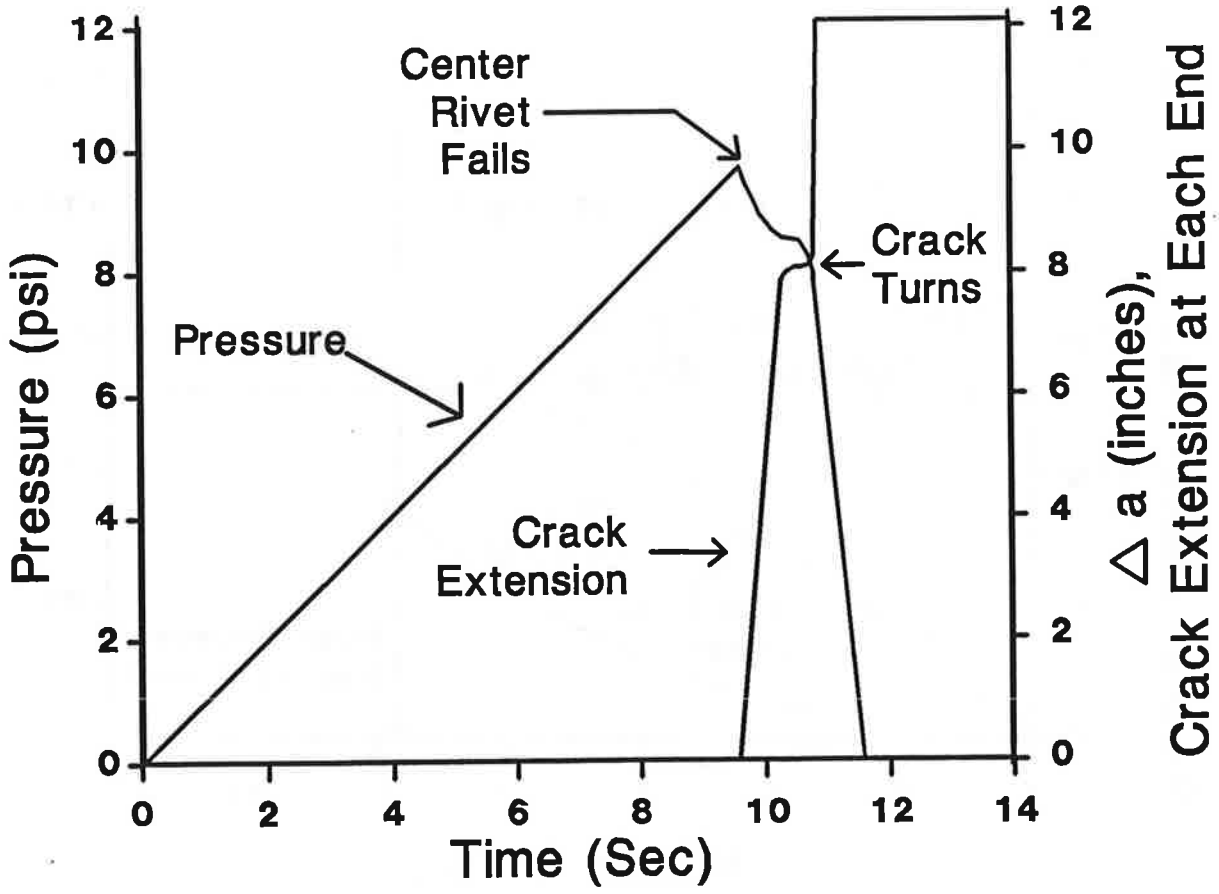

Figure 6-9. Pressure Variation and Crack Growth

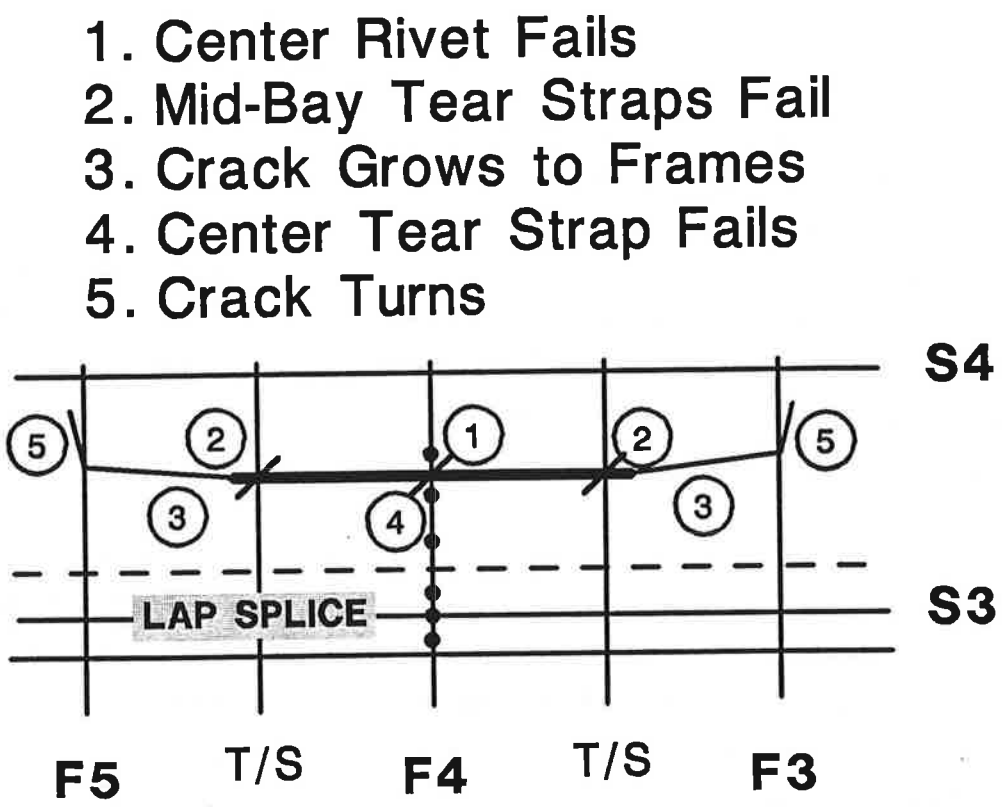

Figure 6-10. Failure Event Sequence for Panel with Initial 24-in. Crack

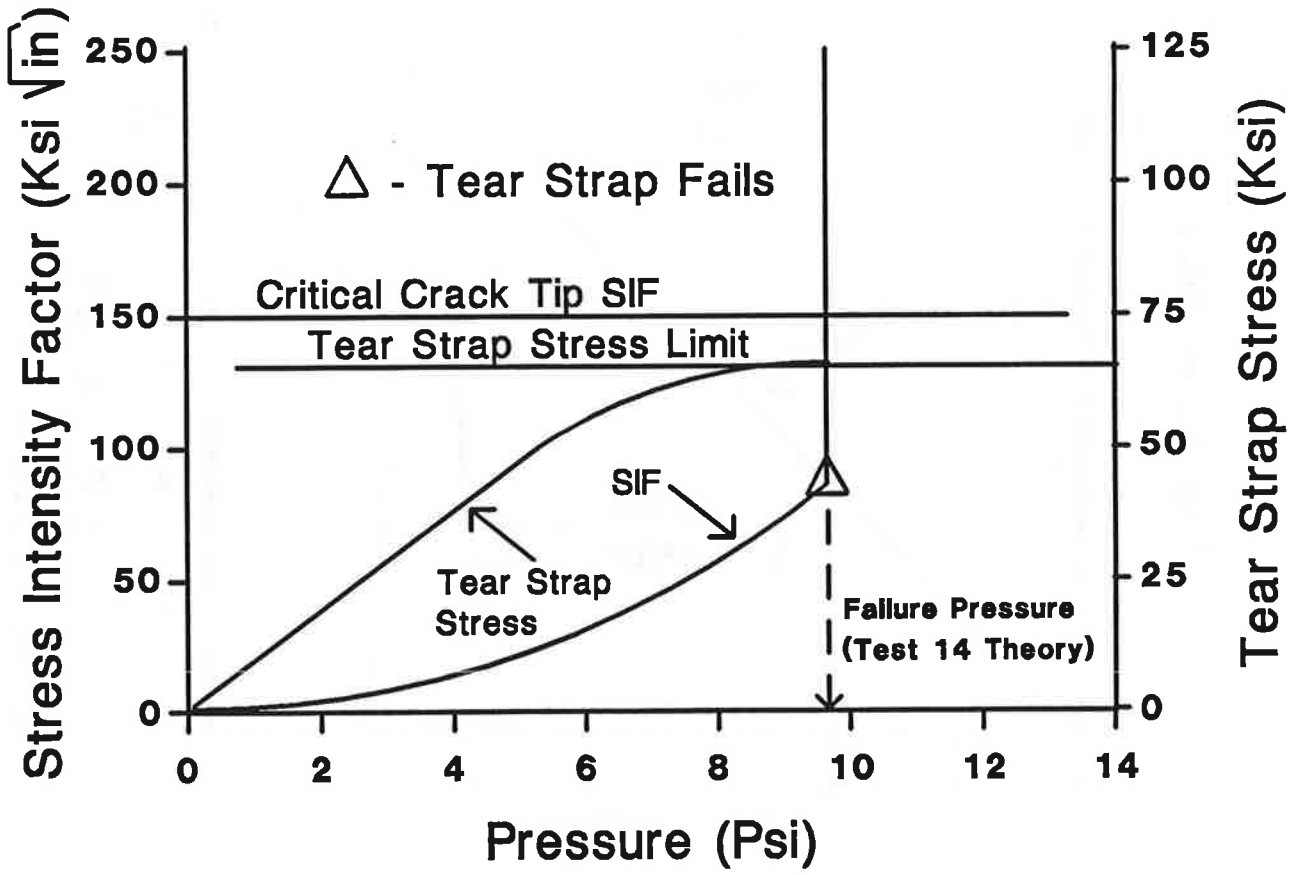

Figure 6-11. Analytic Predictions for 24-in. Crack

Test No. 9 (36-in. Crack)

In this test, the initial 36-in. skin crack extended over two frame bays. Pressurization was done at the rate of 1 psi/sec. At 7.4 psi, the crack propagated into adjacent frame bays and stopped near tear straps as shown in Figure 6-12. The cracks showed a small tendency to turn and all five intermediate tear straps in the cracked skin region broke. A view of the fractured panel is shown in Figure 6-13.

Pressure variation and crack extension with time are shown in Figure 6-14. In this test, although the center rivet failed at about 5 psi, significant crack growth occurred at 7.4 psi which is considered to be failure pressure. Due to the failure of the seal, water pressure dropped significantly, but the skin crack continued to propagate for an additional 5 in. at each end of the crack.

No computer simulation of this test has been made.

The residual strength data for panels with mid-bay cracks is summarized in Table 6-2 and plotted in Figure 6-15. The splice crack data of Table 6-2 are obtained from the following tests.

6.2 Panels with Splice Cracks - Effect of MSD

Test No. 6 (12.4-in. Crack, No MSD)

A 12.4-in. crack was initially cut in the top rivet row of the upper skin in the lap splice of the panel, as shown in Figure 6-16. At 10.5 psi, fast fracture of the skin crack occurred resulting in a final crack length of about 56.5 in. The crack propagated like a "zip fastener opening" with no tendency to turn. Figure 6-17 shows two views of the fracture.

The close-up view reveals that the crack did not follow a straight line joining the rivet hole centers, but rather had a zigzag pattern. A similar pattern has been noted in some of the lap splice failures in the field. The zigzag path is attributed to the shear load present in service conditions; however, there was no shear load in the laboratory test.

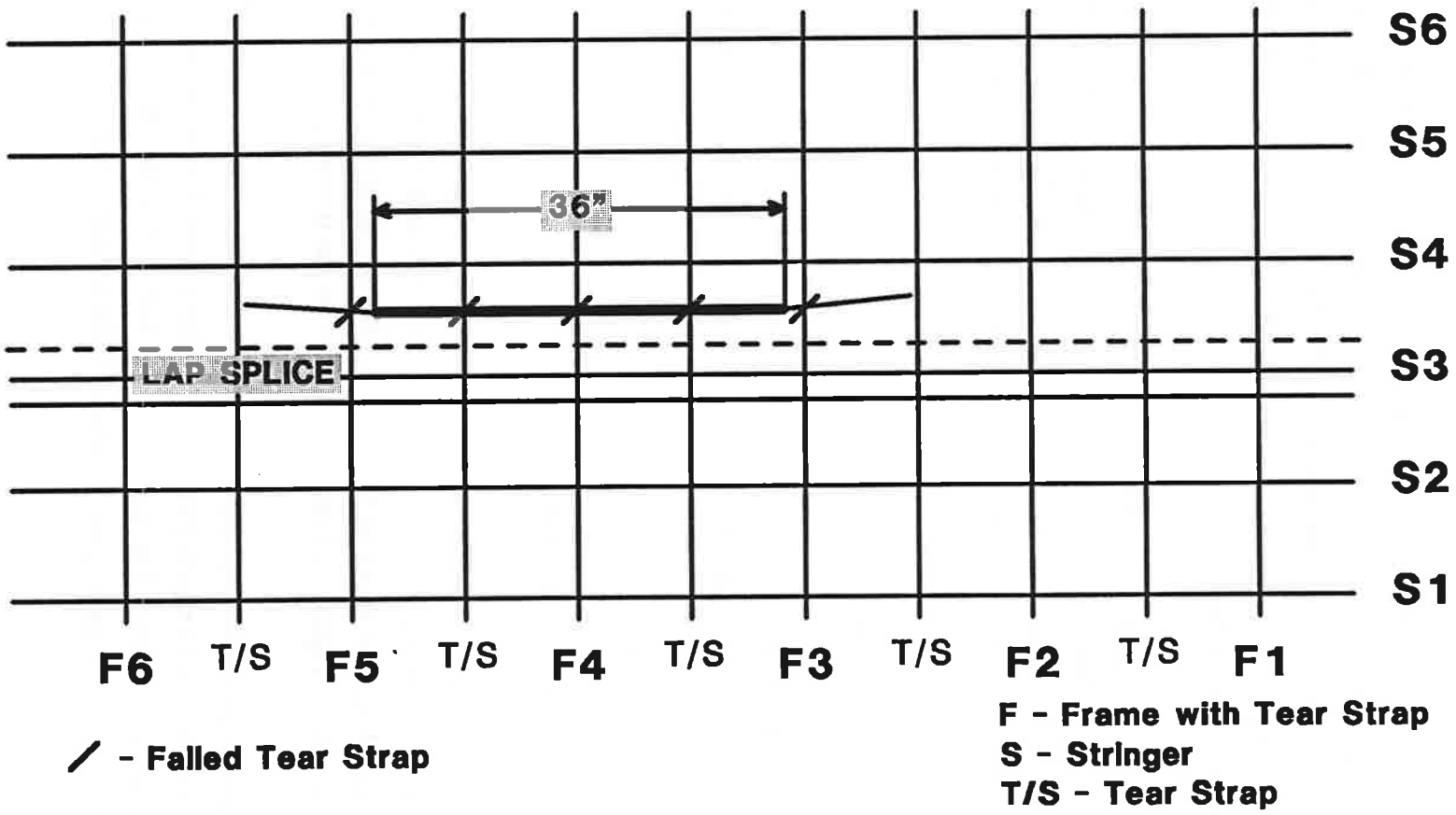

Figure 6-12. Panel Fracture with Initial 36-in. Skin Crack

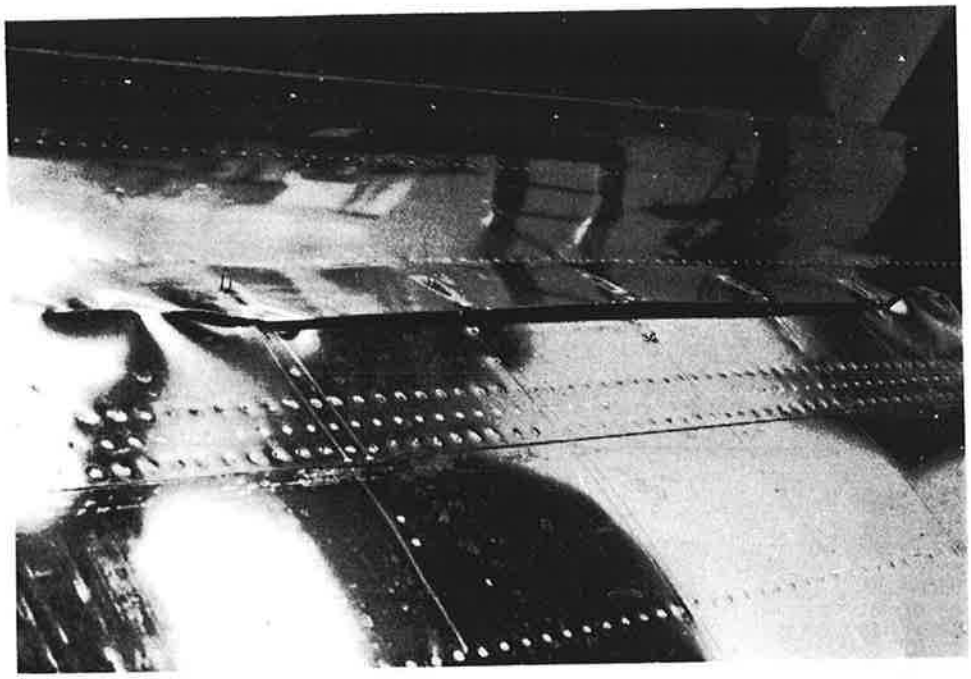

Figure 6-13. Fractured Panel with Initial 36-in. Crack

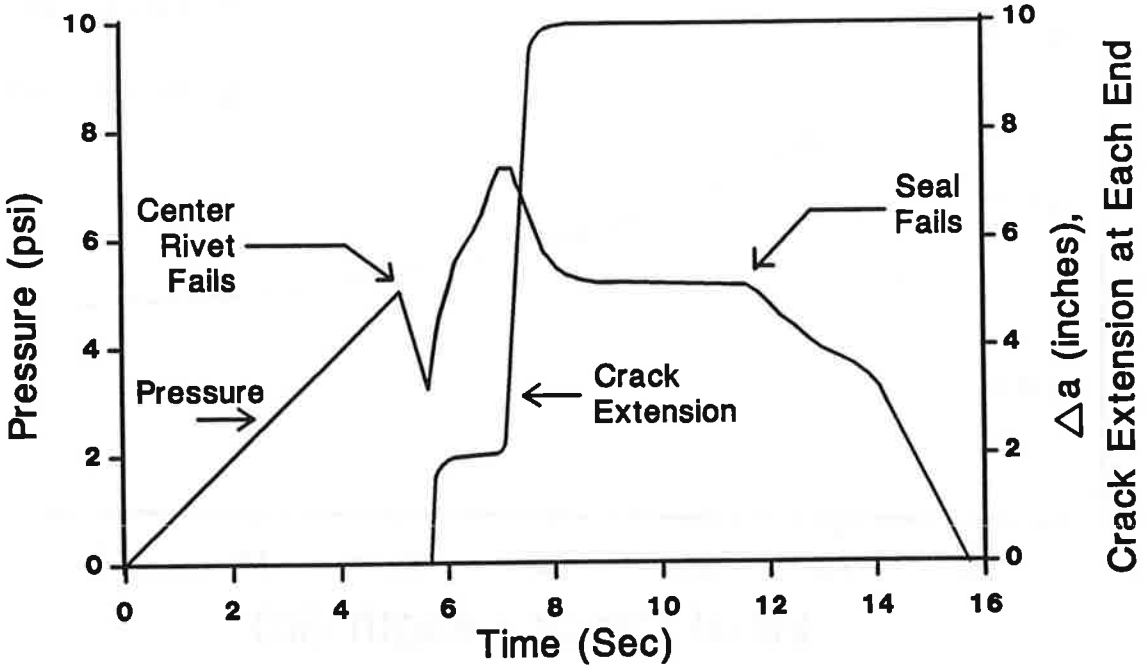

Figure 6-14. Pressure Variation and Crack Growth with Time (Panel with 36-in. Initial Crack)

Table 6-2. Static Failure Pressure

Crack Type \ Crack Length (In.)	12.4	16	24	36
Single mid-bay	-	13.0	9.6	7.4
Single splice	10.5	-	-	-
Single with MSD splice	8.5	-	-	-

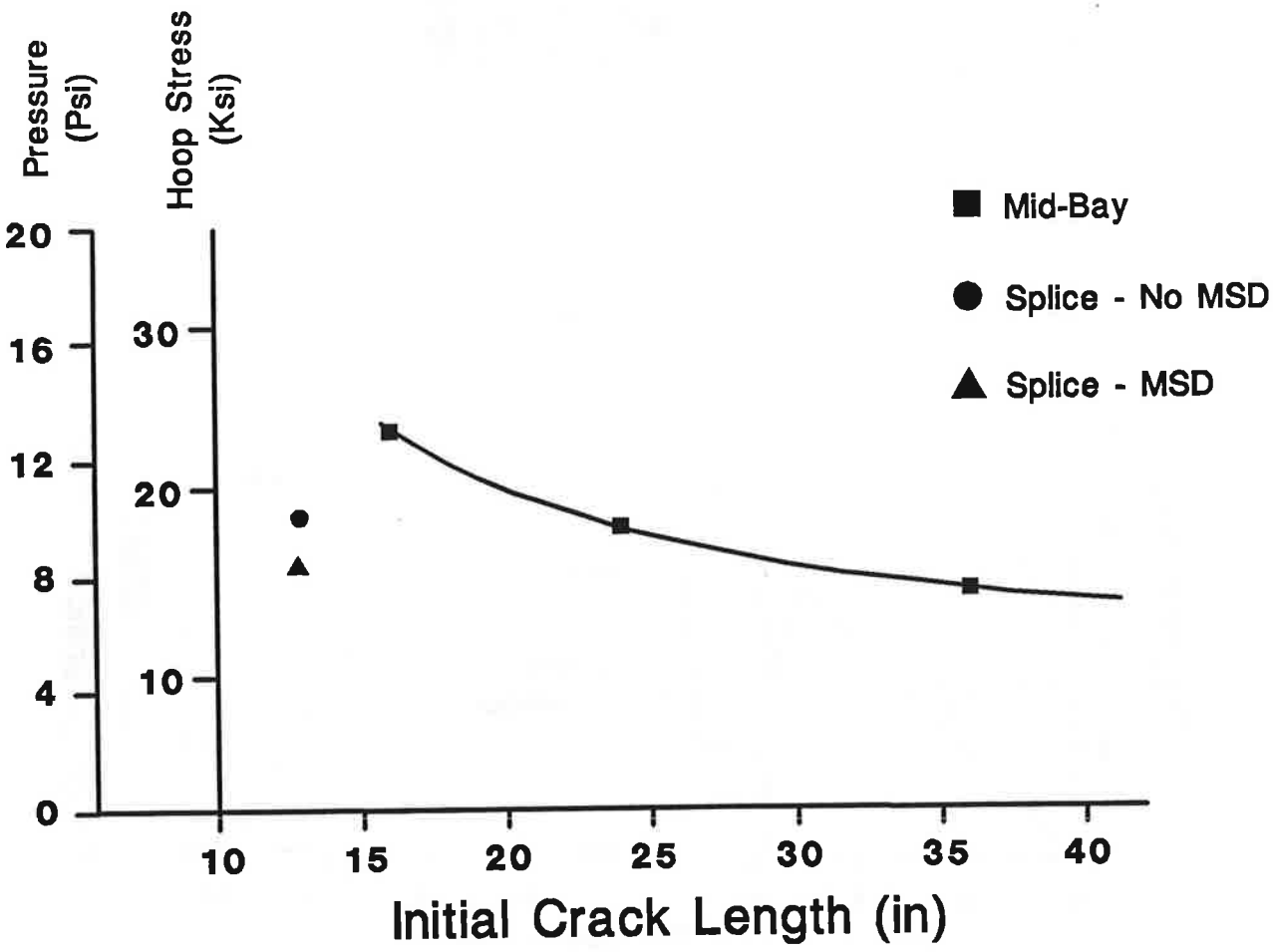

Figure 6-15. Test Results on Failure Pressures/Residual Strength

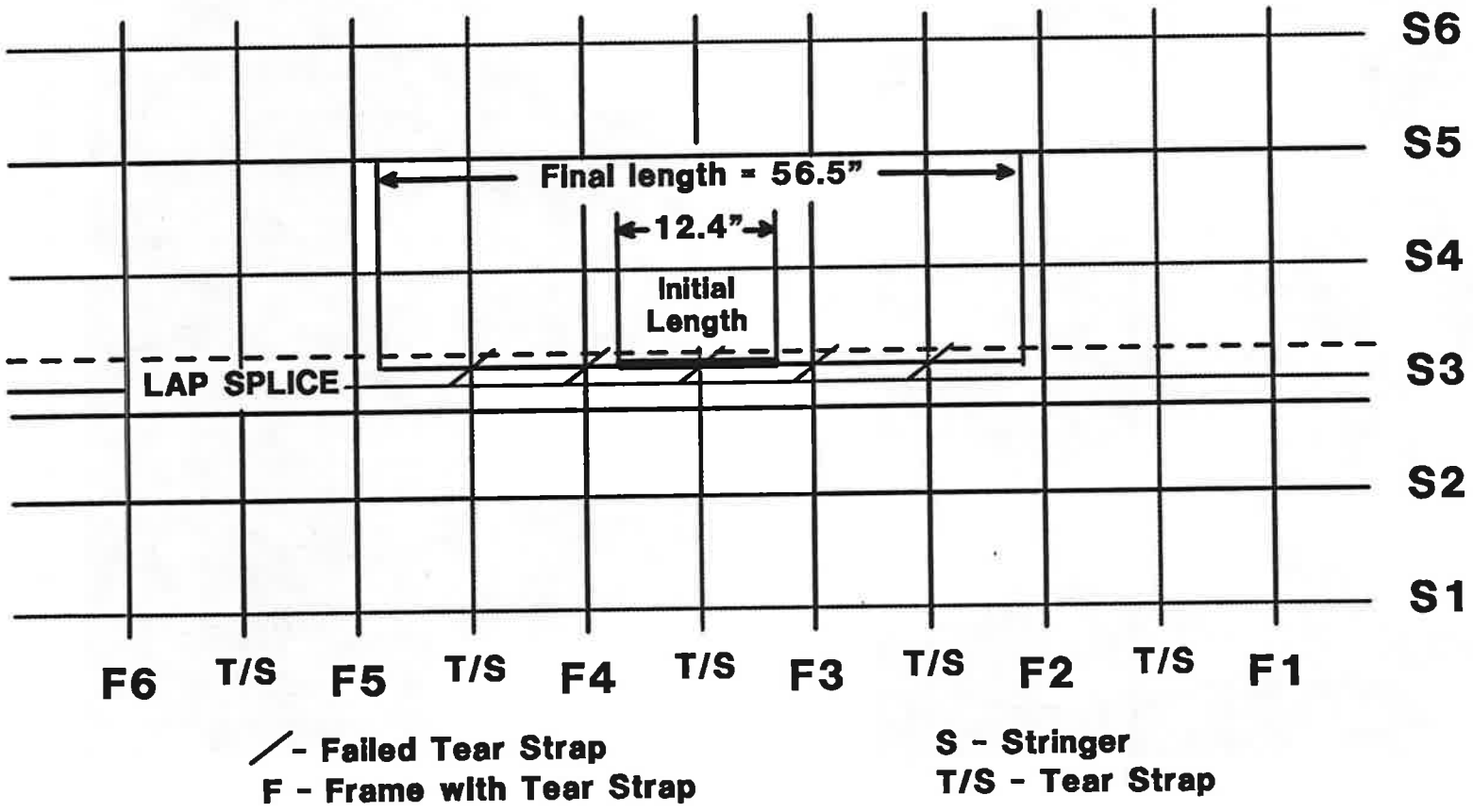

Figure 6-16. Panel with 12.4-in. Splice Crack (No MSD)

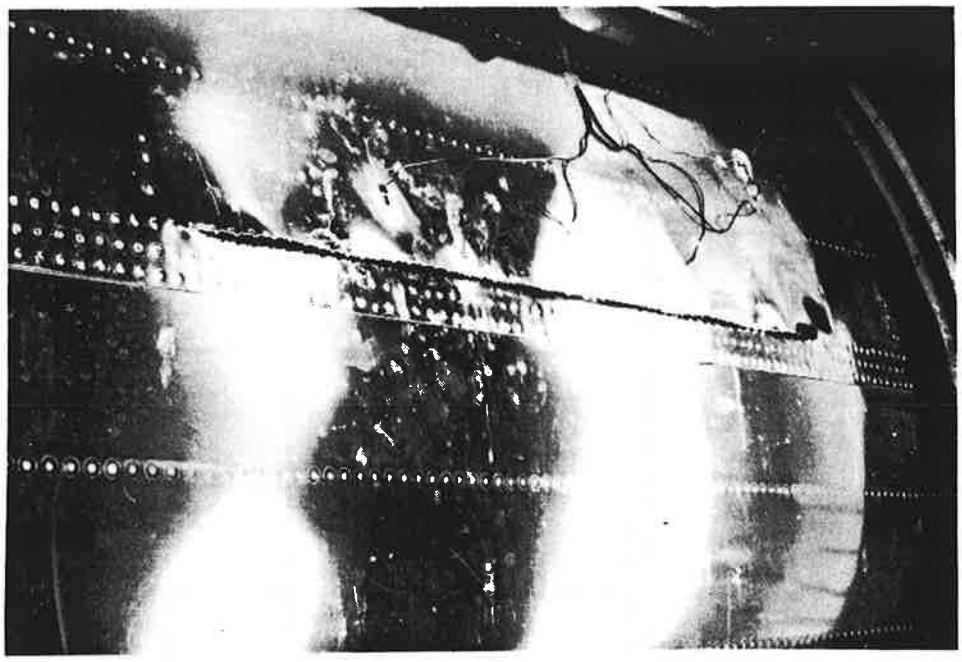

a) FRACTURED PANEL

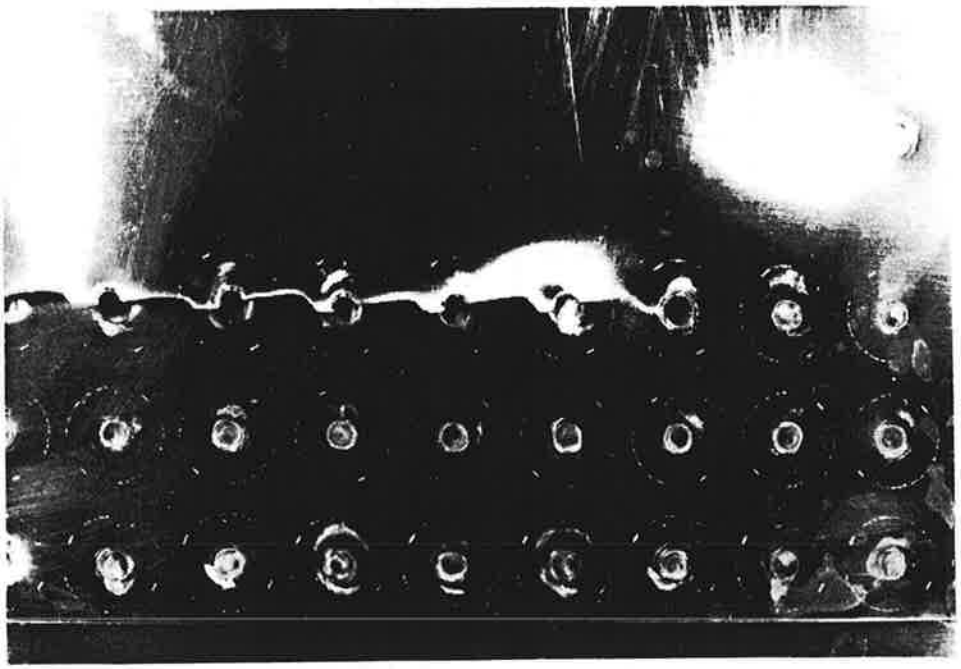

b) CLOSE-UP OF CRACK PROPAGATION

Figure 6-17. Fractured Panel and Close-Up of Crack Propagation (12.4-in. Splice Crack, No MSD)

Test No. 3 (12.4-in. Crack with MSD)

In this test, the top row of the upper skin lap splice joint had MSD at three rivet holes on one side and eight rivet holes on the other side of the lead crack which was kept at 12.4 in. as in the previous test (see Figure 6-18a for detail). The length of each small crack at the rivet holes was about 0.4 in. inclusive of one hole radius. In this test, panel fracture occurred at 8.5 psi, 2 psi less than in the previous case of the single lead crack with no MSD. The crack extended asymmetrically at the ends due to the initial asymmetric MSD, as shown in Figure 6-18b.

Fractured panel views are shown in Figure 6-19. As in the previous test, the crack propagated along the top row of rivets in a zigzag pattern, but with no overall tendency to turn.

The reduction in panel residual strength due to MSD has been a concern and has been anticipated by Swift. No computer simulations have been carried out to determine the reduced strength under MSD. However, an elementary analysis has been performed based on the net section. Figure 6-20 presents the results of this analysis. The failure pressures for the two cases are approximately proportional to the net section areas of the **first ligament**. The ratio of the overall net section areas in the panels does not appear to predict the failure pressure ratio. However, these conclusions cannot be generalized without additional testing.

The data obtained for the splice cracks are plotted in Figure 6-15 along with the data for mid-bay skin cracks. From this figure, the splice crack is apparently more critical. However, this conclusion must be examined further. Recall that the lead splice cracks were centered on mid-bay tear straps, whereas the mid-bay skin cracks were centered on frames; thus the conditions were not identical in the two series of tests.

Conclusions

- For the particular panel configuration tested, a 36-in. long mid-bay skin crack resulted in a residual strength of 15 Ksi at an internal pressure of 7.4 psi.

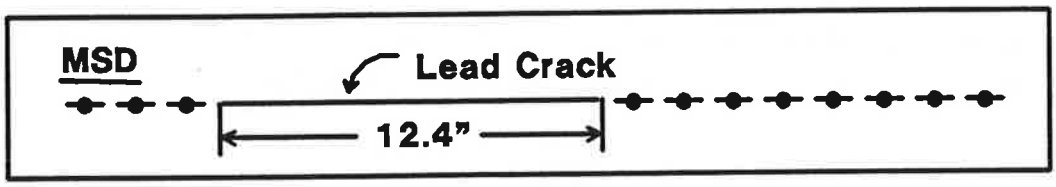

a) INITIAL DAMAGE DETAIL

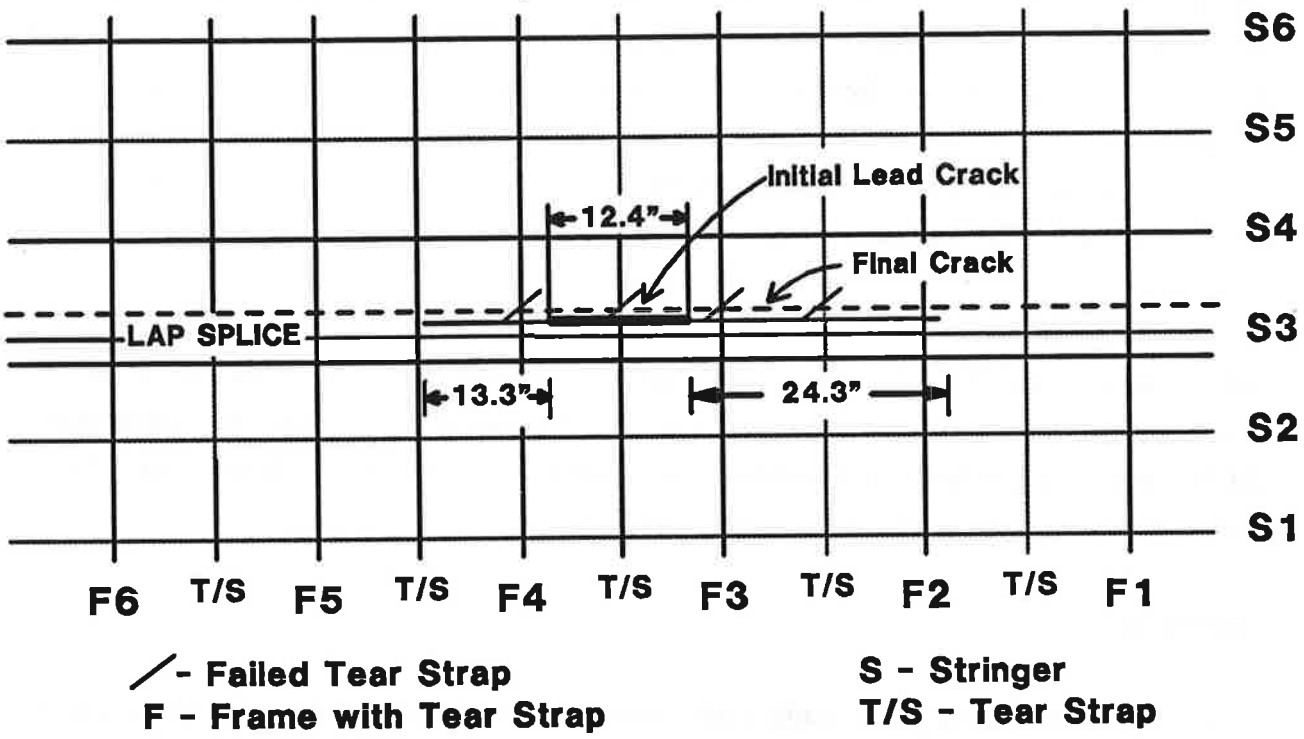

b) INITIAL AND FINAL DAMAGE

Figure 6-18. Panel with MSD

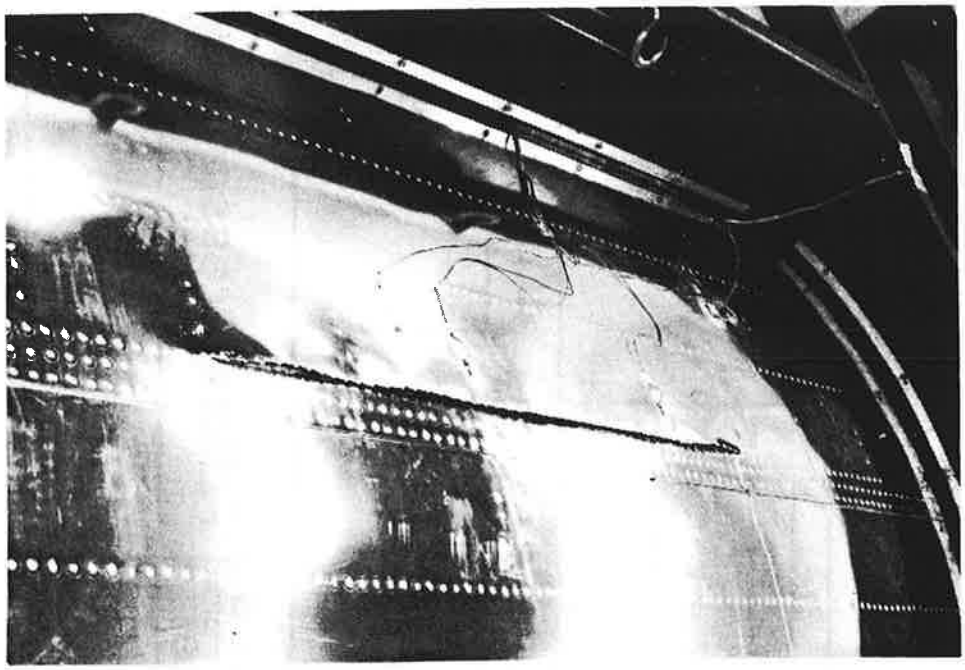

a) FRACTURED PANEL VIEW

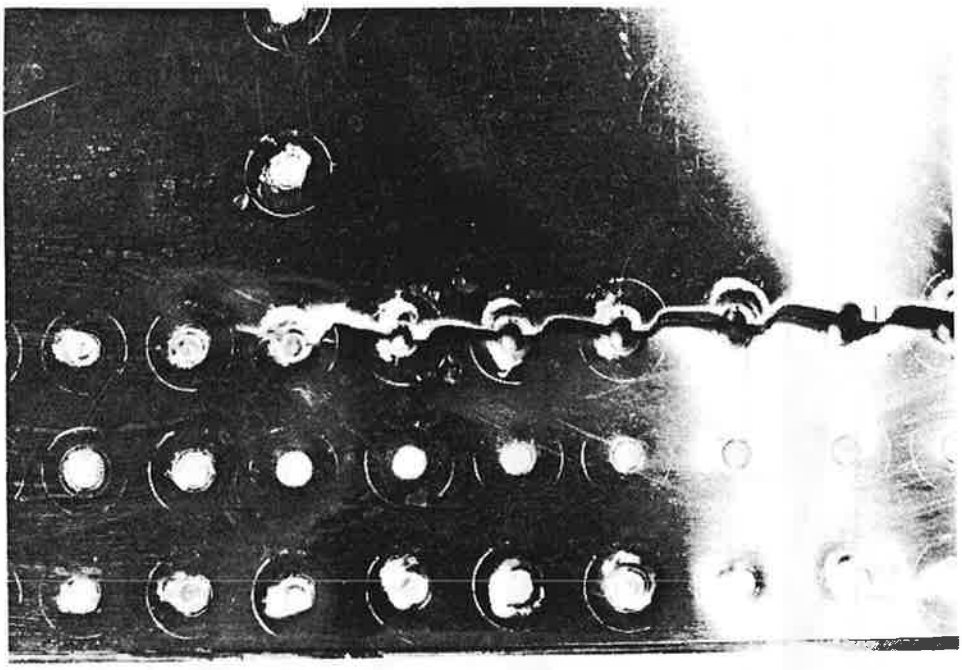

b) CLOSE-UP OF CRACK PROPAGATION

Figure 6-19. Fractured Test Panel with MSD

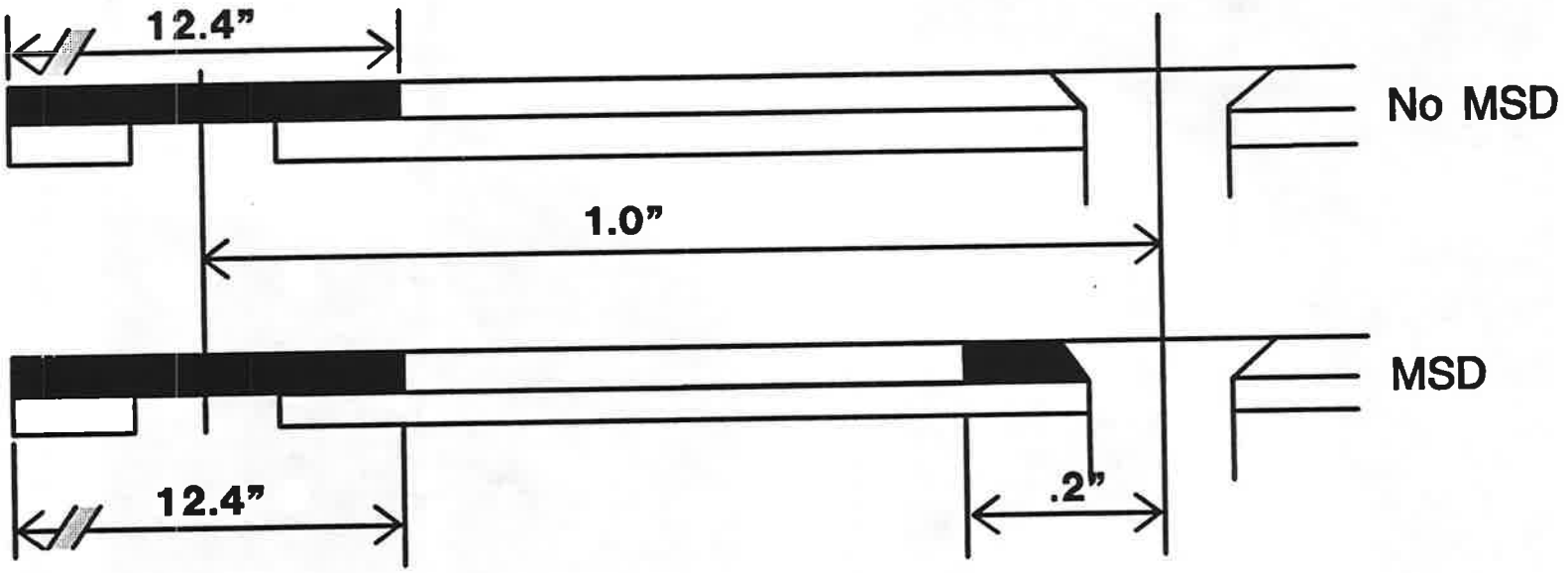

Panel	Top Skin Section Area		Failure Pressure
	1st Ligament	Panel	
No MSD	.029	3.05	10.5
MSD	.024	2.97	8.5
Ratio	1.21	1.03	1.24

Figure 6-20. MSD Strength Reduction Correlation with Net Section Area

- The skin fractures tend to propagate away from the stiffer lap splice zone. The cracks are generally arrested at the tear straps and, in the case of a 24-in. mid-bay crack, skin flapping did occur.

- Skin cracks in unbonded splices seem to have lower residual strength then those at mid-bay. However, further work is required to firmly establish this conclusion.

- MSD decreases the residual strength. For the particular panels tested with a 12.4-in. lead crack, the reduction is about 20 percent. For a given crack length, the reduction in strength seems to be approximately in inverse proportion to the first ligament net section area.

7. MATERIALS DATA

Complete understanding of the structural problems of the aging fleet and the behavior of cracks in fuselage lap joints requires data on basic material properties and on the behavior of these materials when configured into lap joint shapes and assemblies. To provide the basic materials data, Foster-Miller conducted a search of the published literature. To determine the behavior of these materials when configured for aircraft structural applications, and particularly in the presence of MSD, additional data were accumulated by laboratory testing. In particular, R-curve tests and rivet stiffness tests were performed. The results of the literature search and these test programs are presented in this section.

7.1 Survey: Data Base

A literature survey was conducted to gather published information on the material properties relevant to the aging aircraft problem. This search resulted in a compilation of the properties into a data base that can be easily accessed and can be expanded as future needs dictate. This aging aircraft materials data base is described in this section with details compiled in Appendix A to this report. The following section describes the materials investigated, sources reviewed, data available in the literature, and a brief summary of the findings. Data specifically relevant to the aging aircraft program, but not available in the open literature, is also identified here.

The search concentrated on the various aluminum alloys commonly used by the aircraft industry. These alloys are used in all structures found in aircraft, not just in the skin, and skin/stringer attachments. The materials investigated are 2014-T6, 2024-T3, 2024-T6, 7075-T6, 7075-T651, 7075-T73, and 7475-T61 in the clad and unclad conditions. These materials do not represent all those used in present aircraft, but they are the most commonly used and serve to initiate the data base. The structural properties pertinent to the performance of aircraft structures were selected. Both static and fatigue related properties were researched. The properties investigated are shown in Table 7-1 with comments as to the appropriateness of the results. These properties will vary in the presence of corrosion. The survey does not include corrosion effects.

Table 7-1. Material Properties Investigated

Property	Comments
Young's modulus, E	Initial elastic modulus
Poisson's ratio, ν	
Ultimate tensile strength, F_{tu}	Statistical "A" basis, L-direction
Tensile yield strength, F_{ty}	Statistical "A" basis, L-direction
Ultimate shear strength, F_{su}	Statistical "A" basis, L-direction
Fatigue endurance limit, F_{en}	At 500 x 10^6 cycles, R = 0.1
Plane strain fracture toughness, K_{IC}	
Plane stress fracture toughness, K_c	Tabular form versus thickness
Stress-strain curve	
Goodman diagram	
Fatigue crack growth rate	da/dN versus ΔK
Rivet stiffness	Countersunk rivet stiffness Not found in the literature
R-curve fracture toughness	Data for plane sheets with multiple rivet holes not found in the literature

Many sources were consulted to develop the data base. Standard references such as MIL-HDBK-5C, and the "Damage Tolerance Design Handbook" provided the bulk of the information. These references provide properties for materials approved for military aircraft. They represent extensive testing and data reduction and are deemed the most authoritative published sources available.

These sources are intended to be a design guide. As such, they present the data predominantly in terms of a statistical basis for use on either primary or secondary structures, as represented by either an "A" or "B" basis allowable. The data extracted for the material data base represent the "A" basis allowables where possible. Therefore, the usefulness of these data is limited if the purpose of the study is to understand failure modes and load at failure. For studies with this goal, the reader is referred to the original source for extraction of the mean data allowables. The complete list of investigated sources is found in Table 7-2.

Table 7-2. Material Data Base Sources

	Source
1.	AGARD Conference Proceedings No. 185, Specialists Meeting on Alloy Design for Fatigue and Fracture Resistance.
2.	*Aluminum Vol. I: Properties, Physical Metallurgy and Phase Diagrams,* edited by Kent R. Van Horn, ASM.
3.	*Aluminum Vol. II: Design and Application,* edited by Kent R. Van Horn, ASM.
4.	*Aluminum and its Alloys,* Frank King, Ellis Horwood Limited.
5.	*ASM Metals Reference Book,* Second Edition, ASM, March 1984.
6.	*Damage Tolerance Design Handbook,* prepared by University of Dayton Research Institute Materials Laboratory, Air Force Wright Aeronautical Laboratories, Wright-Patterson Air Force Base, Dec., 1983.
7.	*Fatigue of Aircraft Structures,* Horace J. Grover, prepared for Research and Technology Naval Air Systems Command Department of the Navy, 1966.
8.	*Fatigue of Metals,* P.G. Forrest, Pergamon Press, 1966.
9.	*Light Alloys Metallurgy of the Light Metals,* J. Polmear, ASM.
10.	*Metallic Fatigue,* W.J. Harris, Pergamon Press, 1961.
11.	*Military Standardization Handbook, Metallic Materials and Elements for Aerospace Vehicle Structures,* MIL-HDBK-5C, Sep., 1976.
12.	*New Materials and Fatigue Resistance Aircraft Design,* editor David L. Sipson, Engineering Materials Advisory Service Limited, 1987.
13.	*Structural Fatigue in Aircraft,* ASTM Special Technical Publication No. 404, a symposium presented at the Fifth Pacific Area National Meeting, ASTM, 1965.
14.	*Symposium on Damage Tolerance in Aircraft Structures,* a symposium presented at the Seventy-third Annual Meeting, ASTM, 1970.

Data Presentation

The aging aircraft material data base is organized and presented in the form of a summary of all the data collected for a particular alloy and heat-treat condition. These summaries are presented in Appendix A. The format for presenting data for 7075-T6 is shown in Table 7-3 as an example of this summary. The single-valued properties are presented in tabular form. Where many values are found for a single property, the various values are presented along with the source number as referenced in Table 7-2. The first value presented in the list is the

Table 7-3. Data Summary for 7075-T6

	E (Ksi)	ν	F_{tu} (Ksi)*	F_{ty} (Ksi)*	F_{su} (Ksi)*	F_{en} (Ksi)**	K_{IC} (Ksi√in.)
Value	10.3	0.33	78,83,83	70,73	47,48	23,20,22	28
Source No.***	11	11	11,2,3	11,2	11,2	2,3,3	3
Stress-strain curve, Source 11, pp. 3-271, 3-275							
Goodman diagram, Source 11, pp. 3-284 to 3-289, Source 7, p. 322							
Crack propagation da/dN versus WK, Source 6, pp. 8.9 to 8.9-93, Source 9, p. 79							

*A-basis.
**500E6 cycles, R = -1.
***Supporting data, Source 6, Table 8.9.2.1, Table 8.9.2.2.

preferred value based on the authoritativeness of the source. Sources such as MIL-HDBK-5C take precedence over sources such as papers or textbooks.

Data which can best be presented in a figure are referenced by page location in the Data Base summary tables. These data include the stress-strain curves, Goodman diagrams, and the fatigue crack growth rate curves. Numerous data have been developed for plane stress fracture toughness of thin aluminum sheets. These data cannot be readily extracted in either a single value or figure representation. Therefore, a page reference is reported as "supporting data" and reproduces the test results as a function of sheet thickness, specimen geometry, grain direction and test temperature. The reader is referred to this tabular summary for the specific data requirements of interest. A sample of this tabular summary for 7075-T6 is found in Table 7-4. These data were originally located in the Air Force Damage Tolerance Design Handbook (12).

Table 7-4. Plane Stress Fracture Toughness for 7075-T6 Aluminum

ALUMINUM 7075 K(C)

CONDITION	--PRODUCT-- FORM	THICK (IN)	TEST TEMP (F)	SPEC OR	YIELD STR (KSI)	---SPECIMEN--- WIDTH (IN) W	THICK (IN) B	CRACK LENGTH INIT (IN) 2A(O)	CRACK LENGTH FINAL (IN) 2A(F)	GROSS STRESS ONSET (KSI) B(O)	GROSS STRESS MAX (KSI) B(MAX)	K(APP) (KSI*SQRT IN)	K(APP) STAN DEV	K(C) (KSI*SQRT IN)	K(C) STAN DEV	DATE	REFER
BUCKLING OF CRACK EDGES RESTRAINED																	
T6	S	0.09	R.T.	L-T	75.9	12.000	0.090	1.040	1.460	---	46.60	59.84		71.22		1969	75599
		0.09			75.9	12.000	0.090	2.340	2.860	---	33.70	66.17		74.04		1969	75599
		0.09			75.9	12.000	0.090	1.060	1.560	---	44.80	58.09		70.87		1969	75599
		0.09			75.9	12.000	0.090	1.560	1.880	---	41.20	65.17		71.89		1969	75599
		0.09			75.9	12.000	0.090	4.500	5.460	11.40	22.50	69.60		75.82		1969	75599
		0.09			75.9	12.000	0.090	1.080	1.420	---	46.10	60.35		69.45		1969	75599
		0.09			75.9	12.000	0.090	1.820	1.920	---	40.00	68.61		70.58		1969	75599
		0.09			75.9	12.000	0.090	1.400	1.860	---	43.60	65.20		75.65		1969	75599
		0.09			75.9	12.000	0.090	3.880	4.720	15.30	25.20	66.55		76.00		1969	75599
		0.09			75.9	12.000	0.090	2.800	3.460	---	29.90	64.90		73.51		1969	75599
		0.09			75.9	12.000	0.090	1.100	1.440	---	44.00	58.14		66.77		1969	75599
		0.09			75.9	12.000	0.090	1.960	2.380	---	35.90	64.05		71.15		1969	75599
		0.09			75.9	12.000	0.090	2.020	2.180	---	38.60	69.98		72.92		1969	75599
		0.09			75.9	12.000	0.090	2.440	3.060	---	33.20	66.71		75.85		1969	75599
		0.09			75.9	12.000	0.090	3.520	4.200	17.00	28.00	69.57		77.89		1969	75599
		0.09			75.9	12.000	0.090	3.180	3.600	---	28.20	65.90		71.04		1969	75599
		0.09			75.9	12.000	0.090	3.060	3.580	---	28.20	64.43		70.80		1969	75599
		0.09			75.9	12.000	0.090	2.040	2.320	---	35.60	64.89		69.57		1969	75599
		0.09			75.9	12.000	0.090	2.620	3.500	---	29.60	61.88		73.29		1969	75599
		0.09			75.9	12.000	0.090	2.100	2.300	---	34.90	64.61		67.88		1969	75599
		0.09			75.9	12.000	0.090	4.940	5.620	13.00	21.10	65.79		72.81		1969	75599
		0.09			75.9	12.000	0.090	3.440	3.700	21.70	27.70	67.86		70.99		1969	75599
		0.09			75.9	12.000	0.090	3.800	4.380	14.50	23.20	60.46		66.39		1969	75599
		0.09			75.9	12.000	0.090	3.560	4.260	13.70	25.10	62.80		70.49		1969	75599
		0.09			75.9	12.000	0.090	2.140	2.400	27.80	36.10	67.52		71.87		1969	75599
		0.09			75.9	12.000	0.090	2.240	2.740	27.80	33.30	63.84	64.6/ 3.2	71.39	71.9/ 2.8	1969	75599
T6	S	0.09	R.T.	L-T	75.9	12.000	0.100	1.980	2.530	---	35.80	64.22		73.39		1969	75599
T6	S	0.10	R.T.	L-T	75.9	1.500	0.100	0.500	0.570	---	44.90	42.76*		46.72*		1962	62306
T6	S	0.10	R.T.	L-T	75.9	3.500	0.100	0.500	0.760	---	53.70	48.20*		60.44*		1962	62306
		0.10			75.9	3.500	0.100	0.770	1.140	---	46.40	52.61		66.49*		1962	62306
T6	S	0.10	R.T.	L-T	75.9	6.000	0.100	2.000	2.450	---	33.50	63.81		73.42		1962	62306

*NOTE- NET SECTION STRESS EXCEEDS 80% OF YIELD STRENGTH. VALUE NOT INCLUDED IN MEAN OR STD. DEV.

The fatigue crack propagation rates are presented in figure form and are referenced by page number in the data base. A typical set of curves is found in Figure 7-1. The data source is the Damage Tolerance Design Handbook. The variation of da/dN with stress ratio, sheet thickness, temperature, and loading frequency is presented.

Two specific data requirements for the aging aircraft program relate to the countersunk rivet stiffness in lap splice joints as found in fuselage skin joints, and the plane stress R-curve for the sheet weakened by rivet holes. These data are specific to the geometries being investigated. The following sections describe the derivation of the data by test at Foster-Miller. The data are compiled in the aging aircraft material data base and are available for reference.

7.2 R-Curve Tests and Data

R-curve testing:

- Determines the maximum permissible lengths of cracks emanating from rivet holes at which link-up leading to a complete fracture of ligaments (i.e., skin material between rivet holes that carry the hoop load in the fuselage structure) does not occur.

- Determines the stable crack growth increment for a given MSD condition and an applied load increase.

Maximum permissible crack length is important in avoiding catastrophic failure of the fuselage under longitudinal crack conditions. An empirical criterion based on the net section stress has been developed in this work.

Determination of the stable crack growth increment is critical for establishing the appropriate intervals for crack inspections.

Test data are required because of the theoretical difficulties in elasto-plastic fracture analysis, which are discussed by Sampath et al. (3).

CONDITION/HT: T6
FORM: 0.13- 0.20"TH SHEET
SPECIMEN TYPE: CCP
ORIENTATION: L-T
STRESS RATIO: +0.02
ENVIRONMENT: R.T.. LAB AIR

YIELD STRENGTH: 74.5- 78.9 KSI
ULT. STRENGTH: 80.0- 86.7 KSI
SPECIMEN THK: 0.020- 0.200"
SPECIMEN WIDTH: 3.900- 11.500"
REFERENCES: 86088, MA009, MA008

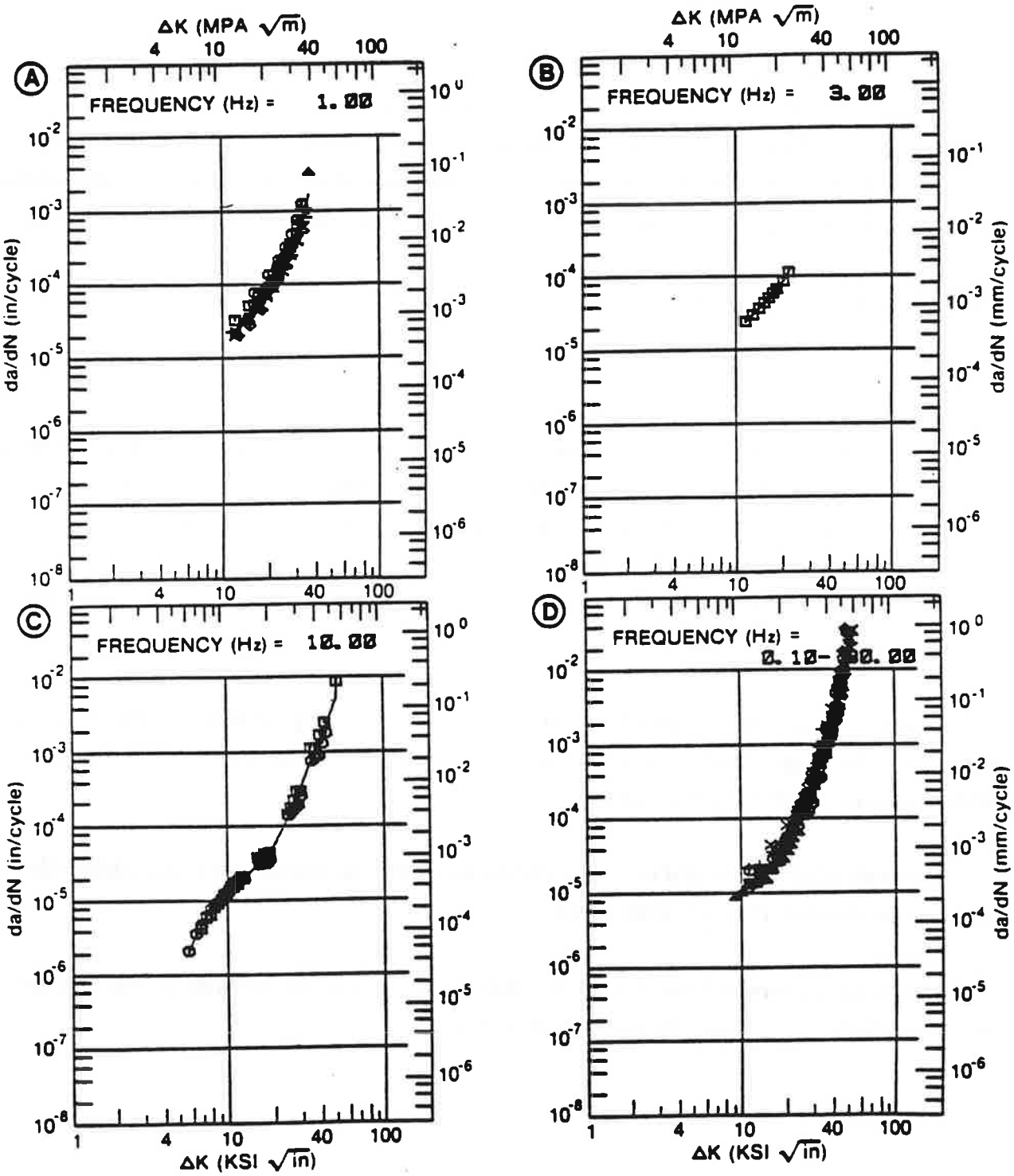

Figure 7-1. Crack Propagation Data for 7075-T6

7.2.1 Coupon Preparation

Two sizes of Alclad 2024-T3 coupons were used in the test; one lot had 4-in. wide coupons with three holes as in Figure 7-2, the other had 10-in. wide coupons with 10 holes (Figure 7-3). The holes were 0.1875 in. in diameter. The thickness of all coupons was 0.04 in.

A jeweler's saw was used to prenotch both sides of the two central holes of the 10-in. coupon. The prenotching was required to initiate fatigue cracks. Fatigue cycling (in the load range of 400 to 2,700 lb for the 4-in. coupon and 675 to 6,750 lb for the 10-in. coupon) was carried out to develop the required initial fatigue crack lengths. After achieving the desired crack length at the center hole(s) (0.15, 0.22 or 0.26 in.), approximately equal crack lengths were machined at other holes. These crack lengths were not truly equal in the 10-in. coupon, but they were measured exactly and the differences accounted for during data analysis.

7.2.2 R-Curve Testing

Each of the coupons was placed in the tensile test machine and loaded at a constant displacement rate of approximately 0.005 in./min. The crack lengths were monitored to fracture failure using an optical microscope. Failure was a very fast fracture across the complete width of the ligaments. The test data for the coupons are presented in Tables 7-5 and 7-6. Typical crack growth histories are shown in Figures 7-4 and 7-5. No significant crack growth was observed on the saw cut cracks. As one would expect, the fatigue cracks were critical and vulnerable to incremental growth under direct load.

The far field stress (load/skin area without holes and cracks) at each load level is plotted against crack extension in Figure 7-6. It is seen that for the 10-in. coupon, with initial crack length of 0.22 in., a stress level of 23 Ksi causes a complete failure.

A plot of net section stress versus crack extension is presented in Figure 7-7. The stress is calculated after accounting for the incremental growth in the cracks. Four of the five coupons failed at a net section stress value between 53 and 55 Ksi. An average of 54 Ksi can be used in the criterion for MSD linkup based on the net section stress. Tensile tests carried out on specimens of this material gave a yield stress of about 49 Ksi and an ultimate of 67 Ksi as shown in Figure 7-8. As one would expect, the net section stress for fracture falls between these limits.

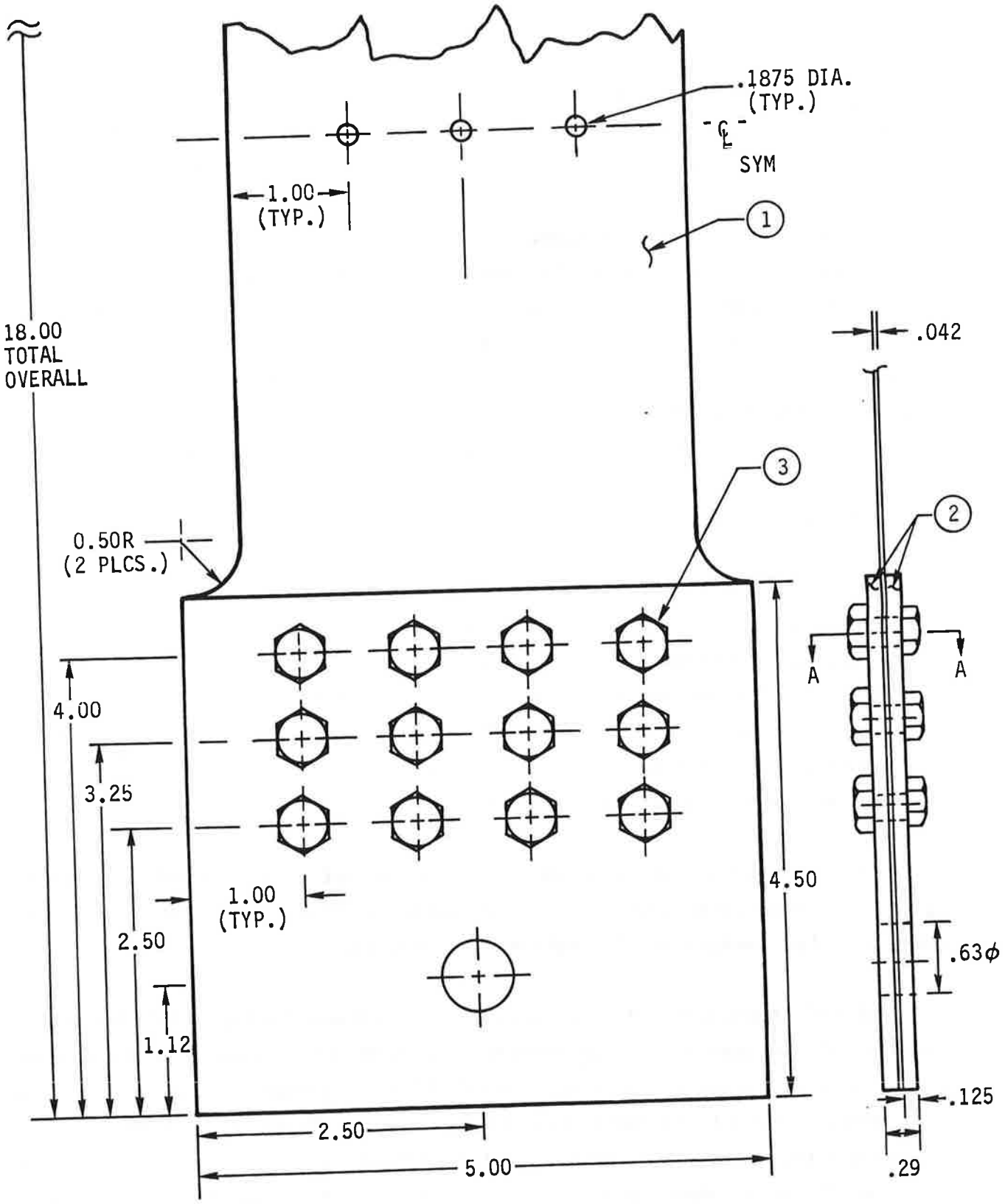

Figure 7-2. Four-Inch Coupon Configuration

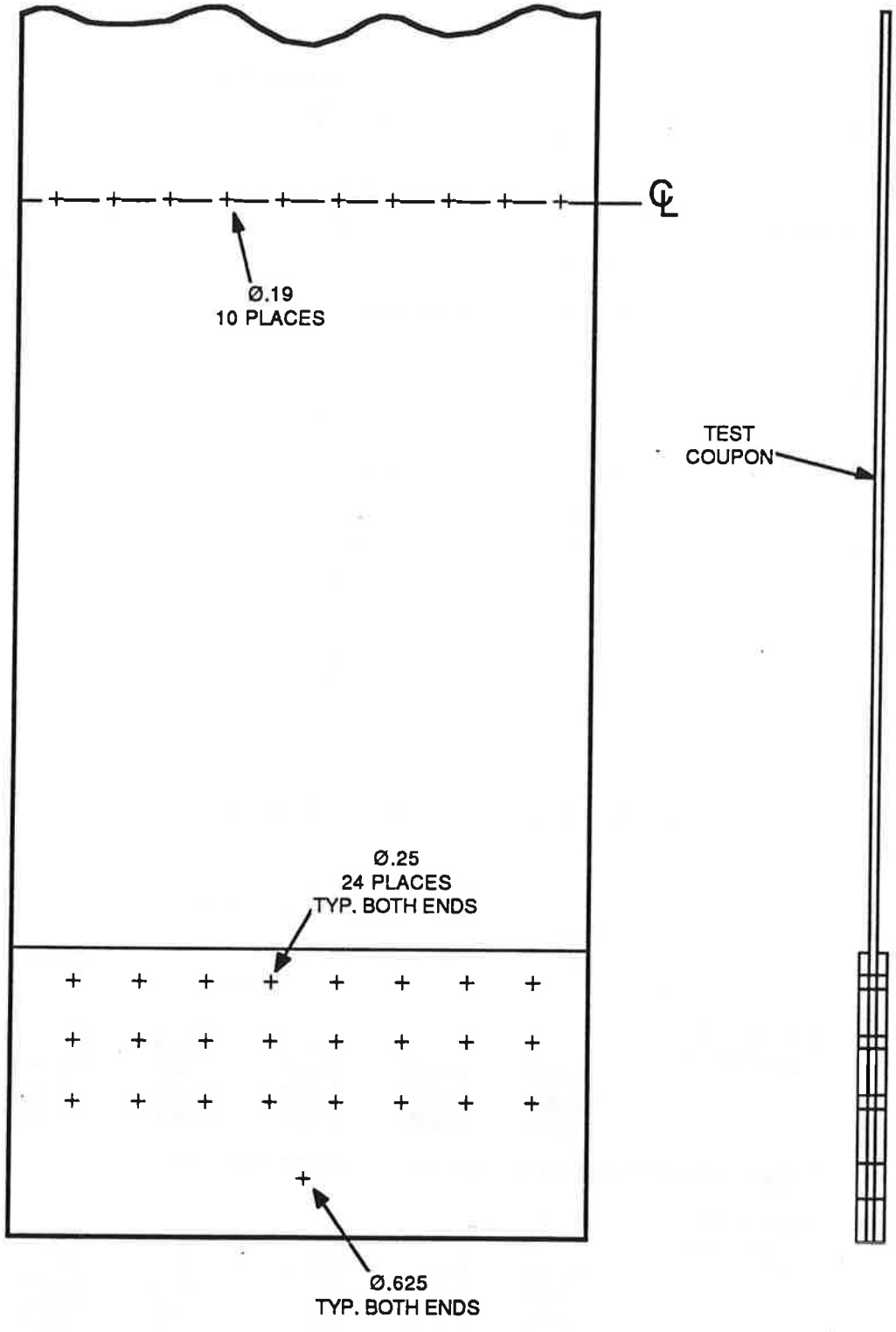

Figure 7-3. Ten-Inch Coupon Assembly

Table 7-5. Four-Inch Coupon Test Data

Coupon No.	Load (lb)	Crack Extension (in.) Right Side	Left Side	
1 (precrack length = 0.15 in.)	4,860	0.012		
	5,000	0.015	0.005	
	5,820	0.025	0.012	
	5,900	0.030	0.028	
	5,990	0.040	-	Fracture
	3,200	Holding load		
2 (precrack length = 0.22 in.)	5,350	0	0.015	
	5,500	0.020	0.020	
	5,660	0.025	0.025	
	5,730	0.035	0.030	
	5,750	0.040	-	Fracture
	3,150	Holding load		
3 (precrack length = 0.26 in.)	3,350	0.015	0.010	
	4,200	0.017	0.016	
	4,650	0.020	0.016	
	4,960	0.030	0.016	
	5,010	0.030	0.020	
	5,140	0.035	0.035	
	5,170	0.038	0.050	
	5,250	0.050	0.050	Fracture
	3,300	Holding load		

Table 7-6. Ten-Inch Coupon Test Data

	Load (lb)	Crack Lengths (in.) 1	2	3	4
Coupon 10-1 (δ_o = 0.15 in.)	0	0.092	0.106	0.148	0.134
	9,000	0.092	0.106	0.148	0.134
	12,200	0.096	0.108	0.156	0.138
	13,000	0.098	0.110	0.160	0.142
Failure occurred as load was being increased from 13,000 lb.					
Coupon 10-2 (δ_o = 0.22 in.)	0	0.216	0.222	0.216	0.210
	5,000	0.216	0.222	0.216	0.210
	7,000	0.216	0.222	0.216	0.210
	8,000	0.218	0.222	0.220	0.210
	8,400	0.220	0.224	0.220	0.216
	8,600	0.222	0.226	0.220	0.216
	8,700	0.228	0.234	0.226	0.217
	8,850	0.229	0.238	0.232	0.218
	8,980	Failure			

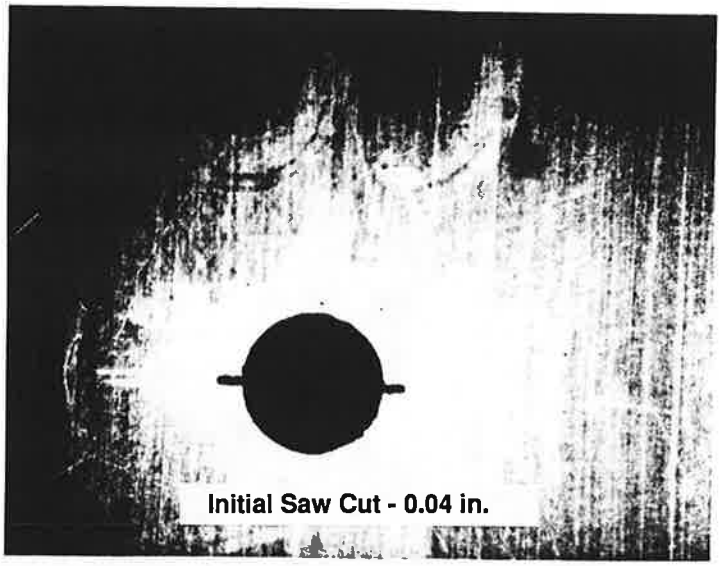

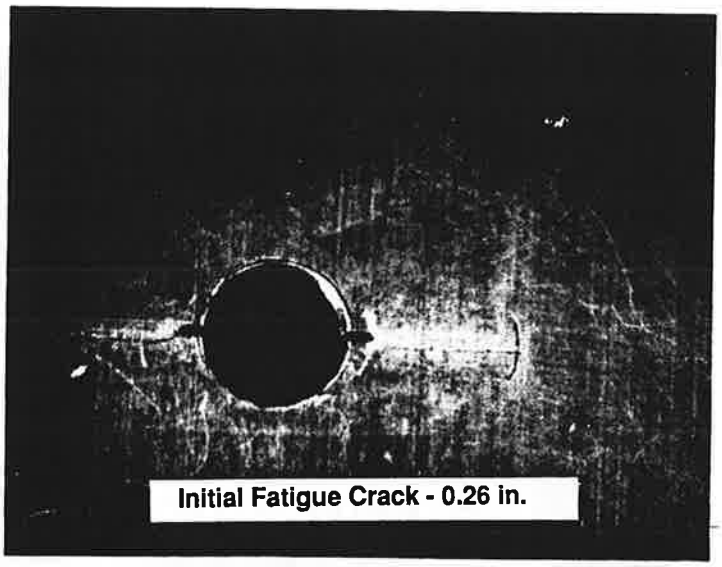

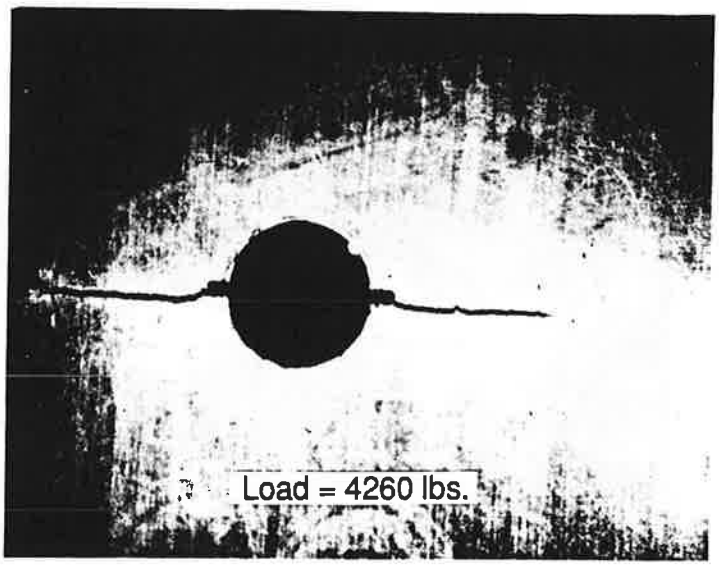

Figure 7-4. R-Curve Test Initial Crack Growth

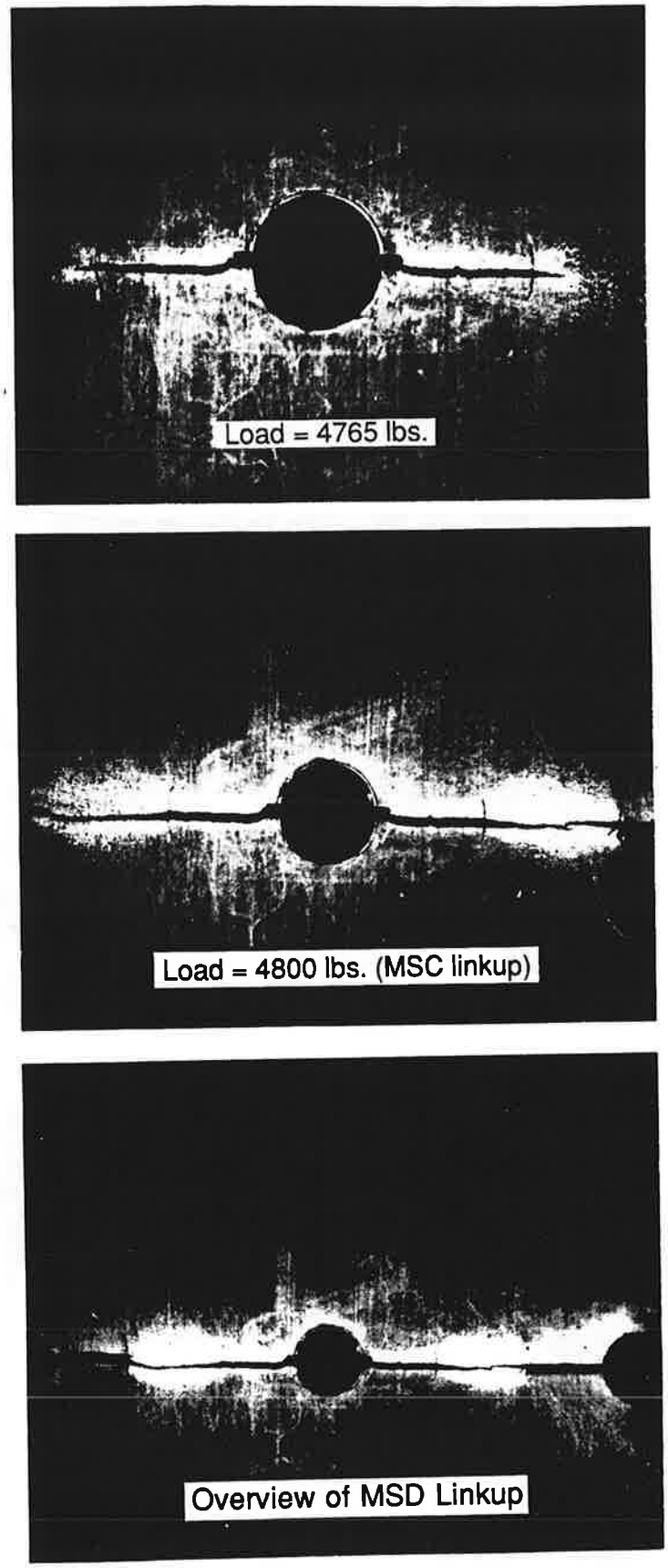

Figure 7-5. R-Curve Test Final Crack Growth

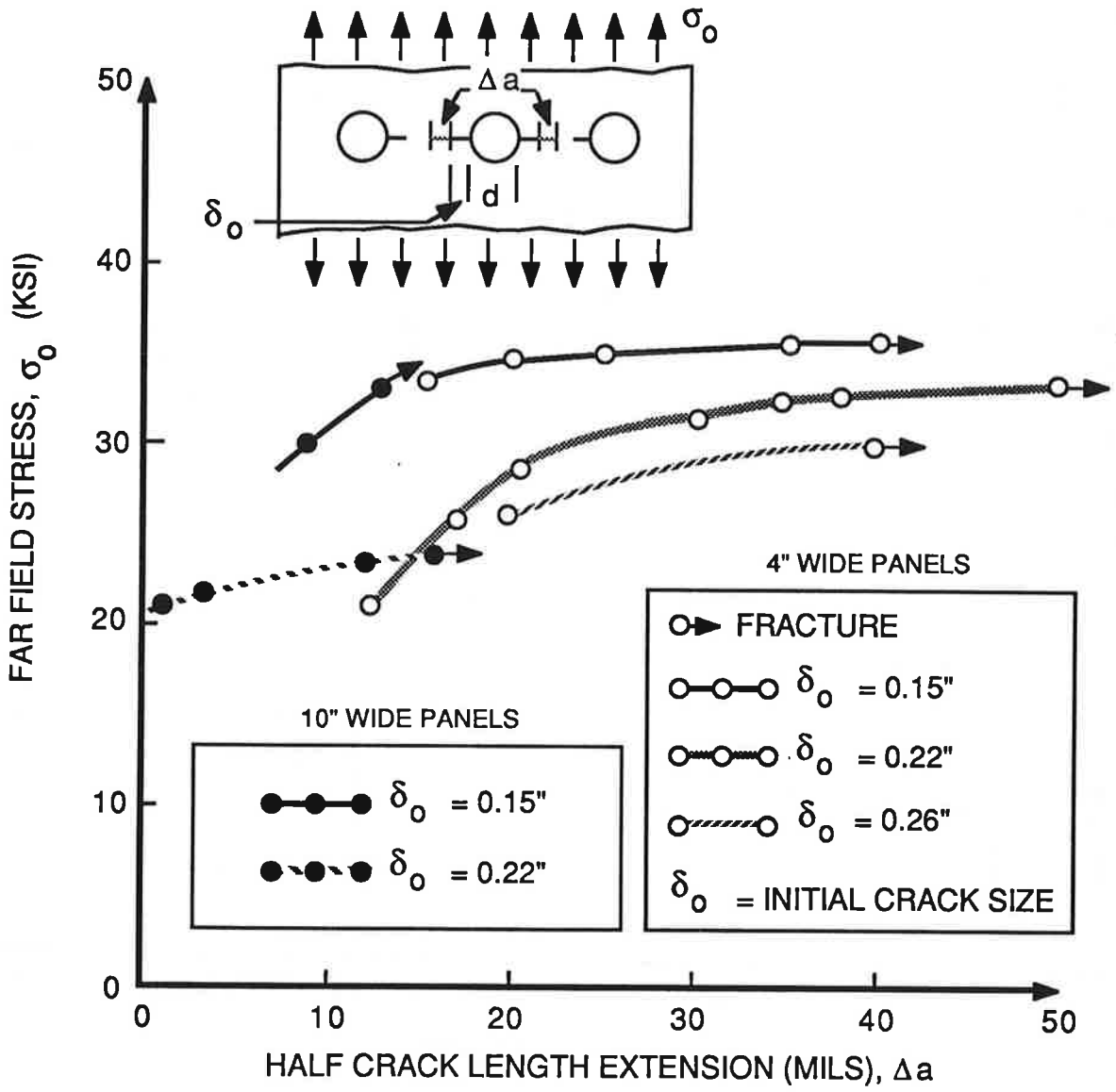

Figure 7-6. Far Field Stress Plotted Against Half Crack Length Extension

Realizing that the majority of the simulated MSD in coupons were saw cut and not fatigue originated, the limiting net section stress for the aircraft panels with fatigue cracks could be even closer to the material yield stress rather than the 54 Ksi quoted earlier. This statement needs to be verified by more rigorous experiments in the future.

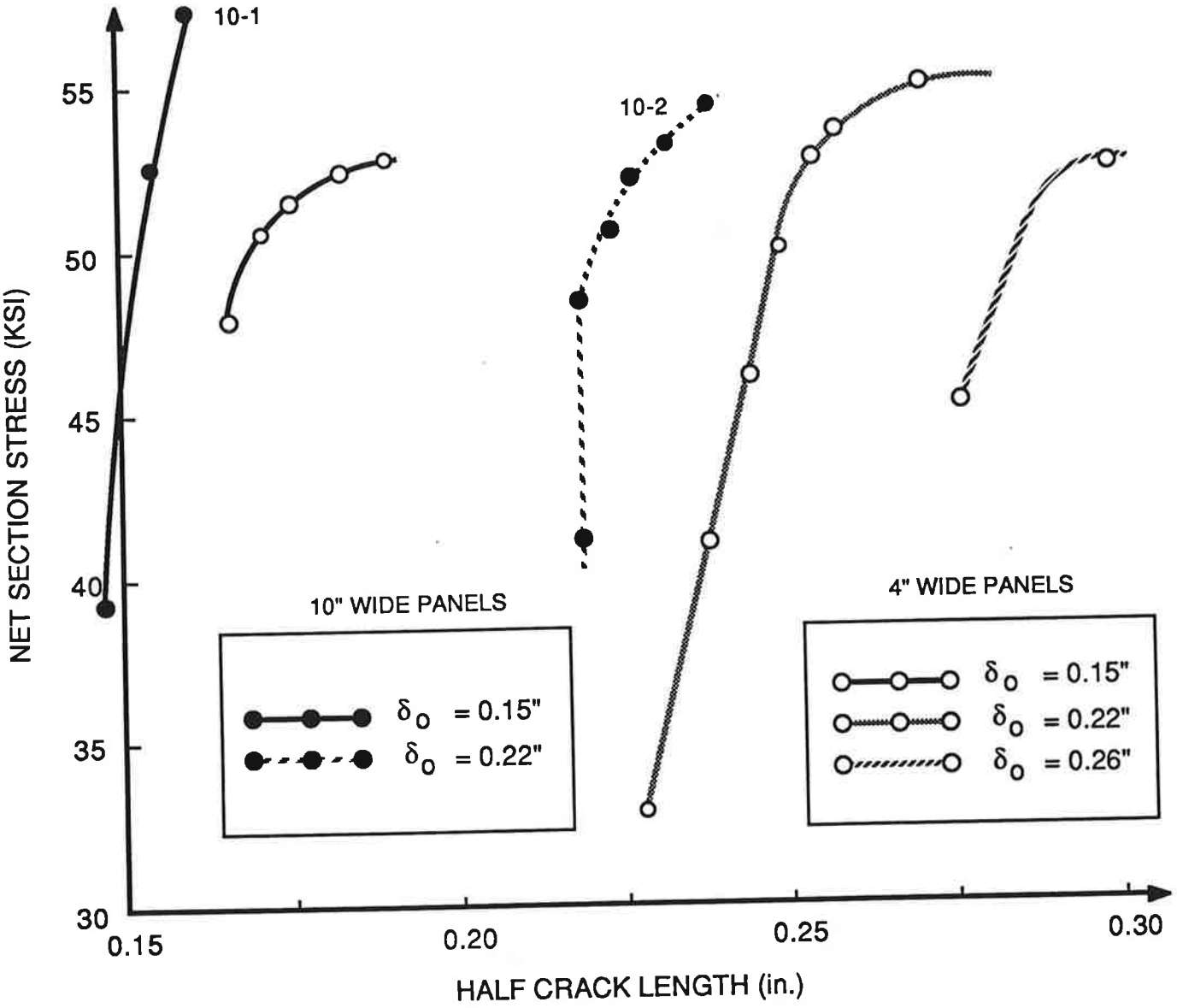

Figure 7-7. R-Curve Reduced Data Based on Net Section Stress

7.3 Countersunk Rivet Stiffness in Thin Sheets

Tests were performed to determine the flexibility of riveted joints in 0.04-in. thick sheets. These tests were necessary as no data could be found in the open literature. A total of six tests were conducted on single rivet joint assemblies. Four of these tests were conducted on 0.04-in. thick coupons. Two tests were conducted on 0.08-in. thick coupons which provided some baseline comparisons with published literature.

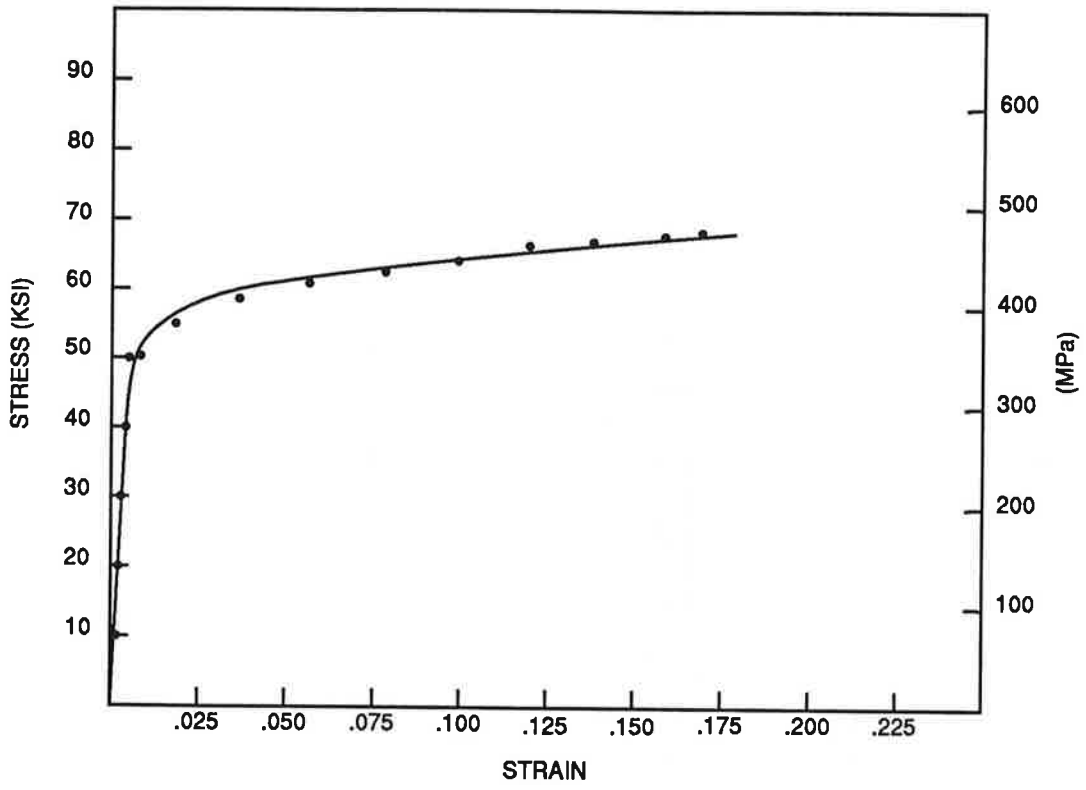

Figure 7-8. Stress-Strain Curve for R-Curve Test Specimen Material (2024-T3)

The back-to-back configuration used in these tests to minimize bending is shown in Figure 7-9. This configuration has been used by other investigators including Swift (1). The coupon material was 2024-T3 Alclad aluminum and the fasteners were 100-deg shear head 2017 aluminum rivets. Testing was conducted on a tensile test machine. Specimens were loaded at a slow constant rate to failure. Load and deflection were recorded throughout the duration of the test. Total deflection (δT) was measured with an extensometer connected to two points, 2 in. apart. The plate deflection (δp) has been accounted for using the following formula:

$$\delta p = \frac{(P_{applied})(L_p)}{(A_p)(E)}$$

The deflection due to rivet shear (δr) has been calculated as follows:

$$\delta r = \delta T - \delta p$$

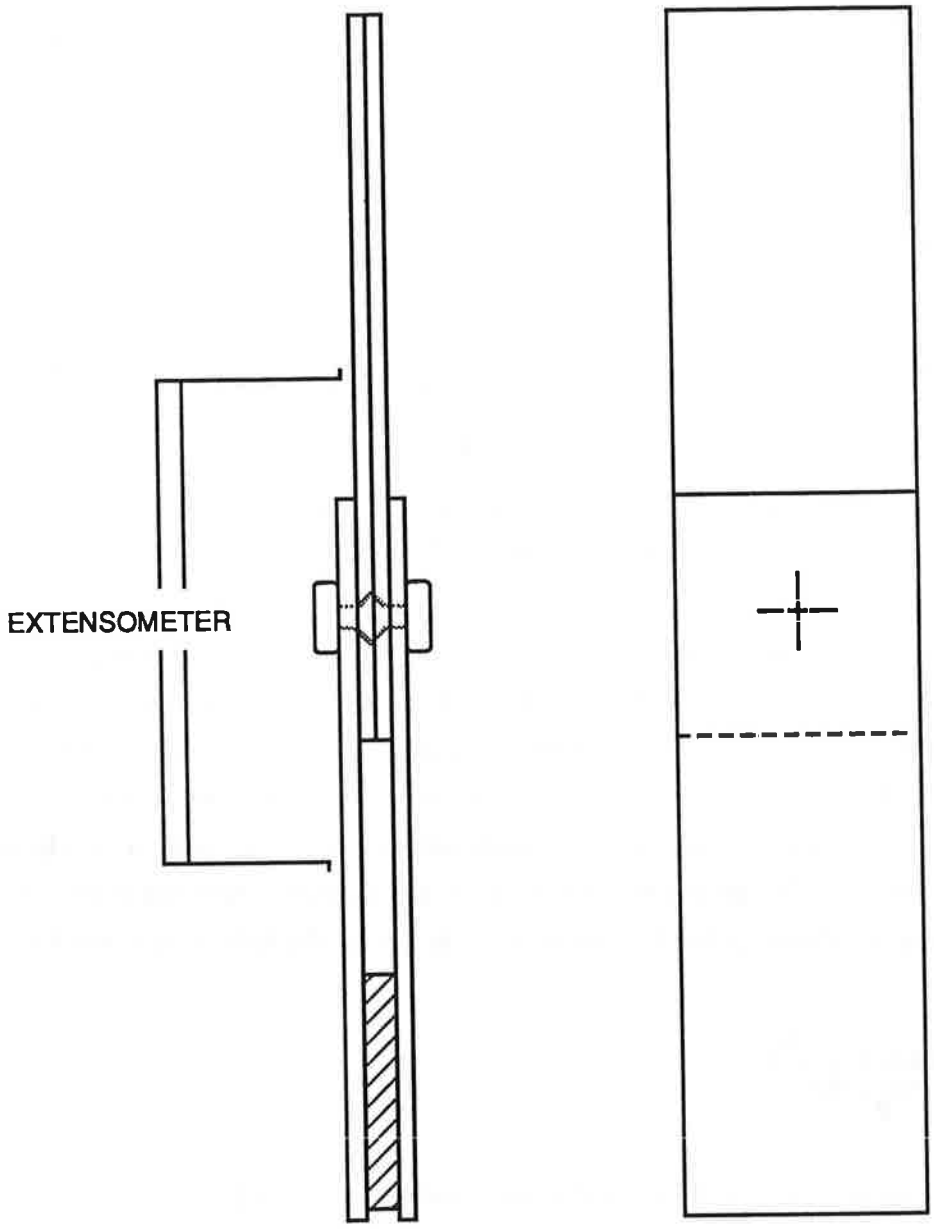

Figure 7-9. Test Assembly Configuration

Results of calculations for all tests are presented in Table 7-7. Typical raw data are shown in Figures 7-10 and 7-11. A comparison between the test results and published test data and formulae is given in Table 7-8. The test results for 0.08-in. thick coupons are in agreement with the published test data of Huth (6) but show significant deviations from Boeing and Douglas/Swift formulae.

The results for the 0.04-in. thick coupons are in agreement with the Boeing formula, and are within about 10 percent of the Douglas/Swift formula. These results differ by 30 percent from Huth's formula. It is important to note that all of these formulae are based on tests of coupons no less than 0.08 in. thick.

Table 7-7. Calculation of Fastener Flexibilities

Test No.	Coupon Thickness (in.)	Measured Total Deflection per Pound (μin./lb)	Calculated Plate Deflection per Pound (μin./lb)	Rivet Shear Deflection per Pound (μin./lb)	Flexibility (μin./lb)
1A	0.08	5.35	1.19	4.16	8.32
1B	0.08	4.00	1.19	2.81	5.62
2A	0.04	6.25	2.38	3.87	7.74
2B	0.04	6.25	2.38	3.87	7.74
2C	0.04	4.55	2.38	2.17	4.34*
2D	0.04	6.25	2.38	3.87	7.74

*This point is not included in the determination of the average stiffness.

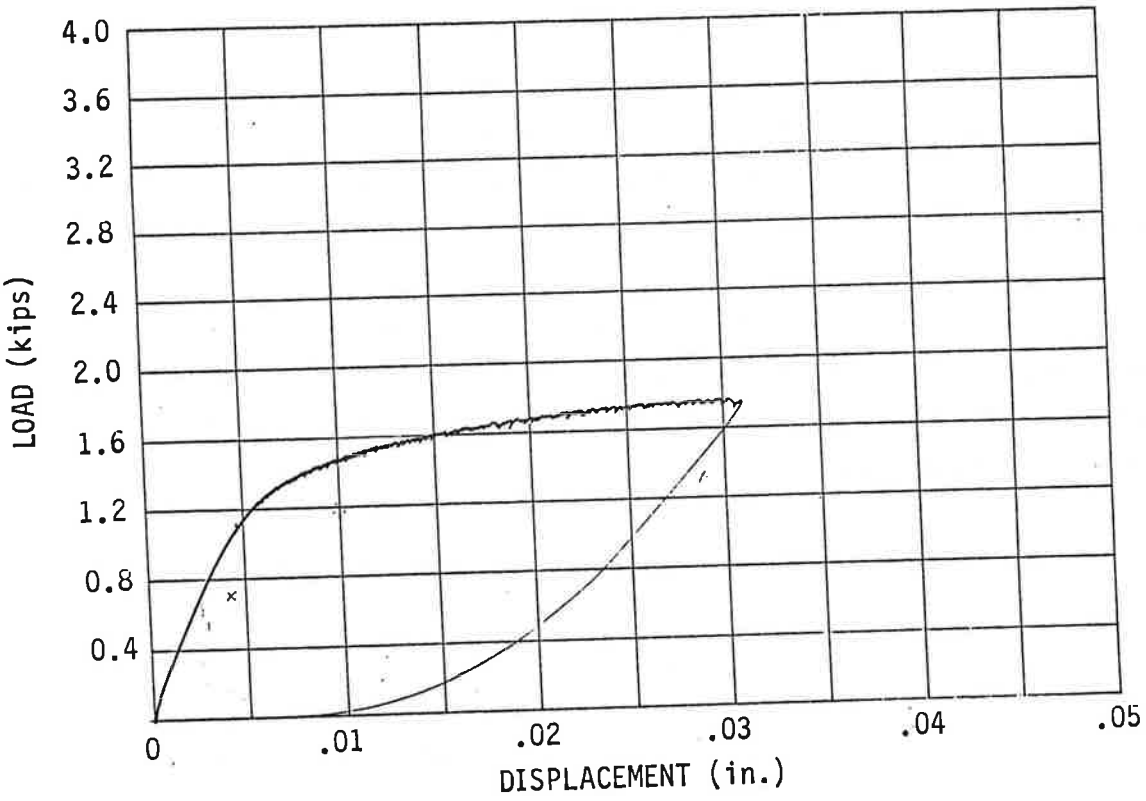

Figure 7-10. Typical Test Data - 0.080-in. Coupons

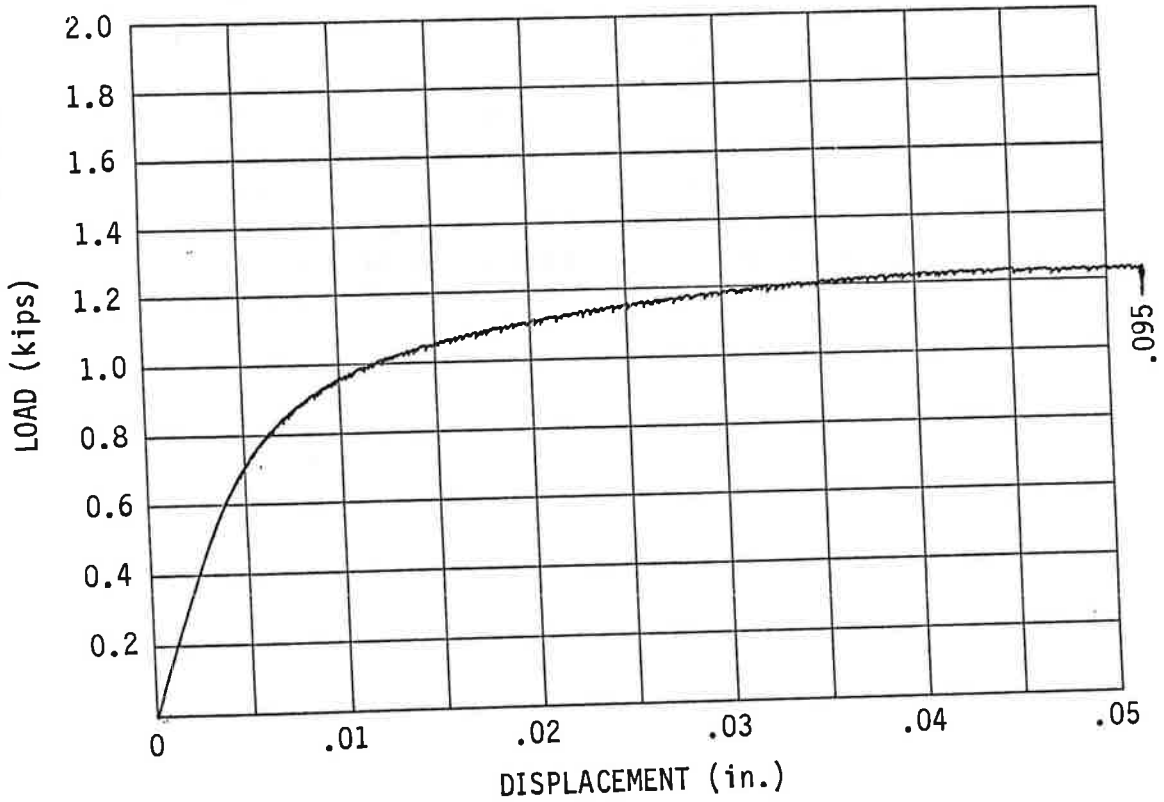

Figure 7-11. Typical Test Data - 0.040-in. Coupons

Table 7-8. Comparison of Fastener Flexibilities (μin./lb)

Configuration	Test Data		Empirical Formulae			
	Foster-Miller	Huth	Huth*	Tate and Rosenfeld	Boeing	Douglas/ Swift
0.04-in. thick coupon	7.7	N/A	10.6	10.1	7.6	6.9
0.08-in. thick coupon	6.9	7.0	7.0	6.2	4.4	5.0

*Based on tests after several loading cycles.

8. ANALYTIC MODELING

Analytic modeling of a generic aircraft fuselage structure using NISA 386 has been carried out with the following objectives:

- To develop equivalent flat coupon configurations for fatigue studies
- To determine rivet loads and stress distributions in the lap joint
- To determine MSD link-up potential in the cracked lap joint
- To develop a rigorous analysis of fracture and residual strength of the structure under a single long lead crack.

These topics are discussed in the following paragraphs.

8.1 Fatigue Coupon Equivalency Analyses

To develop equivalent flat coupon configurations, the static stress distribution in the stiffened curved fuselage shell is first determined using the finite element (FE) method. FE solutions have also been developed for flat coupons with different configurations. The flat coupon configuration with a stress distribution similar to that in the curved fuselage is considered suitable for fatigue testing.

Stress Distribution in Fuselage Panel

A linear analysis of the fuselage structure using the FE idealization has been performed. The structural members have been represented by either four- or eight-noded thin shell elements, as indicated in Table 8-1. Symmetric boundary conditions along stringers and frames have been assumed in the analysis.

Figure 8-1 shows the radial deflection plot. The radial bulging between strap and frame stiffeners is clearly seen. No significant deflection occurs along the stringer.

Table 8-1. FE Model for Fuselage Structure

	Element	Number of Elements
Skin	Four-noded thin shell	16 x 40 = 640
Tear straps	Four-noded thin shell	16 x 1 = 16 16 x 2 = 32
Longitudinal strap	Four-noded thin shell	2 x 40 = 80
Frame	Eight-noded thin shell	16 x 6 = 96
Stringer	Eight-noded thin shell	7 x 20 = 140
Shear clip	Eight-noded thin shell	12 x 4 = 48
DOF = 5,944		

Figures 8-2 through 8-4 show the hoop membrane and bending stress distributions. The membrane stress of 15 Ksi in Figure 8-2 is slightly lower than the value of 16 Ksi derived from the elementary theory. The bending stress in the skin is influenced by the stiffeners as seen in Figure 8-4. The peak bending stress is about one-third of the peak membrane stress.

Stress Distribution in Coupons

Four types of flat coupons, as shown in Figure 8-5, have been analyzed using the FE method. Details of each configuration are shown in Table 8-2. Coupon widths equal one frame spacing in a typical aircraft fuselage. Coupons with smaller width may be inadequate for MSD simulation. The height of the coupon should be sufficient for the applied pin load to yield the desired stress distribution near the lap joint. A 30-in. coupon seems reasonable from the results presented here.

Hoop stress distributions in the curved fuselage and coupons are compared in Figure 8-6. Coupons A and B are clearly not acceptable. Coupon C defines the optimum height of the stiffeners and should be adequate in the fatigue studies, although Coupon D with tapered stiffeners would yield better accuracy.

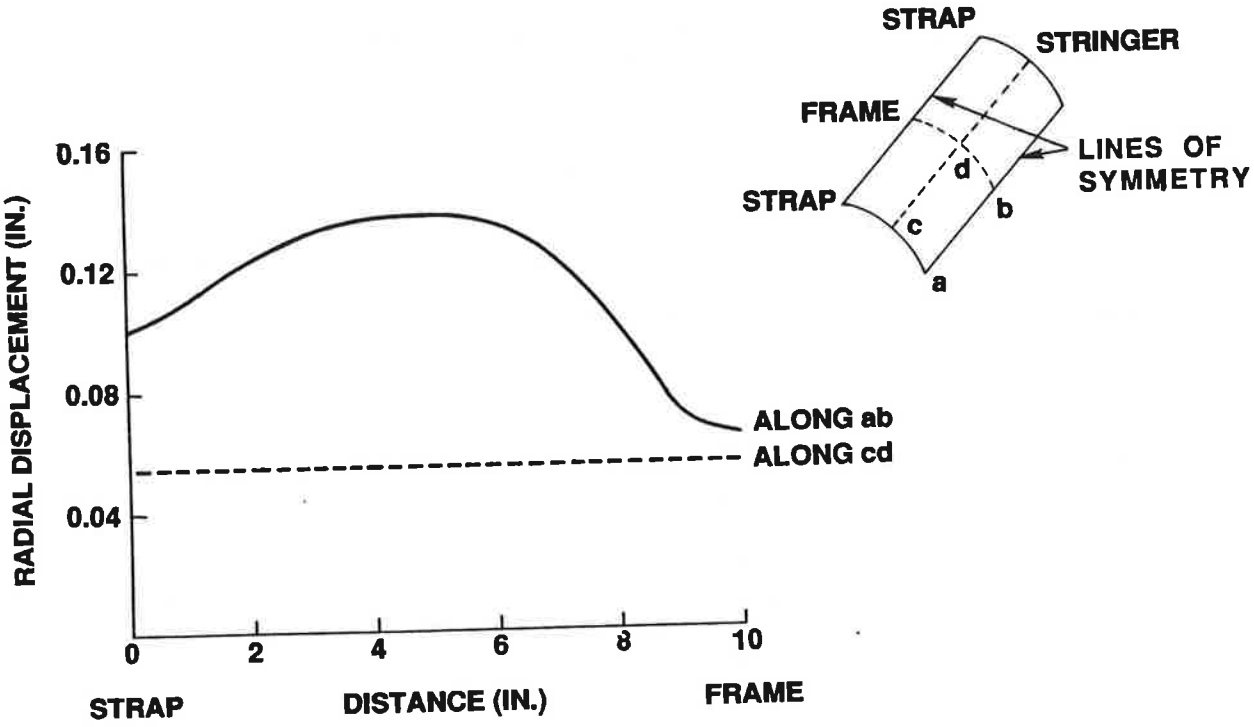

Figure 8-1. Deflected Shape of the Pressurized Fuselage due to Internal Pressure (P = 8.6 psi)

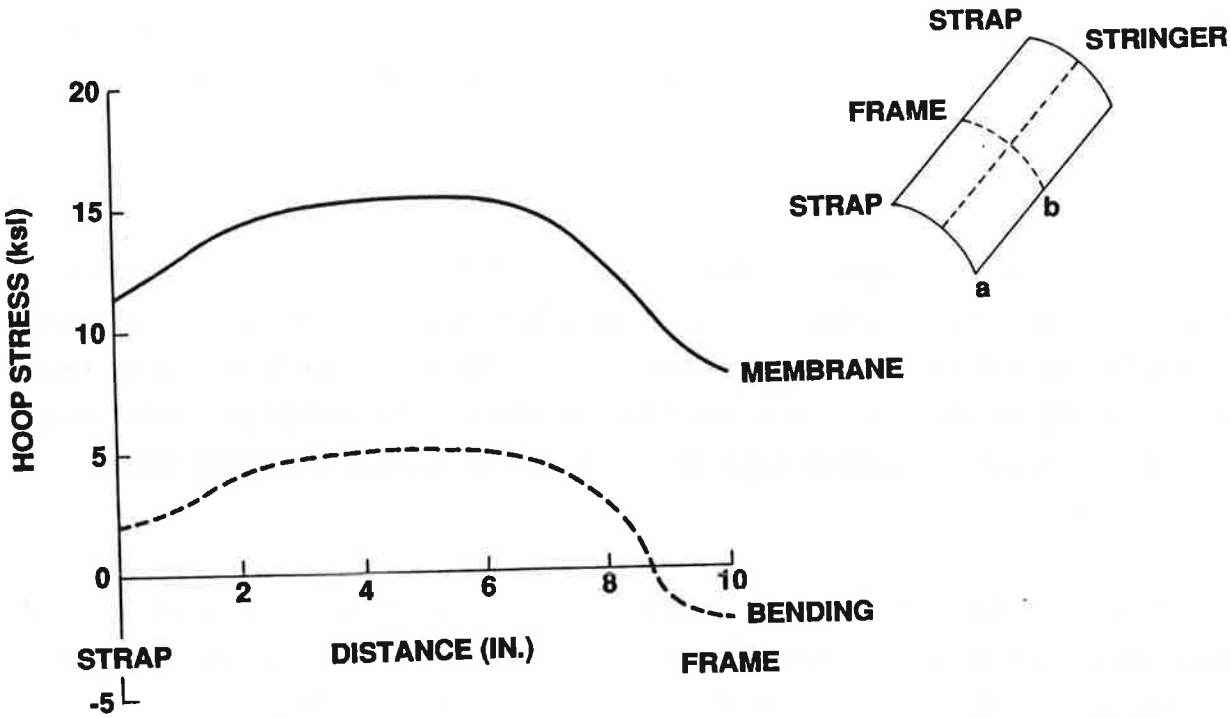

Figure 8-2. Hoop Stress Distribution Along a-b due to Internal Pressure (P = 8.6 psi)

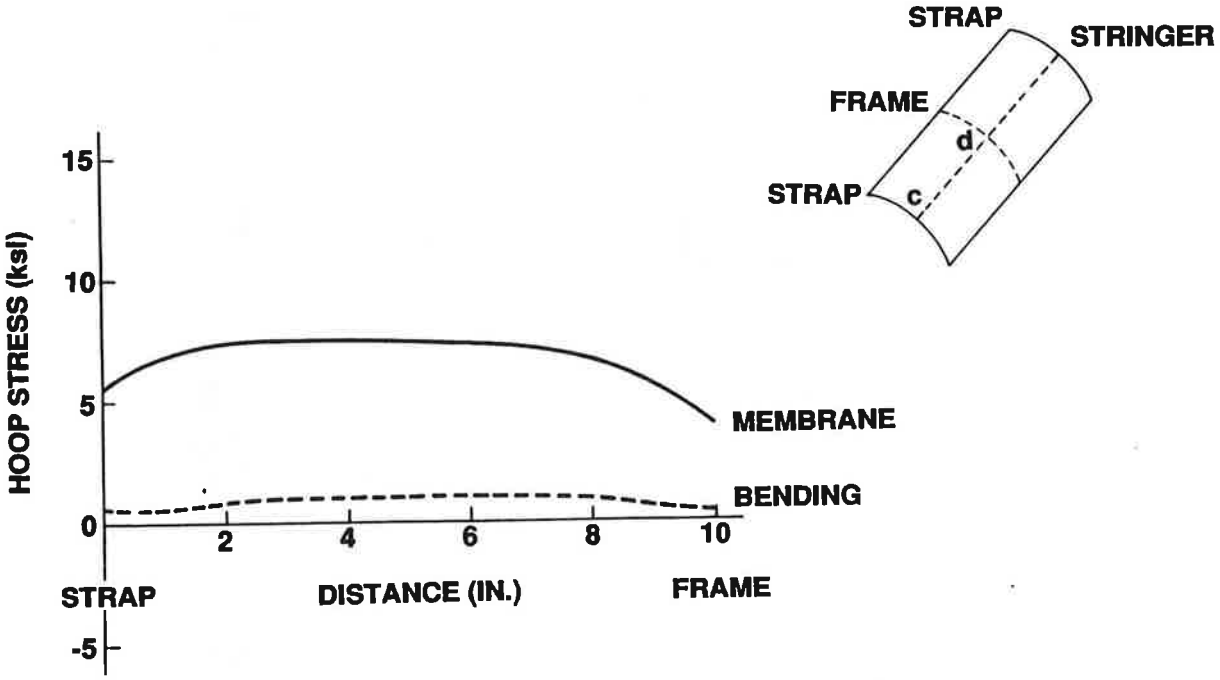

Figure 8-3. Hoop Stress Distribution Along c-d due to Internal Pressure (P = 8.6 psi)

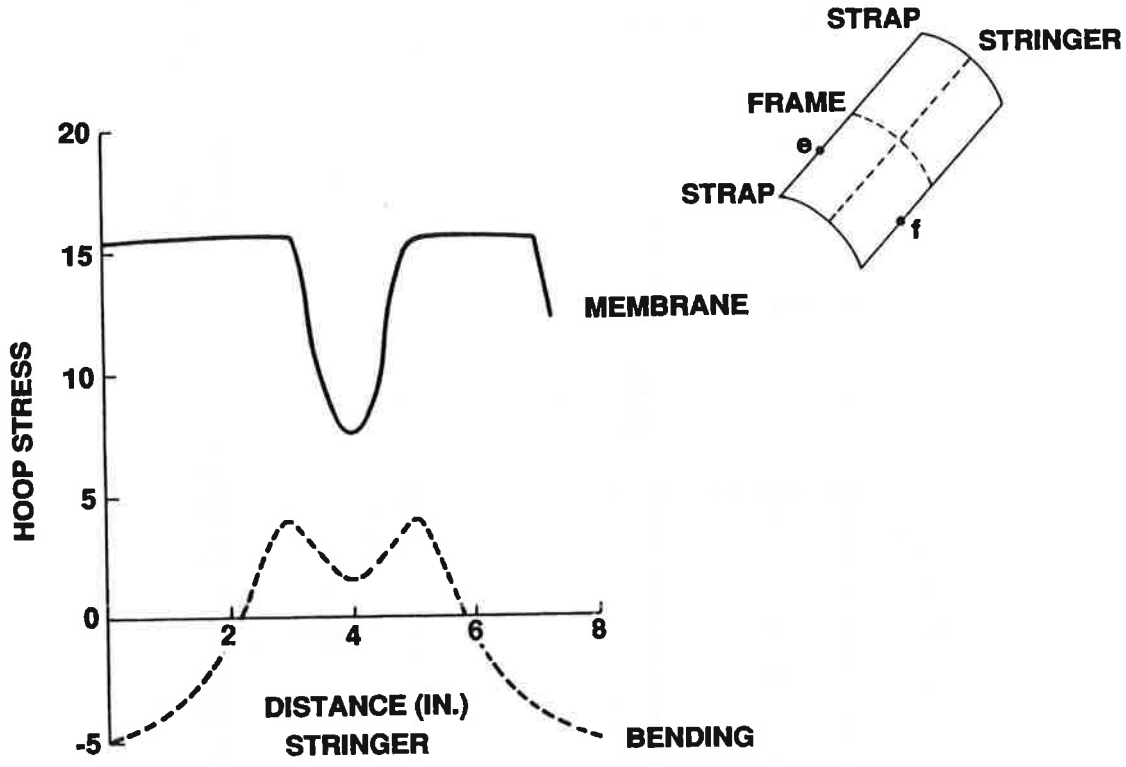

Figure 8-4. Hoop Stress Distribution Along e-f due to Internal Pressure (P = 8.6 psi)

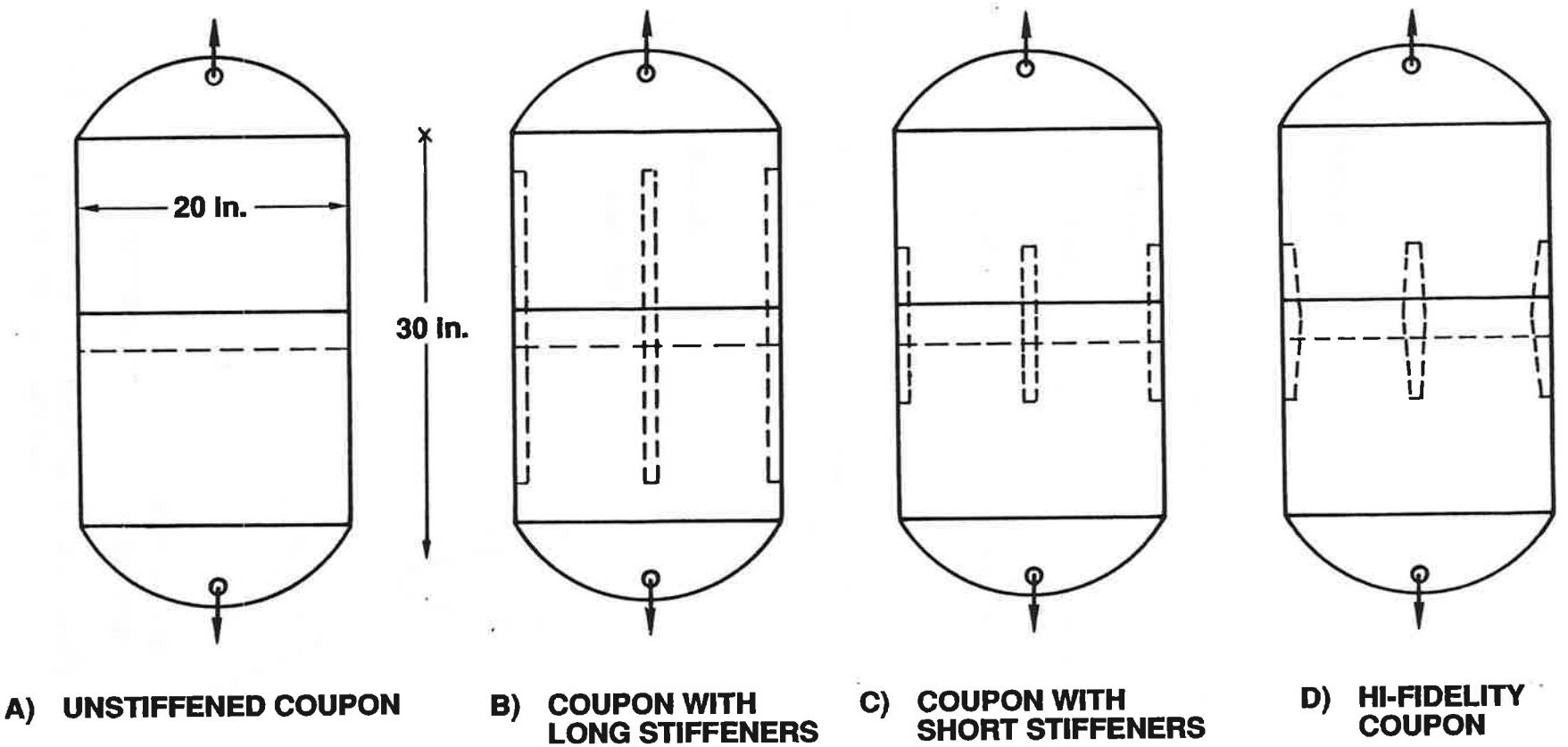

Figure 8-5. Coupon Configuration

Table 8-2. Coupon Details

Coupon Designation	Size (in.)	Stiffener Length (in.)	Stiffener Area ($in.^2$)
A. Unstiffened	20 x 30	-	-
B. With long stiffeners	20 x 30	18	0.2 (uniform)
C. With short stiffeners	20 x 30	10	0.2 (uniform)
D. High-fidelity	20 x 30	10	Central: 0.2 at end 0.36 at center Edge: 0.12 at end

In the foregoing analysis, no details of the lap joints (rivet and hole sizes and spacings) have been considered. Although such details can be incorporated, it is not recommended here. This will preserve the simplicity of the equivalent coupon approach. Experimental studies on fatigue initiation, crack growth and MSD link-up in the lap joint can be performed using the coupons. Parametric variations of material, thickness, type of rivets, hole spacing, interference fit, etc., can be simulated within the overall coupon configuration.

8.2 Lap Joint Analysis

A 3D FE model has been developed using the NISA software to determine the load distribution in the three rows of rivets and to evaluate bending and membrane stress distribution in the skin area surrounding the lap joint. The sensitivity of rivet loads and skin stress distribution to the rivet stiffness will also be studied using the FE model.

Assumptions in the model are:

- Rivet stiffness is assumed to be linear. Two values of rivet stiffness in shear are used. The first case assumes a value of 0.15×10^6 lb/in. as per Swift's formula. In the second case, the stiffness is reduced by 50 percent.

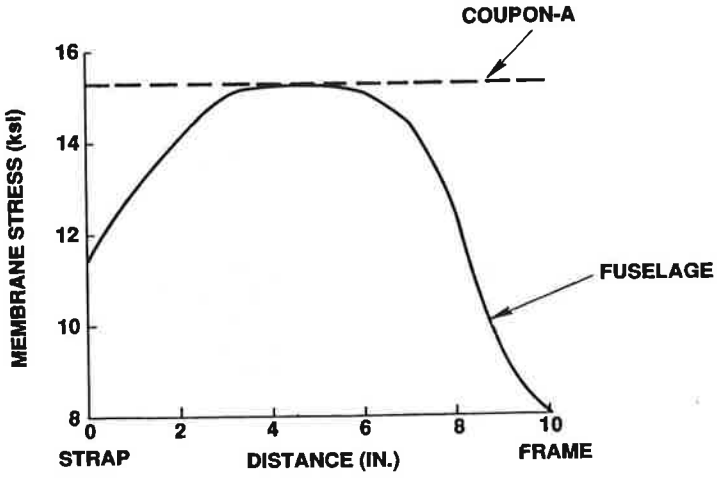

Figure 8-6a. Comparison of Stress Distribution in the Fuselage and Unstiffened Coupon

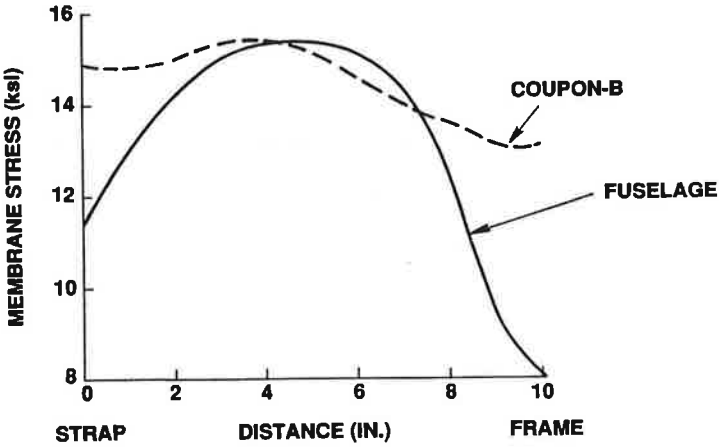

Figure 8-6b. Comparison of Stress Distribution in the Fuselage and Coupon with Staff Stiffeners

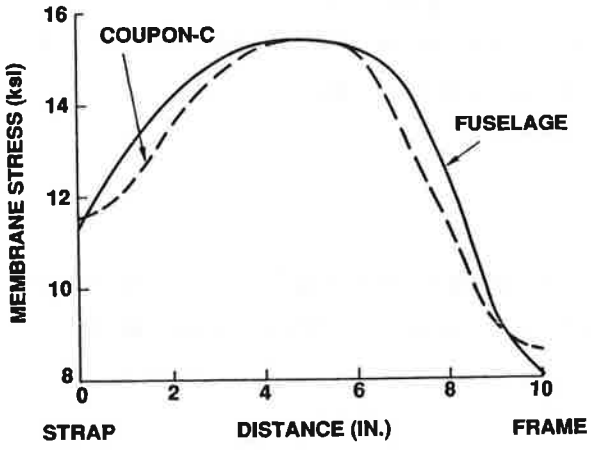

Figure 8-6c. Comparison of Stress Distribution in the Fuselage and Coupon with Short Stiffeners

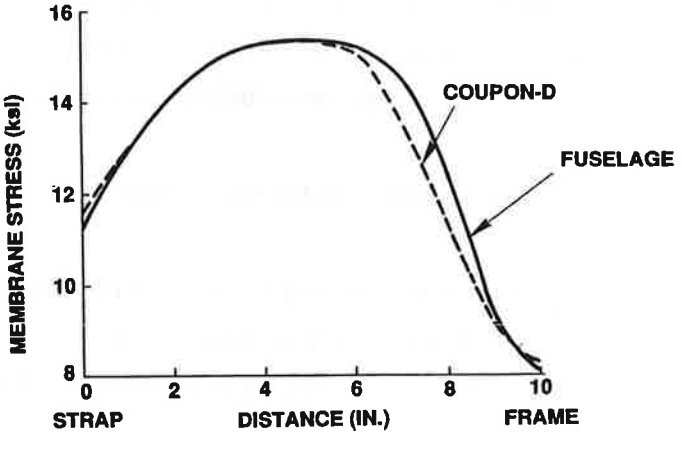

Figure 8-6d. Comparison of Stress Distribution in the Fuselage and High-Fidelity Coupon

- The structure modeled is a generic fuselage section. This has tear straps on 10-in. spacing and frames at 20-in. intervals. The frames are connected to stringers only by shear clips which are assumed to be rigid links.

- In the lap joint, the skins are considered to be in an unbonded state at all three rivet rows (see Figure 8-7). The tear strap is completely bonded to the skin. The model maintains continuity of displacement between these two members at their interface. The assumption of complete disbond between the skins is conservative. Partial disbond down to the first rivet row from the free edge of the inside skin (top row in Figure 8-7) can be a realistic situation. The rivet loads at the critical top row (Figure 8-7) in such a partial disbond case may not differ greatly from the complete disbond case studied here.

Taking advantage of symmetry, we have modeled the portion of fuselage between a frame and an adjacent strap. In the circumferential direction, three stringer bays (one bay on each side of the lap joint and half bay each of the farther side of the outside stringers) are considered. Symmetric boundary conditions are prescribed at the longitudinal edges of the model (see Figure 8-8): zero slope, zero in-plane shear, zero transverse shear, zero tangential displacement.

Results and Discussion

Case 1 - Rivet Flexibility = 6.6 μin./lb

Rivet Loads

Figure 8-9 presents the rivet loads which peak at the strap and the frame locations. The top row has the largest loads. In the central location between the strap and the frame, the top row values are about 25 percent higher than the middle row and about 16 percent higher than the bottom row. This could partially explain why the top row is generally the most fatigue prone.

Ligament Stress

The top row rivet load of 215 lb in the central region produces a net section stress of about 17.5 Ksi in the uncracked central ligament. If there are cracks of 0.26 in. in the skin, emanating

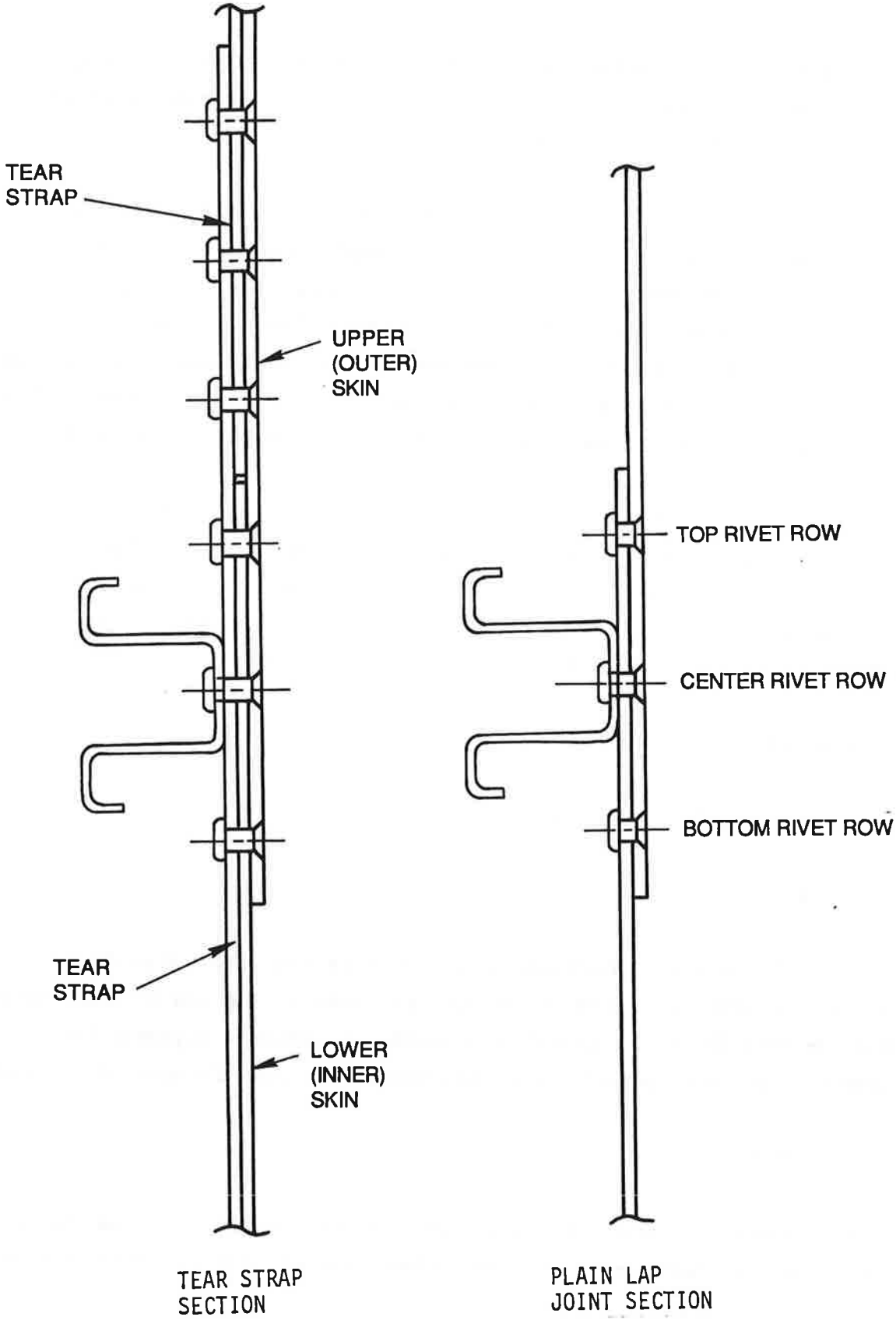

Figure 8-7. Lap Joint

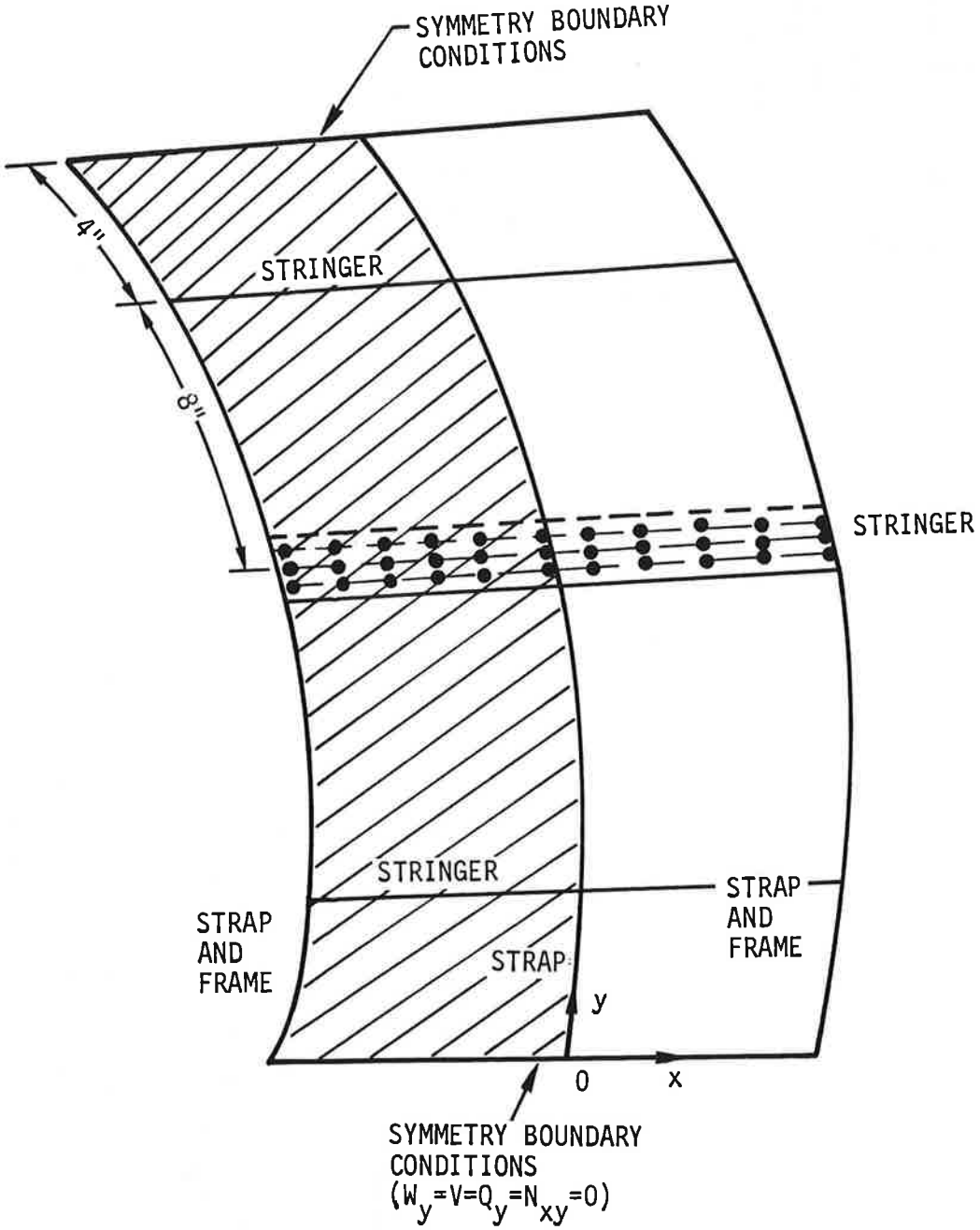

Figure 8-8. Fuselage Portion Modeled on NISA FE (Shaded Area)

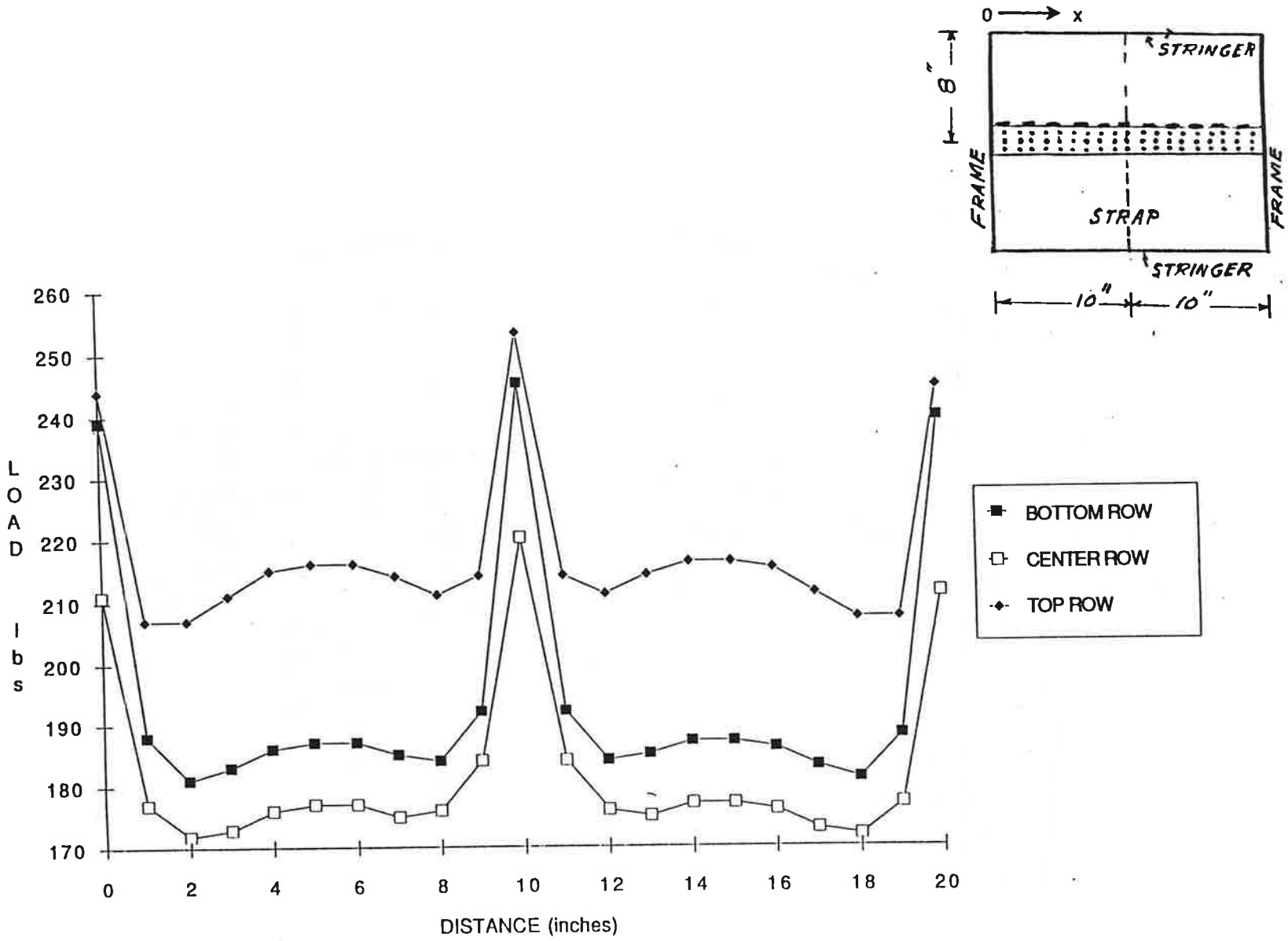

Figure 8-9. Rivet Load Distribution

from the rivet holes, this stress reaches 50 Ksi. According to R-curve test data, the ligament will be in the state of incipient fracture. Verification of this conclusion by a rigorous elasto-plastic analysis of the cracked shell may be desirable.

Skin Stress

The bending and membrane stresses 4 in. from the lap joint in the longitudinal direction is shown in Figure 8-10. The membrane stress is about 15 Ksi. This stress value is of the same order as previously obtained for the case when there is no lap joint. The bending stress, however, has increased to about 7 Ksi from the previous value of about 5 Ksi (without lap joint).

The stress distribution on the inner skin in the circumferential direction is shown in Figure 8-11. Substantial bending stress in the skin is present at the stringer location. The stresses form a complex pattern in the lap joint hole area. They are not shown here since details at holes are not modeled in the present FE analysis.

Case 2 - Rivet Flexibility = 13.2 μin./lb

Figure 8-12 shows the rivet load distribution. The rivet loads in the top row are reduced by about 8 percent and those in the second row increased by about the same percentage, when compared with the results for stiffer rivets.

The skin stress distributions are shown in Figures 8-13 and 8-14. These do not differ significantly from the values shown in Figures 8-10 and 8-11 for stiffer rivets.

8.3 Analysis of MSD Link-up in Lap Joints

A lap joint FE model using plate elements has attempted to analyze the link-up of MSD in an aircraft fuselage. The model simulates the following:

- Two elasto-plastic aluminum plates with an overlap
- Three rows of elasto-plastic rivets
- Cracks of given lengths within one rivet row
- Combined geometric and material nonlinearity
- Load stepping optimized to study the plastic front growth
- Various material behavior idealization.

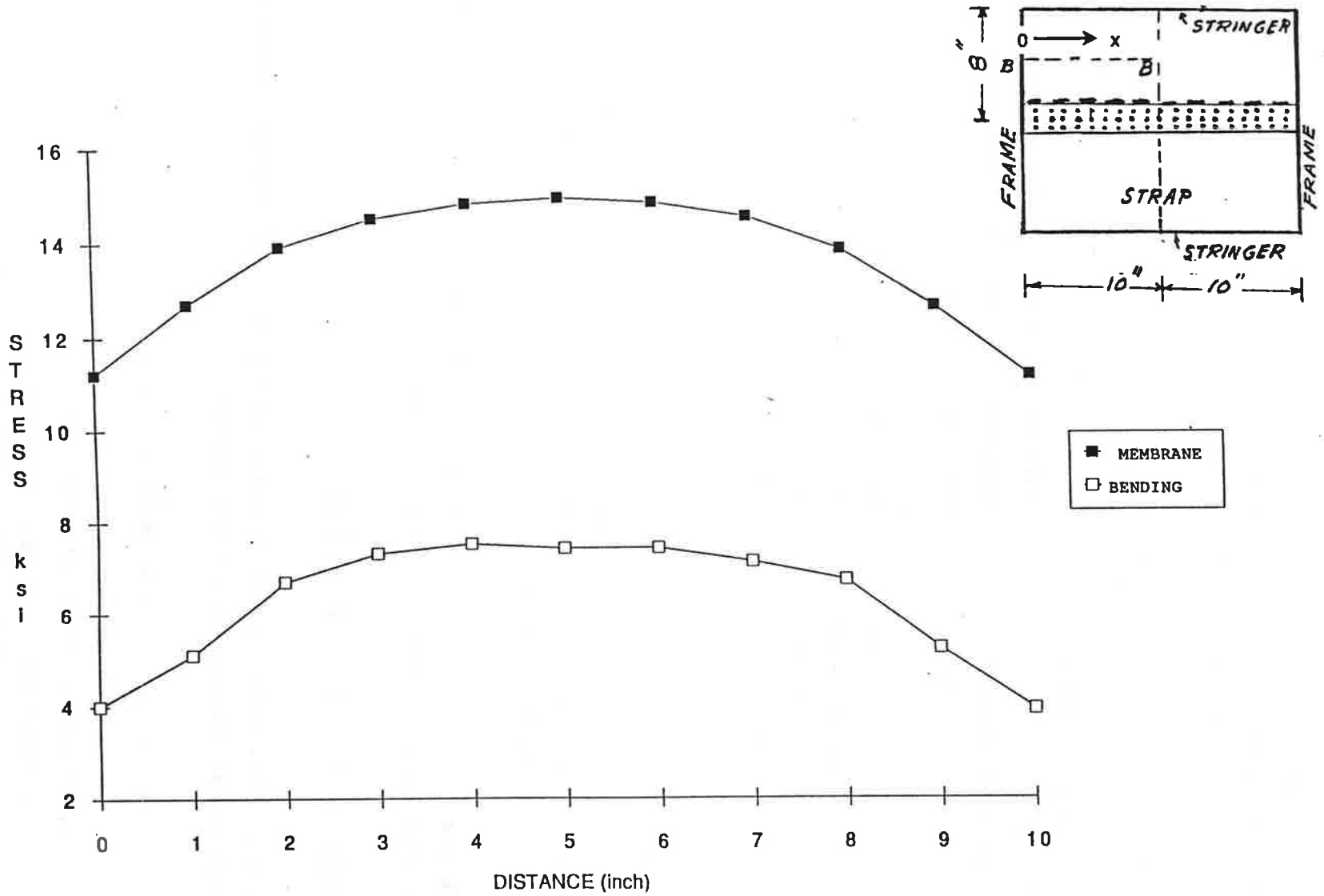

Figure 8-10. Skin Stress Distribution

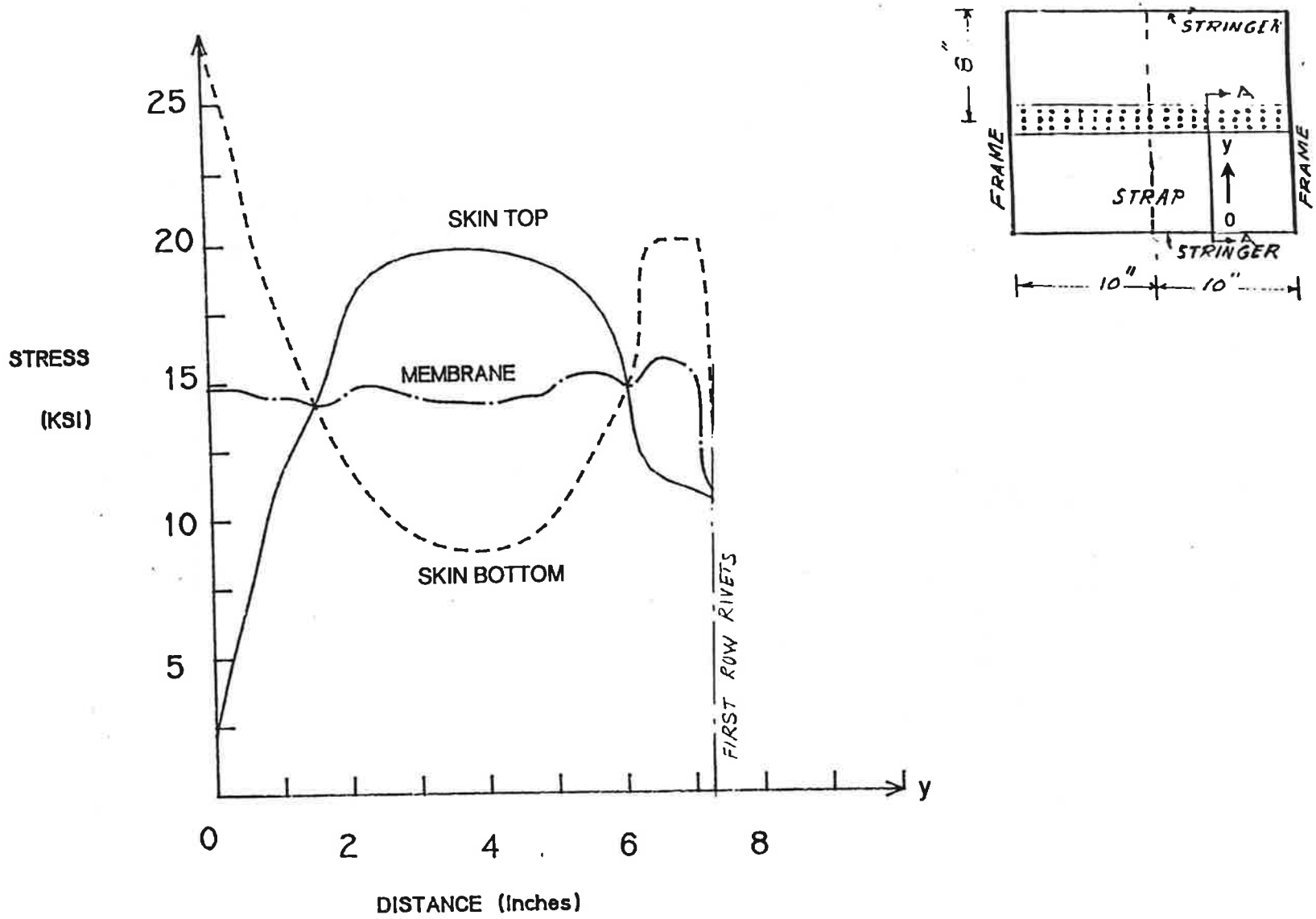

Figure 8-11. Stress Distribution in Circumferential Direction

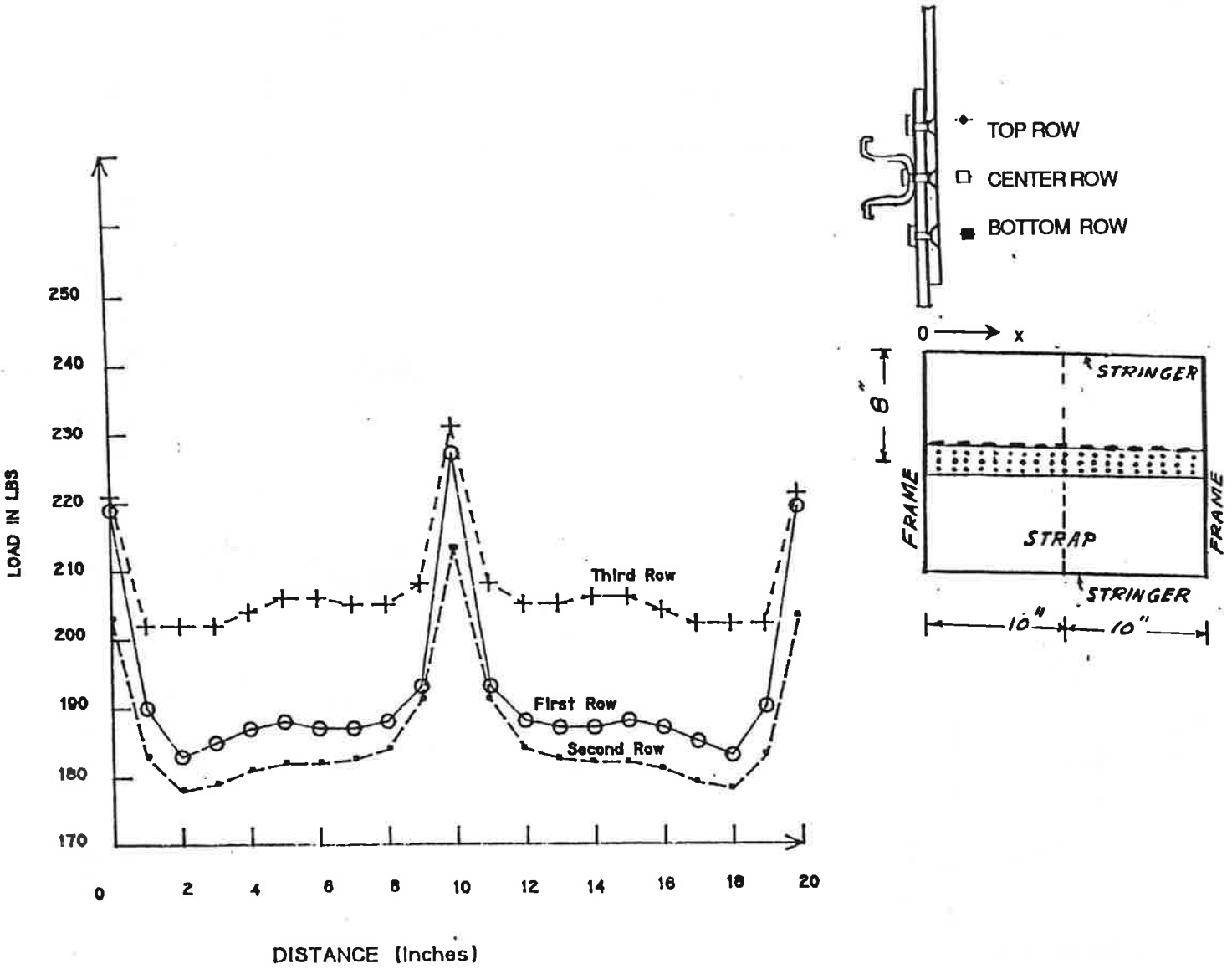

Figure 8-12. Rivet Load Distribution Reduced Rivet Stiffness

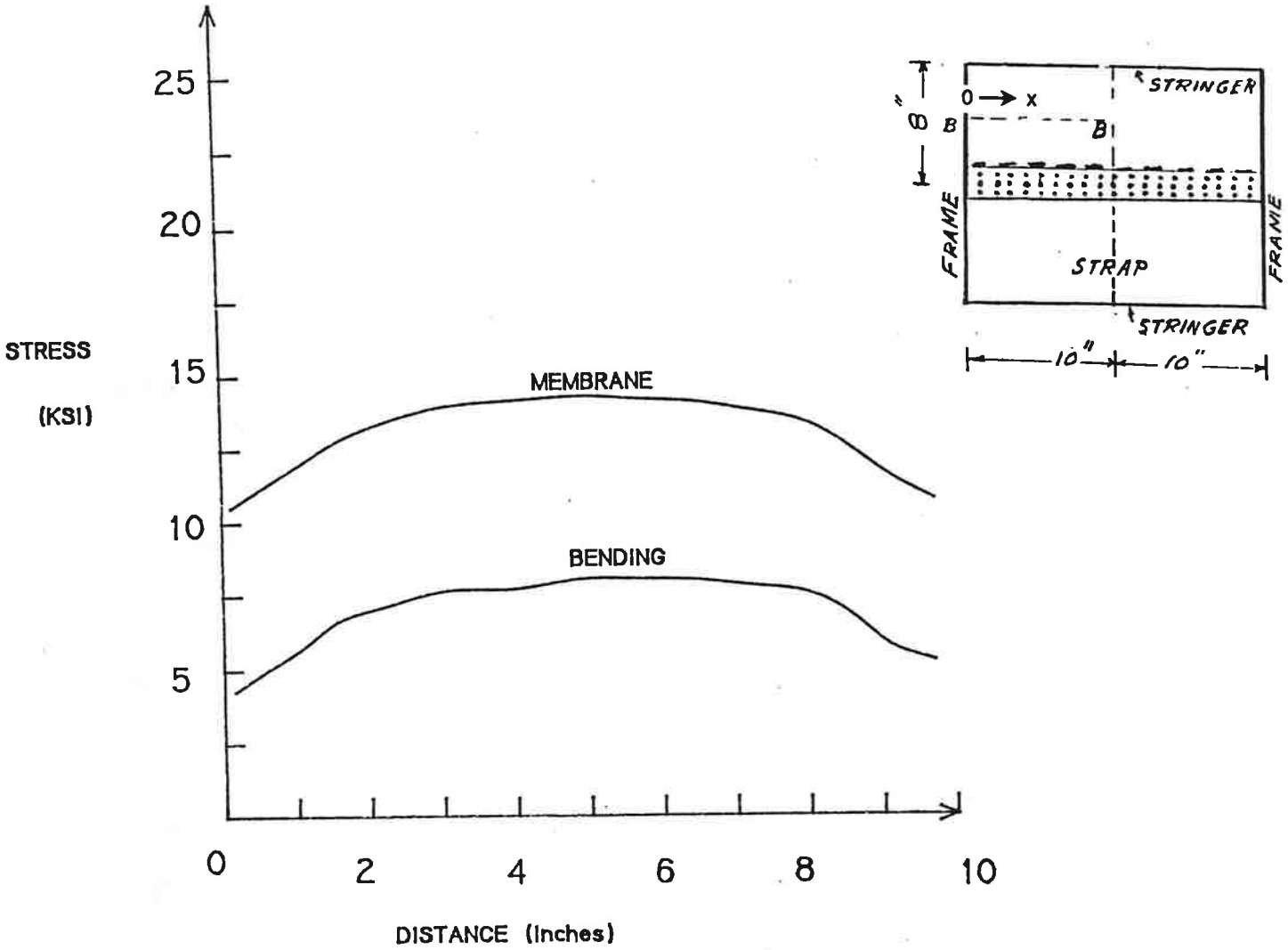

Figure 8-13. Circumferential Stress Distribution along B-B with Reduced Rivet Stiffness

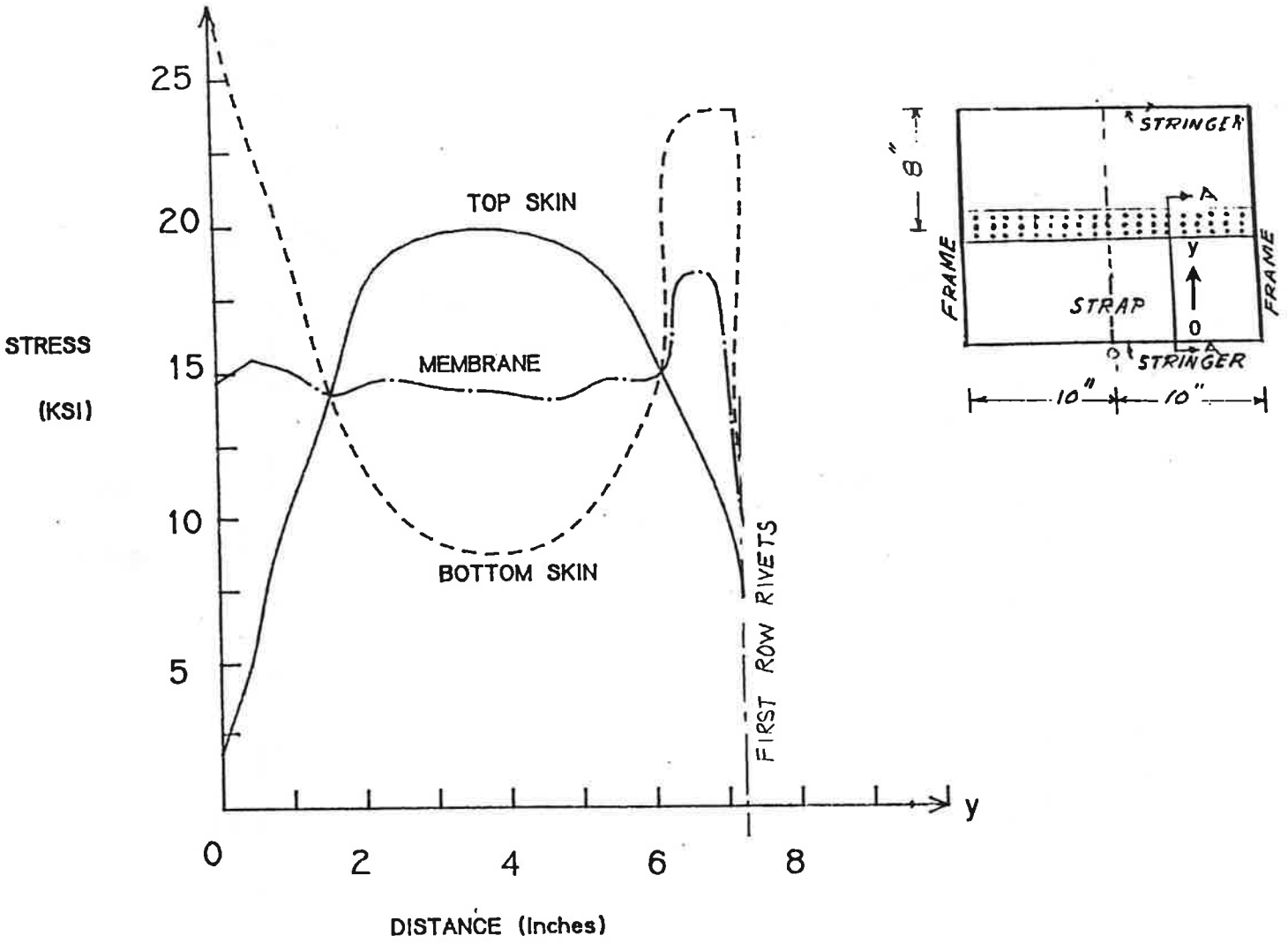

Figure 8-14. Stress Distribution in Circumferential Direction with Reduced Rivet Stiffness

Figure 8-15 shows the geometry of the model (shown with lap joint separated). The denser mesh zone represents the lap joint region. The model consists of 1833 elements with 11,100 degrees-of-freedom. Clearly, the size of the problem can be reduced to one-tenth by taking advantage of symmetry in the case of equal MSD.

The stress distribution around the crack tips is very sensitive to the elasto-plastic properties of the rivets connecting the two plates. The convergence of the model is sensitive to the load step increments. The interaction of two elasto-plastic materials has required trial and error load stepping to get convergence of the problem within six to ten iterations. Convergence criterion is based on displacement energy and nodal forces being within stipulated limits.

The one-tenth model has permitted study of the problem using various stress-strain curves, elastic-perfectly plastic, Ramberg-Osgood and elastic piecewise linear hardening. The stress-strain data for representation of the plate material with Ramberg-Osgood formulation and representation of the rivet material with elastic piecewise linear hardening formulation have given meaningful plastic zone growth that results in crack front linkup.

Figures 8-16 through 8-19 show the stress contours from the initiation to the complete plastic failure of the ligament between the crack tips. Figure 8-20 shows the plot of ligament stresses as a function of percentage of applied pressure required to completely fail plates with no cracks. The crack tip stresses are denoted by circles. The crack tips reach plastic stresses within 30 percent of the failure pressure and the stresses are relieved as the plastic front grows. The triangles denote a location of 0.05 in. from the crack tip and the squares relate to a location 0.2 in. from the crack tip.

General Case of Unequal MSD

The general case of the lap joint with unequal crack lengths can be handled in the above manner up to the first ligament failure, but determination of the load redistribution for subsequent analysis poses a difficult problem. NISA does not have the restart capability and other available commercial codes suffer from this deficiency, too. Therefore, further activity in this area has been suspended. Experimental and/or semianalytical approaches may provide alternative solutions to the problem.

```
TOTAL NUMBER OF ELEMENTS ..............= 1833
TOTAL NUMBER OF NODES    ..............= 7575
TOTAL NUMBER OF ACTIVE NODES ..........= 5775
LARGEST NODE NUMBER      ..............= 8737
```

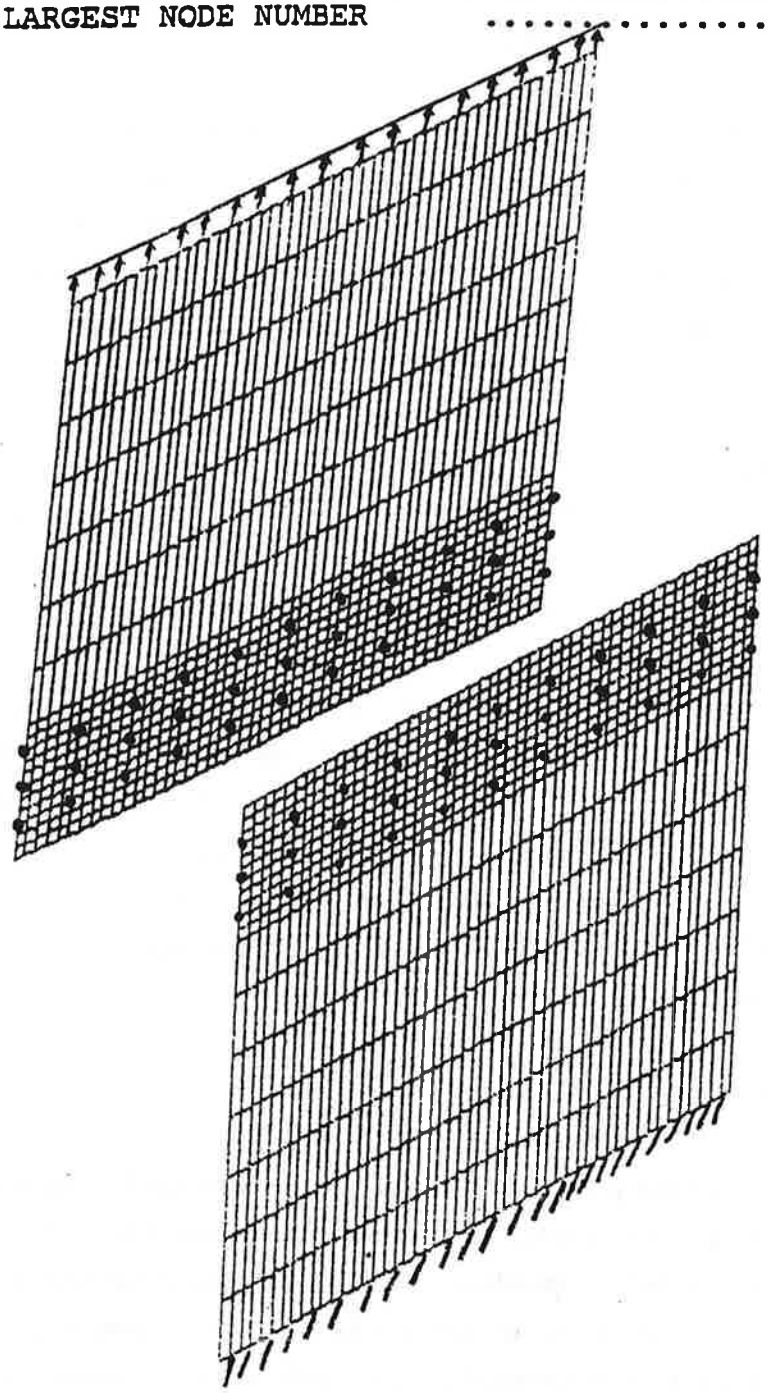

Figure 8-15. Lap Joint Plate Model (Shown Separated)

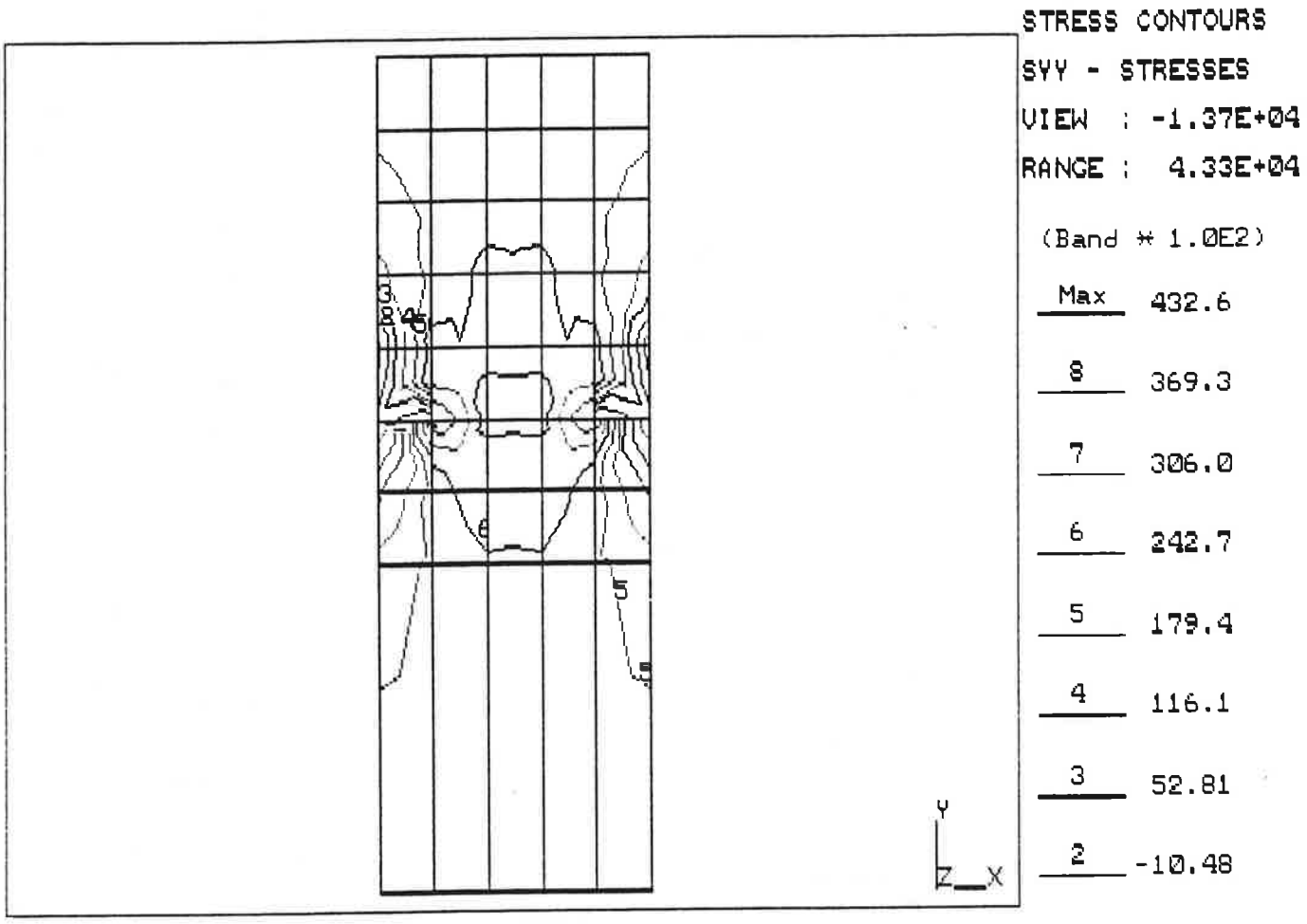

Figure 8-16. Stress Contours at 40 percent of Plate Yielding Load

8.4 Fracture Strength Analysis

The purpose of this study is to evaluate theoretically the fuselage fracture strength in the presence of a single long crack and/or MSD. A review of the published literature has been carried out with the objective of finding an accurate and economic solution to the problem.

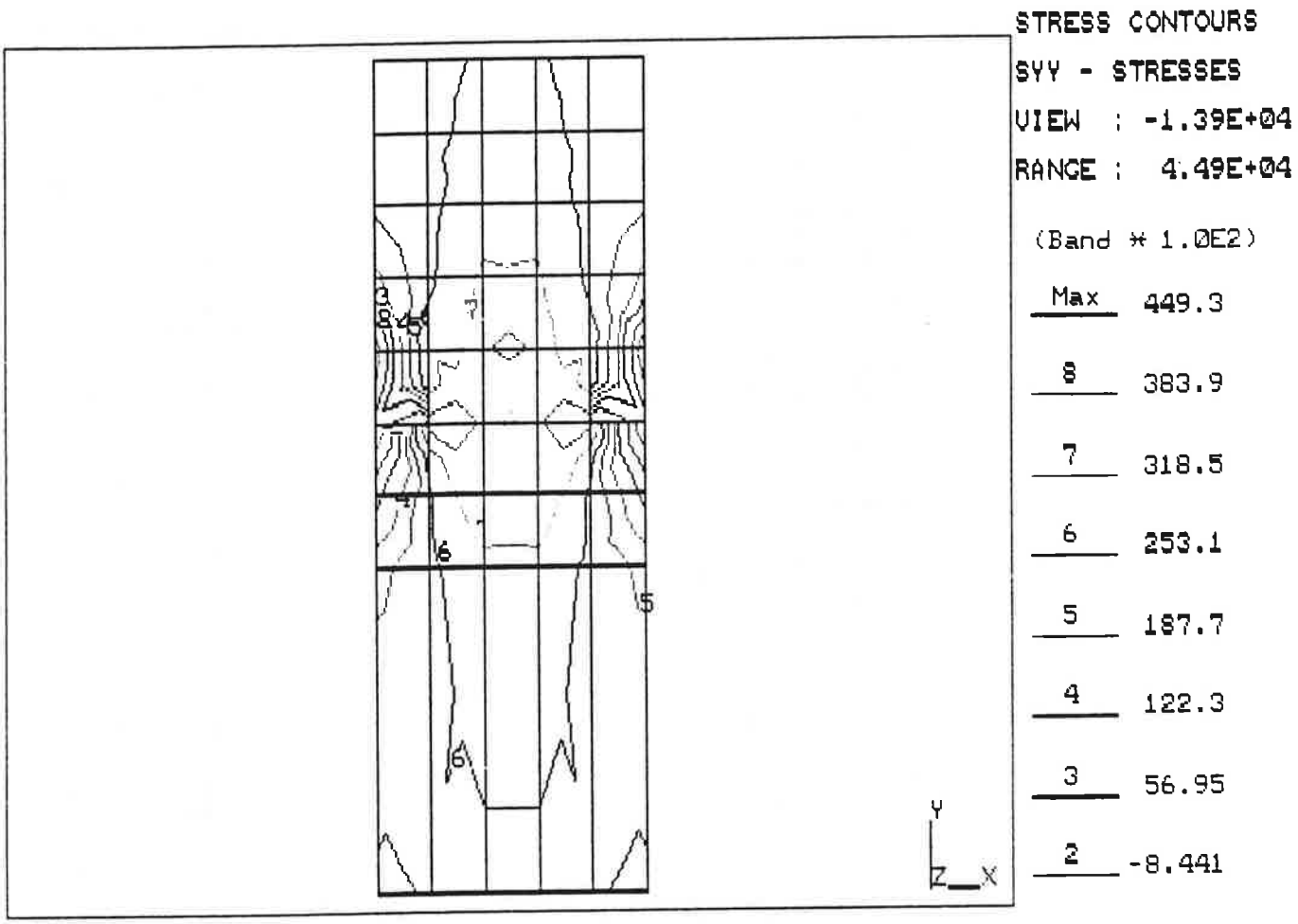

Figure 8-17. Stress Contours at 50 percent of Plate Yielding Load

Literature Review

Vlieger (7) presented an analytical solution for stiffened flat plates, which includes stiffener bending, nonlinear connections and broken stiffeners, but not effects of curvature and MSD. Significant effort will be required to modify his model for curved fuselage panels.

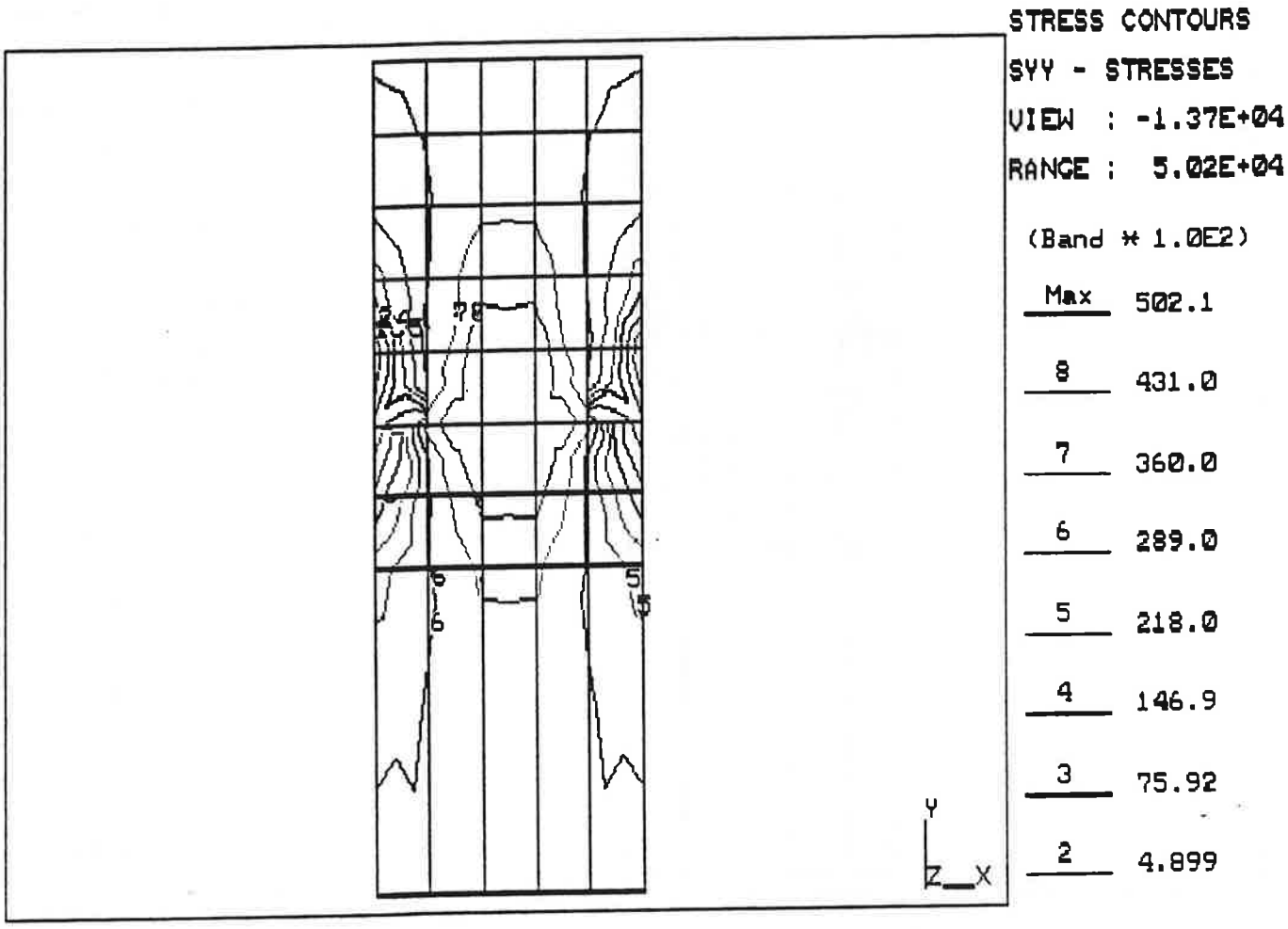

Figure 8-18. Stress Contours at 60 percent of Plate Yielding Load

Swift's work (1) on flat panels is well known and based on the Matrix Force Method. The panels are divided into discrete bars and shear panels. The stiffeners are represented by additional lumped bars connected to the main panel by a series of continuous shear panels. The crack is simulated by successive disconnection of the reactions of the skin. He also discussed the use of the displacement compatibility method for damage tolerance analysis of flat stiffened panels. This method is economical due to the relatively small number of degrees of freedom. Due to the importance of curvature and MSD, a more rigorous shell model seems to be desirable.

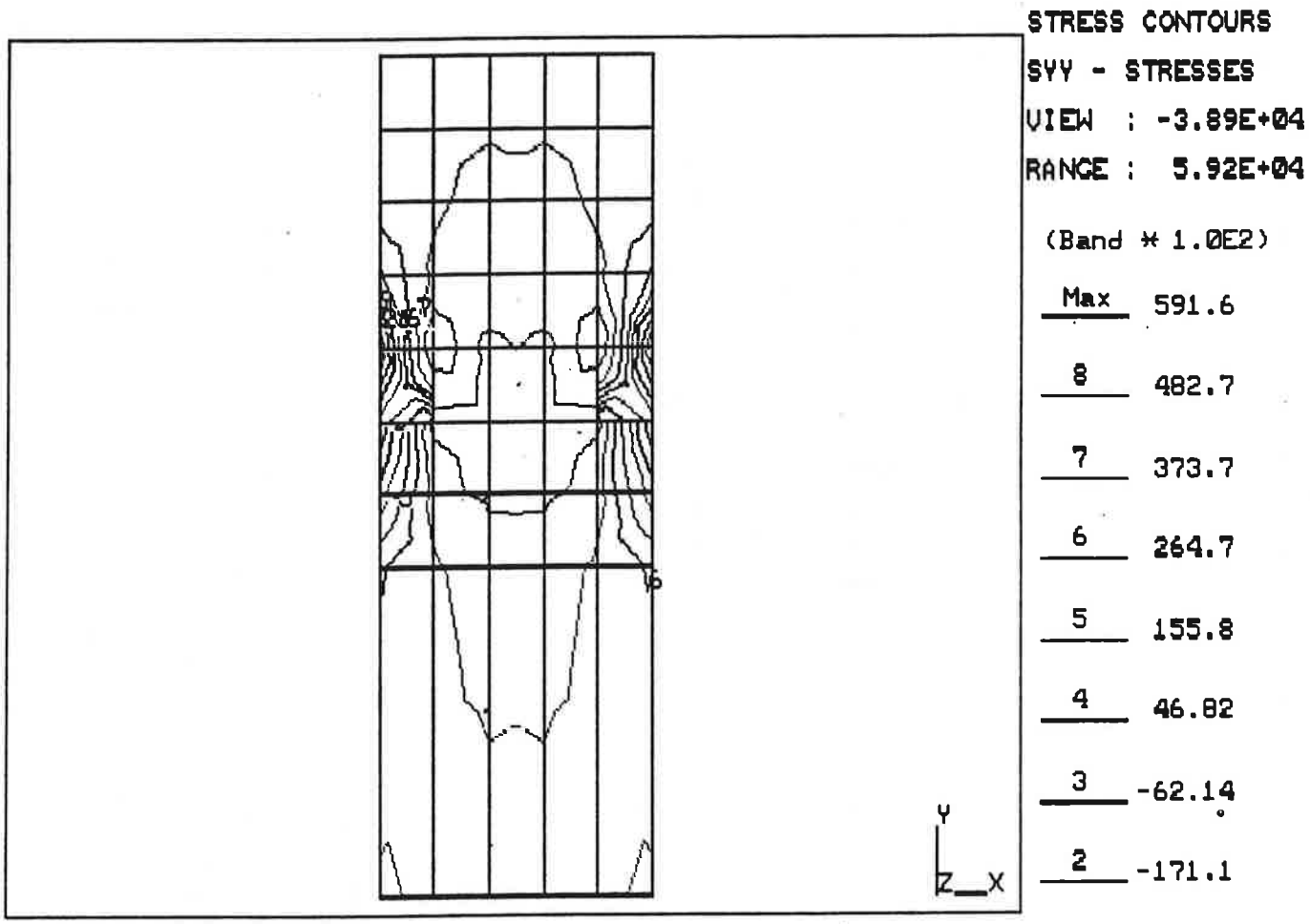

Figure 8-19. Stress Contours at 73 percent of Plate Yielding Load

Shah (8), et al. used a direct FE approach for stiffened panels with partially cracked stiffeners. Techniques with singular elements are better than the direct approach and more economical for flat panels since the crack tip stress field is accurately represented. Alternately, hybrid FE methods such as the one developed by Tong (9) can also provide a powerful tool for the problem.

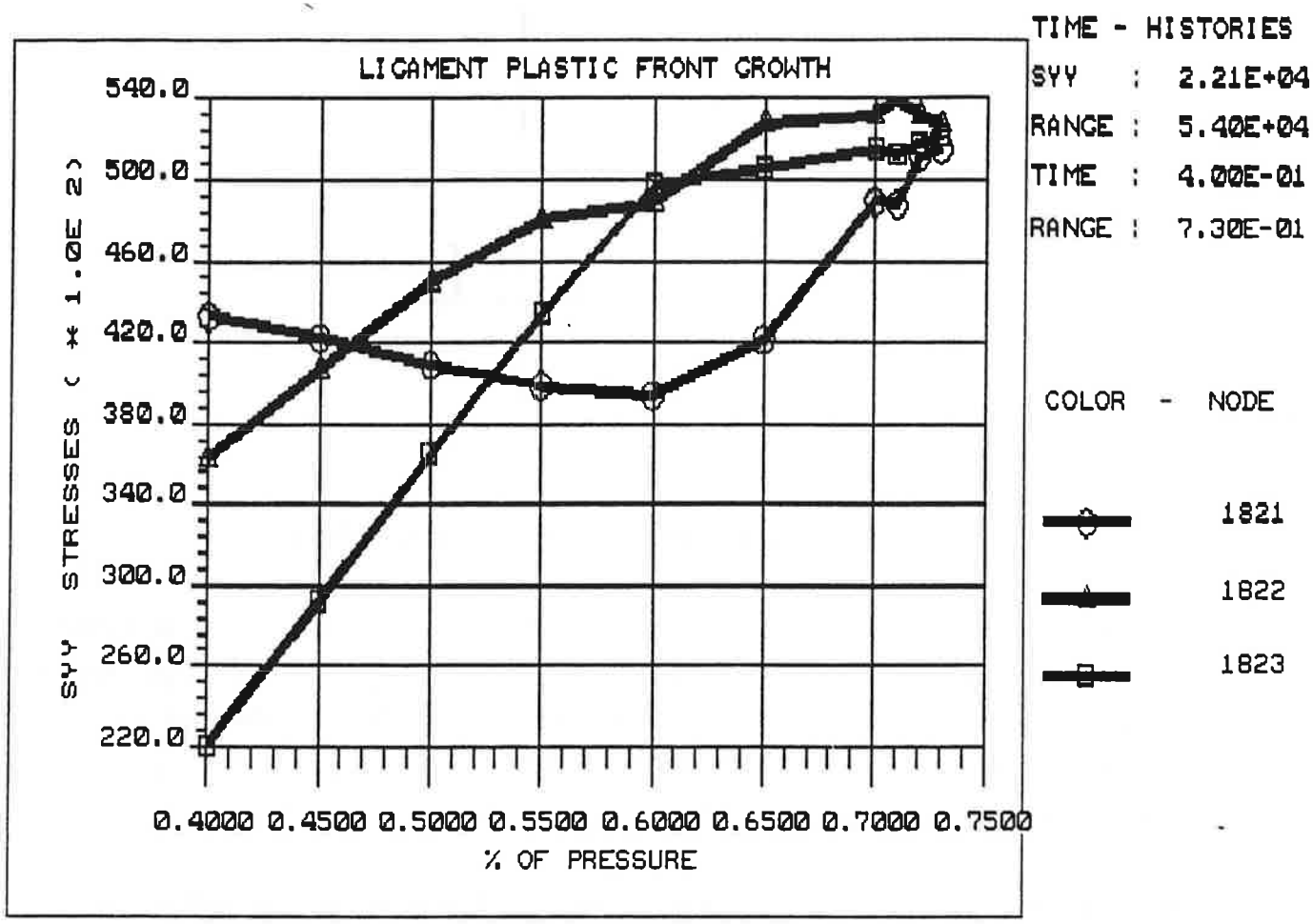

Figure 8-20. Stress Variations near Crack Tip in the Ligaments as a Function of Applied Loading

FE with Singular Elements

Commercial FE codes such as ABAQUS, NASTRAN and NISA can be used effectively for damage tolerance analysis if the crack tip singularity is simulated using a quarter-point or other element (Figure 8-21). Although triangular or collapsed quadrilateral elements are slightly more accurate, quadrilateral quarter-point elements may be adequate and they can be applied with ease in the commercial codes.

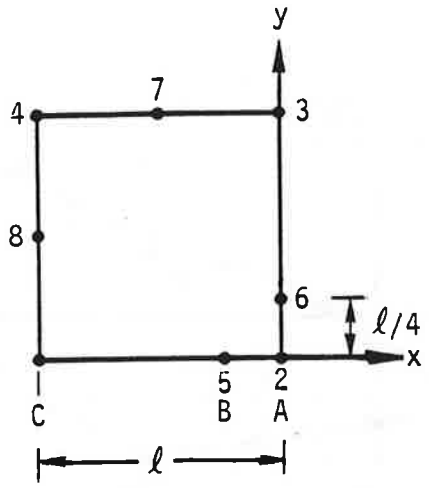

Figure 8-21. Quarter-Point Noded Rectangular Element

The following methods are available in some advanced codes for indirect SIF calculation: displacement extrapolation; J-integral, i.e., Griffith's energy, $G = (\pi_2 - \pi_1)/(\ell c_2 - \ell c_1)$, where π is the potential energy. ABAQUS determines J-integral explicitly; hence, only one FE run is required for SIF calculation while NISA and NASTRAN determine potential energy, π, explicitly, requiring two runs for SIF calculation.

Accuracy of quarter-point elements with respect to SIF calculation is demonstrated in Table 8-3 for a centrally cracked plate under remote uniform tension. Similar results have been obtained for single edge and double edge cracks, employing a uniform and fairly coarse mesh (Figure 8-22).

Selection of FE Code

NISA 386 code has all the desired features including elasto-plastic and geometric nonlinear capabilities and is available on a PC. Foster-Miller, therefore, has selected this software for the fuselage fracture strength evaluation. The structural members are modeled as in subsection 8.1, with the inclusion of singular elements at the crack tip and geometrically nonlinear analysis.

Table 8-3. Percent Differences of Calculated SIF for a Central Crack under Uniaxial Tension

Method	Number of Elements	Regular (%)	Quarter-Point (%)
Displacement extrapolation	100 (10 x 10)	5.4	-1.8
Displacement equation	100 (10 x 10)	-	4.5
J-integral	100 (10 x 10)	2.2	0.37
Stiffness derivative	100 (10 x 10)	2.0	0.21
G (eight-nodal points)	49 (7 x 7)	2.4	0.37
G (eight-nodal points)	121 (11 x 11)	1.6	0.37
G (four-nodal points)	49 (7 x 7)	6.3	-
G (four-nodal points)	121 (11 x 11)	4.1	-

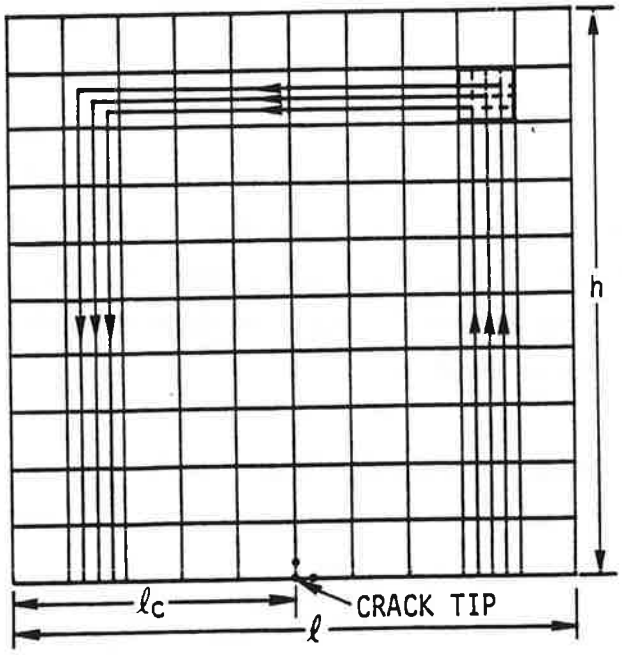

Figure 8-22. Uniform FE Mesh for Centrally Cracked Panel

Nonlinear Analysis

In the crack region, due to internal pressure of the fuselage, significant out-of-plane (radial) deformation occurs. This deflection is many times larger than the skin thickness and influences the extensional strains. Consequently, a large deflection analysis based on geometric nonlinearity is required. However, material nonlinearity, although appropriate for aircraft materials, will be ignored due to the difficulty in the definition of SIF. Following earlier workers, we define the critical SIF, K_c, as

$$K_c = \sigma_h \sqrt{\pi a}\ C$$

where

σ_h = hoop stress
a = half crack length

C is a combined factor of stretching, S, and bending, B. The latter are defined as:

$$K_S = \sigma_h \sqrt{\pi a}\ S$$

$$K_B = \sigma_h \sqrt{\pi a}\ B$$

The definition of $C = S^2 + B^2/3$ as given by Erdogan (10) will be used here. This and similar definitions by others are all empirical. However, the value of C is not greatly different from S, the familiar SIF, since the value of B is generally small. Even though B is small, the coupling between bending and stretching is important since it significantly reduces the value of the stress intensity factor due to stretching.

The method of calculating SIF is shown in Figure 8-23.

Benchmark Test Cases

A few test cases were run to determine the accuracy of the present FE modeling of the cracked cylindrical shell. The solutions have been compared with classical analytical solution of Erdogan (10) and numerical solutions of Barsoum (11) and Ansell (5). Reasonable agreement has been found in these solutions. For the split cylinder of Figure 8-24, the results of the present analysis and that of Erdogan are compared in Figure 8-25.

- Local energy approach

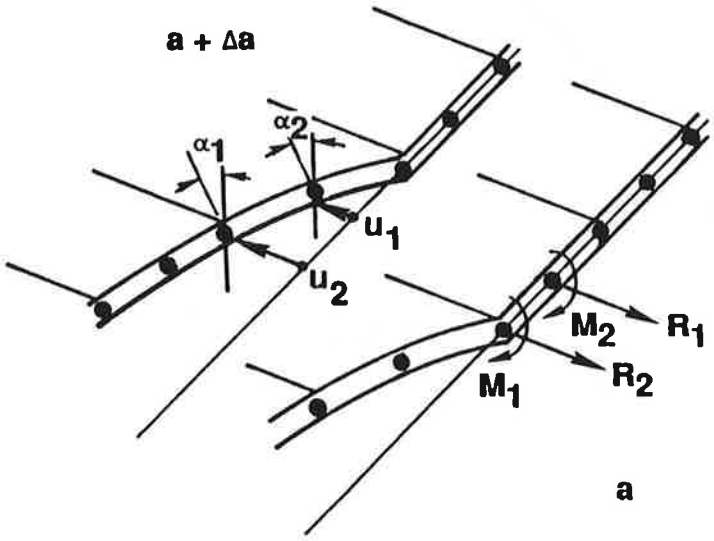

- Energy release rate,

$$G = 1/t\Delta a\ (W_{mid} + W_{side})$$

$$W = 1/2\ (R \cdot u + M \cdot \alpha)$$

- Stress intensity factor

$$K = \sqrt{EG}$$

Figure 8-23. Method for SIF Calculation

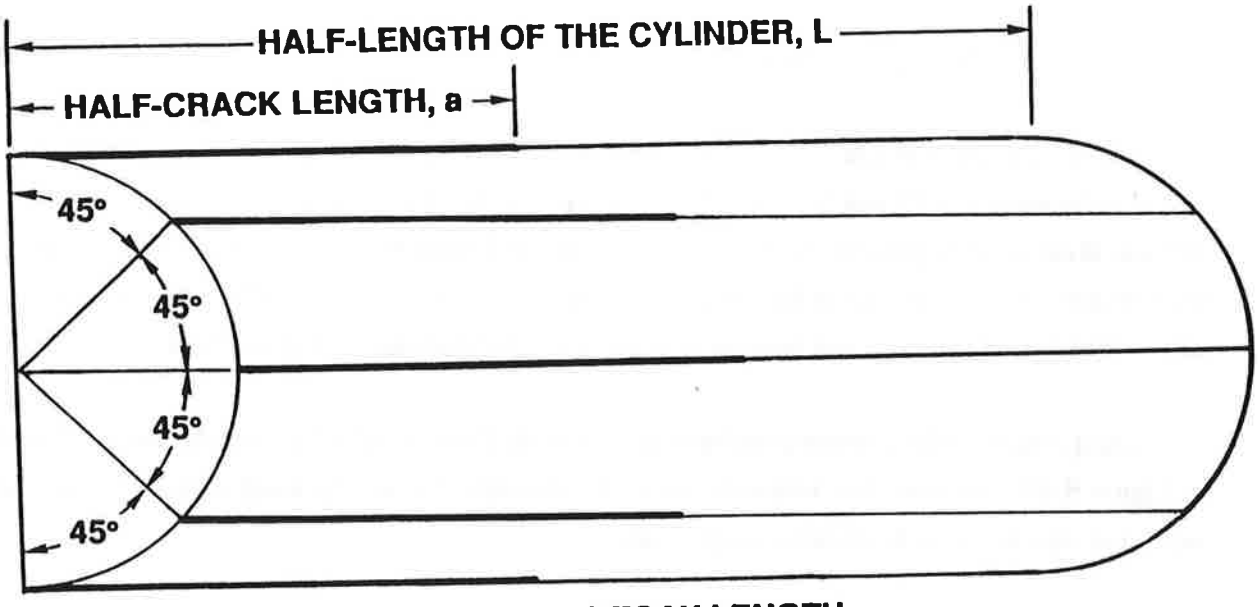

R = 72 in.
t = 0.04 in.
a_{max} = 9 in.
L = 35 in.

DECAY LENGTH

$L_c = 2.5\ \sqrt{Rt} = 4.3$

$L >> a + L_c$

Figure 8-24. Test Problem

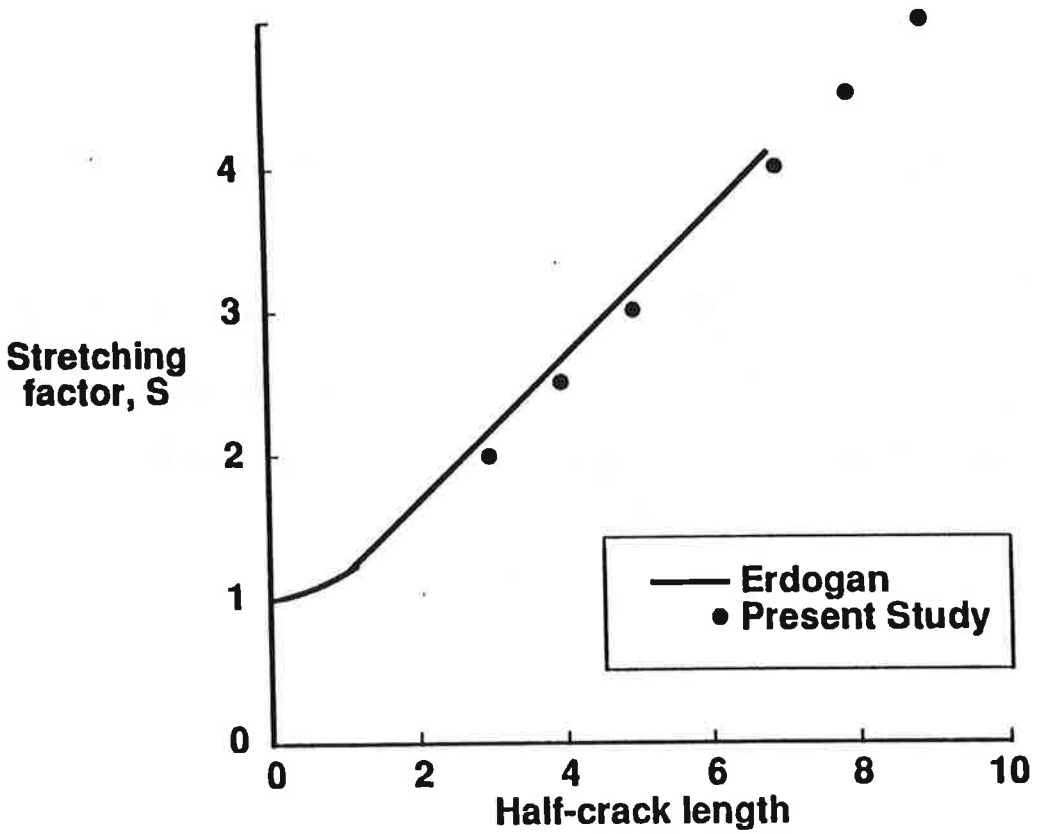

Figure 8-25. Comparison with Benchmark Solution

SIF for Cracked Aircraft Fuselage

SIF for a typical aircraft fuselage without intermediate tear straps were evaluated using the NISA software. The FE mesh is sketched in Figure 8-26. For an internal pressure of 8.6 psi, the SIF variation with respect to crack length is shown in Figure 8-27. To predict fracture pressure, the SIF must be determined at higher pressure levels, since the critical SIF value is on the order of 150 Ksi √in. (1) and has not been reached in the results shown in Figure 8-27.

Comparison of the present nonlinear results with linear results for a stiffened shell is shown in Figure 8-28. As seen, the linear theory overestimates the SIF by a significant factor and is much too conservative for practical application.

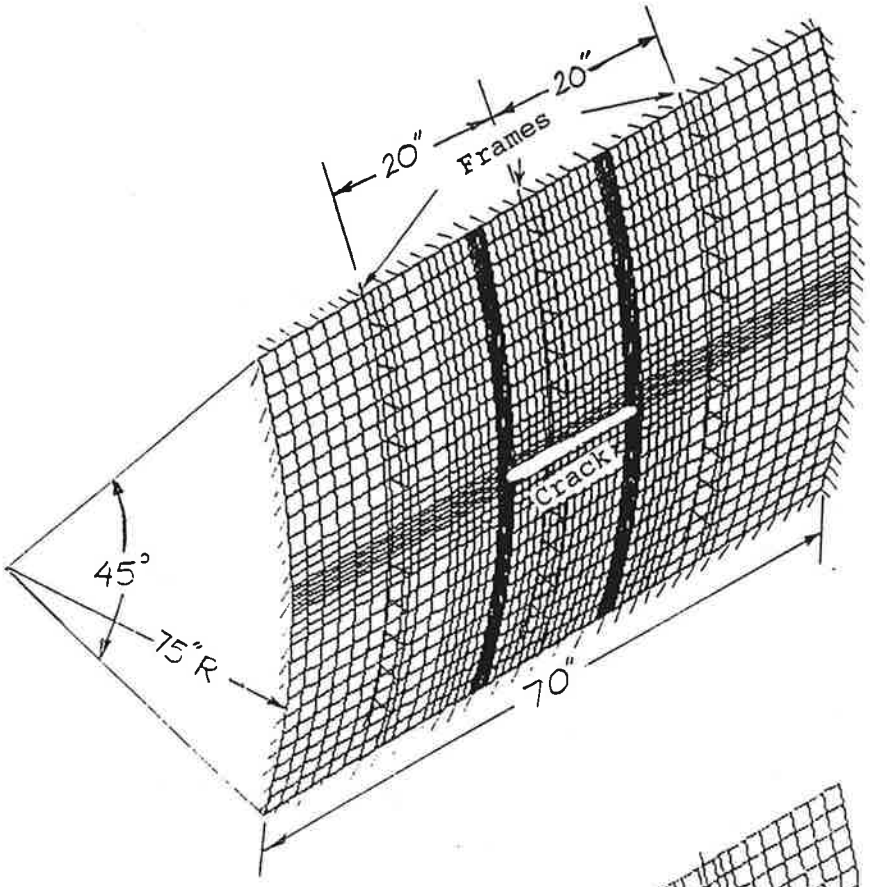

(a) STIFFENED SHELL MODEL WITH 16 INCH CRACK

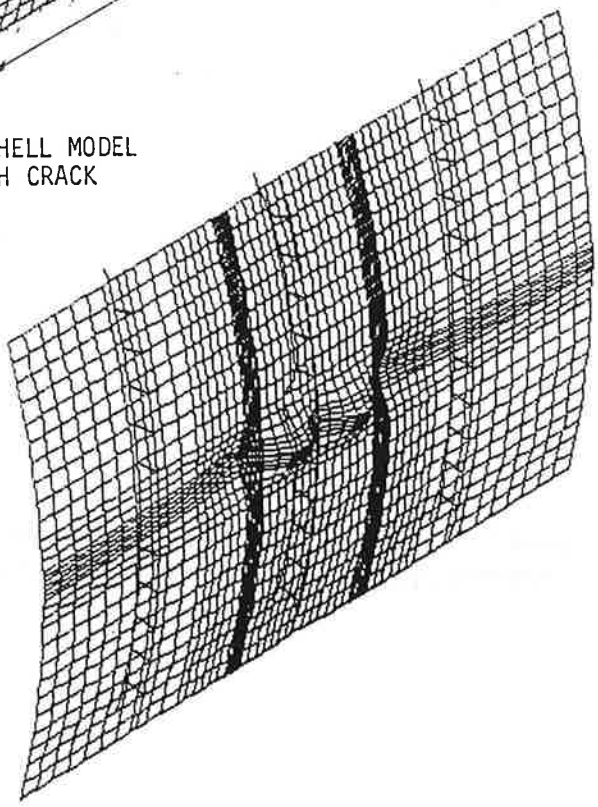

(b) BULGING DEFORMATION UNDER INTERNAL PRESSURE

Figure 8-26. FE Idealization of Cracked Fuselage

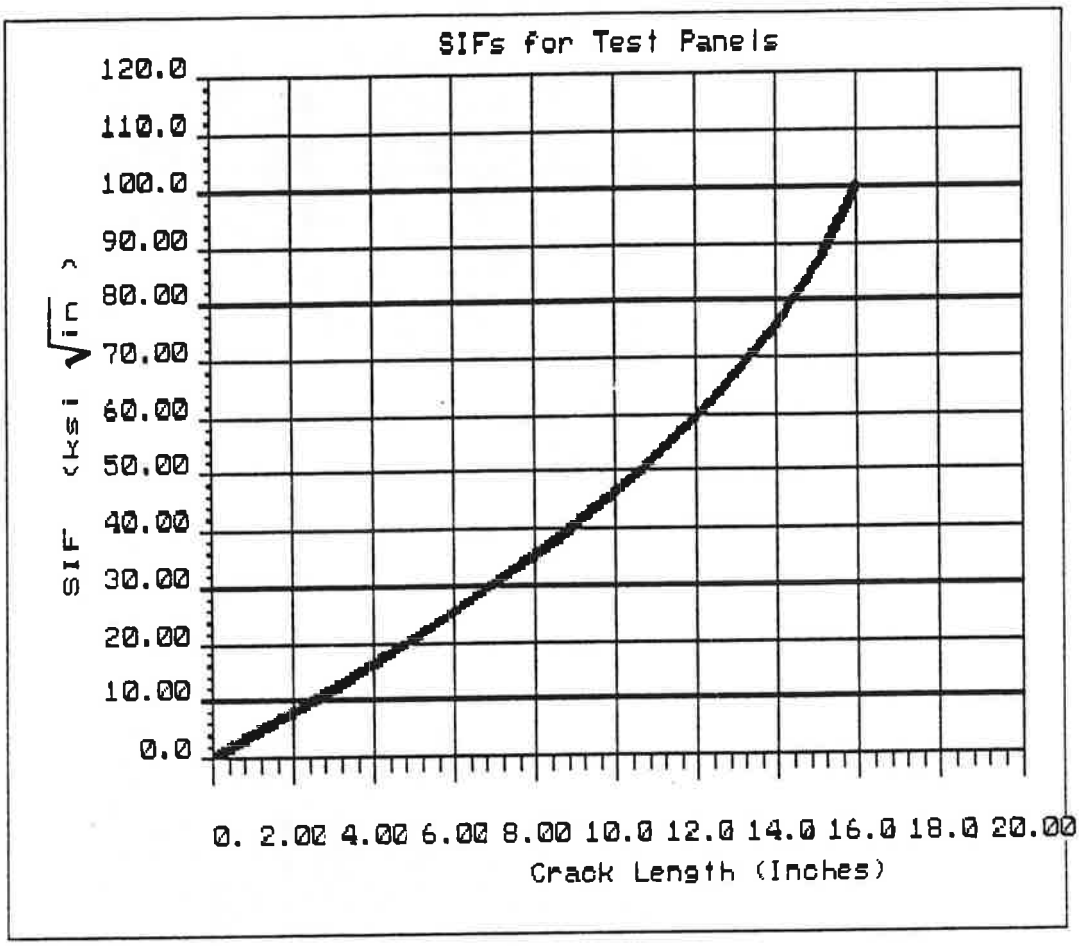

Figure 8-27. SIF for Cracks Symmetrically Situated over the Frame (Frame Spacing = 20 in., No Intermediate Straps, p = 8.6 psi)

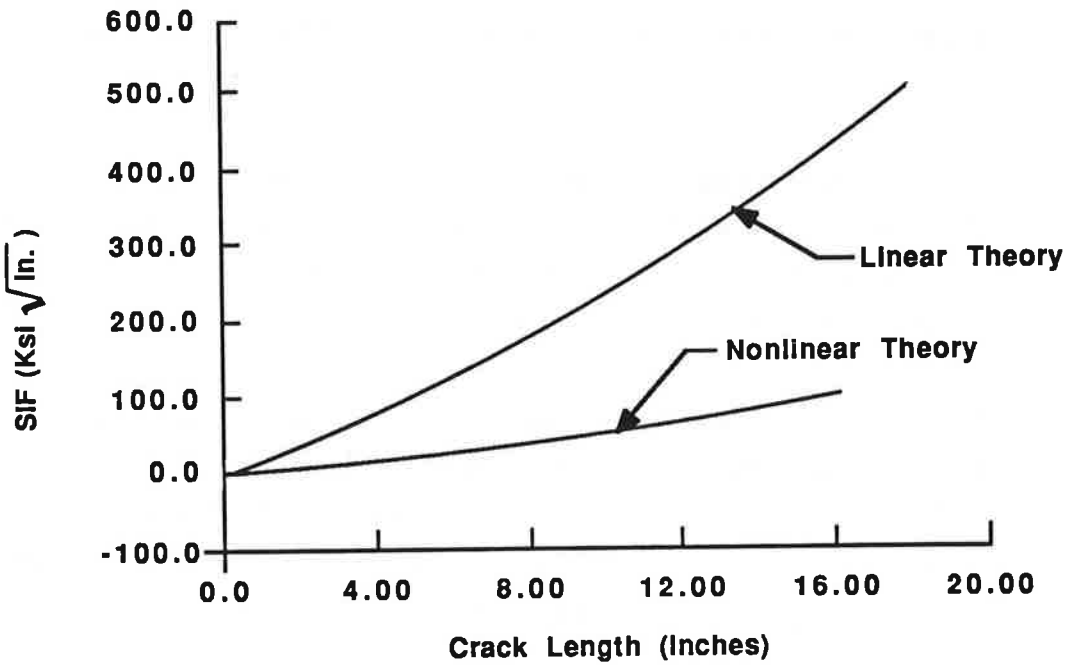

Figure 8-28. Comparison of Linear and Nonlinear Theory (Cracks Symmetric over Frame, Frame Spacing = 20 in., No Intermediate Straps, p = 8.6 psi)

9. CONCLUSIONS

- Dimensional analysis and other technical considerations have shown that subscale fuselage models are not suitable for fracture and fatigue strength evaluations. Stiffened flat panels under in-plane loads are also inadequate for test evaluation due to the absence of curvature and bulging. The testing of full-size round structures is expensive. Curved panel tests under internal pressure and longitudinal end loads seem most appropriate for the planned evaluation of MSD and other issues related to aging aircraft.

- Stiffened curved panels with about six stringer and frame bays can be economically fabricated to include salient structural details typical of any aging commercial aircraft. The test results in regard to stress distribution residual and fatigue strength are representative of the full-size aircraft fuselage.

- The shakedown, static, fatigue and fracture tests successfully demonstrated the test fixture capabilities. Fatigue testing can be carried out at the rate of about 720 cycles/hr. If the fixture is operated in two shifts (16 hr/day), 80,000 flight cycles can be simulated in a 7-day period. Maximum internal pressures of 20 psi can easily be applied to the panel for residual strength evaluation.

- A material data base, listing published properties relevant to the aircraft residual and fatigue strength, is being compiled under the contract in a separate document. Data not readily available in the open literature are being generated in the Foster-Miller laboratory.

- R-curve tests on multi-holed, thin 2024-T3 aluminum alloy specimens have shown that a net section stress of about 54 ksi is required to completely fracture a ligament with existing fatigue cracks emanating from the holes.

- Analytical models have been developed for evaluation of stress distributions in typical stiffened aircraft fuselage structures, and for determination of SIF in cracked fuselage.

- Significant bending stress exists in the skin due to the action of the stiffeners and lap splices. Generally, the extreme fiber bending stress is about one-third the membrane stress.

- The analysis shows that a stiffened flat tension coupon can be designed such that it will have a distribution of stress across its width that is similar to the hoop stress in one frame bay of the curved fuselage. Such coupons can be used in fatigue test evaluations. These coupons will not account for bulging at crack edges due to internal pressure.

- The distribution of rivet loads in the unbonded lap splice has a complex pattern. Peak rivet loads are of the order of 250 lb. The rivet stiffness variations do not seem to produce significant changes in the rivet loads at least for the case studied in this report.

- Prediction of MSD link-up using elasto-plastic FE analyses is very involved. Simple cases of equal MSD can be dealt with. The general case with unequally distributed MSD leads to convergence problems. The first ligament failure can be predicted, but subsequent load redistribution seems to be a problem in some of the existing codes, including NISA.

- The SIF, hence the fracture strength of cracked fuselage, can be numerically evaluated using quarter-point singular elements to represent the crack tip stress singularity. Geometrically nonlinear analysis is required due to large bulging deflections, several times larger than the skin thickness. Linear theory overestimates the stress intensity factor by an order of magnitude and hence grossly underestimates the facture strength.

- MSD decreases the residual strength. For these particular panel configurations with a 12.4 in. lead crack in the lap splice, the reduction is about 20 percent. The strength reduction seems to correlate with the reduced net section area in the presence of MSD.

10. REFERENCES

1. Swift, T., "The Application of Fracture Mechanics in the Development of the DC-10 Fuselage," Fracture Mechanics of Aircraft Structures, AGARD-AG-176.

2. Swift, T., "Important Considerations in Commercial Aircraft Damage Tolerance," Int. Journal of Vehicle Design, Vol. 7, Nos. 3/4, 1986.

3. Sampath, S., D. Broek, and S. Patil, "Estimation of Requirements for Inspection Intervals Associated with Multiple Site Damage Panels," International Symposium of Structural Integrity of Aging Airplanes, Atlanta, GA, March 1990.

4. Goranson, U. and M. Miller, "Boeing Aging Aircraft Programs," Int. Symposium of Structural Integrity of Aging Airplanes, Atlanta, GA, March 1990.

5. Ansell, H., "Bulging of Cracked Pressurized Aircraft Structures," Ph.D. Thesis, Dept. of Mech. Eng., Institute of Technology, Linkoping University, Sweden, 1988.

6. Huth, H., "Influence of Fastener Flexibility on the Prediction of Load Transfer and Fatigue Life for Multiple Row Joints," Fatigue in Mechanically Fastened Composite and Metallic Joints, ASTM STP927, John M. Potter, Ed., American Society for Testing and Materials, Philadelphia, 1986, pp. 221-250.

7. Vlieger, H., "Residual Strength of Cracks Stiffened Panels," AGARD Fracture Mechanics Survey (1974).

8. Shah, R.C., et al., "SIF for Stiffened Panels with Partially Cracked Stiffeners," Fracture Mechanics, 14th Symposium.

9. Tong, P., "A Hybrid Method for Damage Tolerance Analysis, Computers and Structures," 19 (1984).

10. Erdogan, F., and J.J. Kibler, "Cylindrical and Spherical Shells with Cracks," International Journal of Fracture Mechanics, Vol. 5, No. 3, September 1969, pp. 229-236.

11. Barsoum, R.S., R.W. Loomis, and B.D. Steward, "Analysis of Through-Cracks in Cylindrical Shells by the Quarter-Point Elements," International Journal of Fracture, Vol. 15, No. 3, June 1979, pp. 259-280.

12. *Damage Tolerance Design Handbook,* prepared by University of Dayton Research Institute Materials Laboratory, Air Force Wright Aeronautical Laboratories, Wright-Patterson Air Force Base, Dec., 1983.

13. Barsom, J.M., S.T. Rolfe, "Fracture and Fatigue Control in Structures," Prentice-Hall, 1987.

APPENDIX A
AGING AIRCRAFT MATERIALS PROPERTY DATA BASE

A list of data base sources is presented in Table A-1.

Tables A-2 through A-12 include material property data summaries for the major aluminum alloys used in Unites States manufactured aging aircraft.

Table A-1. Material Property Data Base Sources

Source No.	Source
1.	AGARD Conference Proceedings No. 185, Specialists Meeting on Alloy Design for Fatigue and Fracture Resistance.
2.	*Aluminum Vol. I: Properties, Physical Metallurgy and Phase Diagrams*, edited by Kent R. Van Horn, ASM.
3.	*Aluminum Vol. II: Design and Application*, edited by Kent R. Van Horn, ASM.
4.	*Aluminum and its Alloys*, Frank King, Ellis Horwood Limited.
5.	*ASM Metals Reference Book*, Second Edition, ASM, March 1984.
6.	*Damage Tolerance Design Handbook*, prepared by University of Dayton Research Institute Materials Laboratory, Air Force Wright Aeronautical Laboratories, Wright-Patterson Air Force Base, Dec., 1983.
7.	*Fatigue of Aircraft Structures*, Horace J. Grover, prepared for Research and Technology Naval Air Systems Command Department of the Navy, 1966.
8.	*Fatigue of Metals*, P.G. Forrest, Pergamon Press, 1966.
9.	*Light Alloys Metallurgy of the Light Metals*, J. Polmear, ASM.
10.	*Metallic Fatigue*, W.J. Harris, Pergamon Press, 1961.
11.	*Military Standardization Handbook, Metallic Materials and Elements for Aerospace Vehicle Structures*, MIL-HDBK-5C, Sep., 1976.
12.	*New Materials and Fatigue Resistance Aircraft Design*, editor David L. Sipson, Engineering Materials Advisory Service Limited, 1987.
13.	*Structural Fatigue in Aircraft*, ASTM Special Technical Publication No. 404, a symposium presented at the Fifth Pacific Area National Meeting, ASTM, 1965.
14.	*Symposium on Damage Tolerance in Aircraft Structures*, a symposium presented at the Seventy-third Annual Meeting, ASTM, 1970.

Table A-2. Material Property Data Summary for 2014-T6

	E (Ksi)	μ	F_{tu} (Ksi)*	F_{ty} (Ksi)*	F_{su} (Ksi)*	F_{en} (Ksi)**	K_{IC} (Ksi√in.)
Value	10.5	0.33	67,70	59,60,65	40,42	18,18	
Source No.***	11	11	11,2	11,2,3	11,2	2,3	
Stress-strain curve, Source 11, pp. 3-45 to 3-53							
Goodman diagram, Source 11, pp. 3-57 Source 7, p. 320							
Crack propagation da/dN versus ΔK, Source 6, pp. 7.1-5 to 7.1-27							

*A-basis.
**500E6 cycles, R = -1.
***Supporting data, Source 6, pp. 7.0-9, 7.0-10.

Table A-3. Material Property Data Summary for 2024-T3

	E (Ksi)	μ	F_{tu} (Ksi)*	F_{ty} (Ksi)*	F_{su} (Ksi)*	F_{en} (Ksi)**	K_{IC} (Ksi√in.)
Value	10.5	0.33	64,70	47,50,51	39,41	20,18	50
Source No.***	11	11	11,2	11,2,6	11,2	2,4	4
Stress-strain curve, Source 11, pp. 3-81 3-90, 3-91							
Goodman diagram, Source 11, pp. 3-103 to 3-107							
Crack propagation da/dN versus ΔK, Source 9, p. 79							

*A-basis.
**500E6 cycles, R = -1.
***Supporting data, Source 6, pp. 7.5-36 to 7.5-44.

Table A-4. Material Property Data Summary for 2024-T3 Alclad

	E (Ksi)	μ	F_{tu} (Ksi)*	F_{ty} (Ksi)*	F_{su} (Ksi)*	F_{en} (Ksi)**	K_{IC} (Ksi$\sqrt{in.}$)
Value	10.5	0.33	69,70	60,60,65	41,42	18,18	
Source No.***	11	11	11,2	11,2,6	11,2	2,3	
Stress-strain curve							
Goodman diagram							
Crack propagation da/dN versus ΔK, Source 6, pp. 7.6-13							

*A-basis.
**500E6 cycles, R = -1.
***Supporting data, Source 6, pp. 7.6-1, 7.6-10.

Table A-5. Material Property Data Summary for 2024-T6

	E (Ksi)	μ	F_{tu} (Ksi)*	F_{ty} (Ksi)*	F_{su} (Ksi)*	F_{en} (Ksi)**	K_{IC} (Ksi$\sqrt{in.}$)
Value	10.5	0.33	64,69,70	50,57,55	41	18,18	55
Source No.***	11	11	11,2,3	11,2,6	2	2,3	6
Stress-strain curve							
Goodman diagram							
Crack propagation da/dN versus ΔK							

*A-basis.
**500E6 cycles, R = -1.
***Supporting data, Source 6, pp. 7.5-44.

Table A-6. Material Property Data Summary for 2024-T6 Alclad

	E (Ksi)	μ	F_{tu} (Ksi)*	F_{ty} (Ksi)*	F_{su} (Ksi)*	F_{en} (Ksi)**	K_{IC} (Ksi√in.)
Value	10.5	0.33	65,68	57,60	39,41	15	
Source No.***	11	11	11,2	8,1	11,2	3	
Stress-strain curve							
Goodman diagram							
Crack propagation da/dN versus ΔK							

*A-basis.
**500E6 cycles, R = -1.
***Supporting data.

Table A-7 Material Property Data Summary for 7075-T6

	E (Ksi)	μ	F_{tu} (Ksi)*	F_{ty} (Ksi)*	F_{su} (Ksi)*	F_{en} (Ksi)**	K_{IC} (Ksi√in.)
Value	10.3	0.33	78,83,83	70,73	47,48	23,20,22	28
Source No.***	11	11	11,2,3	11,2	11,2	2,3,3	3
Stress-strain curve, Source 11, pp. 3-271, 3-275							
Goodman diagram, Source 11, pp. 3-284 to 3-289 Source 7, p. 322							
Crack propagation da/dN versus ΔK, Source 6, pp. 8.9-79 to 8.9-93, Source 9, p. 79							

*A-basis.
**500E6 cycles, R = -1.
***Supporting data, Source 6, Table 8.9.2.1, Table 8.9.2.2.

Table A-8. Material Property Data Summary for 7075-T6 Alclad

	E (Ksi)	μ	F_{tu} (Ksi)*	F_{ty} (Ksi)*	F_{su} (Ksi)*	F_{en} (Ksi)**	K_{IC} (Ksi√in.)
Value	10.3	0.33	72,76	64,67	44,46	13	
Source No.***	11	11	11,2	11,2	11,2	3	
Stress-strain curve, Source 11, pp. 3-267, 3-274							
Goodman diagram							
Crack propagation da/dN versus ΔK, Source 6, pp. 8.10-15, 8.10-17							

*A-basis.
**500E6 cycles, R = -1.
***Supporting data, Source 6, Table 8.10.1.2, Table 8.2.2.2.

Table A-9. Material Property Data Summary for 7075-T651

	E (Ksi)	μ	F_{tu} (Ksi)*	F_{ty} (Ksi)*	F_{su} (Ksi)*	F_{en} (Ksi)**	K_{IC} (Ksi√in.)
Value	10.3	0.33	77,72	69,64	44		28
Source No.***	11	11	11,3	11,3	11		3
Stress-strain curve, Source 11, pp. 3-271, 3-275, 3-267							
Goodman diagram							
Crack propagation da/dN versus ΔK Source 6, pp. 8.9-97 to 8.9-119							

*A-basis.
**500E6 cycles, R = -1.
***Supporting data, Source 6, Table 8.9.13 to Table 8.9.2.1.

Table A-10. Material Property Data Summary for 7075-T651 Alclad

	E (Ksi)	μ	F_{tu} (Ksi)*	F_{ty} (Ksi)*	F_{su} (Ksi)*	F_{en} (Ksi)**	K_{IC} (Ksi√in.)
Value	10.3	0.33	74,76	62,67	42,46		
Source No.***	11	11	11,2	11,2	11,2		
Stress-strain curve, Source 11, p. 3-267							
Goodman diagram							
Crack propagation da/dN versus ΔK,							

*A-basis.
**500E6 cycles, R = -1.
***Supporting data

Table A-11. Material Property Data Summary for 7075-T73

	E (Ksi)	μ	F_{tu} (Ksi)*	F_{ty} (Ksi)*	F_{su} (Ksi)*	F_{en} (Ksi)**	K_{IC} (Ksi√in.)
Value	10.3	0.33	73	63	37		35
Source No.***	11	11	6	6	11		3
Stress-strain curve							
Goodman diagram							
Crack propagation da/dN versus ΔK Source 6, pp. 8.9-149 to 8.9-161							

*A-basis.
**500E6 cycles, R = -1.
***Supporting data, Source 6, Table 8.9.1.5 to Table 8.9.2.1.

Table A-12. Material Property Data Summary for 7475-T61

	E (Ksi)	μ	F_{tu} (Ksi)*	F_{ty} (Ksi)*	F_{su} (Ksi)*	F_{en} (Ksi)**	K_{IC} (Ksi√In.)
Value	10.3	0.33	69	64	40		
Source No.***	11	11	11	11	11		
Stress-strain curve, Source 11, p. 3-370							
Goodman diagram							
Crack propagation da/dN versus ΔK							

*A-basis.
**500E6 cycles, R = -1.
***Supporting data